

**Modelling Studies on the Impact of
Heterogeneous Ice Nucleation on
Mixed-Phase Clouds**

by

Ross James Herbert

Submitted in accordance with the requirements for the degree of Doctor of
Philosophy

University of Leeds

School of Earth and Environment

May 2014

Declaration of Authorship

The candidate confirms that the work submitted is his own, except where work which has formed part of jointly-authored publications has been included. The contribution of the candidate and the other authors to this work has been explicitly indicated below. The candidate confirms that appropriate credit has been given within the thesis where reference has been made to the work of others.

A first version of the Si-MCS model in *Chapter 2* was developed jointly by the candidate and S. Broadley, and forms part of a jointly-authored manuscript that has been published in *Atmospheric Chemistry and Physics* (details below). All subsequent development and application of the Si-MCS was performed by the candidate. The experimental data on NX-illite was obtained by S. Broadley and the data on K-feldspar was obtained by T. Whale using experiments jointly designed by the candidate and T. Whale.

Broadley S. L., Murray B. J., Herbert R. J., Atkinson J. D., Dobbie S., Malkin T. L., Condliffe E. (2012) Immersion mode heterogeneous ice nucleation by an illite rich powder representative of atmospheric mineral dust, *Atm. Chem. Phys.*, 12, pp.287-307

The derivation and development of the FROST framework in *Chapter 3*, along with the application of FROST to experimental data in *Chapter 4* was accepted for publication as a first author paper in *Atmospheric Chemistry and Physics* and is available online as a discussion paper (details below). The derivation and development of the FROST framework was carried out by the candidate. The experimental data on K-feldspar and the kaolinite MICROLITRE dataset were obtained by T. Whale; the experiments were designed jointly by the candidate and T. Whale. The manuscript was written by the candidate, and all co-authors provided comments.

Herbert, R. J., Murray, B. J., Whale, T. F., Dobbie, S. J., and Atkinson, J. D. (2014),
Representing time-dependent freezing behaviour in immersion mode ice nucleation, *Atmos.
Chem. Phys. Discuss.*, 14, 1399-1442, doi:10.5194/acpd-14-1399-2014

This copy has been supplied on the understanding that it is copyright material and that no
quotation from the thesis may be published without proper acknowledgement.

The right of Ross J. Herbert to be identified as Author of this work has been asserted by him
in accordance with the Copyright, Designs and Patents Act 1988.

© 2014 The University of Leeds and Ross J. Herbert

Acknowledgements

I would first like to thank my supervisors Ben Murray and Steven Dobbie. I am extremely grateful for the opportunity they gave me and for their continued support and guidance throughout my PhD.

Secondly I would like to acknowledge the members of my research group who have always provided an interested ear for any discussion that involves the word ice or nucleation. The same acknowledgment goes to those who had the good fortune of also being present. I would particularly like to thank Thomas Whale, Daniel O'Sullivan, and James Atkinson for the valuable discussion and advice they provided throughout my PhD, as well as Theo Wilson, Nsikanabasi Umo, Tamsin Malkin, Kelly Baustian, Hannah Price, Jo Browse, and Sarah Broadley.

I could not have reached the position in life that I am now without the support and love of my family; I could never thank you enough. I would like to thank all of my dear friends who have made the past four years some of the best in my life, with a special thanks to Tim, Erin, Tom, and Ed who have provided countless distractions. Finally I would like to thank Cat, my best friend.

Abstract

Clouds are a critical component of Earth's climate and hydrological cycle. The formation of ice in the atmosphere, especially at lower altitudes, can substantially impact the evolution of clouds and their radiative properties, and represents the initiation of the cold rain precipitation process. In mixed-phase clouds quantitatively understanding the interactions between ice and liquid, and the subsequent impact on the cloud development, is fundamentally dependent on the process of ice formation and its representation within cloud models.

Experiments show that ice nucleating particles (INPs) exhibit variability in both freezing efficiency and time-dependent behaviour. The variability in freezing efficiency is currently well characterised and represented, but variability in time-dependence is poorly characterised and rarely represented in models and parameterisations. The primary aim of this thesis is to understand the role that time-dependence plays in the freezing behaviour of droplets, and secondly to examine the sensitivity of mixed-phase clouds to time-dependence in immersion mode freezing. It is initially found that CNT-based models are unable to reproduce the observed time-dependent behaviour. A new model is therefore presented that uniquely incorporates the variability in both freezing efficiency and time-dependent behaviour; this is applied to experimental data to understand the manifestation of time-dependence in experiments. The model is then used to derive a new theoretical framework for use in experimental analysis and cloud modelling studies. The framework is underpinned by the finding that the temperature dependence (named λ) of the nucleation rate coefficient solely determines the time-dependent behaviour observed in droplet freezing experiments. New and existing experimental data is used to demonstrate the ability for the framework to reconcile data obtained on different timescales with different experimental methods. Finally, an efficient and representative parameterisation is used to explore the sensitivity of mixed-phase clouds to time-dependence. Using a series of increasingly complex models (0D to 2D) it is shown that the inclusion of time-dependence impacts cloud properties in regimes where the updraught speed is relatively low.

Contents

Chapter 1: Introduction	13
1.1 Clouds and The Earth's Energy Budget.....	13
1.2 Mixed-Phase Clouds	15
1.3 Ice Phase Interactions in Mixed-Phase Clouds	16
1.4 Ice Nucleation	17
1.5 Homogeneous Ice Nucleation	18
1.5.1 Classical Nucleation Theory	18
1.5.2 Homogeneous Ice Nucleation Measurements	20
1.6 Heterogeneous Ice Nucleation	21
1.6.1 Nucleation Pathways.....	22
1.6.2 Relative Importance of Nucleation Pathways in Mixed-Phase Clouds.....	23
1.6.3 Classical Nucleation Theory (Heterogeneous).....	24
1.6.4 Heterogeneous Nucleation Sites	25
1.6.5 Experimental Methods	26
1.6.6 Experimental Analysis	28
1.7 Observations and Sources of INPs	29
1.8 Characteristics of INP Species Determined from Experiments	33
1.8.1 Temperature Dependence	33
1.8.2 Time Dependence in the Immersion Mode.....	34
1.8.2.1 Cooling-Rate Dependence	35
1.8.2.2 Residence-Time Dependence.....	36
1.8.2.3 Freeze-Thaw Experiments	38
1.9 Heterogeneous Freezing Models.....	39
1.9.1 The Single-Component Stochastic Model	39
1.9.2 Singular Freezing Model.....	39
1.9.3 Multiple-Component Stochastic Models.....	41
1.10 Modelling Studies of Heterogeneous Ice Nucleation.....	44
1.10.1 Immersion Mode Freezing Schemes.....	44
1.10.2 Importance of Time-Dependence.....	47
1.11 Aims of Thesis	51
Chapter 2: The Simplified Multiple Component Stochastic (Si-MCS) Model	53
2.1 Introduction.....	53

2.2	CNT-based MCS Models	53
2.2.1	Cooling-Rate Dependence in CNT-based MCS Models	55
2.2.1.1	Using a CNT-based MCS Model to Reproduce NX-illite Freezing Data	58
2.2.1.2	Using a CNT-based MCS Model to Reproduce K-feldspar Freezing Data.....	61
2.3	A New Simplified MCS Model	62
2.3.1	Deriving the Si-MCS Model.....	63
2.3.2	Applying the Si-MCS to Experimental Data	66
2.3.2.1	NX-illite Mineral Dust.....	66
2.3.2.2	K-feldspar Mineral Dust	68
2.3.3	The Manifestation of Time-Dependence	70
2.3.3.1	Cooling-Rate Dependence	71
2.3.3.2	Residence-Time Dependence	75
2.3.3.3	Freeze-Thaw Variability	77
2.4	Conclusions	79

Chapter 3: The Framework for Reconciling Observable Stochastic Time-Dependence (FROST)

3.1	Introduction	81
3.2	Deriving the Framework.....	81
3.2.1	Cooling-Rate Dependence	82
3.2.2	Extending to Residence-Time Dependence.....	85
3.2.3	Reconciling Isothermal Experiments with Cooling Experiments.....	86
3.2.4	The FROST Framework	89
3.3	Incorporating the FROST Framework into a Singular Model.....	90
3.4	Conclusions	93

Chapter 4: Reconciling Time Dependencies in Experimental Data using FROST

4.1	Introduction	95
4.2	Immersion Mode Terminology.....	95
4.3	Application of the FROST Framework with Experimental Data	97
4.3.1	Kaolinite Data (KGa-1b) from Two Cold-Stage Instruments	97
4.3.2	K-feldspar Data from a Cold-Stage Instrument.....	101
4.3.3	Mineral Dust Freezing Experiments using the ZINC CFDC Instrument	105
4.3.4	Volcanic Ash from ZINC and AIDA.....	108
4.4	The Sensitivity of Freezing Probability to the Time-Dependence of Nucleation....	111
4.5	Comparing the Time-Dependencies of Atmospherically Relevant INPs	112
4.6	Implications for In-situ INP Measurements	114

4.7	Conclusions.....	118
Chapter 5: Time-Dependence Sensitivity Studies using a Cloud Model with Detailed Microphysics		121
5.1	Introduction.....	121
5.2	Model Description and Development	121
5.2.1	Incorporating the FROST framework	123
5.2.2	Mixed-Phase Cases	124
5.3	0D Modelling Studies	128
5.4	1D Modelling Studies	138
5.4.1	Stratus Cases	138
5.4.1.1	Mixed1 – SHEBA Profile	138
5.4.1.2	Mixed3 – SHEBA Profile	140
5.4.1.3	Comparisons to M-PACE Profile	142
5.4.2	Convective Cases	145
5.4.2.1	Deep1 Convective Case ($w_{\max} = 10 \text{ m s}^{-1}$).....	145
5.4.2.2	Comparison to Slowly Ascending Clouds ($w_{\max} = 5 \text{ cm s}^{-1}$).....	147
5.4.2.3	Deep2 Case	149
5.5	2D Modelling Studies	150
5.5.1	Stratocumulus ISDAC Case.....	150
5.5.2	Squall Line Case	156
5.6	Conclusions.....	163
Chapter 6: Conclusions, Implications, and Further Work		165
6.1	Summary of Results.....	165
6.2	Implications for Experimental Measurements	168
6.3	Implications for Modelling Ice Formation in the Atmosphere	170
6.4	Further Work.....	172
6.4.1	Improving Knowledge of Fundamental Heterogeneous Ice Nucleation Mechanisms	172
6.4.2	The Continued Characterisation of Atmospherically Relevant INP Species..	172
6.4.3	Improving the Representation of Ice Nucleation in Models	173
References		175

List of Tables

Table 1.1. Range of INP species tested by Wright et al. (2013) with the corresponding range of cooling rates used and the gradient between the shift in temperature ΔT and the change in cooling rate $\Delta \log r$	36
Table 4.1. Values of λ from various immersion mode studies. λ determined using the FROST framework.	113
Table 5.1. Constants for J_v in Eq. (5.2).	123
Table 5.2. Summary of each set of simulations performed.	128
Table 5.3. Description of the hydrometeor mass growth sources referred to in the chapter.	134

List of Figures

Figure 1.1. Characteristics of clouds that can influence their radiative properties.	13
Figure 1.2. Radiative forcing bar chart for the period 1750–2011.....	15
Figure 1.3. Gibbs free energy as a function of ice germ radius and temperature.	19
Figure 1.4. Graphic representation of the heterogeneous ice nucleation pathways.	22
Figure 1.5. Schematic of a typical cold-stage instrument.	27
Figure 1.6. Atmospheric observations of INP concentrations from various studies.....	30
Figure 1.7. Graphic showing relative contributions from in-situ observations.....	30
Figure 1.8. $n_s(T)$ for a range of atmospheric INPs	34
Figure 1.9. $J(T)$ determined from droplets containing kaolinite.....	36
Figure 1.10. Fraction frozen for populations of droplets containing a 400nm kaolinite particle in the ZINC instrument.	37
Figure 1.11. CNT-based freezing models.	43
Figure 1.12. Simulated ice number concentration in a parcel model using three different immersion freezing schemes.....	47
Figure 1.13. Modelled ice number concentration (a), IWC and LWC (b), and IWC/LWC ratio (c) for five different freezing models in a parcel model with polydisperse INP population.....	48
Figure 2.1. Heterogeneous nucleation rate coefficient J_s against temperature T derived using CNT for a range of contact angles $40 \leq \theta \leq 180$	54
Figure 2.2. Examples of various PDFs used in CNT-based MCS models.....	55
Figure 2.3. A conceptual diagram of how the cumulative fraction frozen (f) changes upon an increase in cooling rate.	56
Figure 2.4. Sensitivity of f to variables in a CNT-based θ PDF model.....	56
Figure 2.5. How the gradient $d\ln(J_s)/dT$ determines the cooling-rate dependence	57
Figure 2.6. NX-illite cooling rate and isothermal data.....	59
Figure 2.7. Reproducing NX-illite data using a CNT-based θ PDF model.	60
Figure 2.8. The gradient $\lambda = -d\ln(J_s)/dT$ as a function of contact angle and temperature derived using CNT.....	61
Figure 2.9. Reproducing K-feldspar cooling data using a CNT-based θ PDF model.....	62
Figure 2.10. Principles of the Simplified MCS (Si-MCS) model.....	63
Figure 2.11. Reproducing NX-illite cooling and isothermal data using the Si-MCS model.	67
Figure 2.12. Reproducing K-feldspar cooling data using the Si-MCS model.	69
Figure 2.13. Reproducing K-feldspar isothermal data using the Si-MCS model..	70
Figure 2.14. The simulated change in the $f(T)$ curve upon a change in cooling rate from 1 to $10 \text{ }^\circ\text{C min}^{-1}$ for two INPs.	71

Figure 2.15. Sensitivity of β (a) and f_{diff} (b) to the temperature dependence of the nucleation rate (λ) and the PDF mean (μ_{normal}) in the Si-MCS model	72
Figure 2.16. Sensitivity of β (a) and f_{diff} (b) to the temperature dependence of the nucleation rate (λ) and the PDF standard deviation (σ_{normal}) in the Si-MCS model.....	73
Figure 2.17. The shift in the $f(T)$ curve, by β °C, upon a factor of ten change in cooling rate for a number of simulations using the Si-MCS model.....	74
Figure 2.18. Simulated decay in liquid droplets ($1 - f$) over time using the Si-MCS model at two temperatures and an increasing diversity of nucleating efficiency.....	75
Figure 2.19. The impact of λ and φ diversity in isothermal simulations using the Si-MCS model as a function of isothermal temperature.	77
Figure 2.20. The resulting standard deviation ($\sigma_{T,\text{freeze}}$) of freezing temperatures for a single droplet frozen over 10^4 freeze-thaw cycles	78
Figure 4.1. Normalised freezing rates $R_s(T)$ values determined from cooling experiments with a range of cooling rates.using kaolinite.....	98
Figure 4.2. The exponential decay of liquid droplets during an isothermal experiment at -18 °C together with an isothermal simulation using kaolinite.....	99
Figure 4.3. Kaolinite cooling experiment data and FROST	100
Figure 4.4. Fitting CNT to PICOLITRE and MICROLITRE experimental data.	101
Figure 4.5. K-feldspar cooling experiment data and FROST	103
Figure 4.6. K-feldspar isothermal experiment data and FROST.	104
Figure 4.7. kaolinite (FLUKA) ZINC CFDC experiment data and FROST.	106
Figure 4.8. Simulated kaolinite (FLUKA) data using FROST.....	107
Figure 4.9. The resulting equivalent function of $n_s(T)$ for different cooling rates using the FROST framework and directly fitting to the experimental data	108
Figure 4.10. Volcanic ash experiment data and FROST	109
Figure 4.11. Values of λ determined from different studies	112
Figure 4.12. The equivalent in-cloud updraught speed as a function of instrument residence time and λ	116
Figure 4.13. The percentage difference in measured and predicted INP concentration when time-dependence is not taken into account for a range of simulated updraught speeds	117
Figure 5.1. The prescribed vertical updraught speeds used for the various 1D simulations.	125
Figure 5.2. The resulting profiles of T and $\text{RH}_{\text{liquid}}$ used for the various 1D simulations.....	126
Figure 5.3. The initial prescribed domains of w , T , and $\text{RH}_{\text{liquid}}$ used in the 2D simulations	127
Figure 5.4. Evolution of several hydrometeor species (right-to-left) throughout a series of simulations of constant $w_{\text{equivalent}}$	131
Figure 5.6. Evolution of IWC and LWC throughout a series of simulations	132

Figure 5.7. The absolute difference between the $\lambda_{5,0}$ and $\lambda_{0,5}$ simulations	133
Figure 5.8. The mass growth rate as a function of T	134
Figure 5.9. Mean number concentrations and mixing ratios for cloud hydrometeor species as a function of $w_{\text{equivalent}}$ and λ	135
Figure 5.10. Same as Figure 5.9 but for the mean diameter of cloud droplets, rain droplets, and cloud ice.....	136
Figure 5.11. Mean number concentrations and mixing ratios for cloud hydrometeor species as a function of $w_{\text{equivalent}}$ and λ	137
Figure 5.12. 1D_m1SHEBA simulations: Total column mass path of cloud ice, snow, and cloud water as a function of λ	139
Figure 5.13. 1D_m1SHEBA simulations: evolution of IWP, LWP, and cumulative number of liquid droplets frozen as a function of simulation time for a range of λ	140
Figure 5.14. Same as Figure 5.12 but for 1D_m3SHEBA simulations.	141
Figure 5.15. Same as Figure 5.13 but for 1D_m3SHEBA simulations.	142
Figure 5.16. Comparison of IWP evolution as a function of λ for the four 1D stratus cases....	142
Figure 5.17. Same as Figure 5.16 but for LWP..	143
Figure 5.18. Same as Figure 5.16 but for characteristic diameter of cloud water.....	144
Figure 5.19. Same as Figure 5.16 but for characteristic diameter of cloud ice.....	145
Figure 5.20. 2D_d1w10 simulations: total column mass path of cloud ice, snow, and cloud water as a function of λ	146
Figure 5.21. Same as Figure 5.20 but showing a comparison between the 1D_d1w10 and 1D_d1w005 simulations	148
Figure 5.22. The fractional difference of iMP, sMP, cMP, and D_c	148
Figure 5.23. 1D_d2 simulations: total column mass path of cloud ice, snow, and cloud water as a function of λ	149
Figure 5.24. Horizontally averaged mixing ratio profiles for cloud ice and snow from the 2D_ISDAC simulations	151
Figure 5.25. Horizontally averaged growth rate profiles for different sources of snow mass from the 2D_ISDAC simulations after 2 hrs	151
Figure 5.26. Cloud ice, snow, and cloud water mass paths as a function of λ in the 2D_ISDAC simulations.....	152
Figure 5.27. Same as Figure 5.26 but for simulations using the nucleation rate of the mineral dust kaolinite.....	153
Figure 5.28. Same as Figure 5.26 but for simulations using a surface area per droplet s_{K-fe} of $1 \times 10^{-7} \text{ cm}^2$	154
Figure 5.29. Comparison of horizontally averaged immersion mode freezing rate profiles between the three sets of simulations using the 2D_ISDAC case.....	154

Figure 5.30. A comparison of horizontally averaged growth rate profiles for snow between simulations where the surface area per droplet s was increased by a factor of 100. 155

Figure 5.31. Ice mass path as a function of λ throughout the evolution of the cloud. 157

Figure 5.32. Horizontally averaged growth rate profiles for cloud ice mass sources..... 158

Figure 5.33. Snow mass path as a function of λ throughout the evolution of the cloud..... 159

Figure 5.34. Horizontally averaged growth rate profiles for cloud snow mass sources 159

Figure 5.35. Graupel mass path (a), rain mass path (b), cloud water mass path (c), and total ice water path (d) as a function of λ 160

Figure 5.36. Ice mass path as a function of λ throughout the evolution of the cloud for the 2D_SQUALL_sa simulations where s_{K-fe} was increased to $1 \times 10^{-7} \text{ cm}^2$ 161

Figure 5.37. Same as Figure 5.36 but for the snow mass path in the 2D_SQUALL_sa simulations..... 162

Figure 5.38. Comparing snow mass growth rate profiles from 2D_SQUALL simulations and 2D_SQUALL_sa simulations..... 162

Abbreviations

AIDA	The A erosol I nteraction and D ynamics in the A tmosphere <i>chamber</i>
ATD	A rizona T est D ust
CCN	C loud C ondensation N uclei
CFDC	C ontinuous F low D iffusion C hamber
CNT	C lassical N ucleation T heory
CRM	C loud R esolving M odel
CSU	C olorado S tate U niversity
FROST	F ramework for R econciling O bservable S tochastic T ime-dependence
GCM	G eneral C irculation M odels
HM	H allet- M ossop <i>process</i>
INP	I ce N ucleating P article
IWC	I ce W ater C ontent
IWP	I ce W ater P ath
KiD	K inematic D river <i>model</i>
LWC	L iquid W ater C ontent
LWP	L iquid W ater P ath
LWR	L ongwave R adiation
MCS	M ultiple- C omponent S tochastic <i>model</i>
MP	M ass P ath (prefixed with either <i>i</i> , <i>s</i> , <i>g</i> , <i>c</i> , or <i>r</i> depending on hydrometeor species)
PDF	P robability D ensity F unction
RH	R elative H umidity
RMSE	R oot- M ean- S quare- E rror
SCS	S ingle- C omponent S tochastic <i>model</i>
Si-MCS	S implified M ultiple- C omponent S tochastic <i>model</i>
SWR	S hortwave R adiation
WBF	W egener- B ergeron- F indeisen <i>process</i>
ZINC	Z urich I ce N ucleating C hamber

Chapter 1: Introduction

1.1 Clouds and The Earth's Energy Budget

The Earth's energy budget is determined by the flux of incoming solar shortwave radiation (SWR) and the fluxes of thermal longwave radiation (LWR) within the atmosphere. Clouds at all altitudes play a substantial role in the transmittance of SWR and LWR through the atmosphere. Around 22 % of the incoming SWR is reflected back to space by clouds. Within the atmosphere clouds also interact with the outgoing LWR and act to absorb, re-emit, and scatter the radiation, thus trapping a proportion of the energy within the atmosphere.

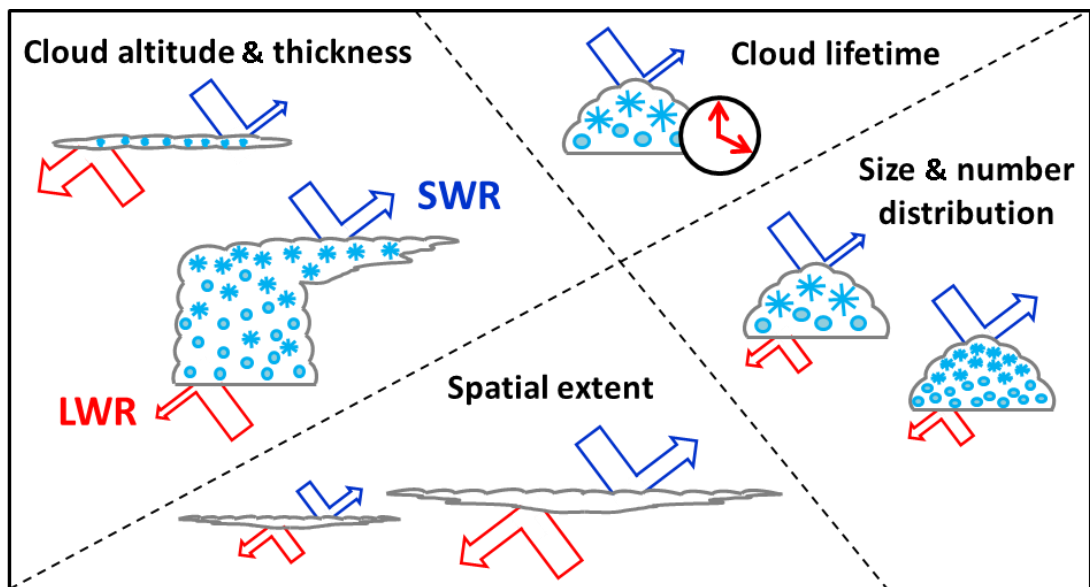


Figure 1.1. Characteristics of clouds that can influence their radiative properties.

The radiative properties of clouds, graphically represented in Figure 1.1, are governed by several factors including the size and number concentration of hydrometeors, the phase of hydrometeors, spatial extent, thickness, and altitude. Clouds close to the surface generally reflect a high fraction of incoming SWR, and exert a negative radiative effect on the climate. High altitude clouds such as cirrus are often optically thin, and do not reflect much incoming SWR. However, due to their cold temperature any absorbed outgoing LWR is

re-emitted with a much lower energy, and thus these clouds exert a positive radiative effect on the climate. Boucher et al. (2013) have estimated a global annual mean radiative effect of -20 W m^{-2} due to cloudy conditions, with clouds therefore having a net cooling effect on the Earth.

Clouds can therefore be seen as a critical component of Earth's climate, especially in a changing climate where an increase in mean surface air temperature may have substantial impacts on the development and evolution of clouds. General Circulation Models (GCMs) numerically simulate the atmosphere and are used to reproduce and forecast long-term changes in the climate. These models provide us with the best estimate of how changes in atmospheric constituents, such as an increase in CO_2 , will impact the climate in the future and subsequent results are commonly used to inform governments and influence policy. A single GCM grid cell is typically 50 to 100 km in the horizontal and 15 km in the vertical (Boucher et al., 2013). There are many sub-grid scale processes (e.g., convection, turbulence, scavenging, precipitation mechanisms, aerosol activation, ice formation) that are either parameterised or neglected; the feedbacks and interactions between these processes occur on microphysical scales that currently cannot be represented within GCMs (Bodenschatz et al., 2010; Ma et al., 2012). Consequently, feedbacks on clouds due to climate change are seen as a major uncertainty (Cess et al., 1989; Randall et al., 2003; Bony et al., 2006).

Mixed-phase clouds, where supercooled water co-exists with ice, are found at all latitudes (Hogan et al., 2004; Nasiri and Kahn, 2008; Hu et al., 2010; Boucher et al., 2013) and observational studies commonly report the existence of supercooled liquid layers at temperatures down to $-35 \text{ }^\circ\text{C}$ (Hogan et al., 2004; Hu et al., 2010; Kanitz et al., 2011). These cloud types represent a large proportion of the cloud-climate feedback uncertainty due to poorly understood microphysical processes that primarily include the initial formation of ice, but also the subsequent in-cloud interactions and feedbacks on cloud properties. This is reflected in Figure 1.2 where each bar represents the best estimate of the radiative forcing due to specific components in the atmosphere between 1750 and 2011. The interactions and feedbacks between aerosol and clouds (expressed as an effective

radiative forcing) remains a significant uncertainty, with the 5 to 95 % confidence range spanning -1.2 to 0.0 W m^{-2} ; reflecting a low level of confidence.

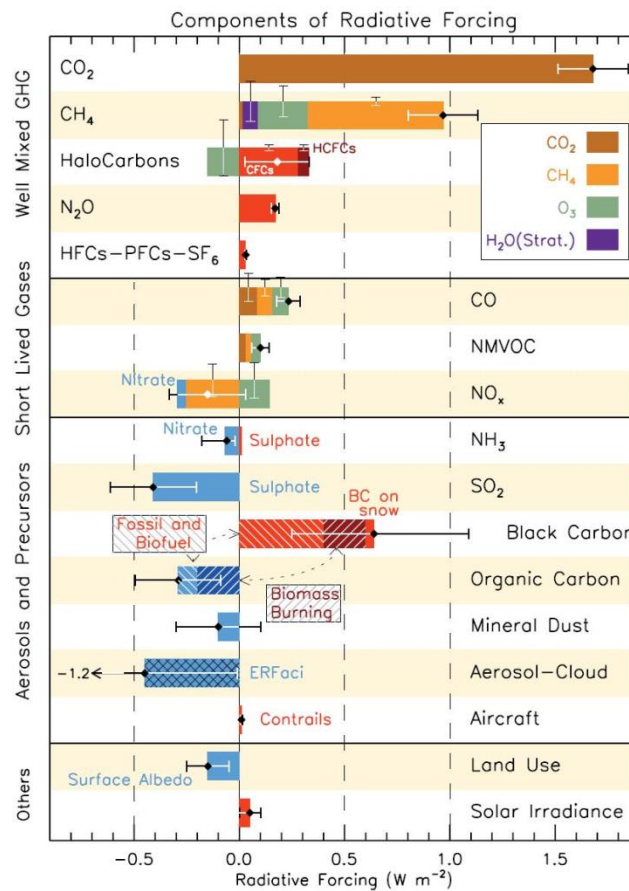


Figure 1.2. Radiative forcing bar chart for the period 1750–2011 based on emitted compounds (gases, aerosols or aerosol precursors) or other changes. Red (positive forcing) and blue (negative forcing) are used for emitted components which affect few forcing agents, whereas for emitted components affecting many compounds several colours are used as indicated in the inset at the upper part of the figure. The vertical bars indicate the relative uncertainty of the radiative forcing induced by each component; reproduced from Myhre et al. (2013) Fig. 8.17 (pg 698).

1.2 Mixed-Phase Clouds

Observations of mixed-phase clouds show diversity in characteristic properties. At high latitudes (e.g., the Arctic) the freezing level is at the surface, so any liquid cloud that forms will be supercooled. Low level ($< 2 \text{ km}$) clouds, such as stratus and stratocumulus, have low updraught velocities ($< 10 \text{ cm s}^{-1}$) and are typically long-lived with low ice number concentrations; McFarquhar et al. (2007) measured average concentrations of 1.6 to 5.6 L^{-1} . In mid-latitudes the large-scale ascent of an air mass above the freezing level can result in persistent mixed-phase stratus clouds with low updraught velocities (~ 5 to 10 cm s^{-1}); Crosier et al. (2011) observed an average ice number concentration of 0.2 L^{-1} in southern

England and Hobbs and Rangno (1985) observed similar concentrations in North America. Similarly formed mixed-phase clouds are also found in the tropics at altitudes of 4 to 8 km (Riihimaki and McFarlane, 2010). In convective and frontal systems the clouds can extend to greater altitudes (up to 12 km) and contain updraught velocities ranging from $\sim 1 \text{ m s}^{-1}$ in cumulus to $> 10 \text{ m s}^{-1}$ in cumulonimbus clouds; these velocities result in high cloud liquid water content, cold cloud top temperatures and high number concentrations (e.g., $> 100 \text{ L}^{-1}$ (Hobbs and Rangno, 1985)).

1.3 Ice Phase Interactions in Mixed-Phase Clouds

The formation of ice in a supercooled liquid cloud can impact its subsequent development and evolution in several ways and is primarily dependent on the existing cloud properties. These include the concentration and composition of aerosol present, existing size and number distribution of cloud hydrometeors, temperature, cloud dynamics, and available water vapour.

Precipitation processes are closely linked to the presence of ice particles, and in particular the process of primary ice formation which initiates glaciation of the cloud. Ice crystals are known to have a lower equilibrium water vapour pressure than supercooled liquid water droplets. As a consequence under supersaturated conditions with respect to ice newly formed ice particles can grow at the expense of the evaporating liquid droplets - known as the Wegener-Bergeron-Findeisen (WBF) process. In clouds where the total water content is high and the number of ice particles small, these ice particles can grow to precipitable sizes and thus enhance precipitation and modify cloud lifetime. The WBF process is thought to be the main pathway for precipitation in mixed-phase clouds ((Pruppacher and Klett, 1997), hereafter PK97, Ch. 1), and importantly, is a process that depends on the presence of pre-existing ice particles.

Secondary ice formation (the multiplication of a single ice particle) occurs either from fragmented ice crystals as a result of evaporation or collisions (Vardiman, 1978) or from the ejection of ice splinters during the process of riming, where sedimenting ice particles collect supercooled droplets. This is thought to occur between -3 and $-8 \text{ }^\circ\text{C}$ and is known as the

Hallett-Mossop (HM) process (Hallett and Mossop, 1974). Modelling studies have shown that providing there is sufficient supercooled water the HM process can multiply the existing number ice crystals by several orders of magnitude (Phillips et al., 2003), which leads to a modification of the cloud hydrometeor size distribution and precipitation. Again, this process will be sensitive to the formation of primary ice particles.

A modification to the size and number distribution of cloud hydrometeors, which includes the WBF and HM process, can have a direct impact on the optical properties of the cloud. Precipitation intensity, onset, and duration can be enhanced or suppressed, which can lead to a modification of the cloud lifetime. The process of riming can alter the size distribution of hydrometeors, and graupel production and subsequent interaction with ice particles is thought to be the mechanism behind cloud electrification.

The freezing of liquid, and the associated latent heat, can enhance cloud updrafts allowing cloud tops to reach higher altitudes (and thus a colder temperature), whereas the melting of precipitation below the cloud base can create strong downdrafts and cold pools that may trigger new convective cells (Tompkins, 2001). These processes can substantially alter the microphysical characteristics of the cloud and therefore its radiative properties.

Interactions and feedbacks between aerosol, ice, and liquid in mixed-phase clouds need to be quantitatively understood and sufficiently represented in models in order to predict the behaviour of developing systems, and predict the response of mixed-phase clouds to changes in the climate. The fundamental process of primary ice formation along with knowledge of cloud microphysical properties is integral to understanding the extent to which the subsequent interactions impact the cloud development and radiative properties.

1.4 Ice Nucleation

Primary ice formation is the transition from the metastable parent phase (liquid or gas) to the stable solid phase via nucleation. This is thought to occur as a result of random fluctuations of embryonic ice-like germs of molecules within the parent phase. With

continued growth of a germ (via collisions and aggregation) a critical size is reached where the new phase is energetically more favourable and the germ grows into a macroscopic crystal. Homogeneous nucleation occurs within the bulk phase of supercooled liquid, whereas heterogeneous nucleation occurs on the surface of a particle either in the supercooled liquid or supersaturated gas phase. These two nucleation modes will be discussed in Sections 1.5 and 1.6.

1.5 Homogeneous Ice Nucleation

In the atmosphere liquid droplets are observed to supercool to temperatures below $-38\text{ }^{\circ}\text{C}$ before freezing occurs. The presence of dissolved solutes in the droplet has also been observed to depress the freezing temperature (Koop, 2004). These processes will play an important role in cloud formation and development in the upper troposphere and therefore represent an important radiative component of the Earth's energy budget. The homogeneous freezing temperature is also the point at which the cloud will inevitably glaciate, and defines the lower temperature limit to the mixed-phase regime.

1.5.1 Classical Nucleation Theory

In a pure water droplet (i.e., no solid inclusions or solutes) the energy barrier required for a freezing event to occur is suggested to be a result of the Gibbs free energies for forming the ice-liquid surface interface and the volume transition from liquid to ice. Classical Nucleation Theory (CNT) is a thermodynamic framework that was developed to calculate and extrapolate these energies under changing conditions. Assuming that ice germs can be approximated by a sphere with macroscopic properties then following PK97 (Ch. 7) the surface interface free energy (G_S) can be expressed as

$$G_S = 4\pi r_i^2 \gamma_{i/w} \quad (1.1)$$

where r_i is the radius of the ice germ and $\gamma_{i/w}$ is the interfacial energy between ice and liquid water. Similarly, the transition energy of the volume (G_V) can be expressed as

$$G_V = -\frac{4\pi r_i^3}{3v_i} k_B T \ln S_i \quad (1.2)$$

where v_i is the volume of water molecule in ice, k_B is the Boltzmann constant, T is the temperature in Kelvin, and S_i is the saturation ratio with respect to ice. The summation of Eqs. (1.1) and (1.2) provide us with the total Gibbs free energy (ΔG) of the energy barrier:

$$\Delta G = -\frac{4\pi r_i^3}{3v_i} k_B T \ln S_i + 4\pi r_i^2 \gamma_{i/w} \quad (1.3)$$

A plot of ΔG and the two components at 270 K is plotted in Figure 1.3a. As the radius of the ice germ increases the magnitude of G_V and G_S increases, but due to different dependencies on r_i there exists a maximum value of ΔG . This maximum at ΔG^* is associated with a critical radius r_i^* , at which point growth of the ice germ is energetically favourable. The dependence of ΔG^* on temperature is shown in Figure 1.3b. The amount of energy required for a freezing event to occur strongly decreases with decreasing temperature.

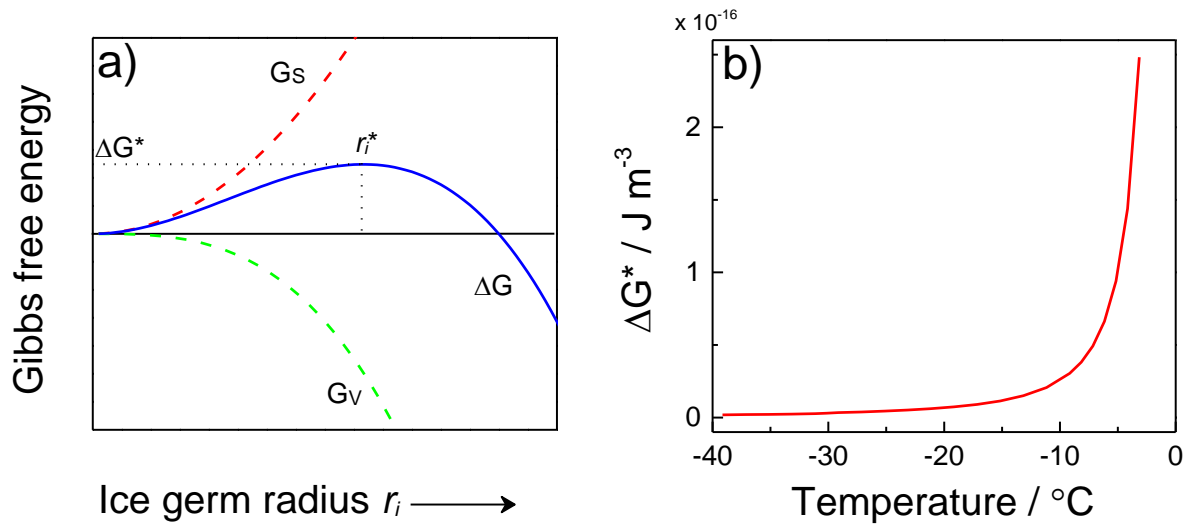


Figure 1.3. (a) shows the Gibbs free energy as a function of ice germ radius; the red (green) dashed line represents the surface (volume) energies and the blue solid line represents the summation of these two terms. The dotted line marks the critical radius and associated critical Gibbs free energy. (b) shows how the critical Gibbs free energy varies with temperature.

Setting the derivative $d\Delta G/dr_i = 0$ in Eq. (1.3) and solving for r_i provides the critical radius (r_i^*) required for an event to occur:

$$r_i^* = \frac{2\gamma_{i/w}v_i}{k_B T \ln S_i} \quad (1.4)$$

and substituting back into Eq. (1.3) provides an expression for the critical Gibbs free energy (ΔG^*) at a given temperature:

$$\Delta G^* = \frac{16\pi\gamma_{i/w}^3 v_i^2}{3(k_B T \ln S_i)^2} \quad (1.5)$$

The nucleation rate for the formation of critical germs per unit volume per unit time, J_v , can then be expressed as:

$$J_v(T) = A \cdot \exp\left(-\frac{\Delta G^*(T)}{k_B T}\right) \quad (1.6)$$

where A is a kinetic factor that accounts for the flux of water molecules to the ice germ interface and the energy required for the reorientation of the molecule associated with the phase transition. This can be calculated following PK97:

$$A = \frac{k_B T}{h} \exp\left(-\frac{\Delta F_{diff}}{k_B T}\right) n_{h_2o} \quad (1.7)$$

where h is the Planck constant, ΔF_{diff} is the diffusion energy across the liquid-ice interface, and n_{h_2o} is the number density of molecules in the bulk liquid. Various expressions for A have been proposed as well as additional factors in Eq. (1.6) that act to refine the expression (see PK97 Ch. 7 and references therein).

1.5.2 Homogeneous Ice Nucleation Measurements

The probability for a critical germ to form in the liquid phase will increase with the volume of the droplet, and as the growth is governed by the random fluctuations in attachment and

detachment of water molecules, the system is stochastic and the probability will also increase for longer periods of time. Assuming that a single critical germ causes the freezing process the rate of change in the number of droplets can be expressed as

$$\frac{dN_l}{N_l} = -J_v V dt \quad (1.8)$$

where N_l is the number of liquid droplets, V the volume of the droplet, and dt the change in time. The number of droplets that freeze (N_f) in a given period of time (t) can be expressed upon integration of Eq. (1.8) and rearranging:

$$\int_{N_{l,1}}^{N_{l,2}} \frac{1}{N_l} dN_l = \int_{t_1}^{t_2} -J_v V dt \quad (1.9)$$

$$\ln \frac{N_{l,2}}{N_{l,1}} = -J_v V t \quad (1.10)$$

$$1 - \frac{N_f}{N_{l,1}} = \exp(-J_v V t) \quad (1.11)$$

$$f_{ice} = \frac{N_f}{N_l} = 1 - \exp(-J_v V t) \quad (1.12)$$

where $N_{l,2} = N_{l,1} - N_f$, and f_{ice} is the fraction of N_l droplets frozen after a duration of time. Essentially $\exp(-J_v V t)$ describes the probability that a freezing event will not occur (P_{not}) so conversely $1 - P_{not} = P$ where P is the probability of a freezing event occurring. Equation (1.12) provides a means for experimentally determining J_v if the volume of the droplet is known.

1.6 Heterogeneous Ice Nucleation

The formation of ice via homogeneous nucleation occurs at supercooled temperatures below ~ -38 °C; however, ice is commonly observed to form at warmer temperatures. The provision of a surface for the ice germ to form on (within either a supercooled droplet or supersaturated water vapour) can reduce the energy barrier required for a critical germ to develop. This is known as heterogeneous nucleation and can occur via several different

pathways (shown in Figure 1.4) depending on the interaction between the ice nucleating particle (INP) and the metastable parent phase. The following descriptions follow those of Vali (1985).

1.6.1 Nucleation Pathways

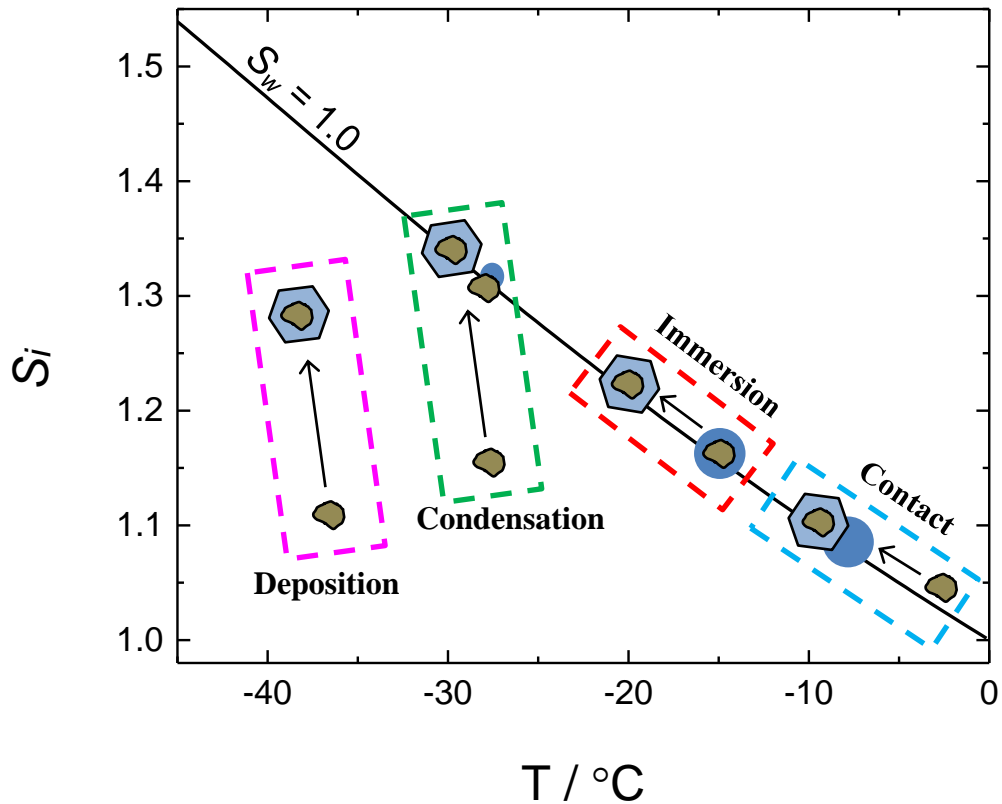


Figure 1.4. Graphic representation of the heterogeneous ice nucleation pathways with respect to temperature and ice supersaturation S_i . Solid line is the water saturation line where $S_w = 1.0$. All modes occur at or above the water saturation line except for deposition.

Deposition mode occurs when an ice germ nucleates directly from the vapour phase onto the INP in conditions where the water vapour pressure is supersaturated with respect to ice but subsaturated with respect to water.

In *immersion mode* freezing the INP is internally immersed within a supercooled water droplet prior to freezing; likely as a result of either previous activation as a cloud condensation nucleus (CCN), melting of heterogeneously frozen ice particles, or an aerosol

scavenging process. Upon a change in temperature or time the immersed particle acts as a nucleation site.

The process of *contact mode* freezing is a result of the INP coming into contact with the supercooled droplet surface; either from an external collision or through an internal process where the particle comes into contact with the liquid-vapour interface through freezing cycles or droplet evaporation (Durant and Shaw, 2005; Fornea et al., 2009). In-cloud collisions can arise as a result of Brownian motion, diffusiophoresis, electrophoresis, or thermophoresis forces (PK97 Ch. 17); the latter is thought to be the more important source (Phillips et al., 2007).

Condensation mode occurs as the result of an INP being activated as a CCN under supercooled conditions. During the condensation process the partially immersed INP acts as a nucleation site with the resulting critical ice germ forming on the particle-liquid interface. This mode is often combined with immersion mode, in the assumption that the INP becomes fully activated as a CCN and therefore fully immersed within a droplet.

1.6.2 Relative Importance of Nucleation Pathways in Mixed-Phase Clouds

Observational studies of clouds above homogeneous freezing temperatures show strong evidence that water saturation is a pre-requisite for the formation of ice, which suggests that deposition mode nucleation plays a minor role. During the SAMUM campaign Ansmann et al. (2009) reported that in 99 % of observed cases the initiation of ice in altocumulus at Cape Verde occurred within the liquid cloud top. Based on observations from the M-PACE campaign Prenni et al. (2009a) concluded that only heterogeneous pathways that act at or above water saturation played a major role in ice formation above $-30\text{ }^{\circ}\text{C}$ with the immersion or condensation mode dominating. Westbrook and Illingworth (2011) analysed 4 years of lidar and radar observations in Southern England and found that in 95 % of cases where cloud ice formed above $-20\text{ }^{\circ}\text{C}$, the ice originated from supercooled liquid clouds. Similarly, using lidar, radar, and microwave observations of arctic stratiform clouds de Boer et al. (2011) found that ice was not observed until after a liquid layer formed. Ansmann et al. (2005) presented lidar observations of an altocumulus above Leipzig, Germany. The

authors found that ice was being produced in the edges of the clouds and in downdraught regions. It was hypothesised that contact mode freezing played a dominant role due to the absence of ice in the cloud interior. However, several modelling studies have shown contact mode freezing is not dominant in many mixed-phase clouds. Cui et al. (2006) and Phillips et al. (2007) used cloud resolving models (CRMs) to simulate deep convective clouds and found that contact mode freezing made little contribution to the production rate of ice. Using a GCM that included an ice nucleation scheme Hoose et al. (2010) found that immersion mode freezing was the dominant process, followed by contact mode. Similarly, using a 1D kinematic framework with detailed microphysics Field et al. (2012) found that observed INP concentrations of a lee wave cloud were best reproduced by immersion/condensation mode freezing (a single parameterisation was used to describe the cumulative production rate). Following these observations and results this thesis will focus on immersion mode freezing due to its potential primary atmospheric importance.

1.6.3 Classical Nucleation Theory (Heterogeneous)

The CNT thermodynamic framework discussed in Sect. 1.5.1 can be extended to include the inclusion of a solid nucleus. This nucleus provides a site for the germ formation to occur and can enhance the probability that an ice germ of critical size will be reached. The inclusion therefore acts to reduce the energy barrier required for the critical size to be achieved. This effect can be incorporated into Eq. (1.6) as a ‘compatibility’ factor, F_c , that represents the substrate’s ability to enhance the probability of a critical germ formation. The nucleation rate for the formation of critical germs per unit surface area per unit time (J_s) can therefore be expressed as

$$J_s(T) = A \cdot \exp\left(-\frac{\Delta G^*(T) \cdot F_c}{k_B T}\right) \quad (1.13)$$

For the immersion mode ΔG^* and A can be calculated using the expression for homogeneous nucleation; Eqs. (1.5) and (1.7) respectively. With regards to the compatibility factor a value $F_c = 1$ would describe a surface that has no effect on the energy barrier (as compared to homogeneous), whereas $F_c \rightarrow 0$ describes an increasing ability to

reduce the energy barrier. To relate this ability to a physical property a conceptual function that relates a wettability parameter to describe F_c has been proposed:

$$F_c = \frac{(2 + \cos \theta)(1 - \cos \theta)^2}{4} \quad (1.14)$$

where θ is the contact angle of a spherical ice germ in contact with the substrate. This is a widely used parameter that is adjusted to fit to experimental data, with the contact angle θ being a reported quantity. This conceptual ‘contact-angle’ model has a significant weakness in the assumed geometric form of the ice germ but it does provide a parameter that is able to describe the relative ability for a substrate to catalyse nucleation.

Assuming that the probability of a critical germ forming on a substrate increases with surface area and that $J_s(T) \gg J_v(T)$ then following Eq. (1.12) the fraction of droplets, or particles, that freeze after a given period of time can be expressed as

$$\frac{N_f}{N_l} = f_{ice} = 1 - \exp(-J_s(T)st) \quad (1.15)$$

where s is the surface area of the available INP and N_l is the number of droplets containing an immersed INP. As in Eq. (1.12) the probability of a freezing event not occurring (P_{not}) is described by $\exp(-J_s st)$.

1.6.4 Heterogeneous Nucleation Sites

Due to observational limitations it is not possible to directly observe the critical germ nucleus experimentally and therefore prove or disprove the contact-angle model. Alternatively, it has been hypothesised that INPs exhibit physiochemical properties that lead to preferred nucleation sites on the surface (PK97 Ch. 9.2.3; Kulkarni and Dobbie, 2010). These may be chemical, crystallographic, or surface features such as cracks, steps, or pores that provide sites where the energy barrier required for nucleation is at a local minimum. A good lattice matching (i.e., a substrate that exhibits an ice like crystallographic structure acting as a template for ice formation) has been ascribed to the nucleating

properties of kaolinite and silver-iodide (PK97 Ch. 9.2.3.4; Mason, 1971), but more recent studies, using molecular dynamics simulations, have shown that for kaolinite at least, a different mechanism is causing nucleation (Hu and Michaelides, 2007; Cox et al., 2012). These mechanisms are difficult to understand and study and as such it is not currently possible to use the known physiochemical properties of a potential INP to predict its freezing behaviour (Hoose and Möhler, 2012).

1.6.5 Experimental Methods

Experiments are performed under a wide range of conditions in an effort to empirically understand ice nucleation and determine rates for use in predictions of freezing behaviour. Some of these instruments are designed to take real-time measurements of ambient air, whilst others are designed for use in laboratories with known samples and quantities. This section will provide a brief description of several common instrument designs and individual instruments that are currently used.

The Continuous Flow Thermal Gradient Diffusion Chamber (CFDC) is an instrument where temperature and supersaturation (with respect to ice and liquid) are controlled using parallel plates held at differing temperatures. Each plate is coated with a layer of ice and held at a specific temperature; the ice-vapour interface is therefore saturated with respect to ice. By changing the temperatures of each opposing plate a supersaturation gradient is created in the region between the plates. A flow of air containing the INP sample is passed through the instrument and the total fraction frozen is measured. These instruments use a short residence time (~ 10 s (DeMott et al., 2011)) which is commonly fixed; the importance of the residence time will be discussed in Chapter 4.

Cold-stage instruments typically consist of a single temperature controlled plate that is used to observe the freezing behaviour of a population of droplets (or single droplet) upon a change in temperature or a change in time. See Figure 1.5 for a typical instrument design. Droplets containing a known concentration of INPs are applied to a substrate and cooled at a constant rate. Freezing events are measured using an optical microscope. Using this method, varying cooling rates can be used to investigate the temperature-dependence of an

INP (ranging from ~ 0.01 to $10\text{ }^{\circ}\text{C min}^{-1}$). Freeze-thaw cycles can be performed in order to understand the reproducibility (or stochastic nature; see Sect. 1.8.2.3), and isothermal experiments, where the temperature is held constant for a duration of time (on the scale of minutes to days (Murray et al., 2011; Wright et al., 2013)), can be used to examine the time-dependent behaviour of an INP.

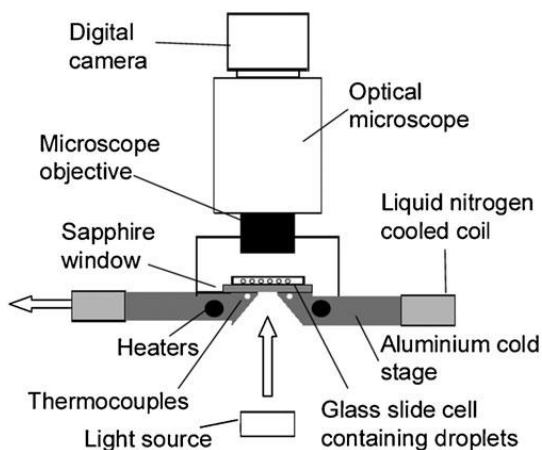


Figure 1.5. Schematic of a typical cold-stage instrument. Figure taken from Murray et al. (2010).

The Aerosol Interaction and Dynamics in the Atmosphere (AIDA) cloud chamber is distinctly different from the previous examples in that it is designed to reproduce the evolution of a cloud. The AIDA cloud chamber is an 84 m^3 insulated chamber that can be cooled down to $-90\text{ }^{\circ}\text{C}$ (Mohler et al., 2006). A representative atmosphere is achieved through mechanical expansion of the chamber using a vacuum and a frost layer on the inside of the chamber. Cooling experiments at a range of rates can be performed where temperature (Connolly et al., 2009) or supersaturation (Mohler et al., 2006) is varied with time. The scale of the AIDA cloud chamber permits the interaction of the hydrometeors and therefore a more realistic treatment of ice formation processes in the atmosphere, however, it is impossible to determine the individual freezing events and the precluding nucleation event. Cooling rates are typically limited to above $\sim 1\text{ }^{\circ}\text{C min}^{-1}$, which in terms of a typical cloud updraught speed is relatively high.

These examples demonstrate the range of temporal conditions that are commonly applied in immersion mode freezing experiments. The effect that this has on the resulting data is not

currently understood, and therefore accurately reconciling data obtained using the range of techniques is not currently possible.

1.6.6 Experimental Analysis

The instruments described previously are all designed to make observations on the fraction of viable droplets that freeze. Some instruments (cold-stage, AIDA) are capable of measuring this fraction as a continuous function of time and temperature, thus producing cumulative fraction frozen (hereafter referred to as $f(T)$) curves, whereas others (CFDCs) are only capable of single measurements, and require multiple experiments to obtain $f(T)$ curves. If the surface area per droplet is known then temperature-dependent ice formation rates can be determined from the fraction frozen data. This rate is either assumed to follow CNT, in that the critical ice germ formation is dependent on temperature and time, or a simplified model where it is assumed that the formation of the germ is simply dependent on temperature. These descriptions will be fully defined in Sect. 1.6.3 but for now are named the stochastic and singular approach, respectively.

The stochastic approach follows from CNT in Sect. 1.6.3 so that on rearranging Eq. (1.15) the nucleation rate coefficient $J_s(T)$, in events per unit surface per unit time, is calculated as

$$J_s(T) = \frac{-\ln(1 - f_{ice})}{s \cdot t} \quad (1.16)$$

where f_{ice} is the fraction of viable droplets frozen at a temperature T for a duration of time t .

The singular approach uses a nucleation coefficient $n_s(T)$, in events per unit surface area, that describes the cumulative number of droplets that freeze, f_{ice} , upon cooling from $T_{273\text{ K}}$ to a temperature T so that:

$$n_s(T) = \frac{-\ln(1 - f_{ice})}{s} \quad (1.17)$$

These two expressions are commonly used to obtain functions that characterise the temperature dependent ability of an INP species or population. A summary of these results will be presented in the following sections.

1.7 Observations and Sources of INPs

The atmospheric loading of INP species, both in terms of concentrations and composition, has been determined through a combination of early ice crystal residue studies and more recent in-situ aircraft observations using CFDC instruments.

Kumai (1951, 1961) examined ice crystal residues with an electron microscope at locations in the US and Japan and found that the nuclei could be categorised into mineral dust, hygroscopic particles, combustion products and micro-organisms. Clay minerals, specifically of the illite, koalinite, and montmorillonite groups, were found to be the dominant component. Isono et al. (1959) used an ice nucleus counter and found that low INP concentrations occurred in maritime air masses, and high concentrations in continental air masses. Particularly high concentrations were found in dust storms originating from arid regions. Concentrations determined at $-20\text{ }^{\circ}\text{C}$ varied from $< 0.1\text{ L}^{-1}$ (maritime) to $> 60\text{ L}^{-1}$ (dust storm) with typical daily concentrations ~ 1 to 10 L^{-1} . This early work showed evidence that mineral dusts made up a significant proportion of atmospheric INP species and that concentrations varied depending on source region.

More recent data on atmospheric INP concentrations are summarised in Figure 1.6. Observations typically range from ~ 1 to 10s L^{-1} , with maximum values of 100s L^{-1} . Compared to typical ranges of aerosol concentrations (10^5 to 10^7 L^{-1}) it is clear that INPs represent a very small subset of all aerosol particles. Similar to the conclusions of Isono et al. (1959), INP concentrations are spatially and seasonally variable, with events such as dust storms correlated with the highest observed concentrations (DeMott et al., 2003a).

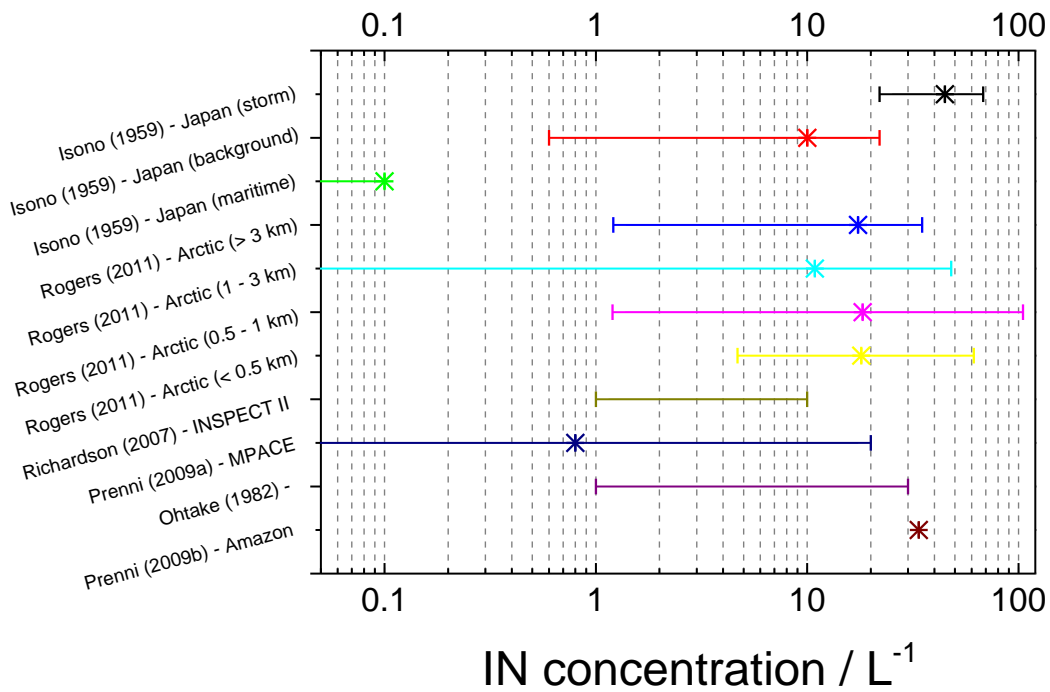


Figure 1.6. Atmospheric observations of INP concentrations from various studies. This figure does not take into account the temperature at which observations were made.

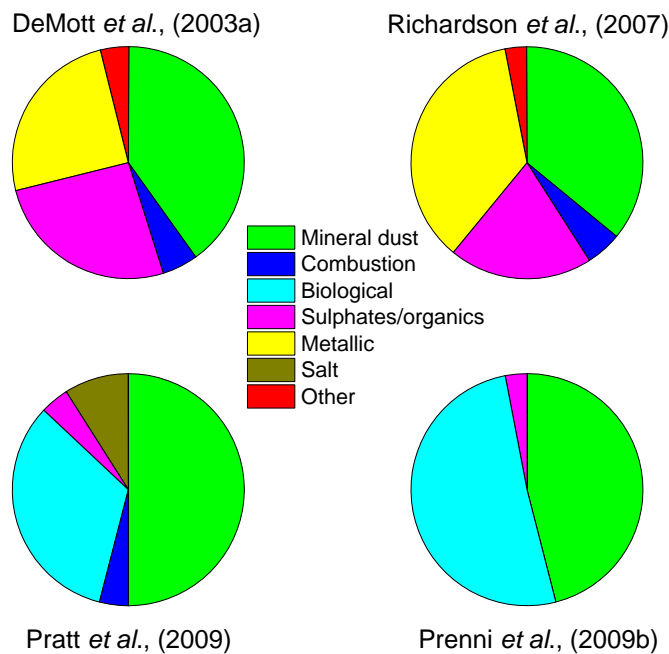


Figure 1.7. Graphic showing relative contributions from different INP species from in-situ observations.

Following from the work by Kumai, several recent observational studies have used mass spectroscopy, or electron microscopy to determine the composition of atmospheric INP species. The results are summarised in Figure 1.7: DeMott et al. (2003a) and Richardson et al. (2007) sampled air at an elevated location in the western US; Pratt et al. (2009) took in-situ samples above Wyoming, US; and Prenni et al. (2009b) sampled air over the Amazon basin. In all studies mineral dust was found to be a major constituent. Combustion products were found in three of the studies and sulphates, important for ice formation in cirrus clouds, were reported in all elevated air samples. Pratt et al. (2009) and Prenni et al. (2009b) both found that biological species accounted for a large proportion of all observed INP species.

Mineral dusts originate from the erosion of crustal rocks followed by uplift from dust storms, dust devils, and other convective processes (Knippertz and Todd, 2012). Prospero et al. (2012) used a satellite product to determine global dust sources and transport. The study found that sources are associated with topographical lows in arid regions that have evidence of past fluvial action. Once airborne dust particles can be transported large distances; mineral dusts from the African continent have been found in the East coast of US, the Amazon and Europe (Sassen, 2002; Prenni et al., 2009b; Klein et al., 2010) and mineral dusts from Asia have been found in the western US and China (Huang et al., 2008). The classification of mineral dust covers a wide range of individual minerals. Using X-ray diffraction analysis Murray et al. (2012) presented the relative mineralogical composition of samples taken from locations across the globe. Similar to Kumai (1961) they found that atmospheric dust predominantly consists of clay minerals (illite, kaolinite, montmorillonite, and chlorite), feldspars (K-feldspar, and Na-Ca feldspar), and quartz.

Carbonaceous combustion products originate from either natural sources, such as wildfires, or anthropogenic sources such as biomass burning and industrial processes. Individual insoluble soot particles range from ~ 0.01 to $0.1 \mu\text{m}$ in diameter but commonly agglomerate to form particles up to $0.5 \mu\text{m}$ (Popovicheva et al., 2008). Using airborne observations Hudson et al. (2004) estimated that $\sim 33\%$ of all particles in the North American troposphere were carbonaceous in origin. Through ageing processes these particles are able

to become activated as CCN and thus potential immersion mode INPs (Sun and Ariya, 2006).

Biological particles (also known as bioaerosols) include pollen, fungal and lichen spores, bacteria, diatoms, and fragments of plants and animals. The relative abundance and concentration of these particles in the atmosphere is highly uncertain, with emission estimates ranging from < 10 to 1000 Tg yr^{-1} (Winiwarter et al., 2009; Hoose et al., 2010). Christner et al. (2008) analysed precipitation from Europe, North America, and Antarctica and inferred that bacteria was present in 95 % of cases, and Elbert et al. (2007) estimated airborne fungal spore concentrations to be on the order of 1 to 10 L^{-1} , demonstrating the potential global importance of bioaerosols as an INP species. Known bacteria species acting as INPs include Pseudomonads, such as *Pseudomonas syringae*. Several companies mass produce these bacteria (grown from cultures) for use in snow makers; commercially available examples include Snomax™ and Icemax™. Fungal species include strains of fungi belonging to the genus *Fusarium*. Known pollens include those from trees, such as birch and alder, and also grasses.

Volcanic material (i.e., fine ash) has also been found to act as an atmospheric INP. Volcanic ash is composed of a crystalline element similar to natural mineral dusts, and a silicate-rich element. The enhancement of INP concentrations during volcanic events has been reported by several studies (Isono et al., 1959; Hobbs et al., 1971; Prenni et al., 2009a). The global abundance and concentration is dependent on volcanic events and also the type of eruption (i.e., duration, lava viscosity, vertical extent, ash production mechanisms); therefore global estimates are missing.

The number of airborne aerosol particles that are able to nucleate ice at a given location is highly variable and dependent on many factors including meteorological conditions, sources and age of the air mass, seasonality, and the species of INP present. In the next section the freezing characteristics of these INP species determined from immersion mode experiments will be discussed.

1.8 Characteristics of INP Species Determined from Experiments

As previously discussed the atmosphere contains a wide range of particles that are able to act as ice nucleating particles (INPs). In order to understand which species are important to ice formation processes experiments into the properties and freezing characteristics of INPs are investigated using the instruments described in Sect. 1.6.5.

Immersion mode experiments are performed using samples of either relatively pure INP species, samples from the field, or atmospheric proxies. Atmospheric proxies, such as Arizona test Dust (ATD) and NX-Illite, are commonly used because they are generally well characterised and available in large quantities. This makes them useful for inter-comparisons and calibrating instruments. Field samples are useful as they provide a source species, which can be assumed to be a direct proxy of atmospheric INPs. Assuming that CNT effectively describes the behaviour between a supercooled droplet and an immersed INP (Sect. 1.6.3) then we expect the freezing behaviour to be dependent on temperature, INP surface area, and time. The vast majority of studies concentrate on determining the former two properties, with a much smaller proportion characterising the time-dependence; this is partly due to the design limitations of many instruments (see Sect. 1.6.5), and also the assumption that time-dependence is not important (see Sects. 1.9.2 and 1.10.2).

1.8.1 Temperature Dependence

The relative importance of different INP species can be illustrated by determining the nucleation rate coefficient $J_s(T)$, or the nucleation coefficient $n_s(T)$, from Sect. 1.6.6. Values of n_s are generally presented as only knowledge of the surface area and temperature is required. Figure 1.8, adapted from Murray et al. (2012), shows experimentally determined values of $n_s(T)$ using Eq. (1.17). Different INP classifications have been colour-coded as mineral dusts, combustion products, biological particles, and volcanic ash. The foremost observation is that the nucleation rate of all species increases with decreasing temperature. However, it is apparent that each species tends to have a unique dependence on temperature. Using $\text{dln}(n_s)/\text{dT}$ as a means to compare gradients: *P. syringae* (Lindow et al., 1989) has a gradient of ~ -8.5 ; birch pollen (Pummer et al., 2012) ~ -1.9 ; soot (Demott,

1990) ~ -0.24 ; and volcanic ash (Hoyle et al., 2011) ~ -0.54 . Species that are active at high temperatures tend to exhibit the steepest experimentally determined gradients.

The second observation from Figure 1.8 is that the different INP classifications generally tend to be active in separate temperature regimes. Some biological particles are active at warm temperatures, whereas mineral dust and volcanic ash are active at much colder temperatures. It is worth noting that the analysis of data using $n_s(T)$ implicitly neglects time-dependence. Thus it is reasonable to propose that some of the variation seen in datasets, especially between instruments, may arise due to time-dependent freezing behaviour. This proposal will be re-addressed in Chapter 4.

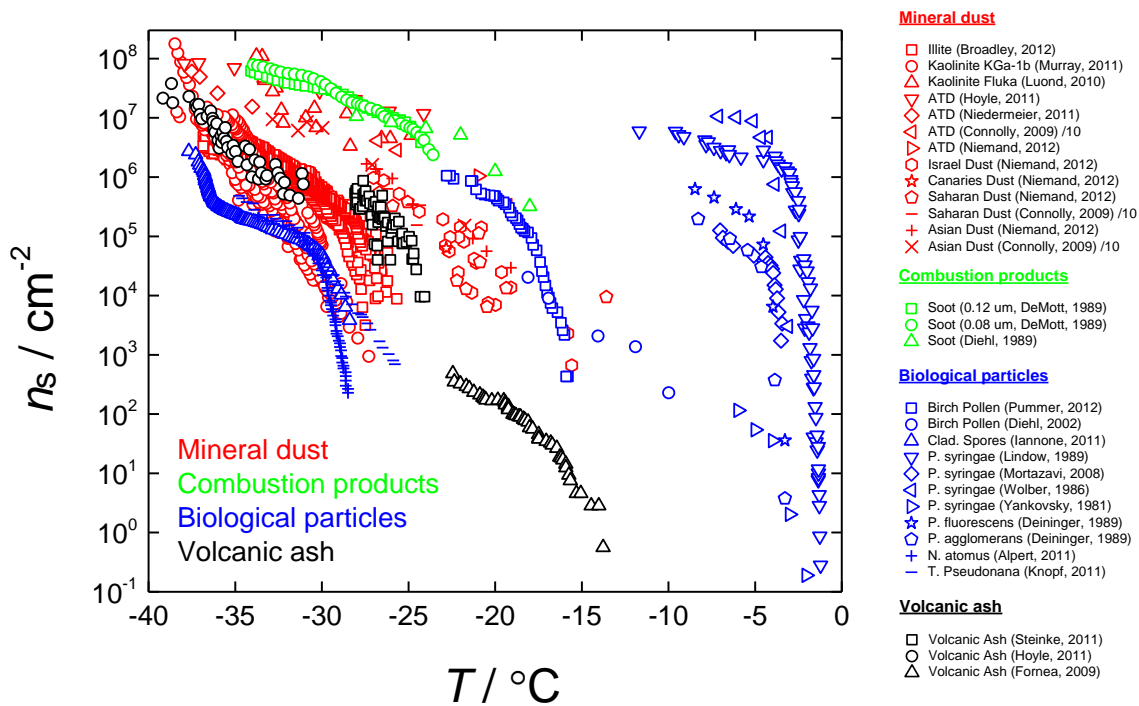


Figure 1.8. Nucleation coefficients $n_s(T)$ for a range of atmospheric INPs determined from immersion mode experiments. Data points are colour coded according to their INP classification: mineral dust (red); combustion products (green); biological particles (blue); and volcanic ash (black). $n_s(T)$ values calculated using Eq. (1.17) with surface area following the individual studies. Figure adapted from Murray et al. (2012).

1.8.2 Time Dependence in the Immersion Mode

Following CNT (see Sect. 1.5.1) at a given temperature the nucleation rate, i.e., the rate at which critical ice-germs are formed, is assumed to be dependent on surface area and time. Cold-stage instruments, along with some CFDCs, are capable of changing temporal

conditions so that the role of time-dependence can be identified. This can be achieved using one of three methods: varying the cooling rate; varying the residence time at constant temperature; or subjecting a droplet, or population of droplets, to a series of freeze-thaw cycles. The observed time-dependence, or stochastic nature, of ice nucleation is expected to differ through each method used; the following sections will illustrate this.

1.8.2.1 Cooling-Rate Dependence

The cooling rate within a system is negatively correlated with time, in that an increase in cooling rate decreases the time required for the system to change from a temperature T_0 to T_1 , and vice versa. From Eq. (1.15) the probability of a single droplet freezing at a temperature T can be described by $P = 1 - \exp(-J_s(T)st)$. Therefore an increase in cooling rate causes a decrease in time and a decrease in P . For a population of identical droplets the probability of an event occurring at all temperatures changes by the same factor causing the $f(T)$ curve to systematically shift. An increase in cooling rate shifts the $f(T)$ curve to colder temperatures, and a decrease to warmer temperatures.

Vali and Stansbury (1966) found evidence of this behaviour in constant cooling experiments with distilled tap water. Using a series of cooling rates (0.5, 1.0, 2.0, and 4.0 °C min⁻¹) they found that the mean freezing temperature of the population of droplets increased by 0.2 °C for each doubling of cooling rate. Similarly, in a study by Murray et al. (2011) droplets containing kaolinite mineral dust were cooled at varying rates using a cold-stage instrument. The data were analysed and $J_s(T)$ values determined using Eq. (1.16). The data, shown in Figure 1.9, collapse onto a single line. If the freezing behaviour was independent of time then a systematic shift in the data would be observed. Wright et al. (2013) also performed multiple cold-stage experiments at a range of cooling rates and found similar behaviour. However, they found that the cooling-rate dependence was not constant for the range of INP species tested; Table 1.1 summarises their results. The gradient $\Delta T/\Delta \log(r)$ is used to illustrate the different cooling-rate dependence between species; a steep gradient relates to a strong cooling-rate dependence. IcemaxTM, a commercially available bacteria INP, shows very little cooling-rate dependence, whereas kaolinite, montmorillonite and flame soot show strong cooling-rate dependence. The two filtered rain

water samples show a similar weak dependence, and the unfiltered sample close to zero. These examples demonstrate a substantial variability in the cooling-rate dependence of atmospherically relevant INPs.

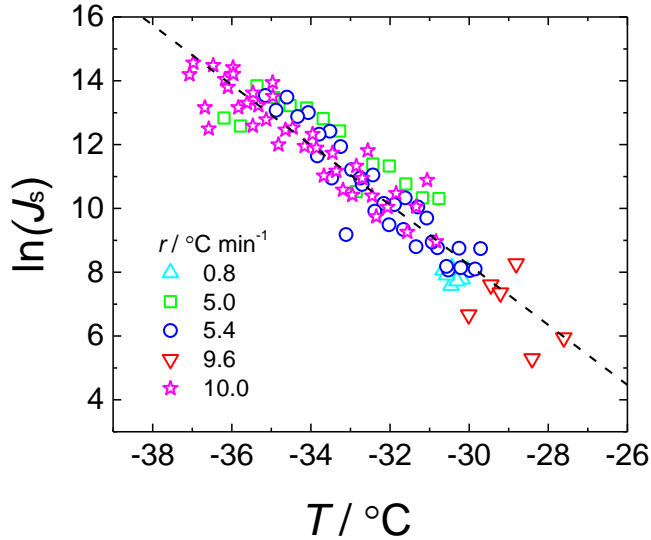


Figure 1.9. Nucleation rate coefficients $J(T)$ determined from droplets containing kaolinite. Multiple experiments were performed at cooling rates (r) ranging from 0.8 to 10.0 $^{\circ}\text{C min}^{-1}$. Figure adapted from Murray et al. (2011).

Table 1.1. Range of INP species tested by Wright et al. (2013) with the corresponding range of cooling rates used and the gradient between the shift in temperature ΔT and the change in cooling rate $\Delta \log(r)$.

INP species tested	Cooling rates used ($^{\circ}\text{C min}^{-1}$)	$\Delta T / \Delta \log(r)$
Icemax TM (<i>bacteria</i>)	0.05 - 2.0	> -0.1
ATD (<i>dust proxy</i>)	0.01 - 5.0	-0.5
Montmorillonite (<i>mineral dust</i>)	0.05 - 5.0	-1.3
Kaolinite KGa-2 (<i>mineral dust</i>)	0.02 - 2.0	-1.4
Flame soot (<i>combustion product</i>)	0.02 - 1.0	-1.7
Rain water sample 1 (filtered)	0.01 - 5.0	-0.5
Rain water sample 2 (filtered)	0.5 - 2.0	-0.5
Rain water sample 3 (unfiltered)	0.5 - 2.0	> -0.1

1.8.2.2 Residence-Time Dependence

Nucleation is thought to be a stochastic process, where an increase in time directly increases the probability that a critical ice germ will form. To examine this form of time-dependence isothermal experiments are performed where droplets containing an INP sample are held at a constant sub-zero temperature for some duration of time.

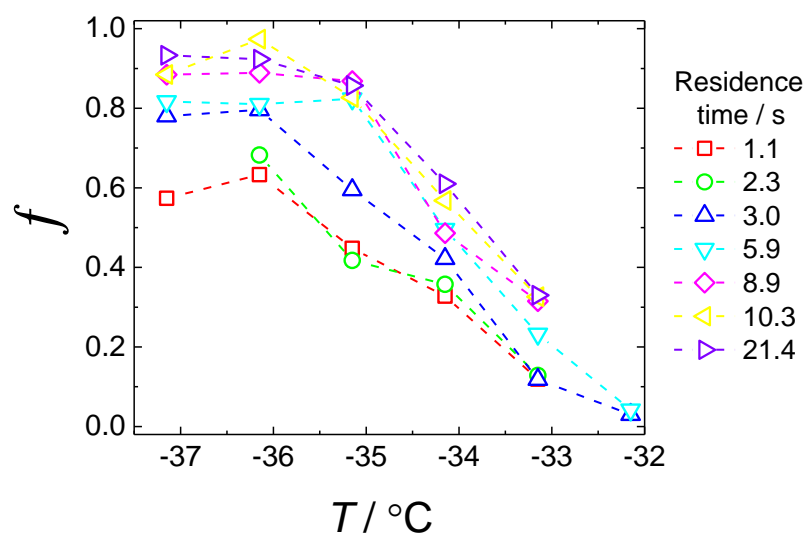


Figure 1.10. Fraction frozen for populations of droplets containing a 400nm kaolinite particle in the ZINC instrument. Experiments were performed at a range of temperatures and the residence time within the ZINC was varied between 1.1 and 21.4 s. The dashed lines are to help guide the eye. Figure adapted from Welti et al. (2012).

Murray et al. (2011) used a cold-stage instrument held at a constant temperature to observe the decay of liquid droplets containing kaolinite with time. They found that the decay in liquid droplets was exponential with respect to time, and that the rate of decay increased with decreasing temperature. Welti et al. (2012) used a CFDC instrument to investigate the time-dependent behaviour of droplets containing single kaolinite (FLUKA) particles. This was achieved by changing the flow rate through the CFDC, thus varying the residence time. Their data for 400nm kaolinite particles are shown in Figure 1.10. At all temperatures the $f(T)$ generally increases with increasing residence time. A factor of ten change in residence time, from 1.1 to 10.3 s, results in roughly double the fraction frozen. Wright and Petters (2013) also used a cold-stage instrument for ‘hold’ experiments where droplets containing a known weight fraction of ATD particles were cooled down at 1 °C min^{-1} to -26.1 °C and held for over 12 hours. They found that the decay of liquid droplets was not constant with time (i.e., non exponential) and instead the decay rate decreased with increasing time. This behaviour was attributed to variability in the freezing behaviour between particles, and therefore droplets. The results from these studies show that there is a relationship between

residence time and f , however, this relationship and how it relates to an INP's nucleating properties is not currently understood.

1.8.2.3 Freeze-Thaw Experiments

In these experiments single, or populations of, droplets are cooled down at some rate until frozen then heated until thawed; this process is then repeated for a number of cycles. The variability in an individual droplet's freezing temperature (T_{freeze}) is thought to be related to the stochastic nature of the nucleation within the droplet.

Vali (2008) used this method with droplets containing two soil samples. Each experiment consisted of between 100 and 144 droplets (0.01 cm^3) and up to 65 freeze-thaw cycles. Rank correlation coefficients were calculated for each run and used to determine how random (i.e., stochastic) the variability in T_{freeze} was from one run to the next. Results from both samples showed little evidence of a stochastic behaviour; the majority of droplets typically had $< 1 \text{ }^\circ\text{C}$ change in T_{freeze} and rank coefficients were > 0.9 . The range in T_{freeze} over the entire population was $\sim 18 \text{ }^\circ\text{C}$, which was much larger than the individual droplet fluctuations. From this it was inferred that the droplet population contained diversity in the ability to nucleate ice. Wright and Petters (2013) also performed this type of experiment with ATD particles and used the standard deviation (σ_{refreeze}) in T_{freeze} for each droplet to describe the stochastic nature of nucleation; $\sigma_{\text{refreeze}} < 0.1 \text{ }^\circ\text{C}$ would correspond to very weak time-dependence. They found that σ_{refreeze} varied between 0.21 and 3.52 $^\circ\text{C}$ with the majority of drops $< 1.0 \text{ }^\circ\text{C}$. With the additional evidence from the isothermal experiments (previous section) the authors concluded that ATD is a heterogeneous surface, i.e., exhibits an inter-particle variability. Similar to the cooling and isothermal experiments, the freeze-thaw experiments demonstrate variability in the time-dependent freezing behaviour of different INP species.

These three observable manifestations of time-dependent behaviour are likely a result of the same stochastic behaviour of ice nucleation on the INP. If this is the case then it should be possible to link the stochastic property of an INP to different manifestations of time-

dependence; the literature shows that this has not been investigated and as such is poorly understood.

1.9 Heterogeneous Freezing Models

In order to reproduce the freezing behaviour observed in experiments a number of freezing models have been developed and are described in the literature. This section will describe the models that are commonly used.

1.9.1 The Single-Component Stochastic Model

The single-component stochastic (SCS) model, previously derived in Sect. 1.6.3 as Eq. (1.15), follows from CNT where the probability of a critical germ forming at a temperature (T) is dependent on the INP surface area (s), the duration of time (t), and a factor (φ) which describes how efficiently a material nucleates ice. The rate at which critical germs form in a droplet is expressed by the nucleation rate coefficient (J_s). In this model the freezing behaviour of each particle is assumed constant and freezing is time dependent. The temperature-dependent function $J_s(T)$ is often expressed as a simple linear function (e.g., Murray et al. (2011)), or derived using CNT (e.g., Chen et al. (2008)). The CNT-based SCS models are often referred to as 1θ models, as they are characterised by a single contact angle. Using this model isothermal simulations will be characterised by an exponential decay of liquid droplets with respect to time.

1.9.2 Singular Freezing Model

It was proposed by Vali and Stansbury (1966) that nucleation occurs on distinct nucleation sites where the energy required for a critical germ to form is at a local minimum. Each site represents a threshold temperature at which point nucleation will occur. A population of particles will contain a distribution of sites, and it is this distribution that determines the formation of ice at a given temperature. As discussed in Sect. 1.8.2.3 Vali (2008) observed that the variability in T_{freeze} for individual droplets in freeze-thaw cycles was much smaller than the overall range in T_{freeze} for the population, and thus was evidence of inter-particle variability. Following the proposed model this was viewed as a distribution of sites that,

assuming time-dependence plays a negligible role, can each be characterised by a single freezing temperature. A droplet containing a number of particles or sites is then characterised by the most efficient site. This turns the probability of freezing into a deterministic function dependent on the number of ‘active’ sites at a given temperature, and is known as the singular model.

In the singular model the cumulative number of sites per unit surface area that are active at a temperature T is denoted by the nucleation coefficient $n_s(T)$, and is experimentally determined using Eq. (1.17). This is often called the ice active site density (Connolly et al., 2009; Murray et al., 2012; Hoose and Möhler, 2012) or the active site density (DeMott, 1995). With knowledge of $n_s(T)$ the cumulative fraction of droplets that will be frozen at a temperature T can be calculated as:

$$f(T) = 1 - \exp(n_s(T) \cdot s) \quad (1.18)$$

This can also be expressed as a differential rate coefficient, $k(T)$, that describes the fraction of droplets that freeze upon a change in temperature dT :

$$f_{dT}(T) = 1 - \exp(k(T) \cdot s \cdot dT) \quad (1.19)$$

From this equation it can be seen that in isothermal experiments, where $dT = 0$, no freezing events will occur as the residence time increases. A change in cooling rate will also have no effect on the $f(T)$ data. This is contrary to the results shown in Sect. 1.6.2. To account for the T_{freeze} variations seen when changing the experimental cooling rate Vali (1994) proposed a ‘modified singular’ freezing model in which a cooling-rate dependent temperature offset is incorporated into the nucleation coefficient for use in cooling experiments:

$$f(T) = 1 - \exp(n_s(T - \alpha) \cdot s) \quad (1.20)$$

where α is of the form $\alpha = C \cdot \log(|r|)$ where r is the cooling rate in $^{\circ}\text{C min}^{-1}$ and C is an empirical parameter determined from experimental data.

1.9.3 Multiple-Component Stochastic Models

None of the previous models can satisfy the observed variability in both time-dependent behaviour and nucleation efficiency. As a result a number of complex models based on the SCS model have been developed, called Multiple Component Stochastic (MCS) models. In these models, a population of droplets, or sites, are divided into sub-populations of identical entities. Each sub-population, or component, can then be described by the SCS model with the summation representing the entire population. The probability of a component occurring with a specific efficiency can be characterised using a probability density function (PDF).

Marcolli et al. (2007) used a CNT-based MCS model to show that a distribution of particles, each characterised by a specific contact angle (θ), was required to reproduce their experimental data. Different PDFs were used to characterise this distribution; it was found that a log-normal distribution was appropriate. This model, named the θ PDF model, was then extended to include a distribution of active sites, which assumed that a single particle exhibits multiple nucleation sites on its surface. The distribution of active sites per particle was calculated as an exponential function of the contact angle. With this method larger particles are more likely to contain sites of better nucleating ability than smaller particles.

Lüönd et al. (2010) developed a similar θ PDF model to describe the total fraction of droplets freezing in the ZINC CFDC of the form:

$$f(T) = 1 - \int_0^{\pi} P(\theta) \exp[-J_s(T, \theta) \cdot s \cdot t] d\theta \quad (1.21)$$

where $P(\theta)$ describes the probability of a particle being characterised by the contact angle θ , and $J_s(T, \theta)$ is the nucleation rate coefficient at a temperature T and contact angle θ . In this MCS model particles are divided into components of equally-efficient populations. The total fraction of frozen droplets (each droplet is assumed to contain a single particle in the

ZINC) is determined by integrating between all possible INP efficiencies ($0 \leq \varphi \leq \pi$). It was assumed that a log-normal distribution was appropriate. Similar to Marcolli et al. (2007) this was extended to include a distribution of active sites per particle, so that each droplet contains a distribution of active sites, and thus contact angles.

Niedermeier et al. (2011) developed a MCS model, named ‘the soccer ball’ model, of the form:

$$f(T) = \frac{1}{N_{\text{droplet}}} \sum_{k=1}^{N_{\text{droplet}}} P_k(T, t) \quad (1.22)$$

where N_{droplet} is the total number of droplets and $P_k(T, t)$ is the probability of freezing occurring in drop k at a temperature T and a time t . Here each droplet is treated as a separate component. In the soccerball model the surface of each particle is assumed to be divided into a number of equal sized patches, with each being characterised by a specific contact angle randomly assigned from a Gaussian distribution. In the simplest form every particle is assigned the same distribution of contact angles; the subsequent population of uniform particles can then be thought of as being internally mixed. In an externally mixed population each particle is separately assigned a distribution. It is clear that with this condition a small number of patches per INP will result in a population with diverse ice nucleating ability, whereas if all particles contain many sites then the probability of a specific site occurring per INP will increase and the population tends towards a uniform ability.

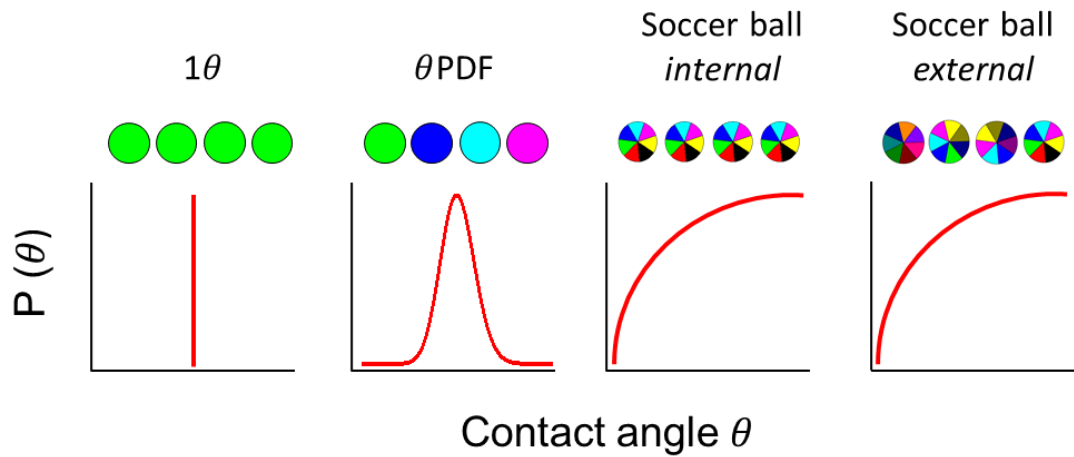


Figure 1.11. CNT-based freezing models. Figure adapted from Ervens and Feingold (2012).

The different treatment of an INPs nucleating ability in the previously mentioned CNT-based models is presented in Figure 1.11. The 1θ picture represents the SCS model where all particles, or all sites, are described by the same contact angle. The θ PDF model is the simplest form of a MCS model; each droplet, or sub-population of droplets, is described by a single contact angle. The ‘internal’ soccer ball model is similar to the 1θ model; each particle or droplet is described by the same distribution of contact angles, and are thus equivalent. The ‘external’ soccer ball model is the more complicated treatment, with randomly assigned distributions of contact angles per particle or droplet.

These models have been used in each respective study to reproduce, or provide evidence for, inter-particle variability in their data. In each case the nucleation rate coefficient $J_s(T)$ is calculated using CNT (see Sect. 1.6.3), and therefore time-dependence is an implicit consequence of the model. Broadley et al. (2012) presented a model in which the nucleation rate was assumed to be approximated by an exponential function of temperature. This allowed flexibility in both the temperature-dependence and the relative efficiency of the nucleation rate coefficient, rather than being constrained by CNT. A PDF was used to describe inter-particle variability through the distribution of droplet sub-populations. A significant benefit to this system is that it is not constrained by theory and therefore, similar to the soccer ball model, additional distributions can be used to represent diversity in nucleation sites on the particle’s surface. The development and application of this MCS model will be presented in Chapter 2. Wright and Petters (2013) used the same method to

investigate the freezing behaviour of ATD. In their MCS model a distribution of active sites per particle was generated using a Poisson distribution and then each site assigned a ‘characteristic temperature’ to describe the site’s ability to catalyse the freezing event.

1.10 Modelling Studies of Heterogeneous Ice Nucleation

1.10.1 Immersion Mode Freezing Schemes

The representation of immersion mode ice formation in cloud simulations has progressed from simple deterministic functions to freezing schemes that are able to capture the diversity of nucleating species in the atmosphere. An early parameterisation was based on experimental data by Bigg (1953b) who found that the nucleation ability of water droplets containing ‘freezing nuclei’ was volume dependent. Although we now have strong evidence that ice nucleation has a surface area dependent mechanism the probability of finding an INP within a droplet may increase with volume due to droplet coalescence and scavenging processes. This parameterisation, and variations of, is still widely used (Reisin et al., 1996; Cui et al., 2006; Morrison and Grabowski, 2008).

Several parameterisations that represent cumulative freezing events by all modes of ice nucleation have been developed based on observations of in-situ ice number concentrations per litre (N_{INP}), where each ice particle is assumed to be the result of a single INP. Fletcher (1962) collated a number of datasets from various global locations and found that N_{INP} could be reasonably approximated by a temperature dependent function:

$$N_{INP} = A \exp(B \cdot T_{\text{supercool}}) \quad (1.23)$$

where $T_{\text{supercool}}$ is the supercooled temperature, $A = 10^{-5} \text{ L}^{-1}$, and $B = 0.6 \text{ }^{\circ}\text{C}^{-1}$. Meyers et al. (1992) found that this function frequently under-predicted at warm temperatures, and, based on CFDC data, presented a new supersaturation-dependent parameterisation valid between -7 and -20 °C, and from -5 to + 4.5 % water supersaturation:

$$N_{INP} = \exp\left(A + B(100(S_i - 1))\right) \quad (1.24)$$

where S_i is the fractional ice supersaturation, $A = -0.639$, and $B = 0.1296$. A more recent parameterisation for N_{INP} has been proposed by DeMott et al. (2010). The authors found that observed N_{INP} in mixed-phase cloud conditions were correlated with the number of particles with a diameter over $0.5 \mu\text{m}$ (R^2 of 0.9); the remaining variability was attributed to the diversity of INP species. The function that describes the relationship is:

$$N_{INP} = A(273.16 - T)^B \cdot (n_{\text{aer},0.5})^{(C(273.16-T)+D)} \quad (1.25)$$

where T is the temperature in kelvin, $n_{\text{aer},0.5}$ is the number concentration (cm^{-3}) of aerosol particles with diameter over $0.5 \mu\text{m}$, $A = 5.94 \times 10^{-5}$, $B = 3.33$, $C = 0.0264$, and $D = 0.0033$. This parameterisation is used for predicting the number of available INPs for subsequent use in heterogeneous ice nucleation pathways, rather than assuming that the presence of ' n ' INPs leads to ' n ' ice particles.

Functions that predict N_{INP} provide an estimate of the number of INPs. In order to subsequently understand the rate of ice formation under any given conditions, or quantify the impact of different modes and INP species on cloud development, several immersion mode schemes have been developed that incorporate multiple classifications, or species, of INPs. Khvorostyanov and Curry (2004) developed a theoretically based scheme for immersion and condensation freezing that allowed the droplet to contain both an insoluble and soluble fraction. Using the CNT framework their scheme (hereafter KC) bases the nucleation efficiency of a droplet on the INP surface properties (contact angle, active sites, and a crystallographic misfit factor) and the water-activity (i.e., freezing depression due to dissolved solutes). A polydisperse aerosol population is incorporated into the KC scheme and permits varying INP species; each characterised by a specific contact angle.

Diehl and Wurzler (2004) presented a more simplified immersion mode scheme based on the singular freezing model. In their scheme (hereafter DW) the freezing efficiency of a droplet that includes an insoluble particle is assumed to scale with volume, but not particle size. The relative efficiency of multiple species (mineral dusts, biological, and soot) is

represented by a temperature dependent nucleation coefficient, in units cm^{-3} , determined from experimental literature. Similar to the KC scheme, freezing point depression from dissolved solutes is included through the introduction of a soluble component to the aerosol species.

An alternative observationally constrained ice nucleation scheme was proposed by Phillips et al. (2008) (hereafter PDA). The PDA scheme uses empirical parameterisations from existing literature of N_{INP} to predict ice formation rates (cumulative contributions from deposition, condensation and immersion) based on the chemistry and surface area of multiple INP species (dust and metallic, inorganic black carbon, and insoluble organic aerosol). The number of INPs that are activated within a specific size bin for each species is a function of temperature, ice supersaturation, and is scaled to a reference particle surface area. The enhancement above water saturation (from immersion and/or condensation freezing) is achieved using a simple factor and freezing rates are constrained by observational data.

Eidhammer et al. (2009) used a parcel model that included ice nucleation to compare the three multiple-species freezing schemes previously described (KC, DW, and PDA). Simulations of mixed-phase clouds were performed with an initial temperature of $10\text{ }^{\circ}\text{C}$ ($-14\text{ }^{\circ}\text{C}$) and constant updraughts of 50 and 500 cm s^{-1} (5 and 500 cm s^{-1}). A detailed treatment of soot and mineral dust INP species was used, and included aerosols with insoluble and soluble fractions, therefore permitting activation as both a CCN and INP. A range of simulations consistently showed a variation in the ice production rates resulting in differences in ice number concentrations over several orders of magnitude, as shown in Figure 1.12. The variation impacted the cloud dynamics (through release of latent heat) and the authors hypothesised that this would affect the cloud radiative properties. Only the PDA scheme was found to compare well against field campaign measurements.

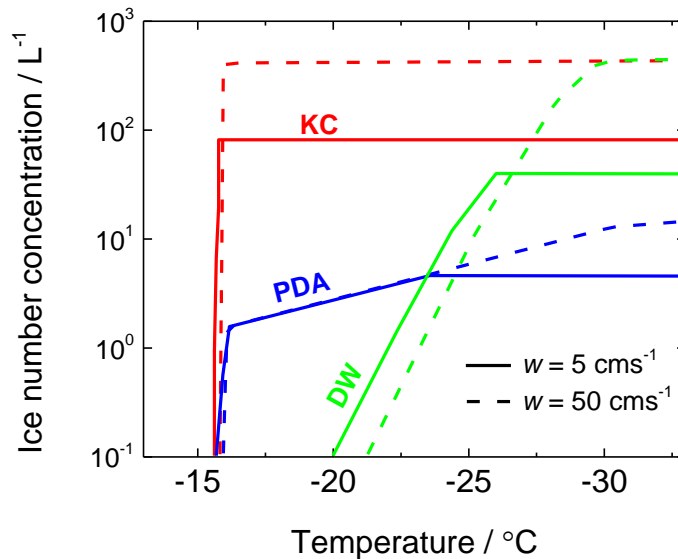


Figure 1.12. Simulated ice number concentration in a parcel model using three different immersion freezing schemes: Khvorostyanov and Curry (2004) (red); Diehl and Wurzler (2004) (green); Phillips et al. (2008) (blue) Solid lines and dashed lines correspond to constant parcel updraught speeds of 5 and 50 cm s^{-1} , respectively. Figure adapted from Eidhammer et al. (2009).

1.10.2 Importance of Time-Dependence

Incorporating an accurate representation of time-dependence into an ice nucleation scheme currently requires the use of a MCS model, such as the KC scheme. This is suitable for box modelling studies but becomes computationally demanding when applied to cloud resolving models. The relative importance of time-dependence in the atmosphere has therefore been the focus of several modelling studies.

Ervens and Feingold (2012) used an idealised box model (constant temperature and saturation) to explore the affect that the choice of freezing model has on the prediction of $f(T)$ as a function of time. Using fitting parameters determined from experimental data in Lüönd et al. (2010) the authors used a CNT-based SCS model, three CNT-based MCS models, and a singular model. It is worth noting that the original fitting parameters were minimised so that each could reproduce the temperature where $f(T) = 50\%$, therefore unsurprisingly, as conditions moved away from the original dataset the predictions diverged. Changing the surface area of the INPs and the temperature both had significant impacts on $f(T)$. The same method was used in a parcel model that includes dynamical and supersaturation feedbacks (i.e., vapour, liquid, and ice interact).

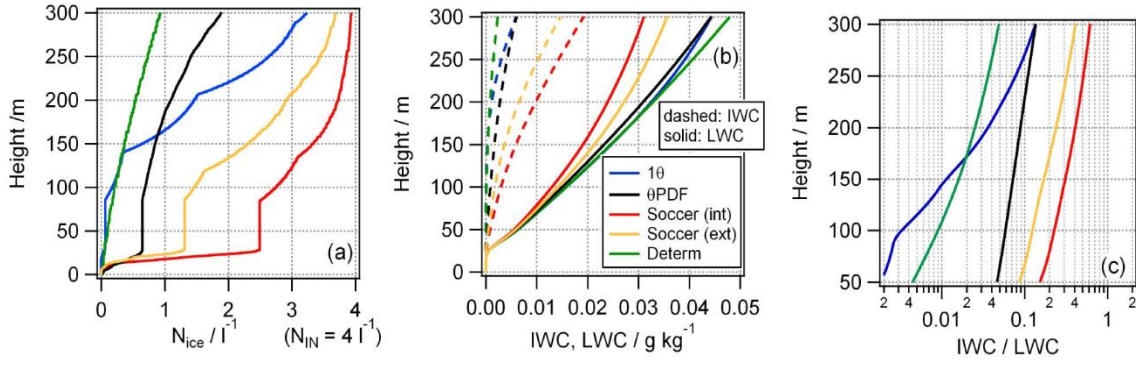


Figure 1.13. Modelled ice number concentration (a), IWC and LWC (b), and IWC/LWC ratio (c) for five different freezing models in a parcel model with polydisperse INP population. Figure reproduced from Ervens and Feingold (2012).

Runs using uniform sized particles showed that at high updraught speeds the rate of ice production was only weakly dependent on the distribution of θ , whereas at low updraught speeds there was a large variation in predicted ice concentrations, specifically from the time-independent singular model and the CNT SCS model. The runs using a polydisperse INP population (representative of atmospheric INPs) are shown in Figure 1.13 and show similar variation between models. The ice concentration at a height of 300 m varied from ~ 1 to 4 L^{-1} for the deterministic and soccer ball (internal) models respectively (Figure 1.13a), and the IWC/LWC ratio exceeded an order of magnitude variability for the same two freezing models (Figure 1.13c).

Ervens and Feingold (2013) used a CNT-based SCS model to understand the sensitivity of immersion mode freezing probability (P_{freeze}) to temperature, contact angle, time, and INP surface area. The sensitivity (ξ) of each variable (X) was determined using $\xi(X) = \partial P / \partial \ln X$. They concluded that $\xi(X)$ decreased with decreasing temperature, and that ice nucleation has a very weak sensitivity to time-dependence.

As previously discussed in Sect. 1.2 arctic stratus clouds are commonly observed to remain in a mixed-phase state for long periods of time (Uttal et al., 2002; Verlinde et al., 2007; de Boer et al., 2009; Shupe et al., 2010). Fridlind et al. (2012) used large-eddy simulations with detailed microphysics to reproduce observations of arctic stratus with persistent low

ice number concentrations. The formation of ice through the immersion mode was represented by a singular freezing model (Fridlind et al., 2007). They found that the available INPs were rapidly depleted through ice formation and subsequent precipitation; it was estimated that an increase in INPs by a factor of 30 would reproduce the observations. On the basis of similar observations Westbrook and Illingworth (2013) proposed that the low ice number concentrations could be maintained if time-dependence played a role: in a diverse INP population the freezing of the most efficient INPs would be followed by the slow production of ice in part due to time-dependence. The authors also hypothesised that in-situ measurements of INP concentrations using CFDC instruments may be under-predicted due to short residence times. This hypothesis will be discussed in Chapter 4.

1.11 Aims of Thesis

The aim of this thesis is primarily to understand and quantify the role that time-dependence plays in the freezing behaviour of droplets, and secondly to determine the importance of this behaviour in mixed-phase clouds.

In *Chapter 2* it is initially shown that CNT-based models are unable to reproduce the observed time-dependence in experimental data. A new MCS model that represents variability in both nucleation efficiency and time-dependent behaviour is presented. The model is applied to experimental data and then used to understand how time-dependence affects droplet freezing behaviour in cooling, isothermal, and freeze-thaw experiments.

In *Chapter 3* a new framework is derived and developed for use in determining the time-dependent properties of INPs, and reproducing their behaviour. The framework provides a means for reconciling experimental data obtained over a range of temporal conditions, and using different techniques. A new accurate and efficient immersion mode parameterisation is then presented for use in cloud modelling studies.

In *Chapter 4* the new framework is applied to experimental data from atmospherically relevant INPs obtained using different instruments and experimental methods. The framework is used to demonstrate the following:

- Determining the time-dependent properties of an INP
- Predicting the freezing behaviour of INPs in experiments
- Determining whether an INP behaves as a single or multiple-component species

The framework is then applied to existing experimental data in order to quantify the range in time-dependent behaviour of a wide range of atmospherically relevant INP species, and finally, using the framework the implications for in-situ INP measurements are presented.

In *Chapter 5* a cloud model with detailed microphysics is used to determine the sensitivity of mixed-phase clouds to time-dependence in the immersion mode production of ice. A series of increasingly complex simulations are performed with different cases in order to answer the following questions:

- How does time-dependence in the immersion mode affect the other hydrometeor species?
- How does this affect the development of the cloud and its bulk properties?

These results will then be used to answer the following:

- Under what conditions is it important to accurately represent time-dependence in the immersion mode?

Chapter 2: The Simplified Multiple Component Stochastic (Si-MCS) Model

2.1 Introduction

In this chapter I show that Classical Nucleation Theory (CNT) based Multiple Component Stochastic (MCM) models are unable to reproduce the time-dependent behaviour observed in immersion mode freezing experiments. A new MCS model is presented which is not based on CNT and simulations are presented to understand the impact of time-dependence on the freezing of droplets in cooling, isothermal, and freeze-thaw experiments. The new model will also underpin the development of the Framework for Reconciling Observable Stochastic Time-dependence (FROST) presented in Chapter 3.

The material presented in this chapter is an extension of work that R. Herbert contributed to in a paper published in Atmospheric Chemistry and Physics (Broadley SL; Murray BJ; Herbert RJ; Atkinson JD; Dobbie S; Malkin TL; Condliffe E (2012) Immersion mode heterogeneous ice nucleation by an illite rich powder representative of atmospheric mineral dust, Atm. Chem. Phys., 12, pp.287-307). R. Herbert developed a first version of the Si-MCS together with S. Broadley, work which is expanded on here. The experimental data on NX-illite was obtained by S. Broadley. The data on K-feldspar was obtained by T. Whale using experiments jointly designed by R. Herbert and T. Whale.

2.2 CNT-based MCS Models

As highlighted in Chapter 1 extensive experimental studies in the immersion mode have shown that INPs exhibit both inter-particle variability in nucleating efficiency and time-dependent variability. In this section existing MCS models, which are all based on CNT, will be applied to immersion mode freezing data. The link between the model and the simulated time-dependence will also be investigated.

CNT is a thermodynamic model that has been used to reproduce the formation rate of critical ice germs in supercooled liquid droplets. The inclusion of an INP is thought to provide a site for nucleation to occur upon, which catalyses the freezing event. In this model a conceptual contact angle θ is used to characterise the ability for an INP to act as a catalyst.

The effect of θ on the heterogeneous nucleation rate J_s is shown in Figure 2.1. J_s has been calculated following the CNT description in Zobrist et al. (2007) with the interfacial energy calculated following Murray et al. (2010) assuming hexagonal ice. Figure 2.1 shows that J_s is a very strong function of contact angle with smaller contact angles resulting in larger values of J_s . In addition, Figure 2.1 also shows that the gradient $\text{dln}(J_s)/\text{dT}$ is dependent on both temperature and contact angle.

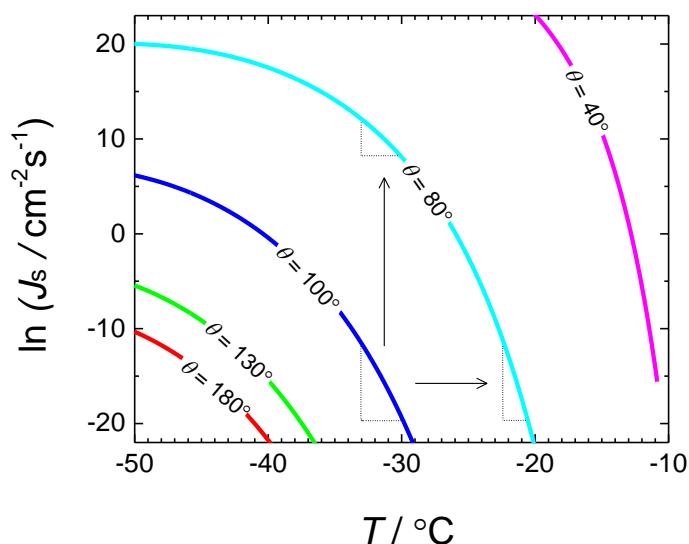


Figure 2.1. Heterogeneous nucleation rate coefficient J_s against temperature T derived using CNT for a range of contact angles $40 \leq \theta \leq 180$. The contact angle represents a proxy for the ability of a substrate to catalyse nucleation, with a decreasing contact angle corresponding to an increasingly effective substrate.

In order to link CNT to heterogeneity in nucleating efficiency several MCS models are described in the literature and are presented in Chapter 1. The basis of these models is that a population of INPs, or nucleating sites, can be characterised by a PDF that describes the probability of a particular contact angle occurring per INP or site. The PDF parameters can be changed in order to fit to experimental data. The distribution of sites cannot be determined directly and therefore must be either inferred from experimental data or

theoretically determined. Marcolli et al. (2007) used a variety of functions and distributions and found that a log-normal distribution of contact angles best reproduced their data, whereas Broadley et al. (2012) found that a normal distribution was more appropriate. Alternatively Sear (2013) proposed that the nucleation efficiency of a population of INPs consisting of a large number of nucleation sites can be described by a Weibull distribution.

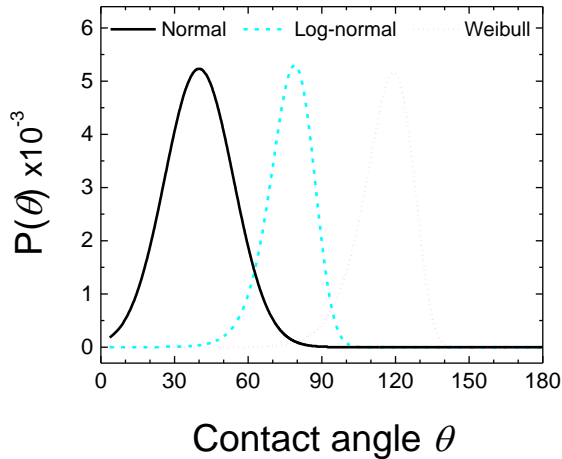


Figure 2.2. Examples of various PDFs used in CNT-based MCS models; the figure shows the normalised probability that a specific INP site is characterised by a contact angle θ ; assuming either a normal, log-normal, or Weibull distribution.

Figure 2.2 shows a series of typical PDFs using a normal, log-normal, and Weibull distribution of contact angles, hereafter referred to as $\text{PDF}_{\mathcal{N}}$, $\text{PDF}_{\ln\mathcal{N}}$ and $\text{PDF}_{\mathcal{W}}$, respectively. The different distributions lead to a variation in the shape of the PDF, especially in the distribution tails. It is not known which is more appropriate and therefore in the examples where experimental data is reproduced, each distribution will be applied and only the most suitable shown.

2.2.1 Cooling-Rate Dependence in CNT-based MCS Models

To investigate time-dependence in CNT-based MCS models a series of cooling simulations were performed using an idealised box model. Results will be used to understand how changes to the mean and variability in θ affect the simulated freezing behaviour. In the simulations the freezing rate of droplets was determined using Eq. (1.22) following Niedermeier et al. (2011). For the probability of freezing occurring per droplet a $\text{PDF}_{\ln\mathcal{N}}$

was used to determine the characteristic contact angle per droplet, and J_s calculated as described in Sect. 2.2.

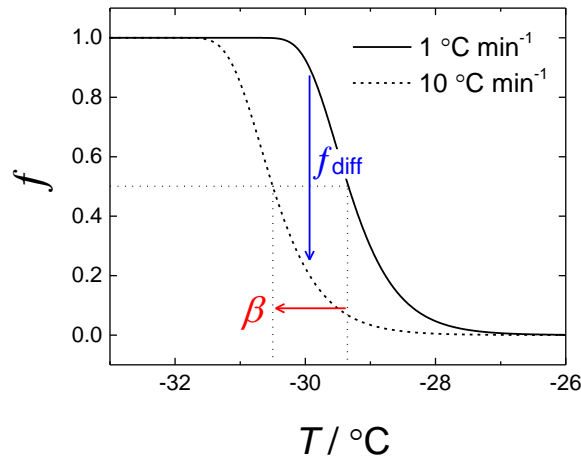


Figure 2.3. A conceptual diagram of how the cumulative fraction frozen (f) changes upon an increase in cooling rate. This change can be seen as both a change by β °C and f_{diff} .

Figure 2.3 shows the characteristic changes that will be used to determine the time-dependent behaviour in the following simulations. An increase in the cooling rate results in a change to the $f(T)$ curve which can be seen as either a change in f at a specific temperature (represented by f_{diff}) or a change in the temperature at a specific f (represented by a temperature β °C). The distinction between the two is required as a large magnitude in β does not necessarily correspond to a large magnitude in f_{diff} , as seen in Figure 2.3.

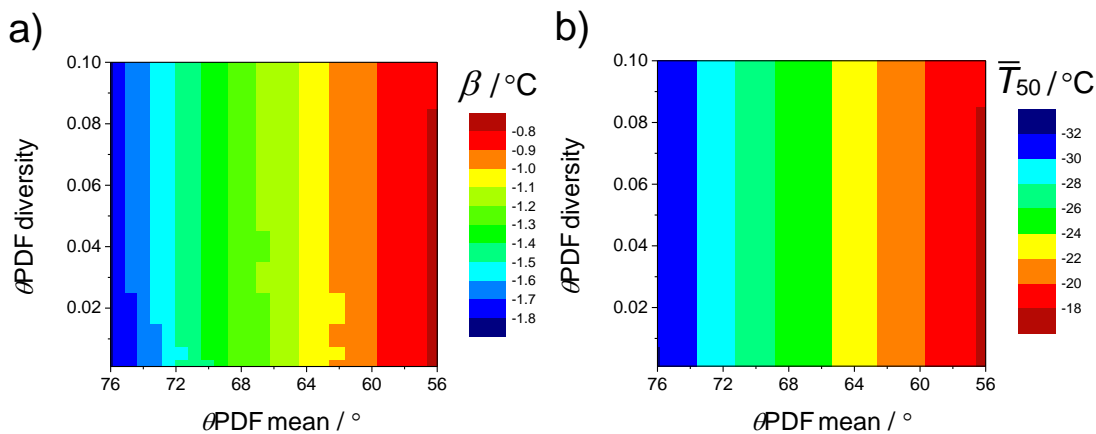


Figure 2.4. Contour plots of (a) the change in temperature β , calculated at $f = 0.5$, between a 1 and 10 °C min⁻¹ cooling simulation using a log-normal CNT-based θ PDF model and (b) the mean temperature \bar{T}_{50} at which $f = 0.5$ for the same set of runs. The x axis shows the effect of changing the θ PDF mean and the y axis the θ PDF diversity. The θ PDF diversity ranges from a monodisperse population (~ 0.01) to an extremely diverse population (0.10).

A series of simulations were performed where the mean and diversity of θ was varied; a log-normal distribution was used for the PDF of θ . The $f(T)$ data from cooling rates of 1 and 10 °C min⁻¹ was used to determine β , as well as the mean temperature at which 50% of droplets had frozen from the two cooling rates, \bar{T}_{50} . This value provides a characteristic temperature at which freezing occurred and the results of these simulations are shown in Figure 2.4. The plot in panel a of Figure 2.4 shows that β is independent of the width of the distribution (diversity), but strongly dependent on the mean θ of the distribution of contact angles. Similarly, panel b shows that \bar{T}_{50} is independent of diversity, but dependent on the mean θ .

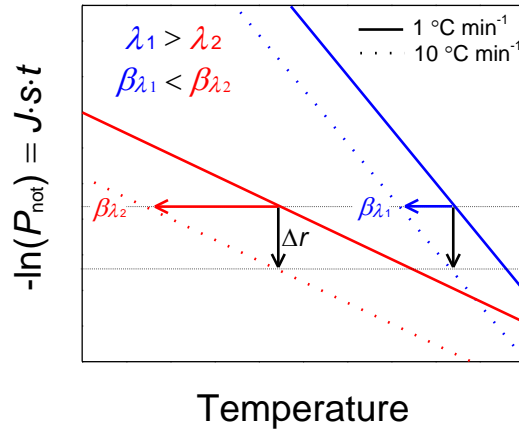


Figure 2.5. How the gradient $d\ln(J_s)/dT$ determines the cooling-rate dependence. A change in cooling rate Δr at a temperature T will result in the same change in $J_s t$ but will manifest with different β values. This results in a negative correlation between the magnitude of λ and β .

The relationship between the mean freezing temperature and time-dependent behaviour can be explained by the temperature dependent nature of the nucleation rate J_s , seen in Figure 2.1. The relation between the temperature dependence $-d\ln(J_s)/dT$ (hereafter referred to as λ) and β is demonstrated in Figure 2.5. For two INP species characterised by λ_1 and λ_2 (where $\lambda_1 > \lambda_2$) a decrease in time at a specific temperature will increase the probability of an event not occurring, P_{NOT} , by the same factor. This reduction can also be seen as an equivalent systematic shift in temperature β that corresponds to the temperature change required so that $J_s t_{r1} = J_s t_{r2}$. The result is that the shift by β °C will be dependent on λ . This relationship, between λ and β describes the behaviour seen in Figure 2.4. λ in CNT varies with temperature as seen in Figure 2.1, and therefore so too does β . The implication of this result

is that the time-dependent behaviour in simulations using CNT is solely a function of temperature. At high temperatures λ is large and therefore weak time-dependence would be expected, whereas at low temperatures λ is smaller resulting in a strong time-dependence.

2.2.1.1 Using a CNT-based MCS Model to Reproduce NX-illite Freezing Data

In the following sections the CNT-based model will be tested against experimental data obtained using a range of cooling rates and it will be shown to be lacking. The first example will use experimental data from cooling and isothermal experiments using NX-illite presented by Broadley et al. (2012). This INP species is thought to be representative of natural desert dust aerosol. The experiments were performed using a cold stage instrument, as described in Chapter 1. A population of droplets containing the mineral dust NX-illite were either cooled at a constant rate or held for a specific length of time at a supercooled temperature. The droplet population was produced by nebulising a volume of ultra-pure water (18.2 M Ω resistivity) containing a suspension of the mineral dust onto a glass slide with a hydrophobic coating. The resistivity of the water sample is a measure of its purity; water is a poor conductor (as compared to any dissolved minerals/salts) and therefore an increasing resistivity corresponds to an increasing purity, for comparison tap water is typically <1 M Ω . The nebulising method ensured that all droplets contained the same dust concentration as the suspension. A specific surface area of $104.2 \pm 0.7 \text{ m}^2 \text{ g}^{-1}$ (Broadley et al., 2012) was used to determine the surface area per droplet. The results are summarised in Figure 2.6.

Figure 2.6a shows the data for cooling experiments performed with a cooling rate (surface area) of 0.8 (6.43), 1.0 (8.54), 6.0 (8.06), and 7.5 °C min⁻¹ ($5.43 \times 10^{-7} \text{ cm}^2$), which corresponds to runs 13a, 15a, 14a, and 12 in Broadley et al. (2012), respectively. The data appear to fall on a single $f(T)$ curve with a variation of less than 1 °C between the four datasets, which strongly suggests that there is very little cooling-rate dependence, and therefore, time dependence. Data from an isothermal experiment are shown in Figure 2.6b. The experiment was performed at -29.5 °C with a population of droplets containing an average surface area per droplet of $2.65 \times 10^{-7} \text{ cm}^2$. In this experiment a decay in the number of liquid droplets is evident, with over 40% of droplets freezing after 11 minutes.

This clearly shows that although there is weak cooling-rate dependence there is time-dependent behaviour. The data also shows that the exponential decay rate decreases with time, which, as described in Chapter 1 suggests that this mineral dust behaves as a multiple-component species.

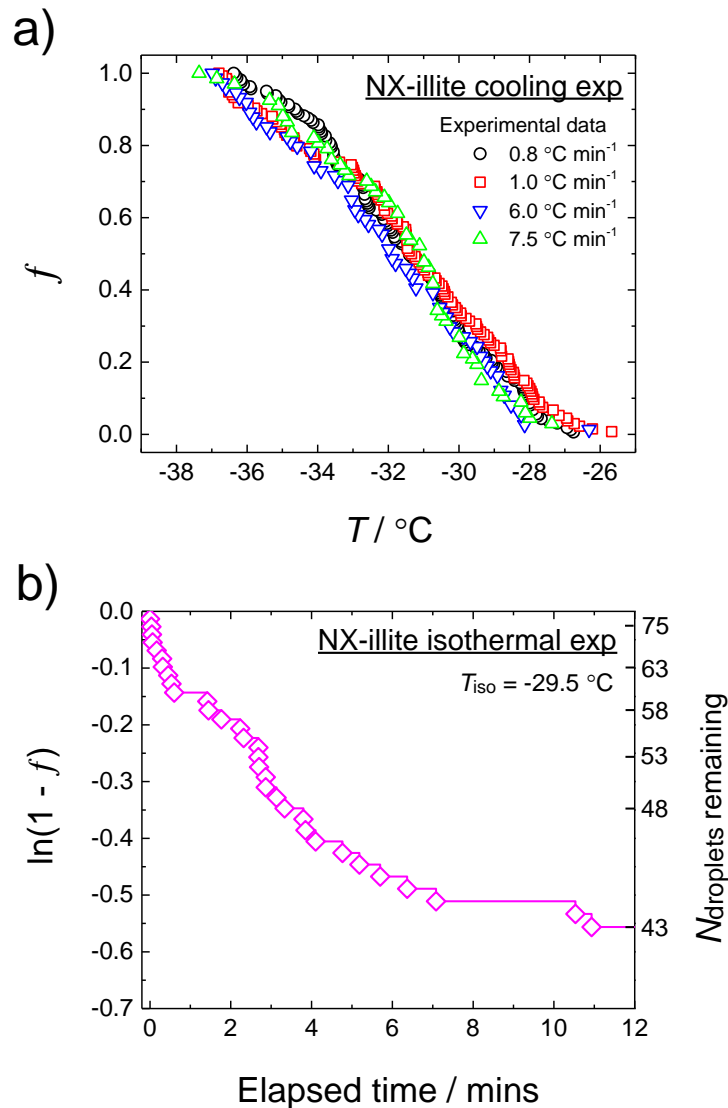


Figure 2.6. (a) The cumulative fraction frozen (f) for a series of experiments using droplets containing particles of the mineral dust NX-illite cooled at a range of cooling rates and (b) the decay of liquid droplets containing NX-illite in an isothermal experiment where the temperature was held constant at $-29.5\text{ }^\circ\text{C}$. Data reproduced from Broadley et al. (2012).

In the CNT-based MCS model the only variables that can be adjusted are those that relate to the PDF. The experimental dataset at $0.8\text{ }^\circ\text{C min}^{-1}$ was used to determine the distribution and θ PDF that best described the data, with the surface area per droplet and cooling rate as per the experiment. Using the root-mean-square-error (RMSE) between the simulated and

experimental dataset, it was found that a normal distribution with a mean $\mu_{\text{normal}} = 78.8^\circ$ and $\sigma_{\text{normal}} = 3.2^\circ$ produced a PDF that resulted in the lowest RMSE ($\text{PDF}_{\mathcal{N}} = 4.2 \times 10^{-4}$, $\text{PDF}_{\ln \mathcal{N}} = 5.2 \times 10^{-4}$, and $\text{PDF}_{\mathcal{W}} = 5.3 \times 10^{-4}$). This distribution was then used to simulate the 0.8 and $7.5^\circ\text{C min}^{-1}$ datasets. Figure 2.7 shows the experimental and simulated $f(T)$ curves. The two simulated $f(T)$ curves are separated by between 1.5 and 2.0°C , which shows that the CNT model over-predicts the cooling-rate dependence (β) of NX-illite. The reason for this is that by using CNT the cooling-rate dependence becomes primarily a function of temperature since the temperature dependence of λ is defined by CNT. In this case a much higher temperature would be required to match the simulated time-dependence with the observations.

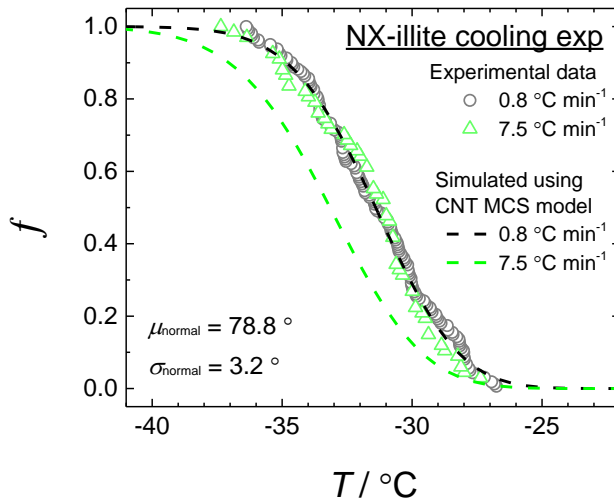


Figure 2.7. $f(T)$ experimental data (symbols) from Figure 2.6a for cooling rates of 0.8 and $7.5^\circ\text{C min}^{-1}$ and simulated $f(T)$ (dashed lines) using a CNT-based θ PDF model.

A potential caveat to this conclusion is that if the experimentally derived surface area per droplet was over estimated then the mean contact angle in the simulation would need to increase in order to reproduce the data. Figure 2.8 shows the gradient λ as a function of temperature and contact-angle. The data in Figure 2.7 lies roughly between -27 and -37°C and is characterised by a mean contact angle of 78.8° . This is indicated in Figure 2.8 and shows that if the mean contact angle was increased then the gradient λ would be higher, resulting in weaker cooling-rate dependence. However, in order to attain this dependence

the actual surface area per droplet in the experiment would need to be larger at $1 \times 10^6 \text{ cm}^2$, which is an unfeasibly large value.

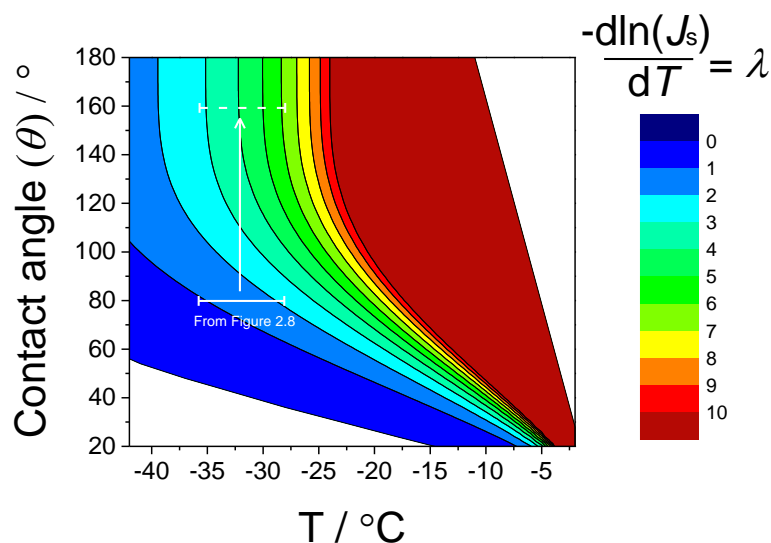


Figure 2.8. The gradient $\lambda = -\ln(J_s)/dT$ as a function of contact angle and temperature derived using CNT. The white bar roughly corresponds to the gradient that characterises the data in Figure 2.7, and the dashed line to a gradient that would result in weaker cooling-rate dependence.

2.2.1.2 Using a CNT-based MCS Model to Reproduce K-feldspar Freezing Data

It was recently proposed by Atkinson et al. (2013) that K-feldspar dominates the freezing behaviour of many multi-constituent species such as natural dusts. Similar to NX-illite, the data was obtained using a cold stage instrument (described in Whale et al. (2014)) upon which ~ 40 identical droplets were cooled at constant rates. The $1 \mu\text{L}$ droplets were produced, via pipette, from a bulk suspension of dust particles in ultra-pure water ($18.2 \text{ M}\Omega$). Thus, the resulting droplets are approximately identical and contain the same surface area per droplet. A specific surface area of $1.86 \pm 0.004 \text{ m}^2 \text{ g}^{-1}$ (Whale et al., 2014) was used to determine the surface area per droplet. The resulting data are shown in Figure 2.9 for cooling experiments performed at 0.2 and $2.0 \text{ }^\circ\text{C min}^{-1}$ with a surface area of $1.86 \times 10^{-2} \text{ cm}^2$ per droplet.

Simulated $f(T)$ curves using the CNT-based MCS model are compared with the experimental values in Figure 2.9. The simulated curves were produced following the method outlined for NX-illite previously. A PDF described by a Weibull distribution was found to best reproduce the $0.2 \text{ }^\circ\text{C min}^{-1}$ data based on RMSE values ($\text{PDF}_{\mathcal{N}} = 5.9 \times 10^{-4}$,

PDF_{ln \mathcal{N}} = 5.4×10^{-4} , and PDF _{\mathcal{W}} = 5.0×10^{-4}), with $\mu_{\text{Weibull}} = 49.8^\circ$ and $\sigma_{\text{Weibull}} = 2.87^\circ$. It is clear from Figure 2.9 that the CNT-based model under-predicts the cooling-rate dependence that is observed in the experiment.

In summary, it is clear from both the K-feldspar and NX-illite examples that the nucleation rate coefficient as predicted by the CNT-based model is unable to capture the time-dependent behaviour that is observed in experimental data.

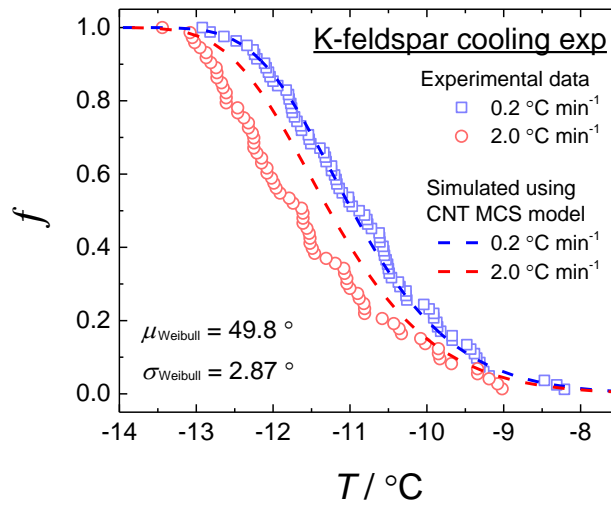


Figure 2.9. The cumulative fraction frozen for droplet freezing experiments using droplets containing particles of the mineral dust K-feldspar cooled at 0.2 and 2.0 °C min⁻¹ and simulated $f(T)$ (dashed lines) using a CNT-based θ PDF model.

2.3 A New Simplified MCS Model

In light of the results of the previous section a new MCS model named the Simplified MCS (Si-MCS) model was developed. This model is unique as it is able to reproduce both inter-particle variability in nucleating efficiency and time-dependent variability that is observed in experiments. The unique feature of this model is that the temperature dependence λ can be controlled, which allows time-dependent variability to be represented. As shown in the previous sections the CNT-based models were unable to represent this.

In this section the principles and assumptions of the Si-MCS will be presented. The model will then be tested using existing experimental data, and finally used to simulate and determine the expected time-dependent behaviour in droplet freezing experiments.

2.3.1 Deriving the Si-MCS Model

As with the previous MCS models it is assumed that the population of INPs, or nucleation sites, can be divided into sub-populations of equally efficient entities. Each sub-population is then treated as a single component where the nucleating efficiency per surface area of particle is equal. The single component stochastic (SCS) model can then be used to determine the number of droplets freezing in each model step, with the summation representing the freezing behaviour of the entire population. The principles of the Si-MCS are shown in Figure 2.10.

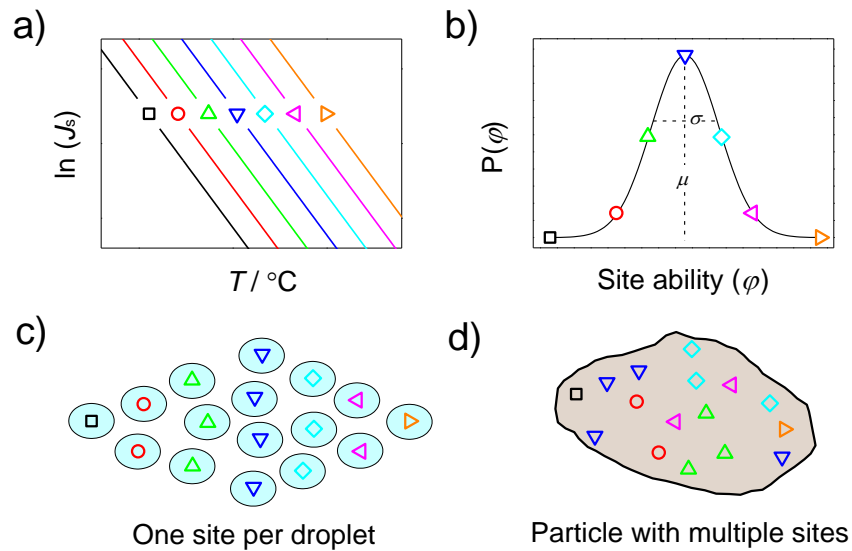


Figure 2.10. Principles of the Simplified MCS (Si-MCS) model. (a) shows the nucleation rate coefficient for a series of sites, represented by the range of symbols, and (b) the associated PDF that describes the probability of occurrence for each site. Assuming one site per droplet results in an externally mixed population of droplets, as in (c), whereas assuming multiple sites per particle, or droplet, results in an internally mixed population as in (d). See Sect. 2.3 for more details.

As an alternative to using CNT to predict $J_s(T)$ a simple exponential temperature-dependent function is used to describe the nucleation rate coefficient of a single component (denoted by i):

$$\ln J_{s,i}(T) = -\lambda_i(T + \varphi_i) \quad (2.1)$$

where λ_i is the gradient $-\text{dln}(J_{s,i})/\text{dT}$ as in Sect. 2.2 and φ_i , a positive value where $0 \leq \varphi_i \leq 50$, represents the relative freezing efficiency of the component. A value of φ_i tending towards zero represents an increasing efficiency to catalyse nucleation.

Each particle or site is assumed to be approximated by a single function of $J_{s,i}(T)$ and the value of λ_i for each INP species is assumed to be constant. With these assumptions the range of φ_i in a droplet will determine the range of $J_{s,i}(T)$ as shown in Figure 2.10a. The variability in φ_i is modelled using a PDF to describe the probability that a specific surface area of the immersed particle will be characterised by φ_i , so that $s_i = s \cdot P(\varphi_i)$. Here s is the total surface area of INP in the droplet and s_i the surface area characterised by φ_i . Using these assumptions an immersed particle contains a number of sites (n_{sites}), each of which has a unique value of φ_i (and therefore function $J_{s,i}(T)$) and a corresponding surface area that relates to the probability of φ_i occurring, as shown in Figure 2.10d.

For a single droplet with n_{sites} the probability that a freezing event occurs at a temperature T over a period of time t can be calculated as:

$$P_{\text{freezing}} = 1 - \exp\left(\sum_{i=1}^{n_{\text{sites}}} -J_{s,i}(T) \cdot s_i \cdot t\right) \quad (2.2)$$

For a number of droplets, each containing the same population of sites, the number that freeze in δt seconds can be calculated as:

$$N_{\text{frozen}} = N_{\text{liquid}} \cdot P_{\text{freezing}} = N_{\text{liquid}} \left(1 - \exp\left(\sum_{i=1}^{n_{\text{sites}}} -J_{s,i}(T) \cdot s_i \cdot \delta t\right)\right) \quad (2.3)$$

This description can be seen as being internally mixed, i.e., a population of droplets containing the same surface area per droplet will exhibit the same distribution of sites per droplet. This description is essentially equivalent to the SCS model; a number of identically sized particles will have the same distribution of nucleation sites and will therefore behave

as a single component, albeit with an internally mixed population of sites. In a single component system a decreasing value of λ will lead to an increasing width in the $f(T)$ curve. Therefore, using the internally mixed assumption in Eq. (2.3) an INP species with a wide $f(T)$ curve will be strongly time-dependent whereas with a narrow $f(T)$ curve it will be weakly time-dependent. Using this hypothesis the NX-illite (freezing over ~ 10 °C) should be more sensitive to changes in the cooling rate than K-feldspar (freezing over ~ 4 °C). However, both NX-illite and K-feldspar show ~ 1 °C change in $f(T)$ upon a factor of 10 change in cooling rate, indicating that the cooling-rate dependence is similar for both mineral dust species, and that the internally mixed description is not applicable to these INP species simultaneously.

Equation (2.3) can be extended to describe a particle-to-particle variability so that the distribution of sites per droplet is externally mixed:

$$N_{\text{frozen}} = \sum_{k=1}^{n_{\text{droplets}}} \left(1 - \exp \left(\sum_{i=1}^{n_{\text{sites},k}} -J_{s,i,k}(T) \cdot s_{i,k} \cdot \delta t \right) \right) \quad (2.4)$$

where k denotes each individual droplet. This can be simplified when it is assumed that the most efficient site present per droplet can be used to characterise its nucleating ability, and thus only one type of nucleation site is present per droplet. Under this assumption Eq. (2.4) can be rewritten as:

$$N_{\text{frozen}} = \sum_{i=1}^{n_{\text{sites}}} n_{\text{liquid},i} \left(1 - \exp(-J_{s,i}(T) \cdot s \cdot \delta t) \right) \quad (2.5)$$

where $n_{\text{liquid},i}$ is the number of droplets characterised by the site i , determined using a PDF so that $n_{\text{liquid},i} = N_{\text{liquid}} \cdot P(\varphi_i)$, and s the surface area per droplet. An example population of droplets following an externally mixed description is shown in Figure 2.10c.

As with the CNT-based models the distribution used to describe the PDF for φ_i was allowed to vary. In the following examples a normal, log-normal and Weibull distribution are used.

2.3.2 Applying the Si-MCS to Experimental Data

In the following sections the new Si-MCS model is used to determine the cooling-rate dependence of two atmospherically relevant mineral dust species: NX-illite and K-feldspar. The model is also used to predict the freezing behaviour of K-feldspar in an isothermal simulation, which is then compared to experimental data.

2.3.2.1 NX-illite Mineral Dust

The NX-illite freezing data presented in Sect. 2.2.1.1 was used with the Si-MCS to determine a value of λ that characterises the INP's time-dependent behaviour. The time-dependence of an INP species should be constant in different experiments. Therefore the model was applied separately to both the cooling and isothermal experiments, and results compared.

Cooling experiments performed at cooling rates of 1.0 and 6.0 °C min⁻¹ were used to determine the value λ that best reproduce the data. These datasets were chosen as both experiments used the same bulk suspension concentration and therefore have a similar average surface area per droplet (8.5×10^{-7} and 8.1×10^{-7} cm², respectively). The distribution of sites per droplet per experiment can then be assumed to be equivalent and the change in $f(T)$ data primarily due to cooling-rate dependence. A least squares minimisation between the experimental and simulated data was performed using each of the three distributions. The normal distribution PDF resulted in the lowest RMSE (PDF _{\mathcal{N}} = 7.725×10^{-4} , PDF _{$\ln\mathcal{N}$} = 1.21×10^{-3} , and PDF _{\mathcal{W}} = 9.815×10^{-4}), with $\lambda = 4.35$, $\mu_{\text{normal}} = 28.9$, and $\sigma_{\text{normal}} = 3.1$. All distributions resulted in a minimised λ of 4.35. The experimental data and simulated $f(T)$ curves are shown in Figure 2.11a. The same procedure was carried out for the isothermal experimental data (from Figure 2.6b) and is shown along with the resulting simulated data in Figure 2.11b. Similar to the cooling experiments a normal distribution PDF best reproduced the data with $\lambda = 4.4$, $\mu_{\text{normal}} = 27.4$, and $\sigma_{\text{normal}} = 0.9$

(minimised RMSE values of $\text{PDF}_{\mathcal{N}} = 6.209 \times 10^{-4}$, $\text{PDF}_{\ln \mathcal{N}} = 6.268 \times 10^{-4}$, and $\text{PDF}_{\mathcal{W}} = 7.761 \times 10^{-4}$).

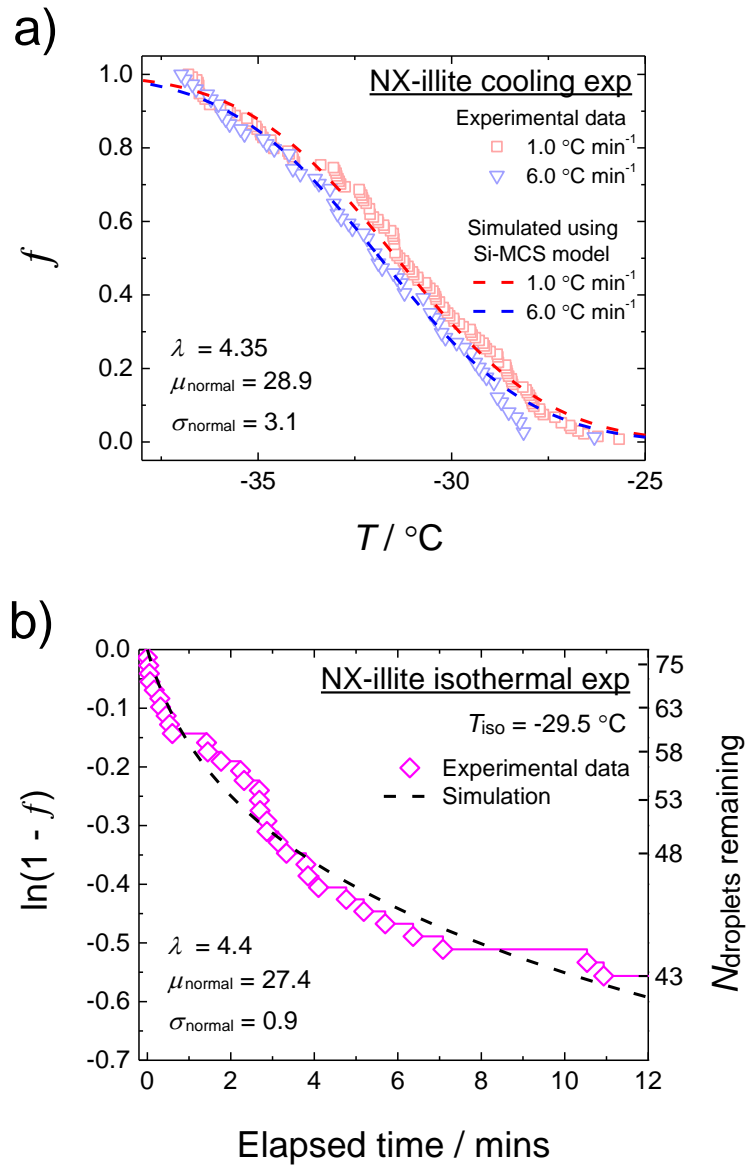


Figure 2.11. (a) Experimental data of $f(T)$ (shown as symbols) from Figure 2.7a for cooling experiments at 1 and $6 \text{ } ^\circ\text{C min}^{-1}$ along with the simulated $f(T)$ data determined using the Si-MCS model. The parameters λ , μ_{normal} and σ_{normal} were systematically varied until the RMSE between simulated and experimental data was minimised, with the resulting values shown in the figure. Similarly, (b) shows the isothermal experimental decay of droplets from Figure 2.7b along with a simulated decay using the Si-MCS model and following the procedure as in (a).

Even though the surface area per droplet was roughly equivalent (~ 3 to $8 \times 10^{-7} \text{ cm}^2$) the fitting parameters for the isothermal experiment suggest that the distribution of nucleation sites (or sub-populations) is considerably narrower than in the cooling experiments. Due to the method used in the isothermal experiment it was not possible to simulate the cooling (from $0 \text{ } ^\circ\text{C}$ to the isothermal temperature) that preceded the isothermal experiment. The

narrowing of the distribution provides evidence that the droplets containing the more efficient nucleation sites have preferentially frozen during the cooling. At the point of the isothermal the distribution of available nucleation sites has decreased and results in a narrower distribution, as demonstrated by the decreased standard deviation (3.1 to 0.9).

The agreement to each separate dataset is unsurprising as the added λ variable in the Si-MCS allows the cooling-rate dependence to be varied. However, the consistency between the cooling experiments and isothermal experiment suggests that the new model is able to represent both the variability in nucleating efficiency and time-dependent behaviour.

2.3.2.2 K-feldspar Mineral Dust

Similar to the previous example the Si-MCS was used to determine the value of λ that best describes a series of experimental datasets for the mineral K-feldspar obtained at cooling rates of 0.2, 0.4 and 2.0 °C min⁻¹.

The 0.2 and 2.0 °C min⁻¹ experimental data were taken from Sect. 2.2.1.2, and the 0.4 °C min⁻¹ data was obtained using the same cold stage instrument and method. The 1 μ L droplets are approximately identical and contain the same surface area per droplet of 1.86×10^{-2} cm² therefore it was assumed that the site PDF was the same for both experiments. A minimisation technique, based on the combined RMSE value between experiment and simulated data, was used for each PDF distribution. The data was best reproduced with $\lambda = 3.2$ and a PDF _{\mathcal{W}} where $\mu_{\text{Weibull}} = 11.67$ and $\sigma_{\text{Weibull}} = 1.22$ (minimised RMSE values of PDF _{\mathcal{N}} = 4.3×10^{-3} , PDF _{$\ln\mathcal{N}$} = 2.37×10^{-3} , and PDF _{\mathcal{W}} = 1.65×10^{-3}). The data and simulated $f(T)$ data is shown in Figure 2.12. The good agreement between the three datasets shows that the Si-MCS model is capable of reproducing the cooling-rate dependent behaviour of the K-feldspar sample.

In addition to the cooling experiments an isothermal experiment was performed using the same cold stage instrument and method. The population of droplets, each containing 1.86×10^{-2} cm² of K-feldspar particles, were cooled down at systematically decreasing rates until a temperature of -11 °C and held constant for 2 hrs. The time at which each droplet

freezing event occurred was recorded and is shown in Figure 2.13. To test whether the Si-MCS model had correctly determined the time-dependence of K-feldspar from the cooling rate experiments, the $\text{PDF}_{\mathcal{W}}$ parameters from Figure 2.12 were used with $\lambda = 3.2$ to determine the expected decay for a population of droplets under the same conditions. The justification in using the $\text{PDF}_{\mathcal{W}}$ parameters is that the droplets were produced from the same bulk suspension and therefore it can be assumed that droplets in both sets of experiments are equivalent. For the simulation the experimental cooling profile prior to reaching T_{iso} was used, which resulted in a number of droplets freezing before T_{iso} , as was observed in the experiment. The experimental uncertainty was estimated by Whale et al. (2014) as ± 0.4 °C; therefore two additional simulations were performed at $T_{\text{iso}} \pm 0.4$ °C. The expected decay, determined using the Si-MCS model, is included in Figure 2.13. The good agreement between experimental and simulated data provides additional evidence that the Si-MCS is able to reproduce the time-dependent behaviour of K-feldspar.

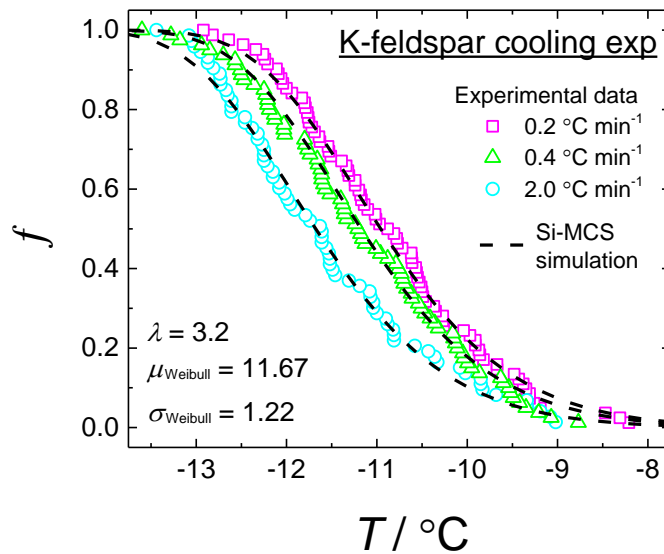


Figure 2.12. Experimentally determined $f(T)$ data (symbols) for droplets containing the same concentration of K-feldspar particles cooled at varying rates (0.2, 0.4, and 2.0 °C min⁻¹). Dashed lines represent the minimised fits to the data using the Si-MCS model. Fits were determined by varying the $\text{PDF}_{\text{Weibull}}$ parameters and λ ; surface area per droplet and cooling rates were as per the experiment.

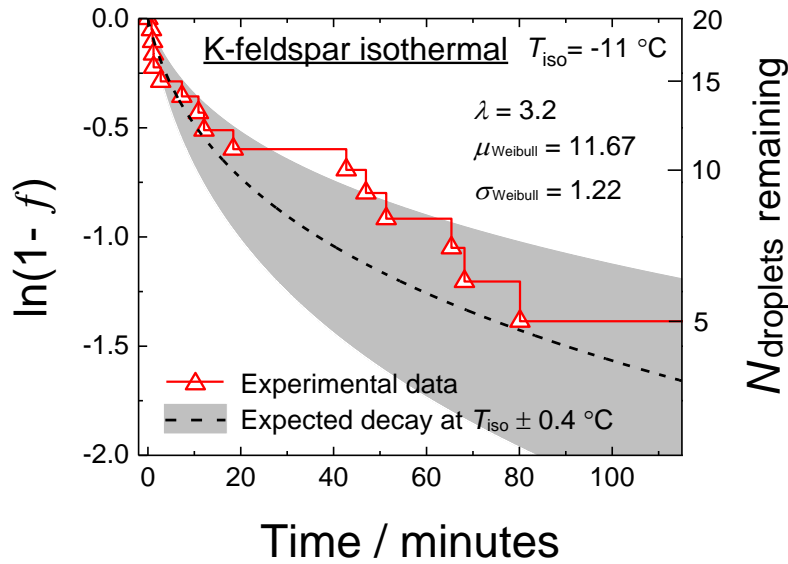


Figure 2.13. Expected decay (dashed line) of liquid droplets in an isothermal simulation at $-11\text{ }^{\circ}\text{C}$ using the Si-MCS with the parameters determined from the K-feldspar cooling experiments shown in Figure 2.12. Symbols show the corresponding experimental data from an isothermal experiment performed at $-11\text{ }^{\circ}\text{C}$ using droplets containing the same concentration of K-feldspar particles as in Figure 2.12.

2.3.3 The Manifestation of Time-Dependence

The Si-MCS model provides a tool that can be used to understand the sensitivity of droplet freezing experiments to the time-dependent properties of an INP species. In this section the Si-MCS model is used to understand how different temporal conditions can impact f in immersion mode experiments.

The stochastic, time-dependent nature of ice nucleation is expected to manifest differently depending on the experimental method and temporal conditions. *Isothermal experiments*, where the temperature is held constant for a duration of time (as in CFDC and cold stage instruments), will describe the time-dependent behaviour of the whole droplet population. The population may exhibit droplet-to-droplet variability in either time-dependent behaviour or nucleation efficiency. *Freeze-thaw experiments*, where single (or populations of) droplets are repeatedly frozen and thawed, will describe the time-dependent behaviour of each droplet. The variation in freezing temperatures over a number of cycles is expected to be equivalent to the droplet's time-dependent properties. *Cooling experiments*, where a population of droplets are cooled at some rate, will exhibit time-dependence upon a change

in cooling-rate. As in the Sect. 2.3.2 the shift in temperature of the $f(T)$ curve is expected to be dependent on the time-dependent properties of the droplet population.

It is clear that although time-dependence plays a role in each method its manifestation is expected to differ between experimental methods. As seen in Sect. 2.3.2.2 the model parameters (mean and diversity of φ , and λ) determined from cooling-rate experiments were used to produce the expected decay of liquid droplets in an isothermal experiment with good agreement. This shows that the Si-MCS model can be used to examine the different manifestations of time-dependence that would be observed in experiments.

2.3.3.1 Cooling-Rate Dependence

A series of simulations were performed in order to determine the impact of time-dependence on f in cooling experiments upon a change in cooling rate. The additional effect of the mean and diversity of site efficiency φ was also examined.

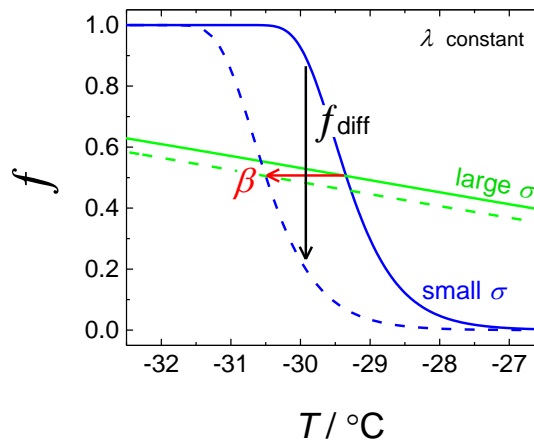


Figure 2.14. The simulated change in the $f(T)$ curve upon a change in cooling rate from 1 to 10 $^{\circ}\text{C min}^{-1}$ for two INPs described with the same λ but different site diversity σ_{normal} . β remains constant but f_{diff} decreases with σ_{normal} .

Following Figure 2.14 the values of β and f_{diff} were determined for a change in cooling rate from 1 to 10 $^{\circ}\text{C min}^{-1}$. The magnitude of β provides the quantitative information on how the $f(T)$ curve shifts in temperature whereas the magnitude of f_{diff} provides qualitative information on how important this effect is. For example, a large shift by β may correspond to a small value of f_{diff} . In terms of experimental observations this would be a negligible

time-dependent effect on the $f(T)$ curve. Conversely, if the magnitudes were reversed then although β is small the observed time-dependent effect would be considerable.

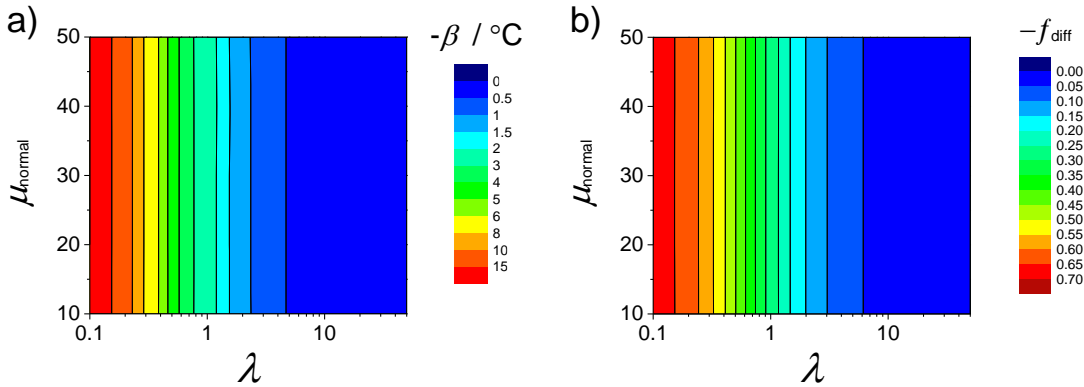


Figure 2.15. Sensitivity of β (a) and f_{diff} (b) to the temperature dependence of the nucleation rate (λ) and the PDF mean (μ_{normal}) in the Si-MCS model. For each data point a simulated cooling experiment was performed at 1 and $10\text{ }^\circ\text{C min}^{-1}$; as shown in Figure 2.3 β was calculated where $f = 0.5$ and f_{diff} was calculated at the mean T_{50} determined for each cooling rate. A normal distribution was used to describe the PDF; the standard deviation was kept constant at $\sigma_{\text{normal}} = 3$ and μ_{normal} was varied.

In these simulations the mean nucleating efficiency (μ_{normal} of $\text{PDF}_{\mathcal{N}}$) was varied along with λ whilst the diversity in efficiency was held constant at $\sigma_{\text{normal}} = 3$. Figure 2.15 shows the sensitivity of β and f_{diff} . It can be clearly seen that changes to the $f(T)$ curve are dependent on λ but independent of the mean efficiency. The time-dependent response of $f(T)$ increases with decreasing λ ; i.e., a shallow temperature dependent nucleation rate will have a stronger time-dependent response. The independence of f_{diff} with respect to μ_{normal} describes a $f(T)$ curve that does not change shape. The independence of β also shows that the $f(T)$ curve will shift by the same value (upon the same change in cooling rate) regardless of the mean efficiency of the droplet population.

To understand the dependency on site diversity a second series of simulations were performed where the diversity of the droplet population was varied along with λ , whilst μ_{normal} was held constant at $\mu_{\text{normal}} = 20$. The results are shown in Figure 2.16. As with μ_{normal} the simulations show that β is dependent on λ but independent of the diversity in droplet efficiency, conversely, f_{diff} is dependent on both μ_{normal} and λ . This happens because as the diversity increases so does the width of the $f(T)$ curve. This then causes f_{diff} to become less

sensitive to changes in cooling rate. This behaviour is demonstrated in Figure 2.14 where β is constant but f_{diff} decreases with diversity.

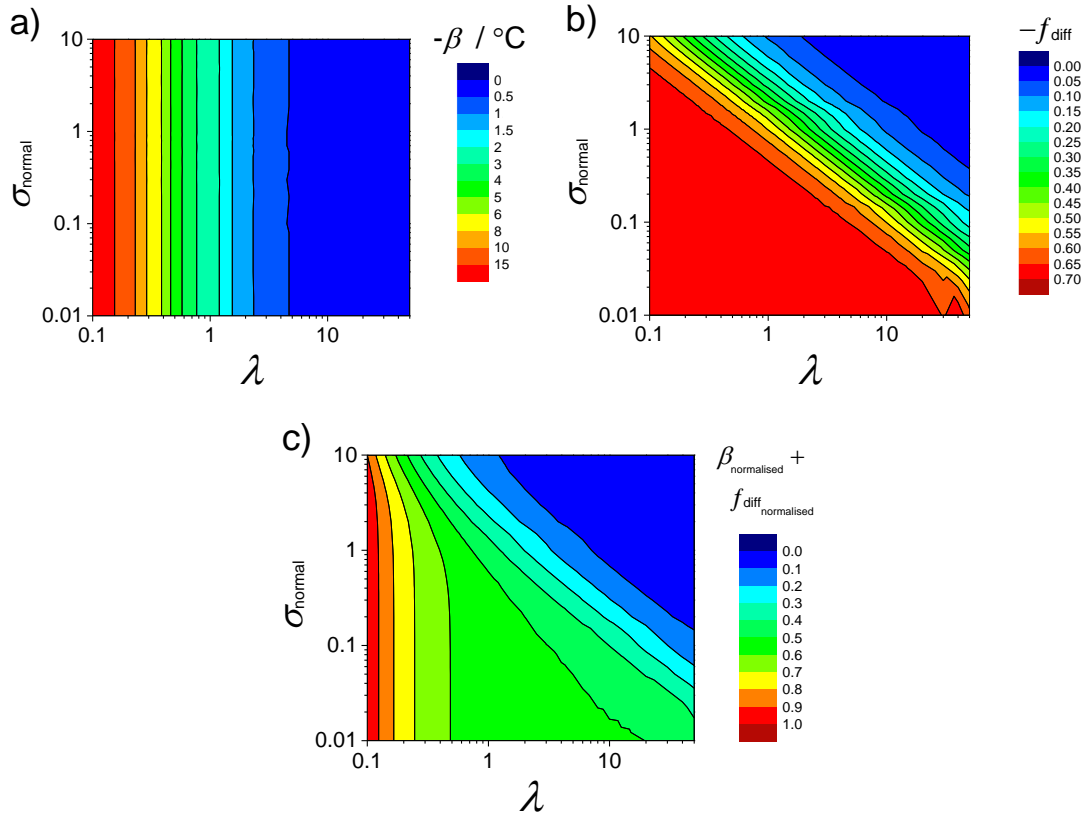


Figure 2.16. Sensitivity of β (a) and f_{diff} (b) to the temperature dependence of the nucleation rate (λ) and the PDF standard deviation (σ_{normal}) in the Si-MCS model. Method as in Figure 2.15 but here the mean was held constant at $\mu_{\text{normal}} = 20$ and σ_{normal} was varied. The normalised impact of both β and f_{diff} is shown in (c); here, the data from (a) and (b) were normalised so that a value of 1 corresponds to $-\beta_{\text{max}} + f_{\text{diff,max}}$. This provides a range, between 0 and 1, that describes the combined time-dependent response to $f(T)$ with an increasing number representing an increasing response.

A combination of β and f_{diff} can be used to provide qualitative information on the overall time-dependent response. For each variable the absolute maximum from the associated panel in Figure 2.16 was used to normalise the corresponding dataset. The summation of these datasets then represents the combined magnitude of both variables. A value of 1 represents a combination of σ_{normal} and λ that results in the maximum combined magnitude of β and f_{diff} . Using this method an increasing value represents an increasingly time-dependent response. The results of this normalisation in Figure 2.16c show that a substantial observable cooling-rate dependence is expected for all values of σ_{normal} when $\lambda < 0.5$. For larger values the cooling-rate dependence decreases with both increasing λ and the

efficiency diversity. INP species that exhibit a very narrow distribution of nucleating efficiencies would have observable cooling-rate dependence at all values of λ , although the magnitude of this would decrease with increasing λ .

In terms of the fundamental effect of λ on $f(T)$ the results from these simulations suggest that β is only dependent on λ . To test this further a set of simulations were run where all free variables in the Si-MCS model were varied. This included the assumed PDF distribution (normal, log-normal, and Weibull) and associated PDF parameters, surface area per droplet, cooling rates, the fraction f at which β was calculated, and λ . The results, shown in Figure 2.17, verify the relationship between the systematic shift in $f(T)$ by β °C and the temperature dependence of the nucleation rate coefficient, $-\ln(J_s)/dT = \lambda$. All this data falls on a single line which can be described by the power law $\beta = 2.3197 \cdot \lambda^{-0.991}$, which describes a near one-to-one relationship.

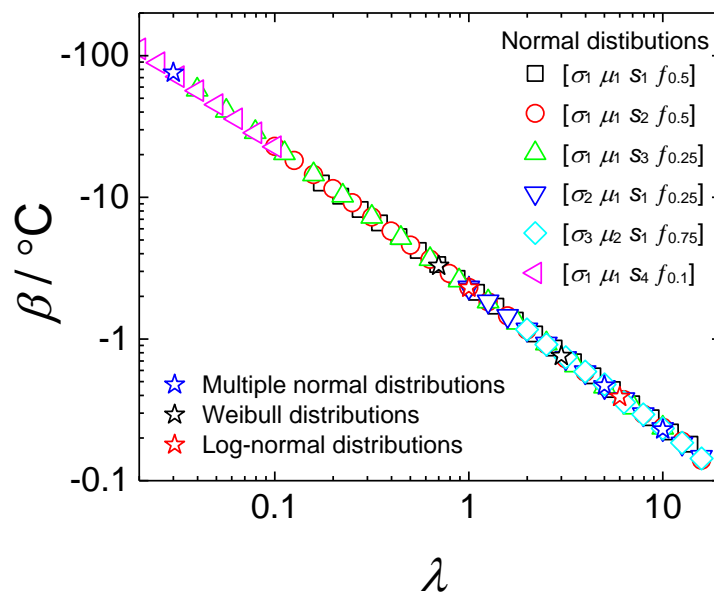


Figure 2.17. The shift in the $f(T)$ curve, by β °C, upon a factor of ten change in cooling rate for a number of simulations using the Si-MCS model. In these simulations all variables in the Si-MCS model were varied; these included the surface area, PDF distribution, PDF mean and standard deviation, cooling rates, the temperature dependence of the nucleation rate λ , and the fraction at which β was calculated. All data fall onto a single line when plotted against λ which shows that the cooling-rate dependence is purely dependent on λ .

The relationship between λ and β suggests that a simple relationship can be used to determine the change to the $f(T)$ curve upon a change in cooling rate. The singular freezing

model presented in Chapter 1 is able to describe the variability in nucleating efficiency using a simple temperature dependent function; with correctly determined characteristics for an INP species the β - λ relationship could be used in conjunction with this in order to predict the freezing behaviour of droplets containing the species. This will be the focus of the following chapter.

2.3.3.2 Residence-Time Dependence

In experiments where the temperature is held constant for a period of time a change in residence time leads to a change in the amount of time that nucleation can occur. As nucleation is thought to be a stochastic process this change is expected to have a corresponding effect on f . A series of isothermal simulations were performed using the Si-MCS in order to understand how the characteristic properties of the INP species (PDF parameters, T , and λ) are expected to affect the decay rate of droplets with regards to a change in residence time. Figure 2.18 shows the dependence of the droplet decay rate as a function of residence time at two isothermal temperatures (T_{iso}). The diversity of the PDF $_{\mathcal{N}}$ distribution was also varied for each T_{iso} whilst μ_{normal} was held constant at $\mu_{\text{normal}} = 17$.

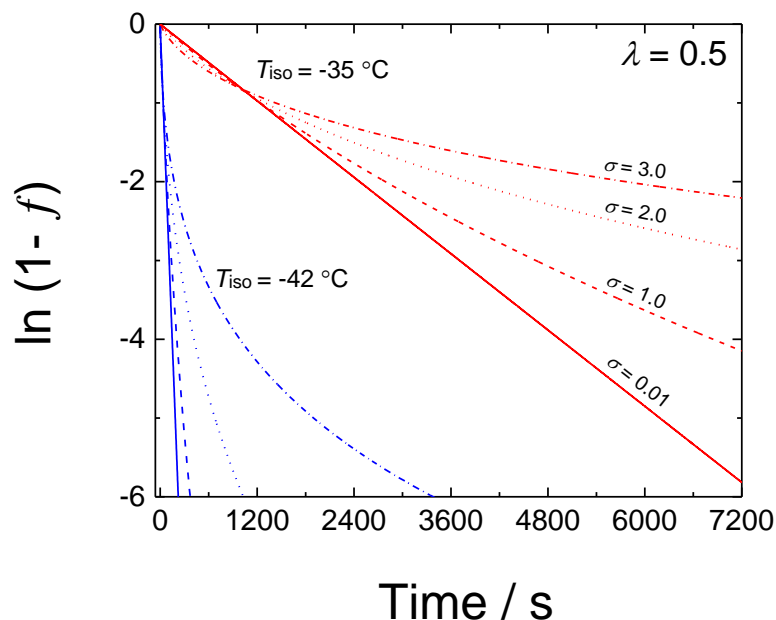


Figure 2.18. Simulated decay in liquid droplets ($1 - f$) over time using the Si-MCS model at two temperatures and an increasing diversity of nucleating efficiency (represented by an increasing standard deviation). A normal distribution is used to represent the PDF, with $\lambda = 0.5$ and $\mu_{\text{normal}} = 17$. In a single component system (where all $\varphi = \mu_{\text{normal}}$, as with $\sigma_{\text{normal}} = 0.01$) the liquid droplets will exponentially decay at a constant rate dependent on λ , whereas in a multiple component system (where a range of φ exist) the decay rate decreases with time.

The distribution where $\sigma_{\text{normal}} = 0.01$ represents a monodisperse population where all droplets are characterised by the value of μ_{normal} . According to Eq. 1.15 a monodisperse population will behave as a single component-system, and therefore liquid droplets will exponentially decay. This behaviour can be seen in Figure 2.18 as a linear relationship between $\ln(1-f)$ and time. As the temperature decreases this decay rate increases due to the increasing value of J_s and therefore the probability of freezing. The monodisperse population generally represents the maximum fraction able to freeze for a given λ and t . An increasing diversity in droplet nucleating efficiency (σ_{normal}) results in a decay rate that decreases with residence time. At a specific residence time the fraction of droplets that freeze will decrease with increasing diversity. This occurs because as the PDF width increases the range of nucleation efficiencies increases, and therefore the droplet population contains both more and less efficient droplets. Due to the exponential relationship between the probability of freezing and time, the less efficient droplets have a more substantial effect on the decay rate than the more efficient ones.

The sensitivity of f with regards to λ , T , and σ_{normal} is shown in Figure 2.19, which shows the residence time required for the simulation to reach a frozen fraction of $f = 0.1$. This provides information on how the decay rate changes with temperature. At low values of λ the time required to attain $f = 0.1$ changes by a factor of 10^4 over 20°C , whereas at high values of λ this results in a change by factor of $\sim 10^{18}$. This shows a change in T_{iso} will have a greater effect on the residence-time dependence for larger values of λ . In CFDC experiments where a constant residence time is used, upon a decrease in T_{iso} the change in f will be greater for higher values of λ .

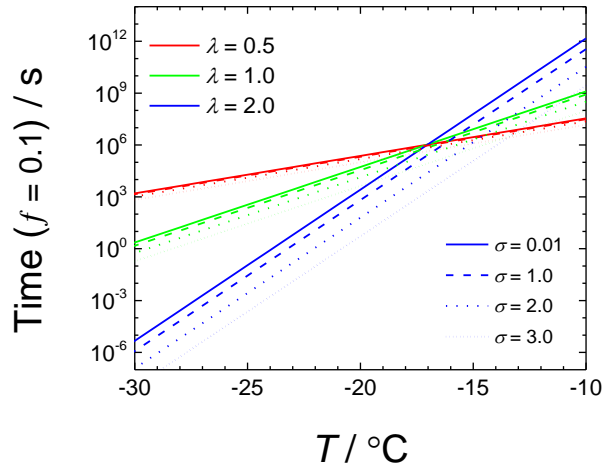


Figure 2.19. The impact of λ and ϕ diversity in isothermal simulations using the Si-MCS model as a function of isothermal temperature. The figure shows the time for the isothermal simulation to reach $f = 0.1$. All simulations used a normal distribution to determine the PDF where the mean was held constant at $\mu_{\text{normal}} = 17$.

Figure 2.19 also shows that an increase in diversity systematically decreases the trend to lower residence times; again the fractional change is lower for small values of λ , and vice versa. This shows that a change in diversity can be described by an equivalent change in the temperature T_{iso} . This change is independent of temperature but is dependent on λ and one can expect this to also be dependent on the chosen fraction (in this case $f = 0.1$) which can be inferred from Figure 2.18. This suggests that a knowledge of how the equivalent shift in temperature manifests for a given diversity and λ could be used to derive a simple means of predicting the isothermal decay of droplets at any temperature for a correctly characterised INP species. An equivalent derivation will be presented in the following chapter.

The key conclusion from these simulations is that in isothermal experiments time-dependence manifests as residence-time dependence and that similar to cooling simulations there is a significant sensitivity to λ . However, unlike the cooling simulations, the diversity of the population efficiency does have an affect on the decay of liquid droplets.

2.3.3.3 Freeze-Thaw Variability

In freeze-thaw experiments single, or populations of droplets are subjected to repeated cycles of freezing and thawing. In this section the Si-MCS model will be used to understand

how the nucleating properties of an INP are expected to affect the variability of T_{freeze} in freeze-thaw experiments.

A freeze-thaw experiment can be simulated in the Si-MCS model when it is realised that one droplet being frozen n times at a cooling rate r is equivalent to n identical droplets being frozen a single time at a rate r . A single-component system where φ equals the median freezing temperature provides a population of identical droplets, which can be used with the Si-MCS to simulate a single cooling experiment. Applying a prescribed n droplets to the resulting $f(T)$ curve provides the temperature at which each consecutive droplet freezes. These temperatures correspond to T_{freeze} values from n freeze-thaw cycles, and therefore the standard deviation in T_{freeze} can be determined, hereafter named $\sigma_{T,\text{freeze}}$. Using this method a series of $1\text{ }^{\circ}\text{C min}^{-1}$ cooling simulations were performed to determine $\sigma_{T,\text{freeze}}$ as a function of the median freezing temperature and λ ; the results are shown in Figure 2.20. The results show that $\sigma_{T,\text{freeze}}$ is solely dependent on λ and is independent of the mean freezing temperature. In a single-component system a change in cooling rate will move the median freezing temperature by β , therefore $\sigma_{T,\text{freeze}}$ is also independent of the freeze-thaw experiment cooling rate. This behaviour was reported by Fornea et al. (2009) who performed freeze-thaw experiments using the same INP species over a range of cooling rates (1 to $10\text{ }^{\circ}\text{C min}^{-1}$) and found no statistical difference in $\sigma_{T,\text{freeze}}$.

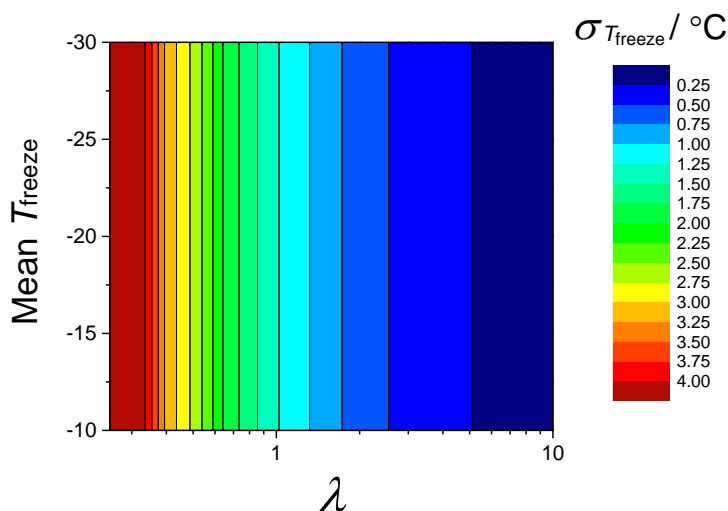


Figure 2.20. The resulting standard deviation ($\sigma_{T,\text{freeze}}$) of freezing temperatures for a single droplet frozen over 10^4 freeze-thaw cycles as a function of the mean freezing temperature and λ . $\sigma_{T,\text{freeze}}$ is only dependent on λ .

The dependency of $\sigma_{T,\text{freeze}}$ on λ shown in Figure 2.20 is described by the following power law

$$\sigma_{T,\text{freeze}} = 1.2691 \cdot \lambda^{-1} \quad (2.6)$$

Wright and Petters (2013) presented a very similar relationship $\sigma_{T,\text{freeze}} = 1.21 \cdot \lambda^{-1.05}$. Their method varied from this in that several other parameters (including n_{sites} per droplet, and cooling rate) were varied. These variables would act to impact the location of the $f(T)$ curve (with regards to temperature) and will ultimately affect the range of T_{freeze} and therefore $\sigma_{T,\text{freeze}}$. The newly presented relationship in Eq. (2.6) is therefore a better representation of how a droplet with specific freezing characteristics (i.e., INP surface area and nucleation efficiency) would be expected to behave upon multiple freeze-thaw cycles.

2.4 Conclusions

In this chapter a CNT-based MCS model was applied to atmospherically relevant immersion mode freezing data. The model is unable to reproduce the observed cooling-rate dependence in immersion mode freezing data for K-feldspar and NX-illite. A sensitivity study using the model shows that the resulting time-dependent behaviour through the use of CNT is primarily a function temperature, which is inconsistent with the observations.

A new simplified MCS model (Si-MCS) model was presented which uniquely allows the temperature-dependency (λ) of the nucleation rate coefficient (J_s) to be varied. The model is able to represent variability in both nucleating efficiency and time-dependent behaviour. As demonstrated by the application to experimental data, the Si-MCS can be used determine the time-dependent behaviour of an INP species, and then simulate its expected time-dependent behaviour in different experimental methods.

Finally, a series of simulations using the Si-MCS were performed to understand the relationship between INP nucleating properties and time-dependent behaviour in cooling, isothermal, and freeze-thaw experiments. The results show for the first time that the manifestation of time-dependence in all experimental methods is solely dependent on λ . It

was also demonstrated that freeze-thaw experiments using a single droplet are equivalent to a cooling experiment with a population of identical droplets.

Chapter 3: The Framework for Reconciling Observable Stochastic Time-Dependence (FROST)

3.1 Introduction

In the previous chapter the simplified multiple component stochastic (Si-MCS) model was presented which is able to represent variability in both nucleating efficiency and time-dependent behaviour. However, the model is too complex for use in cloud modelling studies. In this chapter a new simplified framework based on the Si-MCS is developed for use in reconciling the time-dependencies in immersion mode freezing experiments. The framework is then incorporated into an existing parameterisation for use in cloud modelling studies.

The derivation and development of the FROST model was published in Atmospheric Chemistry Physics and Discussions (Herbert, R. J., Murray, B. J., Whale, T. F., Dobbie, S. J., and Atkinson, J. D.(2014), Representing time-dependent freezing behaviour in immersion mode ice nucleation, Atmos. Chem. Phys. Discuss., 14, 1399-1442, doi:10.5194/acpd-14-1399-2014). All development and derivations were carried out by R. Herbert.

3.2 Deriving the Framework

The results from Chapter 2 suggest that the manifestations of time-dependence in immersion mode freezing are all dependent on λ . If these results can be verified analytically then it may be possible to link the varying time-dependent behaviour across different instruments and therefore reconcile data obtained under differing temporal conditions.

3.2.1 Cooling-Rate Dependence

The aim of this derivation is to determine the temperature change β that occurs for a specific fraction $f(T)$ upon a change in cooling rate. Using the Si-MCS the number of droplets that freeze (n_f) within a single time step δt at a temperature T can be determined by:

$$n_f = n_l (1 - \exp(-J_s(T)s\delta t)) \quad (3.1)$$

where n_l is the number of liquid droplets at the beginning of the time step. For a population of droplets (each containing a surface area s of an INP species), the cumulative number that will freeze upon cooling in n_r steps of δt from the melting point of ice (T_0) to T can be calculated using the product of the probability for an event not happening (P_{not}) at each consecutive step. The probability of an event occurring is therefore $1 - P_{not}$ so that:

$$n_f = N_l \left(1 - \prod_{k=0}^{n_r} P_{not,k} \right) \quad (3.2)$$

where,

$$P_{not,k} = \exp(-J_s(T_k) s \delta t_r) \quad (3.3)$$

$J_s(T_k)$ is the nucleation rate coefficient at time step k , s is the surface area of INP, and N_l is the initial number of droplets at T_0 °C. The cumulative fraction frozen after n_r steps, $f(n_r)$, can be expressed as:

$$f(n_r) = \frac{n_f}{N_l} = 1 - \prod_{k=0}^{n_r} P_{not,k} \quad (3.4)$$

Incorporating Eq. (3.3) into Eq. (3.4) gives:

$$f(n_r) = 1 - \prod_{k=0}^{n_r} \exp(-J_s(T_k) s \delta t_r) = 1 - \exp\left(-\sum_{k=0}^{n_r} J_s(T_k) s \delta t_r\right) \quad (3.5)$$

In the Si-MCS model the nucleation rate coefficient J_s at T_k is expressed as $\ln J_s(T_k) = -\lambda(T_k + \varphi)$. To calculate $J_s(T_k)$ for any number of δt_r steps this can be expanded:

$$J_s(T_{k=0}) = \exp(-\lambda(T_0 + \varphi)) = \exp(-\lambda T_0 - \lambda\varphi)$$

$$J_s(T_{k=1}) = \exp(-\lambda(T_0 + \delta T) + \lambda\varphi) = \exp(-\lambda T_0 + \lambda\varphi) \cdot \exp(-\lambda\delta T)$$

$$\begin{aligned} J_s(T_{k=2}) &= \exp(-\lambda(T_0 + \delta T + \delta T) + \lambda\varphi) \\ &= \exp(-\lambda(T_0) + \lambda\varphi) \cdot \exp(-\lambda\delta T) \cdot \exp(-\lambda\delta T) \\ &= \exp(-\lambda(T_0) + \lambda\varphi) \cdot \exp(-\lambda\delta T)^2 \end{aligned}$$

$$\begin{aligned} J_s(T_{k=3}) &= \exp(-\lambda(T_0 + \delta T + \delta T + \delta T) + \lambda\varphi) \\ &= \exp(-\lambda T_0 + \lambda\varphi) \cdot \exp(-\lambda\delta T) \cdot \exp(-\lambda\delta T) \cdot \exp(-\lambda\delta T) \\ &= \exp(-\lambda T_0 + \lambda\varphi) \cdot \exp(-\lambda\delta T)^3 \end{aligned}$$

Therefore it can be seen that:

$$J_s(T_k) = \exp(-\lambda T_0 + \lambda\varphi) \cdot [\exp(-\lambda\delta T)]^k = J_s(T_0) \cdot [\exp(-\lambda\delta T)]^k \quad (3.6)$$

Incorporating into Eq. (3.5):

$$f(n_r) = 1 - \exp\left(-s \cdot \delta t_r \cdot J_s(T_0) \sum_{k=0}^{n_r} [\exp(-\lambda\delta T)]^k\right) \quad (3.7)$$

The summation term can be removed using a geometric summation of series where

$$\sum_{k=0}^{n-1} ar^k = a \frac{1 - r^n}{1 - r}.$$

Rearranging Eq. (3.7) identifies the series:

$$\frac{-\ln(1 - f(n_r))}{A \cdot \delta t_r \cdot J_s(T_0)} = \sum_{k=0}^{n_r} [\exp(-\lambda\delta T)]^k \quad (3.8)$$

Substituting the right hand side into the geometric summation of series formula where $a = 1$; $r = \exp(-\lambda\delta T)$; and $n - 1 = n_r$ (therefore $n = n_r + 1$) gives:

$$\frac{-\ln(1 - f(n_r))}{s \cdot \delta t_r \cdot J_s(T_0)} = \frac{1 - [\exp(-\lambda\delta T)]^{n_r+1}}{1 - \exp(-\lambda\delta T)} \quad (3.9)$$

This can now be rearranged and solved for the number of steps n_r :

$$\frac{-\ln(1 - f(n_r)) \cdot (1 - \exp(-\lambda\delta T))}{s \cdot \delta t_r \cdot J_s(T_0)} = 1 - \exp(-\lambda\delta T(n_r + 1)) \quad (3.10)$$

$$1 - \left[\frac{-\ln(1 - f(n_r)) \cdot (1 - \exp(-\lambda\delta T))}{s \cdot \delta t_r \cdot J_s(T_0)} \right] = \exp(-\lambda\delta T(n_r + 1)) \quad (3.11)$$

$$\ln \left[1 - \left[\frac{-\ln(1 - f(n_r)) \cdot (1 - \exp(-\lambda\delta T))}{s \cdot \delta t_r \cdot J_s(T_0)} \right] \right] \frac{1}{-\lambda\delta T} = n_r + 1 \quad (3.12)$$

$$n_r = \ln \left[1 - \left[\frac{-\ln(1 - f(n_r)) \cdot (1 - \exp(-\lambda\delta T))}{s \cdot \delta t_r \cdot J_s(T_0)} \right] \right] \frac{1}{-\lambda\delta T} - 1 \quad (3.13)$$

A change in the cooling rate from r_1 to r_2 results in a change in the number of steps required to reach fraction f , so that $f = f(n_{r1}) = f(n_{r2})$:

$$n_{r2} - n_{r1} = \ln \left[\frac{1 - \left[-\ln(1 - f) \cdot (1 - \exp(-\lambda\delta T)) \cdot \frac{1}{s \cdot \delta t_{r2} \cdot J_s(T_0)} \right]}{1 - \left[-\ln(1 - f) \cdot (1 - \exp(-\lambda\delta T)) \cdot \frac{1}{s \cdot \delta t_{r1} \cdot J_s(T_0)} \right]} \right] \frac{1}{-\lambda\delta T} \quad (3.14)$$

where δT is constant in both simulations, and δt is dependent on the cooling rate.

Introducing the constant $C = -\ln(1 - f) \cdot (1 - \exp(-\lambda\delta T))$ gives:

$$n_{r2} - n_{r1} = \ln \left[\frac{1 - \left[\frac{C}{s \cdot \delta t_{r2} \cdot J_s(T_0)} \right]}{1 - \left[\frac{C}{s \cdot \delta t_{r1} \cdot J_s(T_0)} \right]} \right] \cdot \frac{1}{-\lambda\delta T} \quad (3.15)$$

When $(s \cdot \delta t \cdot J_s(T_0)) \ll C$, Eq. (3.15) is approximated by the following equation:

$$n_{r_2} - n_{r_1} = \ln \left[\frac{C \cdot s \cdot \delta t_{r_1} \cdot J_s(T_0)}{C \cdot s \cdot \delta t_{r_2} \cdot J_s(T_0)} \right] \cdot \frac{1}{-\lambda \delta T} \quad (3.16)$$

This condition may break down in situations where either s or $J_s(T_0)$ is very large, corresponding to atmospherically unrepresentative sizes or exceptionally efficient nucleating INPs, respectively. This will also break down as C approaches zero, which occurs when either $f \approx 1$ or $\delta T \ll 1$ (e.g., 1×10^{-8}).

Cancelling terms in Eq. (3.16) provides:

$$n_{r_2} - n_{r_1} = \ln \left[\frac{\delta t_{r_1}}{\delta t_{r_2}} \right] \cdot \frac{1}{-\lambda \delta T} \quad (3.17)$$

Multiplying the change in n_r by the temperature step δT (constant in both cases) provides a formula for the change in temperature:

$$\Delta T = (n_{r_2} - n_{r_1}) \delta T = \ln \left[\frac{\delta t_{r_1}}{\delta t_{r_2}} \right] \cdot \frac{1}{-\lambda} \quad (3.18)$$

Substituting $r_1 = \frac{\delta T}{\delta t_{r_1}}$ and $r_2 = \frac{\delta T}{\delta t_{r_2}}$ into Eq. (3.18) provides a formula that can be used to calculate the change in temperature observed at a fraction f upon a change in cooling rate:

$$\Delta T = \ln \left[\frac{r_1}{r_2} \right] \cdot \frac{1}{\lambda} \quad (3.19)$$

where λ describes the temperature dependence of J_s ; $-\ln(J_s)/dT$. This can be seen as being directly equivalent to the empirically determined value of β in the previous chapter, and confirms the relationship between λ and β . A comparison between this equation and the fit from Figure 2.17 strengthens this finding: applying a change in cooling rate from 1 to $10 \text{ }^\circ\text{C min}^{-1}$ leads to $\Delta T = \ln \left[\frac{1}{10} \right] \cdot \frac{1}{\lambda} = 2.31 \cdot \lambda^{-1}$.

3.2.2 Extending to Residence-Time Dependence

In this section Eq. (3.19) will be extended to isothermal conditions.

Using $r = \Delta T/t$ the relative change in cooling rate described by $\ln(r_1/r_2)$ can also be expressed as a relative change in time $\ln(t_2/t_1)$:

$$\Delta T = \ln \left[\frac{t_2}{t_1} \right] \cdot \frac{1}{\lambda} \quad (3.20)$$

ΔT is the shift in temperature (T_{iso}) required to produce the same frozen fraction in two isothermal experiments with duration times of t_1 and t_2 , so that $f(T_{\text{iso}}, t_1) = f(T_{\text{iso}} + \Delta T, t_2)$. This temperature change is equivalent to that relating to cooling-rate dependence, and therefore the two variations are referred to as $\beta(r)$ and $\beta(t)$ for cooling-rate dependence and residence-time dependence, respectively.

3.2.3 Reconciling Isothermal Experiments with Cooling Experiments

In the previous chapter a potential relationship for reconciling cooling and isothermal simulations was presented. To examine this further a similar derivation can be performed to analytically determine how the change in cooling rate corresponds to a change in residence time for an isothermal simulation. This can be achieved by equating the fraction frozen in a cooling experiment simulation (denoted as ‘cool’) to that of an isothermal simulation (denoted as ‘iso’), so that $f_{\text{cool}}(T) = f_{\text{iso}}(T)$.

For the cooling experiment the fraction frozen is expressed as previously, so that from Eq. (3.5):

$$f_{\text{cool}}(T) = 1 - \exp \left(- \sum_{k=0}^{n_{\text{cool}}} J_s(T_k) s \delta t_r \right) \quad (3.21)$$

The probability of a freezing event occurring in an isothermal experiment is as described by Eq. (3.21) but here the temperature T_k is constant so that $J_s(T_k) = J_s(T)$:

$$f_{\text{iso}}(T) = 1 - \exp \left(- \sum_{k=0}^{n_{\text{iso}}} J_s(T) s \delta t_{\text{iso}} \right) = \exp(-J_s(T) \cdot s \cdot \delta t_{\text{iso}} \cdot n_{\text{iso}}) \quad (3.22)$$

In the isothermal simulation, the total time for a fraction to be reached is simply a product of the time step and number of steps where $t_{\text{iso}} = n_{\text{iso}} \cdot \delta t_{\text{iso}}$. Incorporating this into Eq. (3.22) gives:

$$f_{\text{iso}}(T) = 1 - \exp(-J_s(T) \cdot s \cdot t_{\text{iso}}). \quad (3.23)$$

For a specific fraction frozen where $f_{\text{cool}}(T) = f_{\text{iso}}(T)$ Eq. (3.23) can be equated to Eq. (3.21). Realising that $J_s(T)$ for the isothermal simulation equals $J_s(T)$ in the cooling experiment after n_{cool} steps gives:

$$1 - \exp\left(-\sum_{k=0}^{n_{\text{cool}}} J_s(T_k) s \delta t_r\right) = 1 - \exp(J_s(T_{n_{\text{cool}}}) \cdot s \cdot t_{\text{iso}}) \quad (3.24)$$

where the left-hand-side represents the cooling experiment simulation and the right-hand-side, the isothermal simulation. Solving for t gives:

$$t_{\text{iso}} = \frac{1}{J_s(T_{n_{\text{cool}}})} \sum_{k=0}^{n_{\text{cool}}} J_s(T_k) \cdot \delta t_{\text{cool}} \quad (3.25)$$

As per Eq. (3.6) the nucleation rate coefficient in the Si-MCS model is represented by $\ln J_s(T_k) = -\lambda(T_k + \varphi)$. Therefore, in a cooling simulation $J_s(T_k) = \exp(-\lambda(T_0 + \varphi)) \cdot [\exp(-\lambda\delta T)]^k$ and in an isothermal simulation $J_s(T_{n_{\text{cool}}}) = \exp(-\lambda(T_0 + \varphi)) \cdot [\exp(-\lambda\delta T)]^{n_{\text{cool}}}$.

Replacing $J_s(T_k)$ and $J_s(T_{n_{\text{cool}}})$ in Eq. (3.25) gives:

$$t_{\text{iso}} = \frac{\delta t_{\text{cool}} \cdot \exp(-\lambda(T_0 + \varphi)) \cdot (\sum_{k=0}^{n_{\text{cool}}} [\exp(-\lambda \cdot \delta T_{\text{cool}})]^k)}{\exp(-\lambda(T_0 + \varphi)) \cdot [\exp(-\lambda \cdot \delta T_{\text{cool}})]^{n_{\text{cool}}}} \quad (3.26)$$

Cancelling out terms gives:

$$t_{\text{iso}} = \delta t_{\text{cool}} \cdot \left(\sum_{k=0}^{n_{\text{cool}}} [\exp(-\lambda \cdot \delta T_{\text{cool}})]^k [\exp(-\lambda \cdot \delta T_{\text{cool}})]^{-n_{\text{cool}}} \right) \quad (3.27)$$

$$t_{\text{iso}} = \delta t_{\text{cool}} \cdot \left(\sum_{k=0}^{n_{\text{cool}}} [\exp(-\lambda \cdot \delta T_{\text{cool}})]^{(k-n_{\text{cool}})} \right) \quad (3.28)$$

The summation term can be removed using a geometric summation of series, for which the sequence must be reversed using

$$\sum_{k=0}^{n_{\text{cool}}} a^{(k-n_{\text{cool}})} \equiv \sum_{k=0}^{n_{\text{cool}}} a^{(-k)},$$

so that:

$$t_{\text{iso}} = \delta t_{\text{cool}} \cdot \left(\sum_{k=0}^{n_{\text{cool}}} [\exp(-\lambda \cdot \delta T_{\text{cool}})]^{-k} \right) \quad (3.29)$$

The summation of series can be performed using:

$$\sum_{k=0}^n ar^k = a \frac{1 - r^{n+1}}{1 - r},$$

which subsequently results in:

$$t_{\text{iso}} = \delta t_{\text{cool}} \cdot \frac{1 - [\exp(\lambda \cdot \delta T_{\text{cool}})]^{n_{\text{cool}}+1}}{1 - \exp(\lambda \cdot \delta T_{\text{cool}})} \quad (3.30)$$

Substituting a variable x for $(\lambda \cdot \delta T_{\text{cool}} \cdot (n_{\text{cool}} + 1))$ it can be seen that where $x \gg 1$, $[\exp(\lambda \cdot \delta T_{\text{cool}})]^{n_{\text{cool}}+1} \rightarrow 0$. Rearranging so that $x = \frac{\delta T_{\text{cool}} n_{\text{cool}} + \delta T_{\text{cool}}}{-\lambda^{-1}} = \frac{T_{\text{iso}} + \delta T_{\text{cool}}}{-\lambda^{-1}}$, it can be seen that this limit is reached for all cases except when, simultaneously, T_{iso} is very high (> -5 °C) and λ is very small ($\lambda < 1$). Therefore, providing the isothermal simulation is below this temperature:

$$t_{\text{iso}} = \frac{\delta t_{\text{cool}}}{1 - \exp(\lambda \cdot \delta T_{\text{cool}})} \quad (3.31)$$

A Taylor expansion of $\exp(\lambda \cdot \delta T_{\text{cool}})$ results in $\left[1 + \lambda \delta T_{\text{cool}} - \frac{(\lambda \delta T_{\text{cool}})^2}{2!} + \frac{(\lambda \delta T_{\text{cool}})^3}{3!} \dots \right]$.

When $\lambda \delta T_{\text{cool}} \gg \frac{1}{2} (\lambda \delta T_{\text{cool}})^2$, $\exp(\lambda \delta T_{\text{cool}}) \cong 1 + \lambda \delta T_{\text{cool}}$ (satisfied when the simulation temperature step $\delta T_{\text{cool}} \ll 1$), therefore Eq. (3.31) can be simplified to

$$t_{\text{iso}} = \frac{\delta t_{\text{cool}}}{\lambda \cdot \delta T_{\text{cool}}} \quad (3.32)$$

Substituting $r_{\text{cool}} = -\frac{\delta T_{\text{cool}}}{\delta t_{\text{cool}}}$, where $r_{\text{cool}} > 0$

$$t_{\text{iso}} = \frac{\delta t_{\text{cool}}}{\lambda \cdot r_{\text{cool}} \cdot \delta t_{\text{cool}}} = \frac{1}{\lambda \cdot r_{\text{cool}}} \quad (3.33)$$

This formula describes the time required for an isothermal simulation at a temperature T_{iso} , to attain the same $f(T)$ as a cooling simulation cooled from 0 °C to T_{iso} at a rate r_{cool} ; this confirms the results found in Chapter 2.

3.2.4 The FROST Framework

The previous sections show that the time-dependent behaviour of immersion mode freezing in cooling and isothermal simulations are dependent on λ , and that the two can be reconciled. As shown in Chapter 2 the third manifestation of time-dependence, observed in freeze-thaw experiments, is also dependent on λ , and additionally is independent of the mean nucleating efficiency and diversity of the INP species.

Assuming that an INP species behaves as per the assumptions in the Si-MCS model (i.e., a linear relationship between $\ln(J_s)$ and T) then these relationships and equations can be combined into a single consistent framework that can be applied to experimental data in order to normalise variable temporal conditions. This includes different residence-times, cooling-rates, instruments, and experimental method.

As previously stated the variability in T_{freeze} from freeze-thaw experiments is only dependent on λ , and therefore does not require reconciliation. The standard deviation of freezing temperatures can therefore be determined using the empirical relationship presented in Chapter 2:

$$\sigma_{T,\text{freeze}} = \frac{1.2691}{\lambda} \quad (3.34)$$

The cooling and isothermal experiments can be reconciled by applying a standard reference cooling rate r_{standard} , for which 1 °C min⁻¹ was chosen. For cooling rate experiments,

replacing r_1 in Eq. (3.19) with r_{standard} and r_2 with the cooling rate r , in $^{\circ}\text{C min}^{-1}$, gives the shift in temperature (β) as a function of cooling rate:

$$\beta(r) = \Delta T = \frac{1}{\lambda} \ln\left(\frac{1}{|r|}\right) \quad (3.35)$$

For isothermal simulations, replacing r_{cool} with r_{standard} in Eq. (3.33) gives the time required for an isothermal simulation to be comparable to a normalised cooling simulation. Substituting t_1 in Eq. (3.20) with t_{total} in Eq. (3.33), and t_2 with the residence time t , in seconds, gives β as a function of residence time:

$$\beta(t) = \Delta T = \frac{1}{\lambda} \ln\left(\frac{\lambda \cdot t}{60}\right) \quad (3.36)$$

where λ describes the temperature dependence of J_s , $-\text{dln}(J_s)/\text{dT}$.

Equations (3.35) and (3.36) can be used with λ to normalise data to a $1^{\circ}\text{C min}^{-1}$ cooling rate using $T' = T_{\text{experiment}} - \beta$ where T' is the normalised temperature, and $T_{\text{experiment}}$ the temperature of the experiment data point. These equations form the basis of a new framework called the Framework for Reconciling Observable Stochastic Time-dependence (FROST).

3.3 Incorporating the FROST Framework into a Singular Model

The FROST framework provides a means for normalising experimental data, regardless of temporal conditions. It can be seen that the framework is essentially predicting the time-dependent behaviour of a species, in order to normalise it. Therefore the framework can also be used to prognostically determine the time-dependent freezing behaviour where $T_{\text{simulation}} = T' + \beta$. Here T' represents the normalised temperature and $T_{\text{simulation}}$ the temperature adjusted for time-dependent effects.

For predicting $f(T)$ in cooling or isothermal simulations this requires the addition of a function that can describe the temperature-dependent freezing behaviour of a species, of which the singular freezing model is well suited.

The singular freezing model is able to describe the inter-particle variability of ice nucleating ability, but not time-dependence. Vali (1994) presented a modification of this (referred to as the modified singular model) which included a cooling-rate dependent temperature offset that introduced an element of time-dependence; however, this was an empirically determined relationship with little theoretical justification.

The fundamental assumption of the singular freezing model is that the probability of a droplet freezing is dependent on the distribution of sites on the immersed INP's surface. Each site has a characteristic freezing temperature, T_c , and therefore the freezing probability at a temperature T is proportional to the cumulative number of sites where the condition $T_c > T$ applies. This distribution of sites is commonly referred to as the active site density (DeMott, 1995), $n_s(T)$ (also called the ice active surface site density (Connolly et al., 2009; Murray et al., 2012; Hoose and Möhler, 2012)).

Using the singular freezing model the fraction of droplets that will freeze at a temperature T is described by

$$f(T) = 1 - \exp(-n_s(T) \cdot s) \quad (3.37)$$

By rearranging Eq. (3.37) it can be seen that $n_s(T)$ (in units cm^{-2}) is directly related to the cumulative fraction frozen:

$$n_s(T) = -\frac{\ln(1 - f(T))}{s} \quad (3.38)$$

It is therefore apparent that a systematic shift in $f(T)$, caused by a change in the cooling rate or residence time, results in a systematic shift in $n_s(T)$ so that, upon incorporating Eq. (3.35) into Eq. (3.38) it can be seen that for a specific cooling rate r (where $r > 0$):

$$f(T, r) = 1 - \exp\left(-n_s \left(T - \frac{\ln(r)}{-\lambda}\right) \cdot s\right) \quad (3.39)$$

The differentiation of n_s with respect to T results in the function $k(T)$ that can be used to determine the change in the fraction frozen occurring upon a decrease in T :

$$\Delta f(T, r) = 1 - \exp\left(-k \left(T - \frac{\ln(r)}{-\lambda}\right) \cdot s \cdot \Delta T\right) \quad (3.40)$$

where $k(T)$ is in units $\text{cm}^{-2} \text{ } ^\circ\text{C}^{-1}$. As mentioned previously equations (3.39) and (3.40) are consistent with the empirical modified singular freezing model outlined by Vali (1994), however here the time-dependent behaviour is directly related to the temperature dependence of the nucleation rate coefficient, λ .

Similar equations can also be defined for isothermal experiments by incorporating Eq. (3.36) into Eq. (3.37) so that at a specific temperature, T_{iso} and residence time in seconds, t :

$$f(T, t) = 1 - \exp\left(-n_s \left(T - \frac{1}{\lambda} \ln\left(\frac{\lambda \cdot t}{60}\right)\right) \cdot s\right). \quad (3.41)$$

Again, upon differentiation an equation is obtained for the change in fraction frozen upon a change in residence time from t to $t + \Delta t$:

$$\Delta f(T, t) = 1 - \exp\left(-k \left(T - \frac{1}{\lambda} \ln\left(\frac{\lambda \cdot t}{60}\right)\right) \cdot s \cdot \frac{1}{-\lambda \cdot t} \Delta t\right), \quad (3.42)$$

where $\Delta t/(-\lambda \cdot t)$ has replaced ΔT through the incorporation of Eq. (3.33) into $\Delta T = -r/60 \cdot \Delta t$; r is in $^\circ\text{C min}^{-1}$ and Δt in seconds.

These equations, as part of the FROST framework, can be used to predict and reproduce the freezing behaviour of droplets containing immersed INPs for use in both experimental related practice, and more importantly, for accurately representing the variability in nucleating efficiency and time-dependence in cloud modelling studies.

3.4 Conclusions

In this chapter the derivation and development of a new framework, named the Framework for Reconciling Observable Stochastic Time-dependence (FROST) was presented. FROST provides, for the first time, a means for determining and reconciling the time-dependent behaviour of immersion mode freezing in cooling, isothermal, and freeze-thaw experiments. The development of FROST highlights the primary role that the temperature dependence of the nucleation rate coefficient, λ , plays in the manifestation of time-dependence.

The framework was incorporated into a deterministic model to produce a simple parameterisation that is able to uniquely represent the variability in both nucleating efficiency and time-dependence that has been observed in experiments. This provides an accurate yet computationally efficient parameterisation for use in cloud modelling studies.

Chapter 4: Reconciling Time-Dependencies in Experimental Data using FROST

4.1 Introduction

The FROST framework can be used to identify the value λ which characterises the time-dependencies in immersion mode freezing experiments, as well as to normalise experimental data obtained over differing temporal conditions. In this chapter the application of the FROST framework will be demonstrated using a combination of original and existing experimental droplet freezing data for atmospherically relevant INPs obtained via a range of methods and instruments.

The application of the FROST model to experimental data was published in Atmospheric Chemistry Physics Discussions (Herbert, R. J., Murray, B. J., Whale, T. F., Dobbie, S. J., and Atkinson, J. D.(2014), Representing time-dependent freezing behaviour in immersion mode ice nucleation, Atmos. Chem. Phys. Discuss., 14, 1399-1442, doi:10.5194/acpd-14-1399-2014). The experimental data on K-feldspar and the kaolinite MICROLITRE dataset were obtained by T. Whale; the experiment was designed jointly by R. Herbert and T. Whale.

4.2 Immersion Mode Terminology

The terminology used in the following chapter will be outlined briefly. The basis of this follows discussions with Gabor Vali, Thomas Whale, and Ben Murray, as well as members of the CNAAC committee including Barbara Hale, Paul DeMott, and Ottmar Möhler.

The foundation of the terminology is based on quantitative measurements that can be directly determined from experimental data. The freezing rate $R(T) = d\ln(1-f)/dt$ describes

the rate at which a population of droplets are observed to freeze per unit time at a temperature T (with units s^{-1}). The similar value $R^*(T) = d\ln(1-f)/dT$ described the rate of freezing per unit change in temperature ($^{\circ}C^{-1}$). These two rates can be seen as physical properties of the experimental dataset, however, they may not offer any physical insight into the nucleating characteristics of the INP species as they only refer to the droplet freezing rate.

By normalising to INP properties, such as surface area s , number of nucleation sites n_{sites} , mass of INP m , or even droplet volume V , the resulting rates can be used to infer the key dependencies of the freezing rate. For example, if, upon normalising $R(T)$ to surface area, a series of experiments performed at varying INP concentrations fall onto a single line, or curve, then this would indicate that the freezing rate is dependent on the surface area of INP per droplet. These normalised rates will hereafter be referred to by including a subscript that corresponds to the INP property being normalised to: $R_s(T)$ and $R_s^*(T)$ are the surface area normalised freezing rates (in units $cm^{-2} s^{-1}$ and $cm^{-2} ^{\circ}C^{-1}$, respectively) and $R_v(T)$ and $R_v^*(T)$ are the volume normalised freezing rates (in units $cm^{-3} s^{-1}$ and $cm^{-3} ^{\circ}C^{-1}$, respectively). The gradient of the freezing rates and normalised freezing rates (assuming droplets with homogeneous properties) is referred to as ω , where $\omega = -d\ln R/dT$.

Following this terminology it can be seen that for an INP species that exhibits a uniform nucleating efficiency per droplet (i.e., all droplets are characterised by the same ϕ) $R_s(T) = J_s(T)$ and therefore $\omega = \lambda$. This type of INP will be referred to as single-component, in that it only requires a single nucleation rate to describe its freezing behaviour. Conversely, for INP species that exhibit a diversity in nucleating efficiency per droplet (i.e., where ϕ is different for each droplet) $R_s(T) \neq J_s(T)$ and therefore $\omega < \lambda$. This INP species will be referred to as multiple-component, in that it requires multiple nucleation rates to describe its freezing behaviour. This is an important distinction as R_s is often reported as J_s , whereas in this chapter it will be shown that this is not always the case and that many materials are not single-component. As a notable point, it is also apparent that $R_s^*(T)$ is analogous to $n_s(T)$ for both single and multiple-component species, and therefore $-d\ln(n_s)/dT = \omega$.

4.3 Application of the FROST Framework with Experimental Data

In this section the FROST framework will be tested using a combination of new experimental droplet freezing data and literature data for atmospherically relevant INPs obtained via a range of methods and instruments.

4.3.1 Kaolinite Data (KGa-1b) from Two Cold-Stage Instruments

In this example data from droplet freezing experiments from two cold stage instruments, including a range of cooling rates, are combined to test the capability of the FROST framework.

The first dataset, referred to as PICOLITRE, is taken from Murray et al. (2011). In their experiments micron sized droplets containing known amounts of kaolinite (KGa-1b, Clay Mineral Society) mineral dust were cooled at constant rates on a cold stage instrument coupled with an optical microscope. Each experiment was characterised by a specific cooling rate and weight percent (wt%) of mineral per droplet. For this study four datasets are used (experiments *vii*, *viii*, *ix* and *xi* in Murray et al. (2011)) corresponding to cooling rates (wt%) of 5.4 (0.34), 9.6 (1.0), 0.8 (1.0) and 5.1 (1.0) °C min⁻¹, respectively.

The second experimental dataset, referred to as MICROLITRE, was obtained on the cold stage instrument previously described in Chapter 2. In this experiment ~40 droplets of 1 µl volume containing known amounts of the same kaolinite sample as Murray et al. (2011) (KGa-1b) were cooled at constant rates of 0.1, 0.2, 0.5, and 1.0 °C min⁻¹. All experiments were performed with a wt% of 1.0, which corresponds to a surface area, s , of $1.178 \pm 0.3 \text{ cm}^2$ per droplet calculated using a specific surface area of $11.8 \pm 0.8 \text{ m}^2 \text{ g}^{-1}$ Murray et al. (2011). The temperature uncertainty, arising from the temperature probe and observed range in melting temperatures, has been estimated by Whale et al. (2014) as $\pm 0.4 \text{ °C}$. Freezing data is limited to $T > -20.5 \text{ °C}$ below which the substrate was observed to influence freezing behaviour.

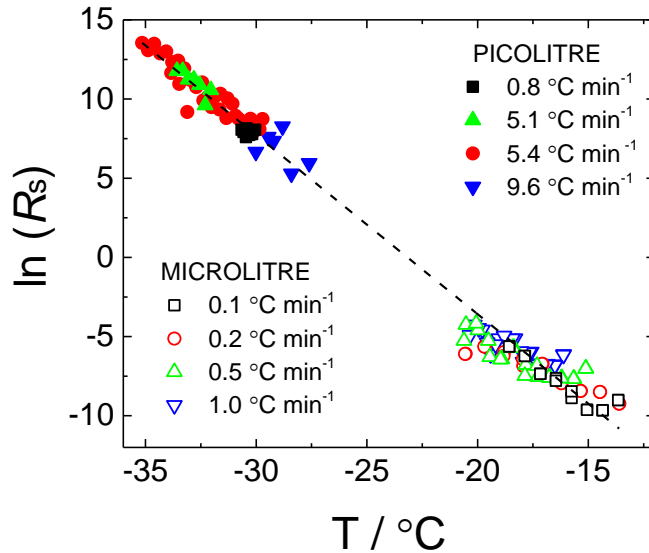


Figure 4.1. Normalised freezing rates $R_s(T)$ values determined from cooling experiments with a range of cooling rates. Open symbols represent experimental data from Murray et al. (2011) and closed symbols represent original data. The black dashed line shows a linear fit to all data ($\ln(R_s) = -1.12(T + 23.1)$). Temperature uncertainty for the MICROLITRE data (not shown) is estimated at ± 0.4 °C, and uncertainty in R_s (not shown) is estimated at -17 % and +25 %.

In a single-component system the gradient $-\ln(R_s)/dT$, named ω , is equal to λ . If the system were multiple component then the slope ω will be smaller than λ because an inappropriate model was used (i.e. ω is a lower limit to λ). For a set of data obtained at a single cooling rate it is not possible to say if the sample is a single or multiple-component species, further tests are required. Murray et al. (2011) did this by performing isothermal experiments in addition to experiments at various cooling rates and found that the values of R_s (presented as J_s values in their study) derived from both styles of experiment were consistent. They concluded that nucleation by kaolinite KGa-1b was consistent with a single-component system between $-37.15 \leq T \leq -27.65$ and therefore $R_s = J_s$. Surface area normalised freezing rates (R_s) for the PICOLITRE and MICROLITRE experiments are shown in Figure 4.1. The larger droplets in the MICROLITRE experiment contain significantly greater s per droplet than the PICOLITRE experiment, which increases the probability of freezing, resulting in higher freezing temperatures. The R_s values determined from a range of cooling rates fall onto a single line, as expected for a single-component.

These conclusions were tested further by comparing the expected freezing behaviour of the kaolinite sample with an isothermal experiment. An isothermal experiment with droplets

containing a single-component species will exponentially decrease with respect to time, this behaviour can be reproduced with a knowledge of λ . A fit to the combined PICOLITRE and MICROLITRE R_s data in Figure 4.1 provides the slope ω , which assuming a single-component species is equal to λ . The fit is described by $\ln(R_s) = -1.12(T + 23.1)$ and thus $\omega = \lambda = 1.12$. The isothermal experiment, shown in Figure 4.2, was performed at $-18\text{ }^\circ\text{C}$ with droplets containing 1.0 wt% of KGa-1b particles. The expected decay was simulated using the value of J_s determined from the fit to $\ln(R_s)$ in Figure 4.1 at $-18\text{ }^\circ\text{C}$ and $\lambda = 1.12$. The expected exponential decay matches the measured decay; this is consistent with a single-component system and additionally demonstrates that the observed time-dependence in the cooling experiments is consistent with the observed time-dependent in the isothermal experiment.

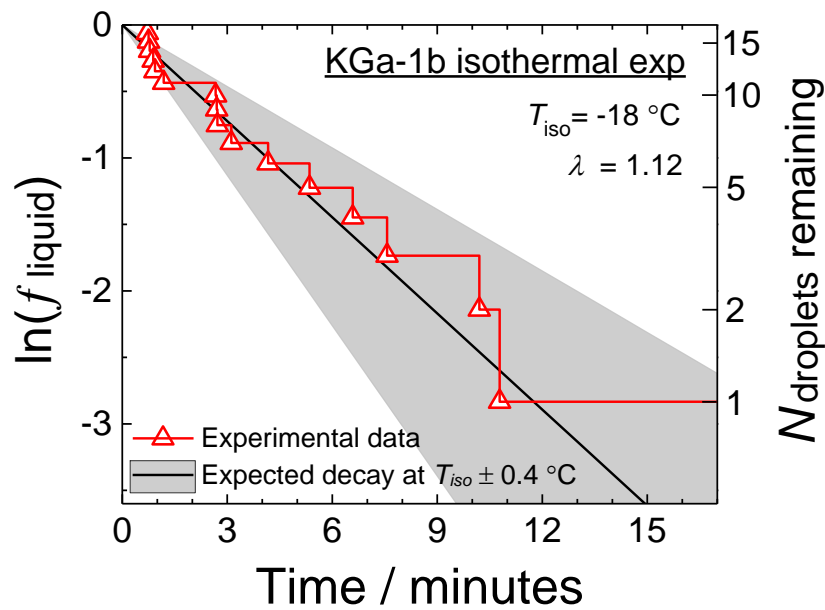


Figure 4.2. The exponential decay of liquid droplets during an isothermal experiment at $-18\text{ }^\circ\text{C}$ together with an isothermal simulation at the same temperature using the linear fit to all data in Figure 4.1. The grey area follows the experimental uncertainty in T around the modelled isothermal. The experiment duration was 17 minutes, at which point one droplet remained unfrozen.

In Figure 4.3 the MICROLITRE dataset is placed in the context of the FROST framework. If the INP species can be characterised with a single λ then the application of Eq. (3.35) will modify each data point by $T' = T_{\text{experiment}} - \beta$. With the correct value of λ in the FROST framework, the data will converge onto the curve of a $1\text{ }^\circ\text{C min}^{-1}$ cooling experiment for the

species tested. Figures 4.2a, b, and c show the cumulative fraction frozen $f(T)$, $n_s(T)$ values, and $R_s(T)$ values from Figure 4.1, respectively. On applying FROST with $\lambda = 1.12$ both the modified $f(T')$ and $n_s(T')$ data converge (Figure 4.3d and e, respectively). This additionally supports the conclusion that kaolinite KGa-1b is well represented by a single-component system.

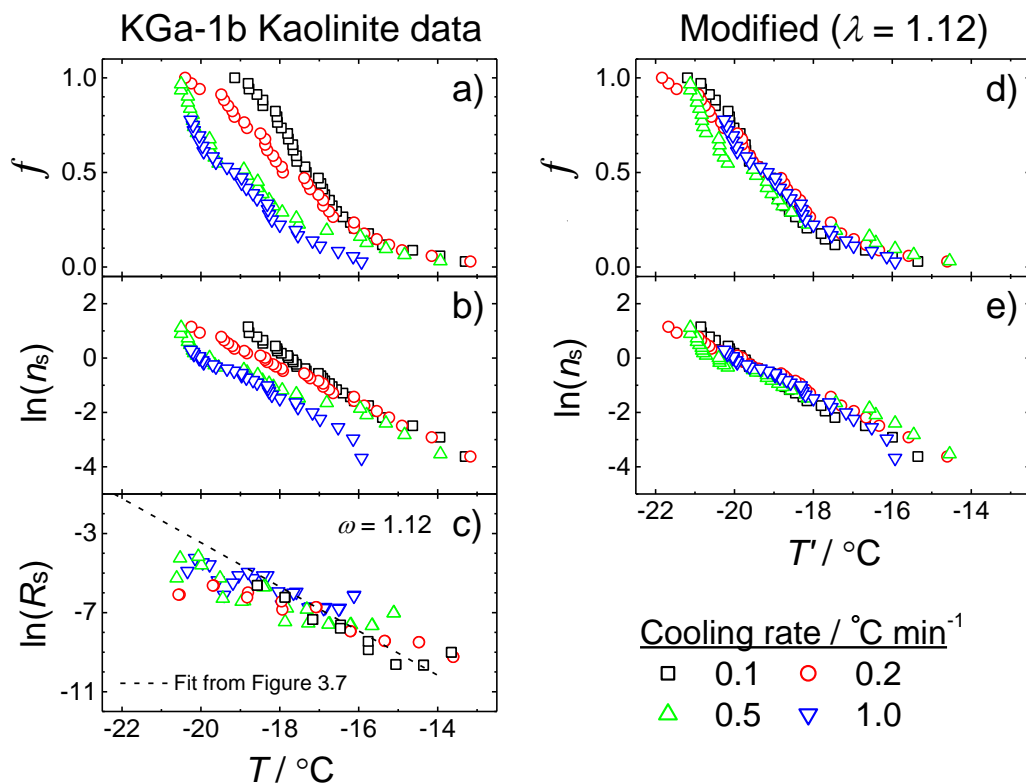


Figure 4.3. Raw $f(T)$ data and derived $R_s(T)$ and $n_s(T)$ values from kaolinite (KGa-1b) MICROLITRE cooling experiments ((a), (b), and (c) respectively), and the corresponding normalised data, $f(T')$ and $n_s(T')$, ((d) and (e), respectively) using the value of λ determined directly from the linear fit to $\ln(R_s)$ against T in Figure 4.1 and reproduced in (c). Temperature and R_s uncertainty is as in Figure 4.1. Uncertainty in n_s (not shown) is estimated as $\pm 20\%$.

The results from Figure 4.1 show that kaolinite exhibits a linear relationship between $\ln(R_s)$ and T over $20\text{ }^\circ\text{C}$ which is at odds with CNT. This might suggest that there is a flaw in CNT theory, or alternatively it may be the case that there are multiple INP populations which happen to give the appearance of a single-component system. To test this further a series of simulations were performed using CNT-based models, including the SCS and MCS models. The CNT-based nucleation rate coefficients were determined as in Chapter 2, and $f(T)$ simulated assuming a $1\text{ }^\circ\text{C min}^{-1}$ cooling rate. The $f(T)$ data was then used to determine the overall $R_s(T)$ function in order to make a comparison to the experimental data. The results

are shown in Figure 4.4. The PICOLITRE and MICROLITRE data is shown along with the linear fit to the data reproduced from Figure 4.1, which has been extrapolated to make clear comparisons. The assumption of a single-component species was simulated using the SCS model with $\theta = 78.5^\circ$ and clearly shows that this assumption can not concurrently reproduce both datasets. The CNT-based MCS model was able to reproduce the data but required the presence of two distinct distributions of contact angles consisting of a uniform contact-angle distribution at low temperatures and a log-normal contact-angle distribution at higher temperatures. In CNT the time-dependent behaviour is related to temperature, therefore it would be expected that the high-temperature experimental dataset would behave with considerably weaker time-dependence than the lower temperature dataset. However, the evidence presented here suggests that KGa-1b behaves with consistent time-dependent behaviour at high and low temperatures, and thus CNT cannot describe the linear nature of $\ln(R_s)$ for this species.

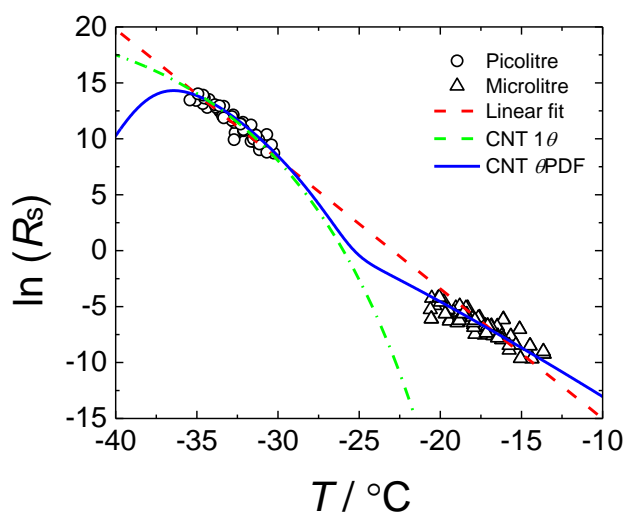


Figure 4.4. Fitting CNT to PICOLITRE and MICROLITRE experimental data from Figure 4.1 assuming either a single contact angle (1θ) or a distribution of contact angles (θ PDF). For the θ PDF simulation a log-normal bimodal distribution of θ was used. For comparison the extrapolated linear fit from Figure 4.1 has been included.

4.3.2 K-feldspar Data from a Cold-Stage Instrument

In this example the cooling-rate dependence of K-feldspar is determined using the microlitre droplet cold stage instrument as in the previous example. In these experiments ~ 40 droplets of $1 \mu\text{L}$ volume were cooled at constant rates of 0.2, 0.4, 1.0 and $2.0 \text{ }^\circ\text{C min}^{-1}$

on a hydrophobic surface. Each droplet contained 0.1 wt% of K-feldspar, corresponding to a surface area of $1.85 \times 10^{-2} \pm 0.004 \text{ cm}^2$ calculated using a specific surface area of $1.86 \text{ m}^2 \text{ g}^{-1}$ (Whale et al., 2014).

Figure 4.5a, b, and c show the experimental $f(T)$ data, and derived $n_s(T)$ and $R_s(T)$ values, respectively. For the 0.2, 0.4 and $2.0 \text{ }^\circ\text{C min}^{-1}$ curves two separate experiments were performed and for the $1.0 \text{ }^\circ\text{C min}^{-1}$ curve five experiments were performed. A systematic shift in $f(T)$ outside of instrumental error ($\pm 0.4 \text{ }^\circ\text{C}$) can be seen for the experiments at 0.2 and $2 \text{ }^\circ\text{C min}^{-1}$, which indicates that there is a cooling-rate dependence for nucleation by K-feldspar.

The data now needs to be tested to establish whether it is a single or multiple-component system. The normalised freezing rates, R_s , for the 0.2 and $2.0 \text{ }^\circ\text{C min}^{-1}$ runs are shown in Figure 4.5c. If K-feldspar behaved as a single-component then the two datasets would fall onto the same line, as they do for kaolinite in Figure 4.1a. However, they do not fall on the same line; the R_s values are significantly different between the two cooling rates, hence this suggests that K-feldspar is multiple-component. In this case derived values of R_s are not equal to the nucleation rate coefficient J_s .

With the correct value of λ in the FROST framework, the modified data will converge onto a single curve. Therefore, in order to determine the value of λ , a procedure was followed where λ was iteratively varied until $n_s(T)$ converged onto a single curve. The best fit was determined by the minimisation of the RMSE between the data and a linear fit to $\ln(n_s)$ for data where $T_{\text{experiment}} \leq -10.5 \text{ }^\circ\text{C}$. This temperature was chosen to limit effects from sporadic events at high temperatures from minor constituents in the K-feldspar sample which include quartz and Na/Ca-feldspar (4 and 15 %, respectively, as reported by Atkinson et al. (2013)). This fitting procedure, with a RMSE value of 0.009, resulted in $\lambda = 3.4$ and is shown in Figure 4.5e. This value is substantially steeper than the gradients ω in panel c (0.85 and 0.9). Recall that for kaolinite, the gradient ω was used to normalise the n_s values in Figure 4.3e which provided additional evidence that that kaolinite is single-component. In K-feldspar the fact that $\omega \neq \lambda$ shows that K-feldspar is multiple-component.

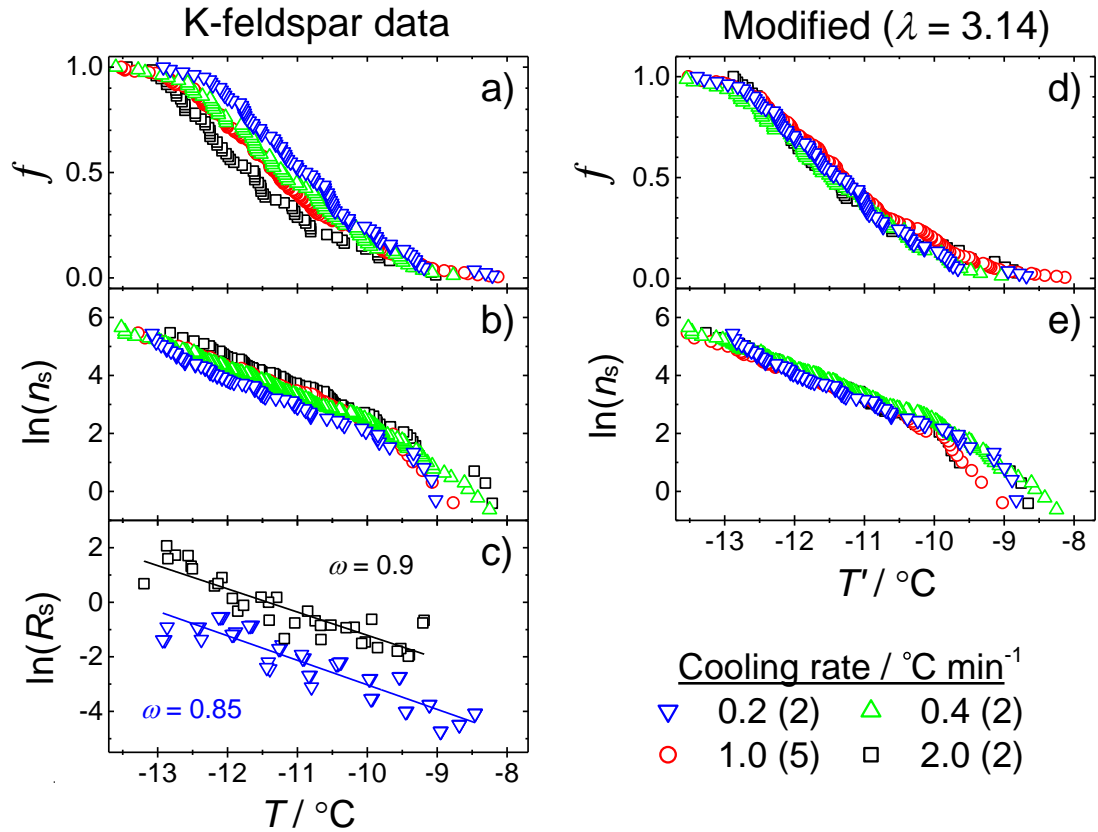


Figure 4.5. Layout as in Figure 4.3 but for the species K-feldspar at cooling rates of 0.2, 0.4, 1.0 and 2.0 °C min⁻¹. Brackets beside the cooling rates indicate the number of experiments performed. Linear fits to derived $\ln(R_s)$ values for runs at 0.2 and 2.0 °C min⁻¹ are shown as solid lines in (c) resulting in $\omega = 0.85$ and 0.9, respectively. Modified $n_s(T')$ data was minimised and resulted in $\lambda = 3.4$. In this example $\omega \neq \lambda$ suggesting that K-feldspar is a multiple-component species.

To identify whether this behaviour is consistent, similar to the kaolinite sample, an isothermal experiment was also performed at $T_{\text{iso}} = -11$ °C with 20 droplets (28 froze during cooling to T_{iso}) containing 0.1 wt% of K-feldspar. The data is shown in Figure 4.6. For a single-component species the decay of liquid droplets over time will be exponential (as was the case for kaolinite KGa-1b), whereas as seen in Chapter 2 a multiple-component species will result in a non-exponential decay. The results from Figure 4.5 suggest that the latter behaviour is to be expected. On inspection of the isothermal data, shown in Figure 4.6, it is clear that the decay of liquid droplets was not exponential, again consistent with K-feldspar being multiple-component. To highlight this, the decay expected from a single-component system was plotted assuming $R_s = J_s$. The two limiting values of R_s from Figure 4.5c at -11 °C were used. The simulated decays clearly over-predict the rate of decay. To simulate the expected decay assuming a multiple-component system, the Si-MCS model

was initially used as a fitting tool to obtain a φ PDF distribution that best reproduced the entire normalised $f(T)$ dataset in Figure 4.5d, using the minimised value $\lambda = 3.4$. This distribution ($\mu = 11.2, \sigma = 1.11$) was then used to simulate an isothermal experiment which included the initial cooling period require to reach T_{iso} . This is required as the more efficient droplets may freeze upon cooling and therefore decrease the number of droplets available for the isothermal experiment, as well as the φ PDF.

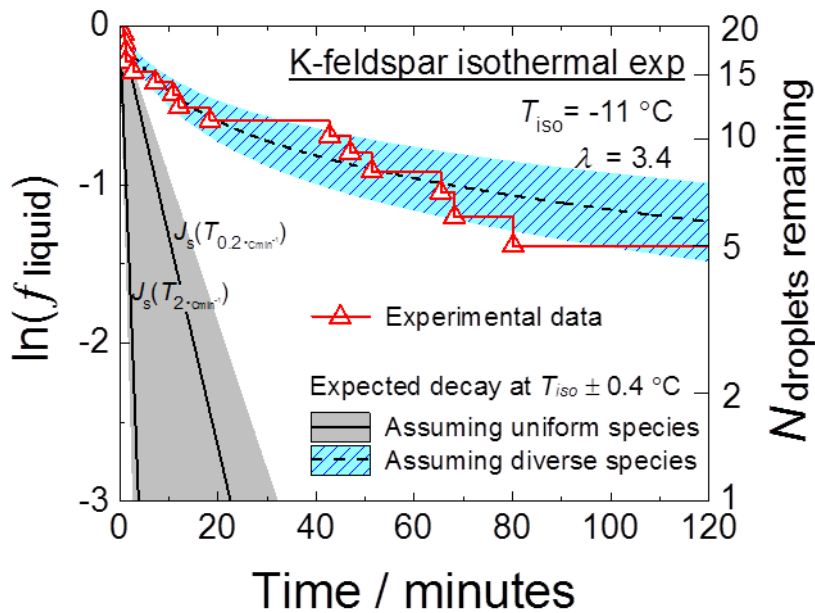


Figure 4.6. Decay of liquid droplets in an isothermal experiment at $T_{iso} = -11$ °C using K-feldspar, and simulated experiments assuming a single and multiple-component species. The shaded regions follow the instrument-based error of ± 0.4 °C around T_{iso} . The triangular symbols indicate when a freezing event occurred, throughout the 120 minute duration of the experiment.

The expected decay, shown in Figure 4.6 as a black dashed line, shows a clear consistency between the multiple-component simulation and the experimental data. This again shows strong evidence that the K-feldspar sample exhibits a range of φ and would require a multiple-component system to describe its freezing behaviour.

This example is important as it illustrates that for a multiple-component species the observed gradient ω of the derived $R_s(T)$ values from a single experiment does not characterise its stochastic behaviour. For these species a series of experiments at different

cooling rates or residence times must be performed in order to determine the value of λ that can be used to characterise its stochastic behaviour.

4.3.3 Mineral Dust Freezing Experiments using the ZINC CFDC Instrument

Welti et al. (2012) (hereafter WELTI) studied the dependence of freezing probability on residence time for droplets containing particles of mineral dust using the ZINC CFDC instrument. The mineral dust used by WELTI was supplied by the chemical company Fluka as kaolinite, but contained a range of minerals including feldspar and it has been suggested that it is this feldspar content which controls its ice nucleating ability (Atkinson et al., 2013). In their experiment, WELTI size-selected single particles, immersed them in supercooled droplets and passed the droplets into ZINC. Within the instrument the droplets experienced isothermal conditions and the frozen fraction was determined using a depolarization detector. Variable flow rates and a series of detection points provide a range of residence times, and by performing experiments at several temperature WELTI built up $f(T)$ curves for a range of residence times. For this example only the data for 400 nm particles is used.

The data is shown in Figure 4.7a along with derived $n_s(T)$ and $R_s(T)$ values in b and c, respectively. Similar to the K-feldspar data the $R_s(T)$ values for the mineral dust do not fall onto a single line and show a separation between residence times consistent with a multiple-component system. Therefore, in order to determine the value of λ that describes the residence-time dependence, the same procedure was followed as in the previous example with K-feldspar. Each data point represents a single isothermal experiment with a single residence time, t . Hence, Eq. (3.36) can be used to modify each data point with $T' = T_{\text{experiment}} - \beta(t)$, assuming that the species can be characterised by a single value for λ . Using derived $n_s(T)$ values, with INP surface area per droplet calculated assuming a spherical particle 400nm in diameter as per the experiment, λ was systematically varied until the $n_s(T')$ values converged onto a single line, again described by an exponential fit to $\ln(n_s)$. This resulted in $\lambda = 2.19$ with a $\ln(n_s)$ RMSE of 0.047, and is shown in Figure 4.7e. For comparison, an exponential fit describing the raw $n_s(T)$ data resulted in a RMSE of 0.076. The two exponential fits were used to reproduce the expected fraction frozen data for

a $1\text{ }^{\circ}\text{C min}^{-1}$ cooling experiment, and are plotted along with the observed and normalised fraction frozen dataset in Figures 4.7a and 4.7d, respectively. The range of ω determined from the $\ln(R_s)$ fits in Figure 4.7c was estimated as 1.2 at $-33\text{ }^{\circ}\text{C}$ and 0.2 at $-36\text{ }^{\circ}\text{C}$. These values are lower than the minimised value of λ (2.19) suggesting that the mineral dust sample used in the WELTI study is multiple-component, which agrees with the conclusions of WELTI.

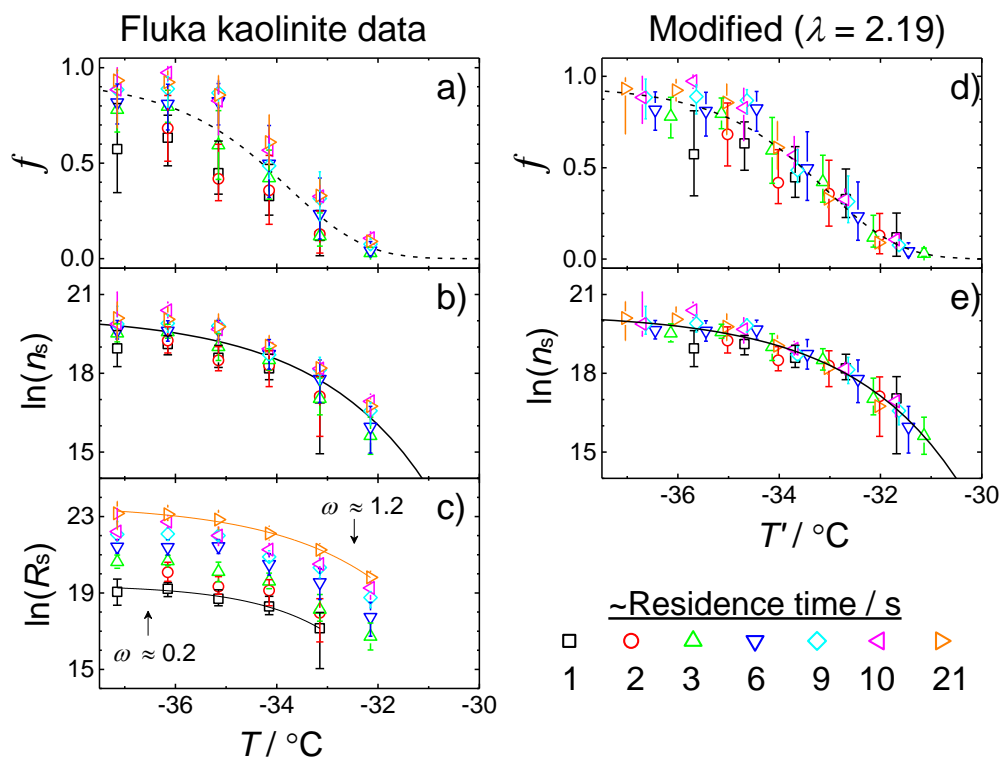


Figure 4.7. Layout as in Figure 4.3 but for 400 nm kaolinite (Fluka) isothermal experiments from Welti et al. (2012) at residence times ranging from 1.11 to 21.4 s and temperatures from -32.15 to $-37.15\text{ }^{\circ}\text{C}$. $R_s(T)$ values, shown in (c), do not fall onto a single line and exhibit a consistent separation with increasing residence time. Modified $n_s(T)$ data resulted in $\lambda = 2.19$. The fits shown in (d) and (e) were used to reproduce a $1\text{ }^{\circ}\text{C min}^{-1}$ cooling experiment and are shown as dashed lines in (a) and (d). Error bars are reproduced from Welti et al. (2012).

Similar to the kaolinite and K-feldspar examples the determined value of λ was used to reproduce the expected decay of liquid droplets over time. With CFDC instruments the cooling from ambient temperature to the experimental temperature is very rapid and therefore the distribution of INP efficiency per droplet in the isothermal experiment can be assumed to be represented by the function of $n_s(T')$ determined in Figure 4.7e. Recall that in the cold stage isothermal previously, a period of cooling was required to reach T_{iso} and therefore the Si-MCS model had to be used in order to keep track of each sub-population. At this point the function $n_s(T)$ could have been determined for the remaining droplets and

used as in the following example. To calculate the expected decay of liquid droplets with time Eq. (3.41) was used with the value of λ (2.19) determined previously. The experimental data, along with the expected decay, is shown in Figure 4.8. It can be seen that at high temperatures (-34.15 to -32.15 °C) the FROST framework is able to reproduce the experimental decay very well. However, at lower temperatures (-35.15 to -37.15 °C) there are large differences. The reported errors bars are large for the lowest temperature data and suggest an increasing uncertainty with decreasing temperature. Also the fraction of droplets frozen is not expected to increase with decreasing temperature as stated by WELTI. This suggests a potential experimental issue, which would explain the discrepancies.

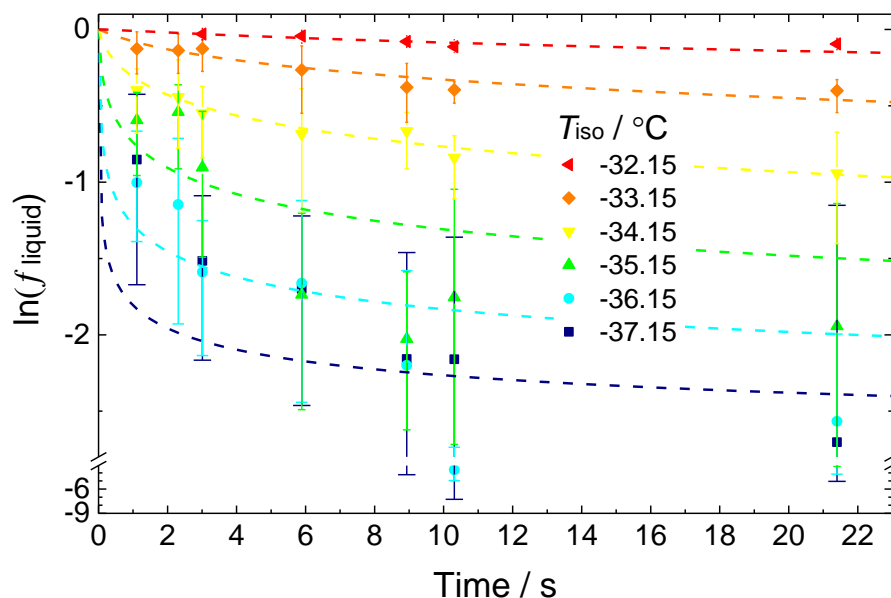


Figure 4.8. Experimental data (symbols) from Figure 4.7a plotted as the decay in liquid droplets over time for each temperature, along with the expected decay determined using Eq. (3.41) with the function of $n_s(T)$ in Figure 4.7e and $\lambda = 2.19$. The expected decay at each temperature is shown as a dashed line.

The implication of not taking into account time-dependence when analysing experimental data is demonstrated in Figure 4.9. The first example, shown as the magenta line, is the resulting $n_s(T)$ function determined directly from the raw experimental data; a change in cooling rate has no affect. The black lines in the figure show the resulting $n_s(T)$ functions determined on application of the FROST framework; using this method a change in cooling rate has a corresponding affect on the n_s function. This may have important consequences in the atmosphere and will be examined further in Chapter 5.

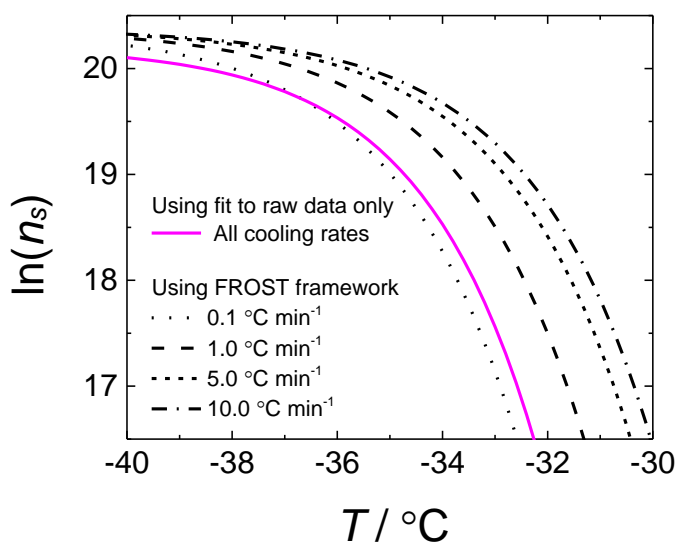


Figure 4.9. The resulting equivalent function of $n_s(T)$ for different cooling rates using the FROST framework (black lines) and directly fitting to the experimental data (magenta line).

Here the FROST framework has been used to both normalise isothermal experiments performed over a range of residence times, and determine a value of λ that can be used to potentially describe the cooling-rate and time-dependent behaviour of this mineral dust in simulations. This example additionally highlights the necessity to use relatively pure samples in order to limit uncertainties due to multiple INP species.

4.3.4 Volcanic Ash from ZINC and AIDA

In this final example the framework is used to normalise droplet freezing data from two fundamentally different experimental methods. Following the eruption of Eyjafjallajökull in Iceland during April 2010, a single sample of volcanic ash was collected and analysed to investigate its freezing characteristics in the AIDA expansion chamber (Steinke et al. (2011), hereafter STEINKE) and the ZINC ice nucleating chamber (Hoyle et al. (2011), hereafter HOYLE). In HOYLE the ZINC CFDC instrument, as described in the previous example, was used to determine the total fraction of droplets frozen over a range of temperatures ($-43.15 \leq T \leq -26.15$ °C) with a residence time of 12 s at each temperature. Each supercooled droplet contained a single immersed particle, which ranged from ~ 0.1 to 3 μm in diameter, D . The 84 m^3 AIDA cloud chamber is capable of simulating an ascending, cooling air parcel, and is coupled to an array of instruments, which were used by

STEINKE to determine the freezing characteristics of the same volcanic ash sample. In this method the dust sample ($\sim 0.1 \leq D \leq \sim 15 \mu\text{m}$) is dispersed into the cloud chamber prior to expansion.

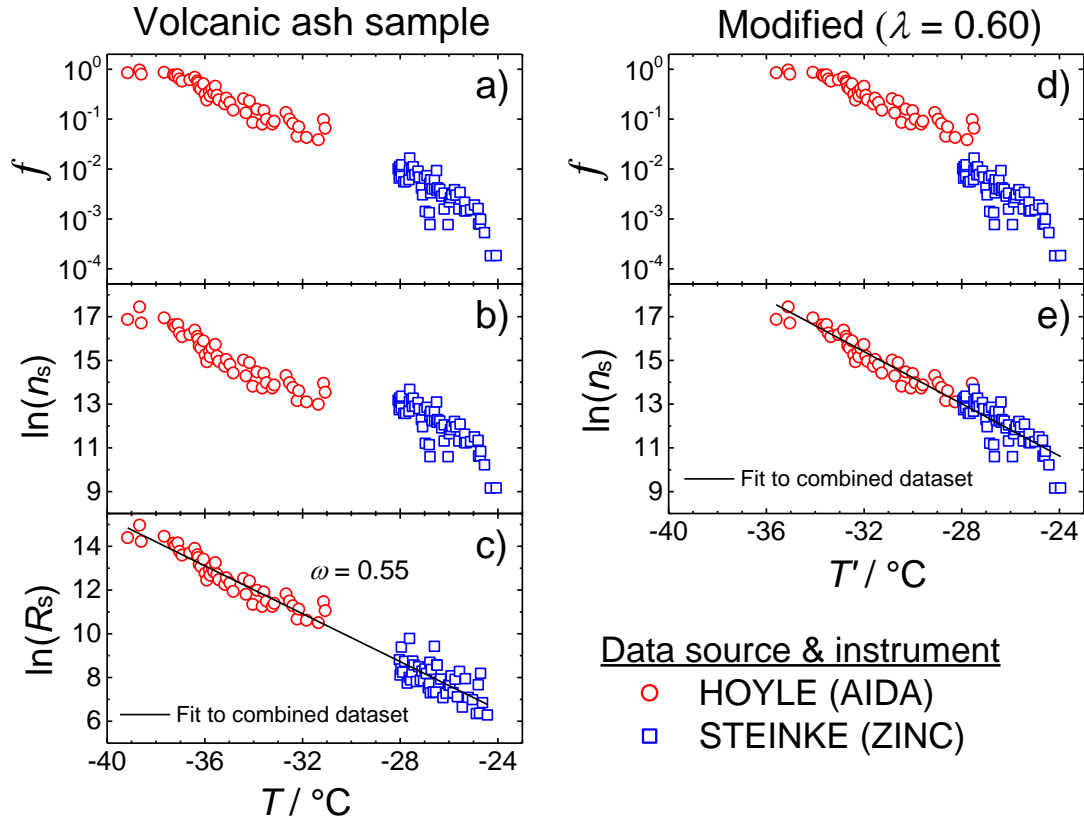


Figure 4.10. Layout as in Figure 4.1 but for a single volcanic ash sample from the Eyjafjallajökull eruption in 2010. Red circles represent data presented in Hoyle et al. (2011) using the ZINC instrument, and black squares represent data from Steinke et al. (2011) using the AIDA expansion chamber. $n_s(T)$ data in (b) was reproduced from Murray et al. (2012); $f(T)$ values in (a) were also determined from this dataset. A fit to determined R_s values in (c) resulted in $\omega = 0.55$. The raw $n_s(T)$ data was modified and resulted in $\lambda = 0.595$. The similarity in ω and λ suggests that this volcanic ash sample behaves as a single-component.

The ice nucleating efficiencies of the two datasets were compared in Murray et al. (2012) and the subsequent $f(T)$ and $n_s(T)$ values are reproduced in Figure 4.10a and b, respectively. Although $f(T)$ appears to be consistent between studies, once plotted as $n_s(T)$ it is clear that the two datasets, albeit with similar gradients, do not show good agreement even though the same sample was used. Figure 4.10c shows the surface area normalised freezing rates, $R_s(T)$, calculated using the temporal conditions of each experiment. For the HOYLE data the experimental residence time of 12 s was used, and for the STEINKE a cooling rate of $1.074 \text{ }^\circ\text{C min}^{-1}$ was used. This was determined from the point at which water saturation was reached, until the elapsed time of the experiment had reached 300 s as per Fig. 2 in

STEINKE. Due to non-cumulative nature of the STEINKE $f(T)$ dataset a polynomial fit to the data was used to determine the differential fraction-frozen required to calculate $R_s(T)$ values. The two datasets fall onto a single line with a $\ln(R_s)$ RMSE of 0.22 with a gradient $\omega = -d\ln(R_s)/dT = 0.55$. Following the previous two examples, λ was systematically varied until the $n_s(T')$ values converged onto a single line described by an exponential fit to $\ln(n_s)$, resulting in $\lambda = 0.596$. Applying this value to Eqs. (3.35) and (3.36) results in $\beta(r) = -0.12$ °C and $\beta(t) = -3.57$ °C for the STEINKE and HOYLE dataset, respectively. Figure 4.10d and e show the subsequently modified $f(T')$ and $n_s(T')$ data. The modified fraction frozen data shows a difference between datasets due to the larger surface area per droplet in the HOYLE experiments (also evident in panel b). The $n_s(T')$ data is shown in Figure 4.10e, with a linear fit to the combined dataset producing a $\ln(n_s)$ RMSE of 0.25.

In this example ω (0.55) and λ (0.596) are similar, which suggests that this INP species is reasonably described by a single-component system (where $\omega = \lambda$). On application of $\lambda = \omega = 0.55$ a fit to the modified data produces a RMSE of 0.26, which is very similar to the minimised value (0.25) used to determine λ , which supports this conclusion. However, Murray et al. (2012), from which these data were reproduced, state that the average surface area per droplet determined for the HOYLE dataset may be over-predicted, which could potentially impact these results. The n_s and R_s values would shift to higher values, and subsequently ω would increase slightly and λ would also increase, but by a larger factor. In this scenario $\omega < \lambda$ which would suggest that the volcanic ash sample is a multiple-component system.

Fornea et al. (2009) also performed an immersion mode experiment using a volcanic ash sample from Mount St. Helens. In their experiments single particles with a diameter of $250 \leq D \leq 300$ μm were immersed within five 2 μL droplets and each subjected to 25 freeze-thaw events. Additionally, as a means of testing the sensitivity to cooling rate, droplets containing the same volcanic ash sample were subjected to freeze-thaw cycles, but cooled at different rates (1 to 10 °C min^{-1}). The freeze-thaw experiments resulted in an average $\sigma_{T,\text{freeze}}$ of 2.0 °C and the variable cooling experiments resulted in a shift in the average freezing temperature by -3.6 °C (upon a change from 1 to 10 °C min^{-1}) without any

change in $\sigma_{T,\text{freeze}}$. Applying these data to the FROST framework Eqs. (3.34) and (3.35) were used to determine λ , resulting in $\lambda = 0.635$ and $\lambda = 0.640$ for the freeze-thaw and cooling experiments, respectively. The first important point worth noting is that these two values, determined from distinct experimental and analysis methods, show very good agreement, providing evidence that the FROST framework is capable of normalising time-dependent behaviour. Secondly, a comparison to the values determined for the first volcanic ash sample previously ($\omega = 0.550$ and $\lambda = 0.595$) shows that there is a strong similarity with regards to the magnitude of λ .

Even though these volcanic ash samples are from different sources these results suggest that they have similar time-dependence properties. These additional results provide evidence that the λ value determined for the Eyjafjallajökull sample is robust, and therefore strengthens the conclusion that the Eyjafjallajökull ash sample tested is a single-component species. Due to the experimental method used by Fornea et al. (2009) it is not possible to determine R_s values, and therefore ω , which would be required to conclude whether the Mount St. Helens volcanic ash sample is also a single-component species.

4.4 The Sensitivity of Freezing Probability to the Time-Dependence of Nucleation

Using Eqs. (3.19) and (3.20) in the FROST framework a first-order indication of the potential importance of time-dependence is shown in Figure 4.11 where values of $\beta(r)$ and $\beta(t)$ for $0.5 \leq \lambda \leq 10$ have been plotted. Each point represents the shift of a specific fraction frozen, by a temperature β °C that results from a fractional change in either cooling-rate or residence-time for a species with a specific value of λ . This plot shows how materials with a small value of λ (corresponding to a shallow gradient ω in a single-component system) are more sensitive to timescale; with a decreasing λ corresponding to an increasing shift by β for the same change in timescale.

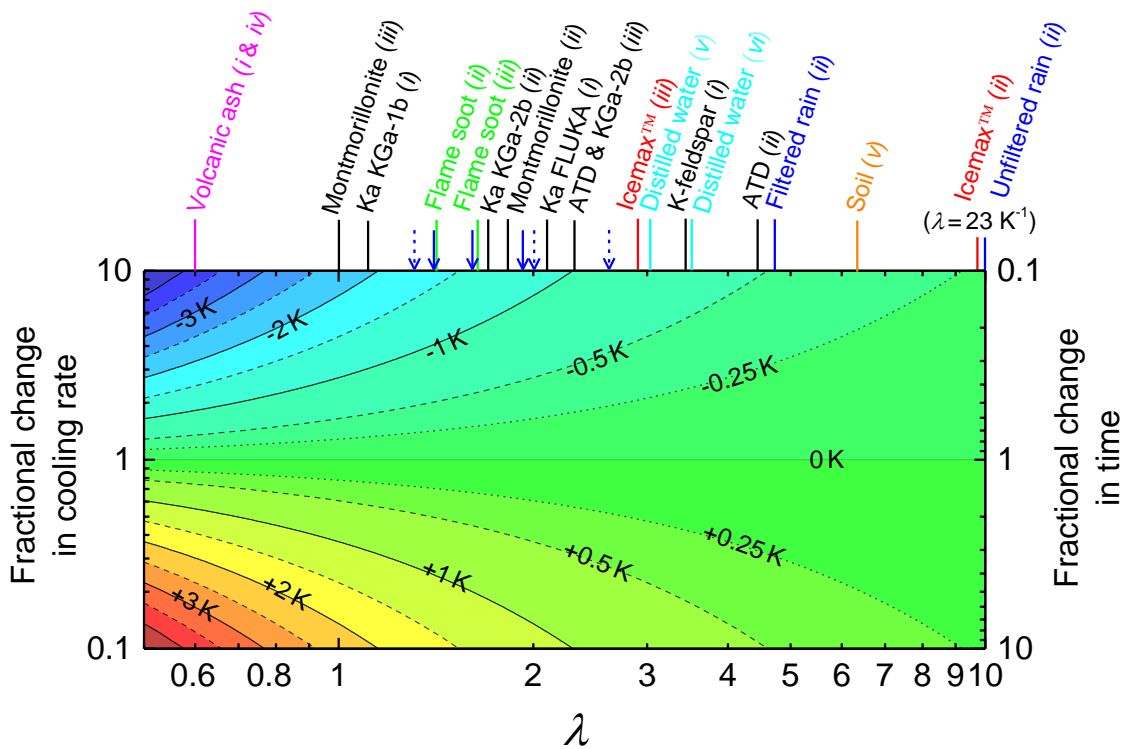


Figure 4.11. The shift in temperature β that will result from a fractional change in cooling rate or residence time for a specific value of λ . Values include those determined from (i) this thesis, (ii) Wright et al. (2013) cooling experiments, (iii) Wright et al. (2013) freeze-thaw experiments, (iv) Fornea et al. (2009), and (v) Vali (2008), and (vi) Vali and Stansbury (1966). INP samples are colour coded depending on INP type. Blue (solid and dashed) arrows correspond to rain samples (unfiltered and filtered) from freeze-thaw experiments by Wright et al. (2013).

4.5 Comparing the Time-Dependencies of Atmospherically Relevant INPs

The application of FROST to the data presented here and existing data can be used to determine the range in time-dependent behaviour for atmospherically relevant INP species obtained using different experimental methods. The various methods and datasets from each study will be briefly presented.

Vali and Stansbury (1966) reported a $0.2\text{ }^{\circ}\text{C}$ shift in $f(T)$ upon each doubling of cooling rate for cooling experiments using droplets of distilled water. Vali (2008) performed a series of freeze-thaw experiments (of up to 65 cycles) with a population of droplets containing a soil sample and a population of distilled water droplets; resulting in $\sigma_{T,\text{refreeze}} = 0.2$ and $\sigma_{T,\text{refreeze}} = 0.42\text{ }^{\circ}\text{C}$, respectively. Fornea et al. (2009) performed a number of freeze-thaw experiments using a droplets containing samples of volcanic ash (from Mt. St. Helens) and presented $\sigma_{T,\text{refreeze}}$ values; a series of cooling experiments at different rates were also

performed using the same volcanic ash sample. Wright et al. (2013) performed a series of cooling experiments to characterise the cooling-rate dependence (over two orders of magnitude change) of several atmospherically relevant INP species, including several mineral dusts, flame soot, a bacterial based substance (IcemaxTM), and rainwater samples. For each experiment median freezing temperatures were presented. Additionally, Wright et al. (2013) performed freeze-thaw experiments with the same INP samples. The standard deviation in freezing temperature for each INP was presented.

Table 4.1. Values of λ from various immersion mode studies. λ determined using the FROST framework.

Study and experimental method	Material	λ
Vali and Stansbury (1966) – <i>cooling</i>	Distilled water	3.5
Vali (2008) – <i>freeze-thaw</i>	Soil	6.3
	Distilled water	3.0
Fornea et al. (2009) – <i>freeze-thaw</i>	Volcanic ash (Mt. St. Helens)	0.6
Fornea et al. (2009) – <i>cooling</i>	Volcanic ash (Mt. St. Helens)	0.6
Hoyle et al. (2011) – <i>isothermal</i> & Steinke et al. (2011) – <i>cooling</i>	Volcanic ash (Eyjafjallajökull)	0.6
Welti et al. (2012) – <i>isothermal</i>	Kaolinite Fluka	2.2
Wright et al. (2013) – <i>freeze-thaw</i>	Icemax TM	2.9
	ATD	2.3
	Montmorillonite	0.9
	Kaolinite KGa-2b	2.2
	Flame soot	1.7
	Filtered rain #1	1.3
	Filtered rain #2	2.0
	Filtered rain #3	2.6
	Filtered rain #4	1.9
	Unfiltered rain #1	1.6
	Unfiltered rain #2	1.4
	Unfiltered rain #3	1.9
	Wright et al. (2013) – <i>cooling</i>	Icemax TM
ATD		4.4
Montmorillonite		1.8
Kaolinite KGa-2b		1.7
Flame soot		1.4
Filtered rain #3		4.6
Filtered rain #4		4.6
Unfiltered rain #1		23.0
This study – <i>cooling and isothermal</i>	Kaolinite KGa-1b	1.1
	K-feldspar	3.4

The corresponding values of λ from each study were determined using the FROST framework. The values are shown in Table 4.1 along with those determined and presented in the earlier sections. A subset has been included in Figure 4.11 to demonstrate the relative importance of each species. From Figure 4.11 and Table 4.1 it is clear that atmospherically relevant INPs exhibit a wide range of time-dependent behaviour. INP species that have a value of λ with a large magnitude ($\lambda > 4$), such as the IcemaxTM and ATD, will exhibit very little time-dependence and would likely be well approximated by a singular freezing model. For those with a small magnitude (especially $\lambda < 1$) such as the volcanic ash from HOYLE and STEINKE the significant cooling-rate and residence-time dependence must be taken into account.

These findings are important because it changes the way that the ice nucleation community should frame the debate of whether time-dependence is important in ice nucleation. In the past the question has been whether time-dependence is important, but this question should be rephrased to whether a particular INP species has a strong time-dependence or not, and at what point this stops having an impact on ice nucleation rates, i.e., is there a limiting value of λ , beyond which the singular freezing model is adequate? This latter question will be addressed in the following chapter.

4.6 Implications for In-situ INP Measurements

The variability in λ shown in Figure 4.11 raises the question of whether the role of time-dependence is being taken into account when measuring INP concentrations in the atmosphere. In this section the FROST framework will be used to understand how a specific instrument residence time (t) relates to a cloud updraught speed. This will provide information on how representative a residence time t is on the cloud being measured.

Atmospheric INP concentrations are generally determined by passing a flow of particles through supercooled conditions (constant T) and measuring the fraction of particles that produce ice particles. By changing the isothermal experiment temperature the number of INPs that are ‘active’ at that temperature can be determined. For the immersion mode, dry particles are subjected to water supersaturated conditions prior to the supercooling in order

to immerse each particle in a single droplet. The isothermal experiments are typically performed with short residence times.

The most extensively used instrument used for in-situ measurements (and post field campaign analysis of in-situ air) is the Colorado State University (CSU) CFDC which has been used in a large number of field campaigns (DeMott et al., 2010). The temporal characteristics of this instrument therefore represent the conditions used for measuring INP concentrations in the atmosphere. The CSU-CFDC residence time is dependent on the air flow used and has a typical range of 3 to 30 s (Rogers et al., 1998; DeMott et al., 2003a; Cziczo et al., 2003; DeMott et al., 2003b). This range will be used to constrain the typical temporal conditions used for measuring the INP concentration.

Equation (3.33) was used to determine the cooling rate (in $^{\circ}\text{C min}^{-1}$) that would be required to reach the same fraction frozen as in an isothermal experiment with a residence time t . This cooling rate can then be used to determine the equivalent in-cloud updraught speed, $w_{\text{equivalent}}$. To determine the $w_{\text{equivalent}}$ a wet adiabatic lapse rate of $5.5^{\circ}\text{C km}^{-1}$ was used so that upon incorporation with Eq. (3.33)

$$w_{\text{equivalent}} = \frac{1}{\lambda \cdot t \cdot 5.5 \times 10^{-3}} \quad (4.1)$$

where t is the residence time in seconds and $w_{\text{equivalent}}$ is in units of m s^{-1} . A range of instrument residence times ($1 \leq t \leq 60$) and values of λ ($0.1 \leq \lambda \leq 10$) were applied to Eq. (4.1), and the results are shown in Figure 4.12. Each data point in this plot describes the updraught speed which would be required to reach the same f as in an instrument with a specific residence time for an INP characterised by λ . The implication shown in this data is that an in-situ measurement of INP concentration is only applicable at a single cloud updraught speed, the value of which is dependent on the instrument residence time and λ . The application of the in-situ measurement to clouds with $w < w_{\text{equivalent}}$ will lead to an over-prediction of the INP concentration and $w > w_{\text{equivalent}}$ to an under-prediction.

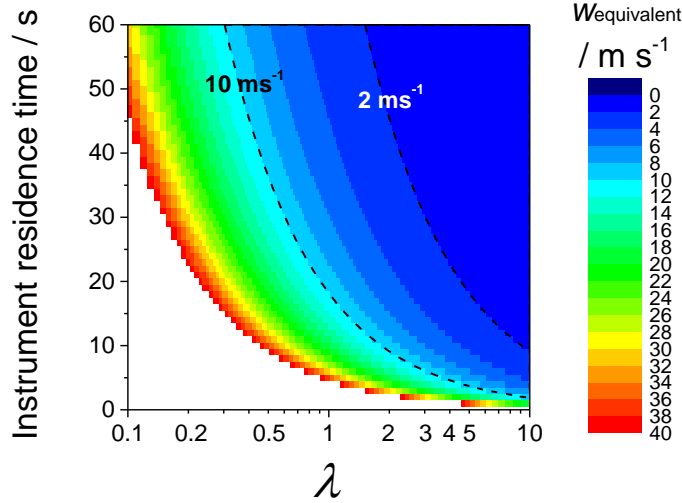


Figure 4.12. The equivalent in-cloud updraught speed as a function of instrument residence time and λ . Colour coded contours are 2 m s^{-1} apart and dashed lines have been included to show where updraught speed is < 2.0 and $> 10.0 \text{ m s}^{-1}$. Updraught speeds calculated assuming a wet adiabatic lapse rate of $-5.5 \text{ }^\circ\text{C km}^{-1}$.

To understand the magnitude of the discrepancy in predicted INP concentration the FROST framework was used to determine the difference in concentration between the in-situ measurement and the expected concentration in a simulated cloud with constant updraught speed w . For these calculations four values of w were used ($1.0, 2.5, 5.0,$ and 10.0 m s^{-1}). Equation (3.19) was used to determine β upon a change in updraught speed from the $w_{\text{equivalent}}$ in Figure 4.12 to the simulated or prescribed w . Assuming a single-component species, equating $f(T)$ with $f(T + \beta)$ can be used to determine the equivalent change in f , which results in the equation:

$$\frac{N_{\text{INP,measured}}}{N_{\text{INP,simulated}}} = \frac{f_1}{f_2} = \exp(-\lambda)\beta \quad (4.2)$$

β values determined from Figure 4.12 were applied to this formula and the results are shown in Figure 4.13. Each separate panel shows the relative difference in INP concentration between an in-situ measurement and a simulated cloud with updraught speed w . The marked region encompasses the range in typical in-situ CFDC instrument residence times and also encompasses the range in λ that most of the INP species shown in Figure 4.11 were observed to exhibit. This can therefore be seen as representative of the experimental method and time-dependent characteristics of atmospherically relevant INP species.

The principal result is that due to the short residence times INP concentrations at low updraught speeds, especially for $w < 1 \text{ m s}^{-1}$, may be substantially under-predicted. For example, if a population of droplets contained kaolinite KGa-1b particles ($\lambda = 1.12$) then the predicted INP concentration (based on a 30 s residence time) would only account for ~20% of the actual number concentration; a weakly time-dependent species ($\lambda = 3$) would be under-predicted by ~50%. Only species that have extremely weak time-dependent behaviour ($\lambda > 6$) would be well represented by the 30 s residence time. As w increases the trends can be seen to systematically shift (with respect to λ) to higher percentages, so that at $w = 5 \text{ m s}^{-1}$, representing a convective cloud, the kaolinite species would be well represented by the 30 s residence time, whereas now the less time-dependent species are being over-predicted.

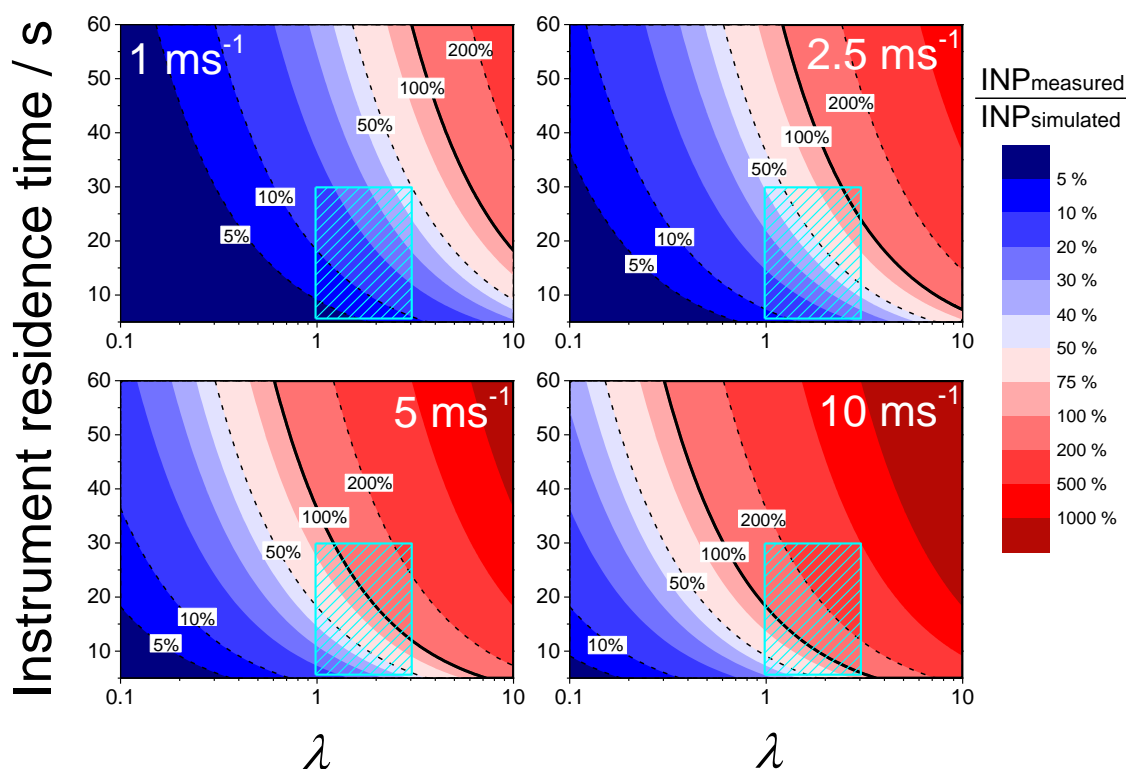


Figure 4.13. The percentage difference in measured and predicted INP concentration when time-dependence is not taken into account for a range of simulated updraught speeds. The measured concentration is dependent on instrument residence time t and λ . These values are assuming a single-component system and are therefore an upper limit to the expected difference. The shaded cyan box represents the area that encompasses the typical in-situ measurement residence times and the estimated range of λ within which most INP species are observed to fall (estimated from Figure 4.11).

This is a significant result as it shows that neglecting time-dependence in the analysis of experimental data can have substantial implications for the subsequent prediction of INP

concentrations used in cloud modelling studies. However, the results shown in Figure 4.13 were determined assuming a single-component species. As shown in Chapter 2 the difference in f upon a change in temporal conditions for a multiple-component species decreases with increasing site diversity. This suggests that the results from Figure 4.13 are an upper limit to the effect that time-dependence has on the measured INP concentration.

The effect on the measurements introduced from using a short instrument residence time could be accounted for using the FROST framework if λ of the species being measured is known. This would require knowledge on the classification of INPs in the atmosphere, and also knowledge on their characteristic λ . A continued experimental characterisation of relevant INPs could accomplish this.

4.7 Conclusions

In this chapter the FROST framework was used to reconcile, for the first time, immersion mode freezing data obtained using different experimental methods and time-scales. The application of FROST and a newly designed set of methods can be used to determine the value λ that characterises the time-dependent freezing behaviour of INPs. With knowledge of λ the freezing behaviour in immersion mode experiments can be prognostically simulated. As demonstrated, experimental data obtained from different instruments and methods can now be reconciled to remove time-dependent effects, allowing the underlying nucleation rate coefficient to be consistently determined.

The FROST framework was used to determine λ from a range of existing experimental datasets obtained using cooling, isothermal, and freeze-thaw experiments. This unique dataset provides information on the variation in time-dependent properties for a wide range of atmospherically relevant INPs. The INPs are predominantly characterised by $1 \leq \lambda \leq 3$ although some species, including volcanic ash samples from Mt. St. Helens and Eyjafjallajökull, and black carbon, show substantial time-dependent behaviour.

Finally the framework was used to highlight the possible implications for in-situ measurements of INP concentrations using instruments with short residence times. Typical

instrument residence times were used to show that single-component INPs with low λ values will be under predicted by up to 80% in a simulated 1 m s^{-1} updraught, whilst only species with $\lambda > 6$ would be well represented. At higher updraught speeds (5 m s^{-1}) this behaviour systemically shifts to higher % so that low λ species are well represented but for species with high λ the INP concentration will be substantially over-predicted.

Chapter 5: Time-Dependence Sensitivity Studies using a Cloud Model with Detailed Microphysics

5.1 Introduction

In Chapters 3 and 4 it was found that the time-dependent behaviour of an INP species can be characterised using λ , which describes the temperature dependence of the nucleation rate coefficient J_s for a particular INP species. A parameterisation was presented in Chapter 3 that is able to represent this time-dependent behaviour for use in modelling studies.

In this chapter the parameterisation that forms part of the FROST framework is incorporated into a detailed microphysics scheme in the Met Office KiD model and used to estimate the sensitivity of mixed-phase clouds to immersion mode time-dependence. A series of increasingly complex modelling frameworks will be used to understand the relationship between λ and various cloud properties.

5.2 Model Description and Development

The Met Office Kinematic Driver (KiD) model was developed and introduced by Shipway and Hill (2012) as a 1D and 2D framework for comparing microphysics schemes without the added complexities of dynamical and radiative feedbacks. To achieve this, radiation and its effect on cloud development is not considered in the KiD modelling framework, and dynamics are prescribed throughout the simulation. Prognostic variables are advected using the advection scheme as described by Leonard (1993), known as ULTIMATE. Several microphysics schemes are already embedded in the framework and include single and double-moment bulk schemes, and a bin scheme. For these simulations the double-moment Thompson09 scheme (Thompson et al., 2008) was chosen. Results from a microphysics-scheme inter-comparison by Shipway and Hill (2012) show that this scheme falls well

within the spread of the other microphysics schemes, including the widely used Morrison 2M scheme.

The Thompson09 bulk microphysics scheme (described in full by Thompson et al. (2008)) predicts the mass mixing ratios of cloud water, rain, cloud ice, graupel, and snow, and also the cloud ice and rain number concentrations. Following observations by Field et al. (2005) the snow size distribution is determined using a combined exponential and gamma distribution, all other hydrometeor species are represented by a gamma distribution. Water vapour condensation is determined using a saturation threshold (Flatau et al., 1992), the autoconversion of cloud droplets into rain follows Berry and Reinhardt (1974) and the collision-collection processes between species is determined following Verlinde et al. (1990). The growth and sedimentation of hydrometeor species is represented, as well as the melting of ice phase species.

The unmodified Thompson09 scheme currently represents freezing in the immersion mode following the parameterisation presented by Bigg (1953b), in which the probability of freezing is dependent on droplet volume and temperature only. All droplets are considered to contain an INP and therefore viable for freezing heterogeneously in the immersion mode. Rain droplets exceeding a mass of 3.27×10^{-6} g (relating to graupel with a diameter of 250 μm) are transferred into graupel, with smaller rain droplets and all water droplets transferred into cloud ice. Ice nucleation via deposition and condensation mode is determined following Cooper (1986) less the contribution from the immersion mode. Homogeneous nucleation is represented by a threshold temperature of -38 °C, at which point all liquid hydrometeors are immediately frozen. Contact mode nucleation is not represented.

For an improved representation of homogeneous freezing the temperature threshold used as a homogeneous freezing temperature was replaced with a parameterisation based on results from Murray et al. (2010) where the probability of a droplet freezing is determined as:

$$P_{\text{freezing,homogeneous}}(T) = 1 - \exp(-J_v \cdot v \cdot \Delta t) \quad (5.1)$$

where v is the droplet volume in units cm^3 , Δt is the model time step in seconds, and J_v is the homogeneous nucleation rate coefficient, described by the formula:

$$J_v(T) = \exp\left(A - B \exp\left[\frac{T - T_0}{C}\right] - D \exp\left[\frac{T - T_0}{E}\right]\right) \quad (5.2)$$

where T_0 is a temperature offset and A, B, C, D and E are constants, with the values given in Table 5.1 as per Murray et al. (2010). Following the observations as discussed in Chapter 1 all other heterogeneous modes were switched off for the simulations.

Table 5.1. Constants for J_v in Eq. (5.2).

Constant	Value
T_0	37.231 °C
A	50.181
B	31.922
C	8.9479
D	0.10188
E	2.6711

5.2.1 Incorporating the FROST framework

As highlighted in Chapter 4 the freezing behaviour of INP species are measured under certain temporal conditions, which might be substantially different to the timescales available in clouds. The incorporation of the FROST framework in the model will provide a means for understanding the significance of this by testing the sensitivity of the cloud evolution to changes in λ . As in the unmodified Thompson09 scheme all droplets are assumed to contain a single INP with a constant surface area, which therefore describes a single-component system. This is an idealised treatment of the INP population but provides a means for exploring the significance of the variation in timescales for different INP species.

The existing immersion mode parameterisation (Bigg scheme) was replaced with the parameterisation presented in Chapter 3 so that the probability of a droplet freezing at a temperature T and cooling rate r (in $^{\circ}\text{C min}^{-1}$) is determined as:

$$P_{\text{freezing}}(T, r) = 1 - \exp\left(-k\left(T - \frac{\ln(r)}{-\lambda}\right) \cdot s \cdot \Delta T\right) \quad (5.3)$$

where λ is the value that characterises the time-dependence of the INP species, s the surface area per droplet, and ΔT the change in temperature per model time step. The function of $k(T)$ describes the differentiated form of the cumulative nucleation rate, $n_s(T)$. The default nucleation rate used is that of the mineral dust K-feldspar which is described by the function $n_{s,\text{K-fe}}(T) = \exp(-1.038T + 275.26)$ as presented by Atkinson et al. (2013), where T is the temperature in kelvin. A corresponding particle surface area $s_{\text{K-fe}}$ per droplet is prescribed as $1 \times 10^{-9} \text{ cm}^2$ which corresponds to an equivalent particle radius of $\sim 0.1 \mu\text{m}$. In addition I also use an n_s function for kaolinite, an example of a less efficient INP; the rate is described by $n_{s,\text{ka}}(T) = \exp(-1.12T + 284.46)$ which was determined from the experimental dataset presented in Chapter 4. A corresponding s_{ka} is prescribed as $3.14 \times 10^{-8} \text{ cm}^2$ corresponding to a radius of $0.5 \mu\text{m}$. The difference in s between the two INP species follows from the observation that K-feldspar is generally found as a minor component of atmospheric dust INPs, and kaolinite found as a major component (Broadley et al., 2012).

5.2.2 Mixed-Phase Cases

The KiD model has a number of pre-existing 1D and 2D mixed-phase cases (Shipway and Hill, 2011) that are used to prescribe the simulation dynamics, as well as the initial profile of potential temperature θ_T , pressure, and water vapour mixing ratio q_v . Hydrometeors and aerosols can also be prescribed but will not be in these simulations. A time and altitude-dependent forcing can be applied to each of the prescribed variables. In this chapter a series of cases will be used to examine the role of time-dependence. An idealised 0D case is developed and used initially, and then followed by a series of existing 1D and 2D cases.

In the *0D simulations* the 1D framework is adapted in order to isolate certain processes for use in an idealised sensitivity study. This is achieved by initialising and running the simulation as a 1D case but only considering a single altitude. Advection is switched off but sedimentation of hydrometeors is allowed. Using this method the boundary conditions are fulfilled by the surrounding 1D column. The case domain is a single column with a maximum height of 1000m. The θ_T profile is initialised to linearly decrease with height, and q_v is initialised so that a relative humidity RH_{liquid} of 100% is attained. For simulations using this case a constant forcing of θ_T with respect to time is applied to the column, so that a single grid cell will experience a constant cooling. By changing the magnitude of forcing a varying equivalent updraught speed $w_{\text{equivalent}}$ is achieved. All 0D simulations are taken at a height $z = 300\text{m}$ from the 1D column which corresponds to an initial temperature of $10.3\text{ }^\circ\text{C}$.

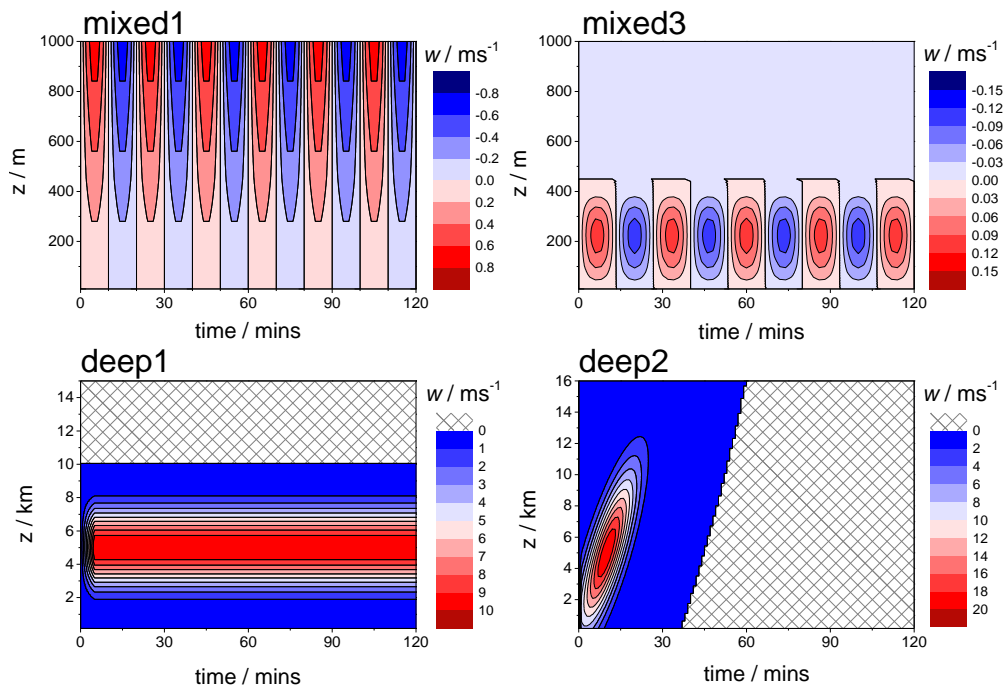


Figure 5.1. The prescribed vertical updraught speeds used for the various 1D simulations. These idealised cases are described in Shipway and Hill (2011).

The *1D simulations* consist of two mixed-phase stratocumulus cases and two convective cases. The corresponding dynamics of each case are shown in Figure 5.1. The *mixed1* case is characterised by an oscillating updraught/downdraught in time with the magnitude

linearly increasing with height where a maximum $w = 0.7 \text{ m s}^{-1}$ is reached. The *mixed2* case is designed to simulate a quasi-steady stratocumulus layer. It exhibits an oscillating updraught/downdraught with a maximum $w = 0.1 \text{ m s}^{-1}$ which is restricted to the lower $\sim 400\text{m}$ of the column, a prescribed constant forcing of the water vapour field is also applied so that a steady precipitation rate is expected to be reached. Default profiles built into the KiD model (Shipway and Hill, 2011) are used to initialise the prescribed variables of θ_T and q_v for both cases. These include the option of either a profile used in the GCSS SHEBA inter-comparison project, or a profile taken from the M-PACE campaign; both are shown in Figure 5.2. The SHEBA profile is characterised by a strong $4 \text{ }^\circ\text{C}$ inversion at $\sim 400 \text{ m}$, whereas the M-PACE profile is characterised by a linearly decreasing temperature with height.

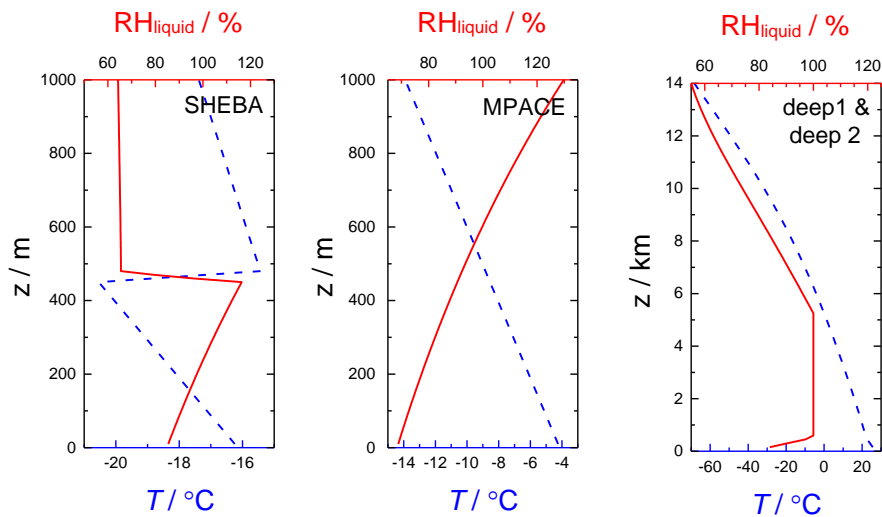


Figure 5.2. The resulting profiles of T and $\text{RH}_{\text{liquid}}$ used for the various 1D simulations following prescribed profiles of θ_T and q_v .

The first convective case, *deep1*, is designed to simulate steady-state convection. A constant updraught characterised by w_{max} is applied along with a constant water vapour forcing which varies with height so that a steady precipitation rate is expected. The *deep2* case is designed to reproduce an updraught core which varies in both height and time and can be seen as a transient case of deep convection, the dynamics of both convective cases are summarised in Figure 5.1. The initial prescribed profiles of θ_T and q_v for both convective cases are shown in Figure 5.2, the overall profile characterises a dry boundary layer followed by a 5 km deep saturated layer. At temperatures below $0 \text{ }^\circ\text{C}$ q_v is prescribed so that a RH_{ice} of 100% is attained.

The *2D simulations* consist of a mixed-phase stratocumulus case and a squall line case, the prescribed variables and dynamics are shown in Figure 5.3. The *stratocumulus* case is based on the dynamics as described in Morrison and Grabowski (2007) combined with a profile taken from the Alaskan ISDAC campaign used to simulate mixed-phase conditions. This results in distinct updraught and downdraught regions with equal magnitudes of w with $w_{\max} = 1 \text{ m s}^{-1}$, and an upper-level 200 m deep saturated layer. The *squall line* case has been taken from Slawinska et al. (2009) and is characterised by an expansive convective region and stratiform region. These simulations only concentrate on the convective region, which occurs between 30 and 70 km in the horizontal and has a maximum w_{\max} of 10 m s^{-1} . As shown in Figure 5.3 the prescribed domain is characterised by a 15 km wide saturated convective cell with a freezing level height of $\sim 4 \text{ km}$. A left-to-right flow of 4 m s^{-1} is prescribed along with a weak left-to-right shear of $0.1 \text{ m s}^{-1} \text{ km}^{-1}$ (Slawinska et al., 2009). The addition of observationally constrained perturbations result in a convergent flow at the base of the cell and divergent upper-level flow.

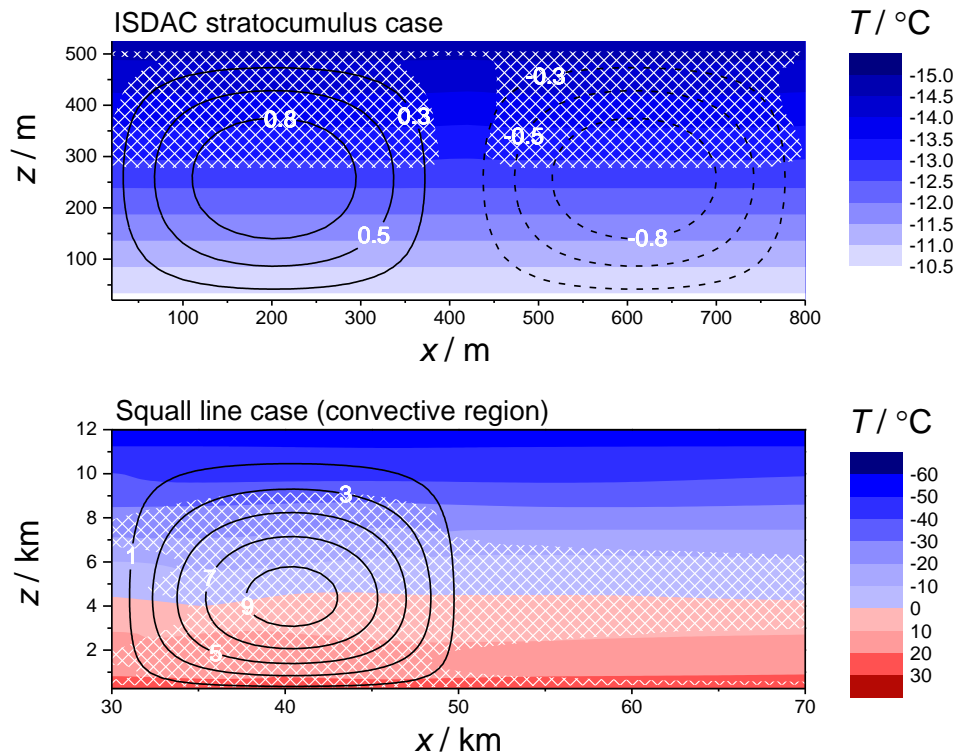


Figure 5.3. The initial prescribed domains of w , T , and $\text{RH}_{\text{liquid}}$ used in the 2D simulations. Solid contours show positive w and dashed contours negative w in m s^{-1} . The white hatched regions show those where $\text{RH}_{\text{liquid}} \geq 100\%$.

Table 5.2. Summary of each set of simulations performed.

	Simulation name	Description*
0D (variable λ , $w_{\text{equivalent}}$)	0D_Kfe	
	0D_Ka	Using kaolinite nucleation rate
1D (variable λ)	1D_m1SHEBA	Mixed1 case, SHEBA profile
	1D_m1MPACE	Mixed1 case, M-PACE profile
	1D_m3SHEBA	Mixed3 case, SHEBA profile
	1D_m3MPACE	Mixed3 case, M-PACE profile
	1D_d1w10 1D_d1w005 1D_d1wmax	Deep1 case, $w_{\text{max}} = 10 \text{ m s}^{-1}$ Deep1 case, $w_{\text{max}} = 0.05 \text{ m s}^{-1}$ Deep1 case, w_{max} varied
	1D_d2	Deep2 case
2D (variable λ)	2D_ISDAC	Stratocumulus case using ISDAC profile
	2D_ISDAC_sa	- with increased $s_{\text{K-fe}}$ per droplet
	2D_ISDAC_Ka	- using kaolinite nucleation rate
	2D_SQUALL	Squall line (deep convective region only)

* Default nucleation rate is K-feldspar with $s_{\text{K-fe}} = 10^{-9} \text{ cm}^2$

A number of simulations were performed for each case where λ was varied, and in some the updraught speed (or corresponding cooling rate) was additionally varied. A description of each set of simulations and its associated name is shown in Table 5.2. A factor of $\times 100$ increase in $s_{\text{K-fe}}$ was used for the simulations where the surface area was varied. Hereafter, the subscripts c , r , i , s , and g will be used to refer to cloud water, rain, ice, snow, and graupel, respectively.

5.3 0D Modelling Studies

These simulations will be used to help understand how the time-dependent behaviour of an INP species influences the evolution of an idealised mixed-phase cloud. This was achieved by simultaneously running the same simulation with a variety of λ values ($\lambda = 0.5, 1, 3, 5,$ and 10) which covers the range observed in experiments presented in Chapter 3. Additionally the prescribed θ_T forcing was varied so that a range of cooling rates, and thus equivalent updraught speeds $w_{\text{equivalent}}$, were achieved; ranging from 0.05 to 30 m s^{-1} . Various cloud properties will be examined in order to determine key cloud variables or properties that can be used to assess the sensitivity of the simulation to time-dependence in the 1D and 2D simulations.

Figure 5.4 and Figure 5.5 show the evolution of each hydrometeor species along with the cumulative mass of liquid droplets frozen via the immersion mode (Σ_{imm}) and through homogeneous freezing (Σ_{hom}). The primary effect of time-dependence is shown by the systematic shift in Σ_{imm} . As expected, small magnitudes of λ cause a greater variation in freezing rates than large magnitudes. At low $w_{\text{equivalent}}$ the highest freezing rates correspond to a smaller magnitude in λ , whereas at high $w_{\text{equivalent}}$ this relationship is reversed. This behaviour is observed because nucleation rates in the FROST framework are normalised to a $1 \text{ }^\circ\text{C min}^{-1}$ cooling rate, which corresponds to $w_{\text{equivalent}} \approx 3.5 \text{ m s}^{-1}$. At updraught speeds above this, the nucleation efficiency is decreased and conversely increased below this speed, which suggests that the immersion mode freezing rate will vary considerably at both extremes of updraught speed (i.e., low and high) when the value of λ is small.

OD_Kfe

$T / ^\circ\text{C}$

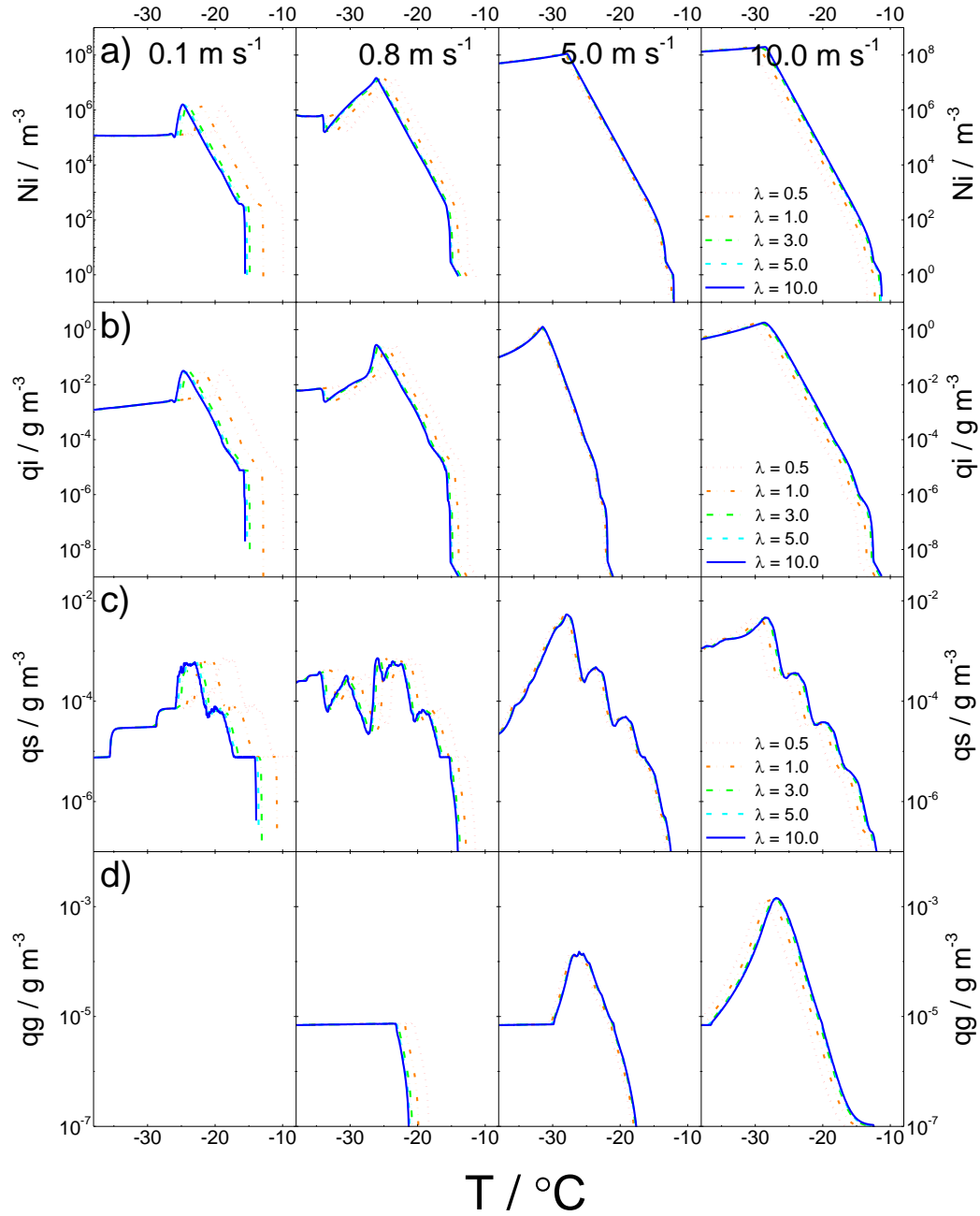


Figure 5.4. Evolution of several hydrometeor species (right-to-left) throughout a series of simulations of constant $w_{\text{equivalent}}$ (0.1, 0.8, 5, and 10 m s^{-1}) for a range of increasing λ , corresponding to a decreasing time-dependent behaviour. a) shows cloud ice number concentration, and b-c) the mass mixing ratio of cloud ice, snow, and graupel, respectively.

0D_Kfe

T / °C

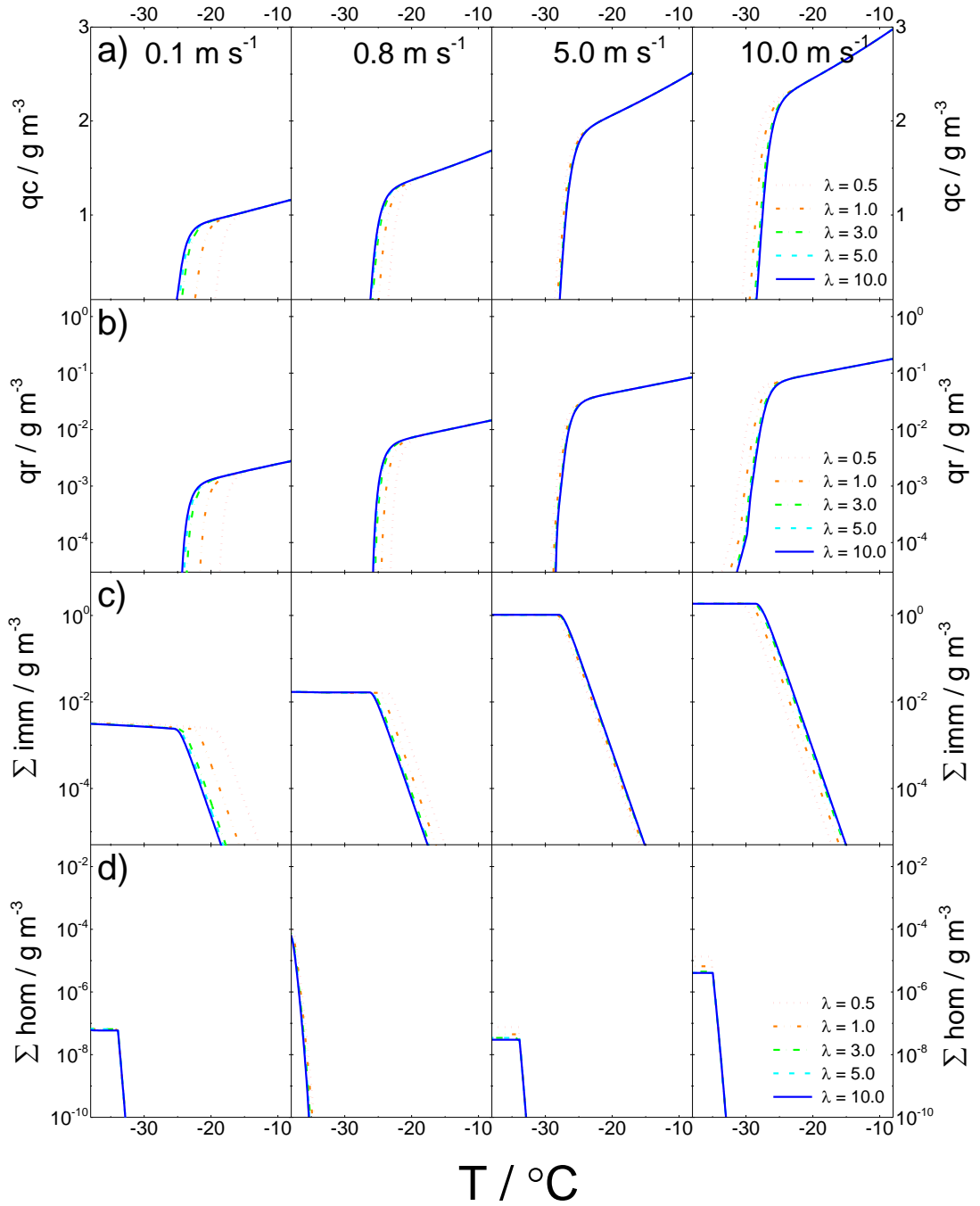


Figure 5.5. Same as Figure 5.4 but for a) the mixing ratio of cloud droplets; b) the mixing ratio of rain; c) the cumulative sum of liquid mass frozen via the immersion mode; and d) the cumulative sum of liquid mass frozen via homogeneous freezing.

The time-dependent effect on ice production can be seen to directly impact the other cloud hydrometeor species. The variation in Σ_{imm} is similarly observed in the resulting ice number concentration N_i and mixing ratios q_i , q_s and q_g . As shown in Figure 5.6 this then causes a comparable variation in the evolution of the cloud's ice water content (IWC). This has a corresponding effect on the cloud's liquid water content (LWC), and shows that the lifetime of the mixed-phase cloud is effected by the magnitude of time-dependent behaviour. For example, with an INP species where $\lambda = 0.5$ the cloud will fully glaciate at -20°C in a 0.1 m s^{-1} updraught but remains in a mixed-phase state until -31°C in a 10 m s^{-1} updraught. By comparison a value of $\lambda = 10$ results in a difference of -2.5°C .

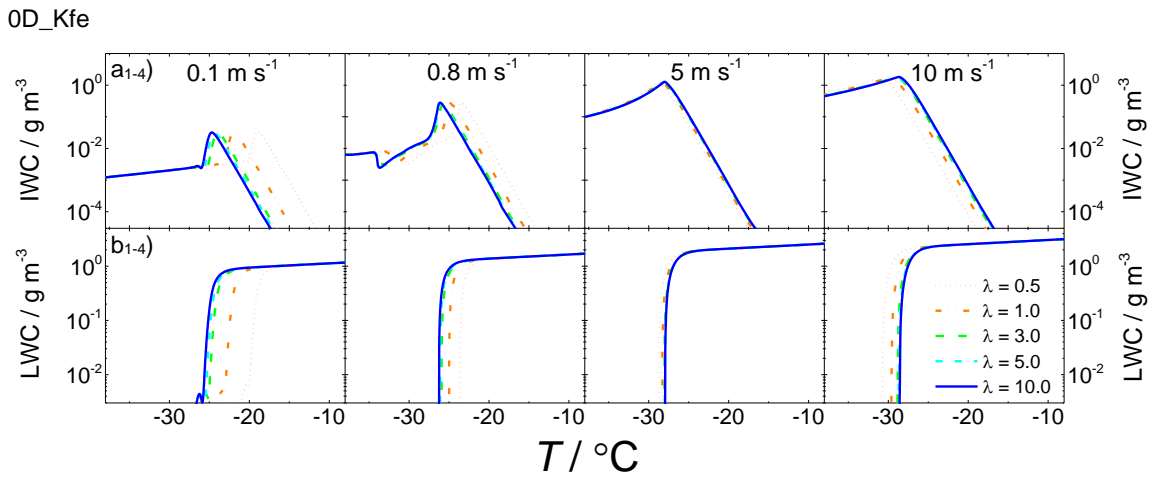


Figure 5.6. Same as Figure 5.4 but for a) Ice water content (IWC) and b) liquid water content (LWC)

The final state of the cloud can also be inferred from the IWC evolution in Figure 5.6. At lower updraught speeds the final state of the glaciated cloud IWC value appears to be independent of λ , whereas at high updraught speeds there is dependence, as seen in Figure 5.7. Here the difference between simulations where $\lambda = 5.0$ and 0.5 has been calculated for q_i , q_s , and q_g at three updraught speeds. A negative value corresponds to times when the $\lambda = 0.5$ simulation has a relatively higher mixing ratio. At low updraught speeds there is negligible difference for all ice species below -35°C whereas for $w_{\text{equivalent}} = 5$ and 10 m s^{-1} there is a considerably greater cloud ice mass in simulations for $\lambda = 0.5$. This is due to a combination of the relatively weaker immersion freezing rate (compared to $\lambda = 5$) and increased cloud water content from higher updraught speeds. The difference in cloud ice

content due to time-dependence could have a radiative impact, especially at high updraught speeds.

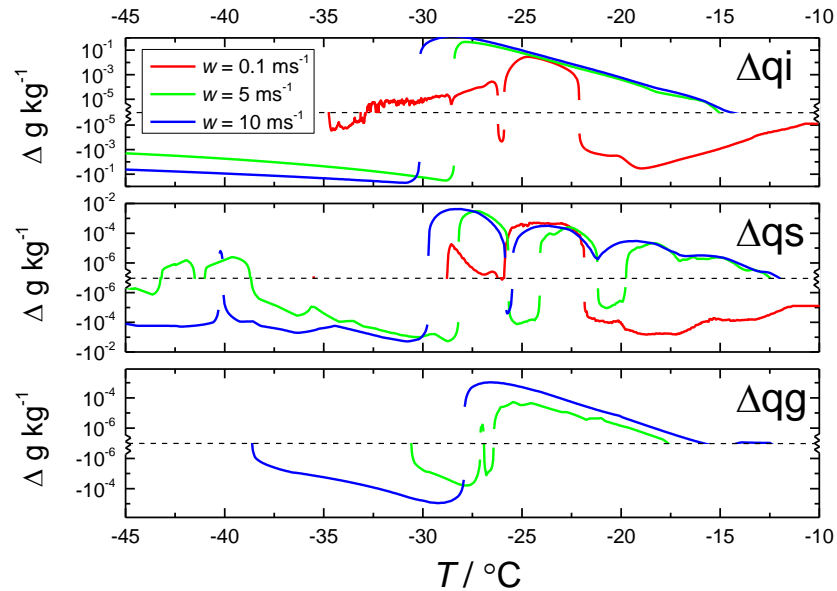


Figure 5.7. The absolute difference between the $\lambda_{5,0}$ and $\lambda_{0,5}$ simulations where $\Delta X = X(\lambda_{5,0} - \lambda_{0,5})$ for q_i , q_s , and q_g . A negative value corresponds to a relatively larger magnitude in the $\lambda_{0,5}$ simulation. The different colours represent the range of equivalent updraught speeds $w_{\text{equivalent}}$. The apparent discontinuity is an artefact from the analysis process.

A relationship between immersion freezing rate and cloud ice species can be observed in the ice, snow, and graupel mass growth rates for the simulations at $w_{\text{equivalent}} = 10 \text{ m s}^{-1}$ shown in Figure 5.8. The sources of snow are all dependent on the presence of cloud ice as can be seen by the comparable systematic shift in growth rates for different values of λ . Other processes, such as the collection of water droplets, may also impact the growth of q_s but are not active in these simulations. In these simulations graupel is only produced via the immersion mode, hence the comparable shift. Collection processes and secondary ice formation may play a more substantial role in the growth of q_g in other cases.

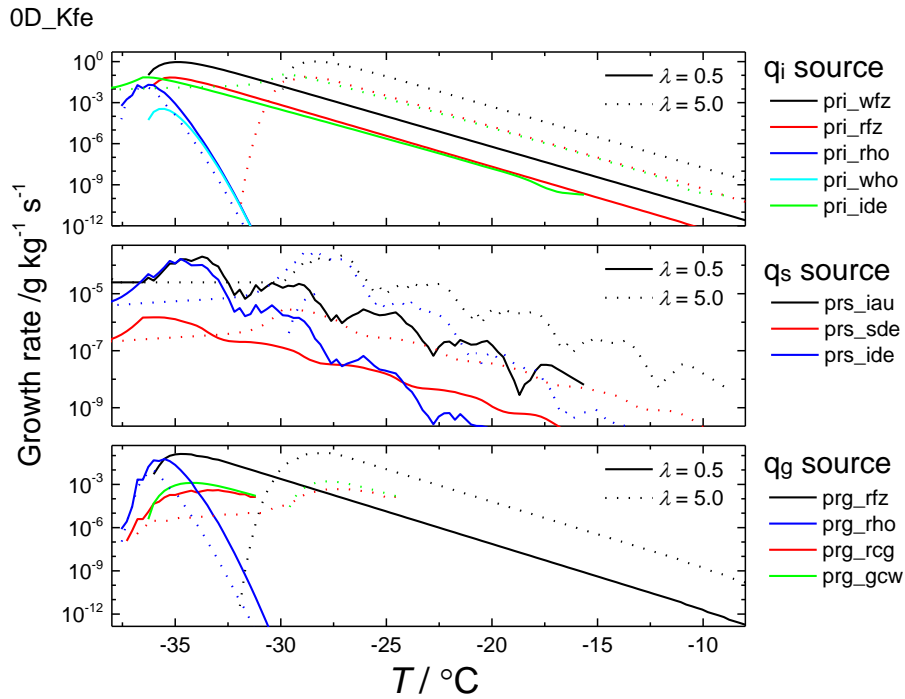


Figure 5.8. The mass growth rate as a function of T for variables corresponding to cloud ice, snow, and graupel. Data is only shown for simulations where $w_{\text{equivalent}} = 10 \text{ m s}^{-1}$ and $\lambda = 0.5$ (solid lines) and 5.0 (dotted line). See Table 5.3 for a description of each variable.

Table 5.3. Description of the hydrometeor mass growth sources referred to in the chapter.

Variable name	Description
Cloud ice	
pri_wfz	Immersion mode freezing of cloud water
pri_rfz	Immersion mode freezing of rain
pri_who	Homogeneous freezing of cloud droplets
pri_rho	Homogeneous freezing of rain
pri_ide	Depositional growth of ice
pri_ihm	Production of cloud ice via HM process
prs_iau	Autoconversion of ice to snow (sink)
pri_inu	Deposition mode nucleation of ice from vapour
Snow	
prs_iau	Autoconversion of ice to snow (source)
prs_sde	Depositional growth of snow
prs_ide	Depositional growth of ice converted to snow
prs_sci	Snow collecting cloud ice
prs_scw	Snow collecting cloud water
Graupel	
prg_rfz	Immersion mode freezing of large rain droplets
prg_rho	Homogeneous freezing of large rain droplets
prg_rcg	Graupel collecting rain droplets
prg_gcw	Graupel collecting cloud water droplets

The bulk mean properties of the OD_Kfe simulations can be used to infer cloud-scale responses to time-dependence. The mean, as a function of $w_{\text{equivalent}}$, was calculated between -8 and -38 °C for N_i and N_r , along with q_i , q_r , q_g , and q_s . The results are shown in Figure 5.9. λ -dependent variation can be seen at low and high updraught speeds, relative to $w_{\text{equivalent}} = \sim 3.5$, in all variables. All ice species are enhanced at low $w_{\text{equivalent}}$ when λ is small and enhanced at high $w_{\text{equivalent}}$ when λ is large. An enhancement in ice production enhances the depletion of rain, and therefore an opposite trend can be seen in rain. This shows that the variation in immersion mode ice production due to time-dependence impacts a cloud throughout its evolution.

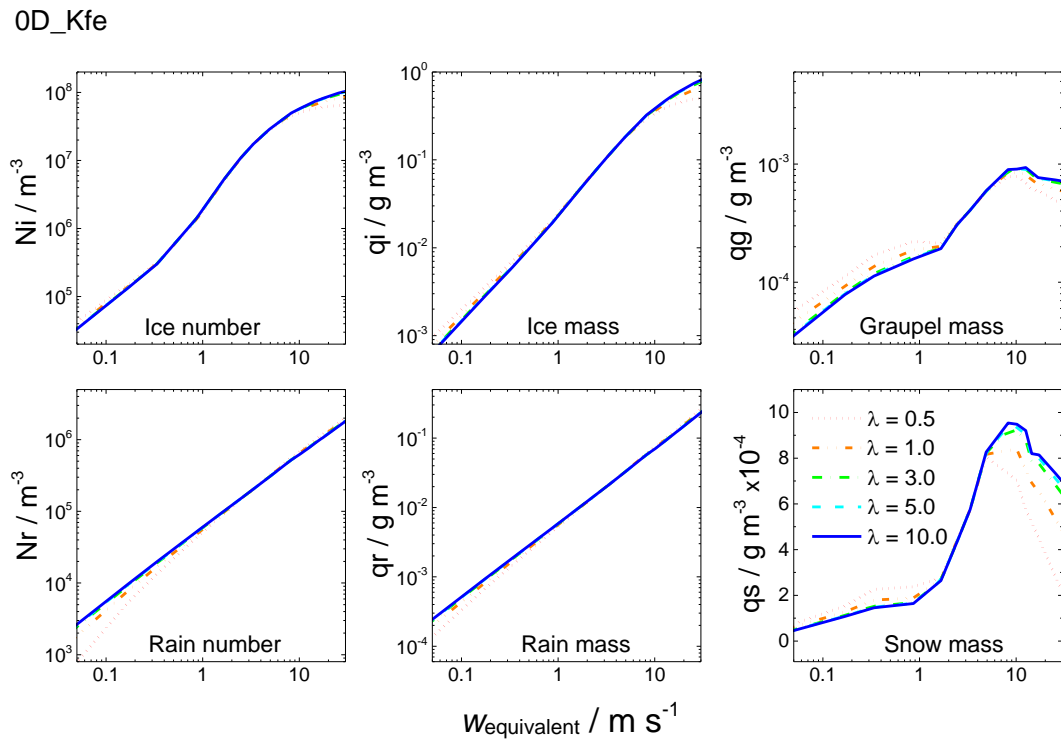


Figure 5.9. Mean number concentrations and mixing ratios for cloud hydrometeor species as a function of $w_{\text{equivalent}}$ and λ . Mean values determined between -8 and -38 °C.

The optical properties of clouds have a dependency on the mixing ratio of the species, the cloud depth, and the effective size of the hydrometeor species (Kokhanovsky, 2004). The simulations can therefore be used to qualitatively assess the significance of λ -dependence on radiatively important parameters. This is highlighted by the variation in the hydrometeor characteristic diameters shown in Figure 5.10. A characteristic diameter, D , was determined from the gamma size distribution following Straka (2010, pg. 20) as the reciprocal of the

distribution slope parameter. This value does not have a quantitative description but provides a simplified view of changes to the distribution, i.e., an increasing characteristic diameter may reflect a distribution shifting to larger sizes or an increasing distribution width. The sensitivity of D to changes in λ will provide evidence of an impact on the hydrometeor size distribution, and therefore potential radiative characteristics. Similar to the previous figure, the mean D for cloud water droplets, rain, and cloud ice was calculated between -8 and -38 °C. At low updraught speeds D_c decreases with a decreasing λ , whereas in high updraughts this is reversed. This relationship correlates with the variation seen in the LWC evolution in Figure 5.6. A similar relationship is seen in D_r at high updraught speeds and λ -dependence results in ~ 2 μm at 10 m s^{-1} and ~ 5 μm variation at 33 m s^{-1} . For D_i low values of λ result in the largest diameters at both extremes of updraught speed. At low $w_{\text{equivalent}}$ this is due to the earlier onset in ice production, whereas at high $w_{\text{equivalent}}$ this is a result of the variation in homogeneous freezing. A later onset of ice production results in more available liquid for homogeneous freezing, and thus acts to increase the mean diameter. This can be seen from the lack of *pri_who* data from the $\lambda = 5$ simulations in Figure 5.8. All three hydrometeor species show that time-dependence in the immersion mode has an impact on the mean radiative properties of the clouds.

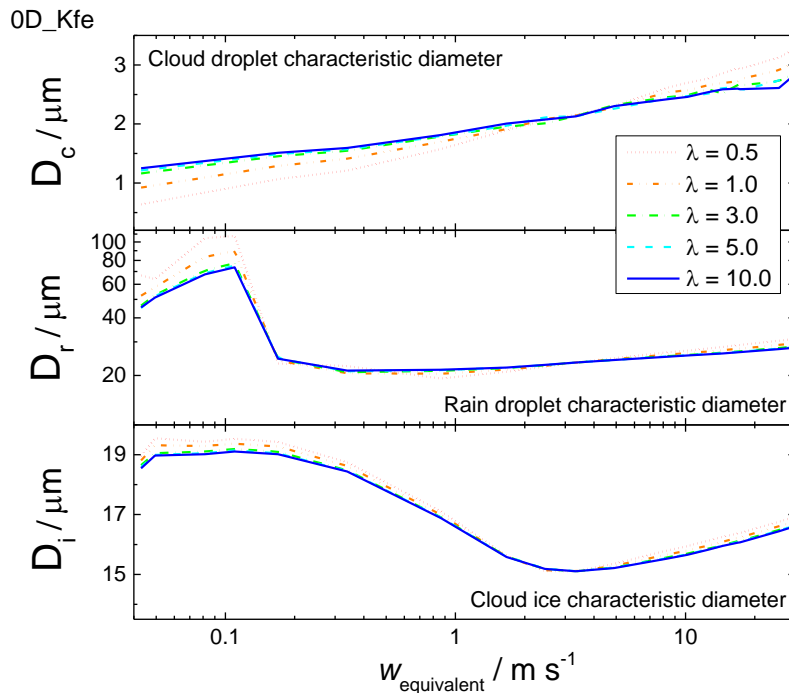


Figure 5.10. Same as Figure 5.9 but for the characteristic diameter of cloud droplets, rain droplets, and cloud ice.

To examine the dependence of these results on the chosen nucleation rate (K-feldspar) the nucleation rate of kaolinite mineral dust was also used in a series of simulations. This provides a contrasting case using a less efficient INP species. Figure 5.11 shows mean hydrometeor properties as in Figure 5.9. Kaolinite is a less efficient species than K-feldspar and therefore the immersion freezing rate is lower. This is reflected in the lower maximums of N_i , q_i , and q_g , and also explains why N_r and q_r are higher. Similar λ -dependent variations can be seen in all plots except for graupel, where a smaller value of λ results in an enhanced mean mixing ratio at high $w_{\text{equivalent}}$. This behaviour is due to an enhanced homogeneous freezing rate as a result of more available liquid at low temperatures. This shows that a relatively less efficient nucleation rate will lead to a smaller time-dependent effect on the cloud properties.

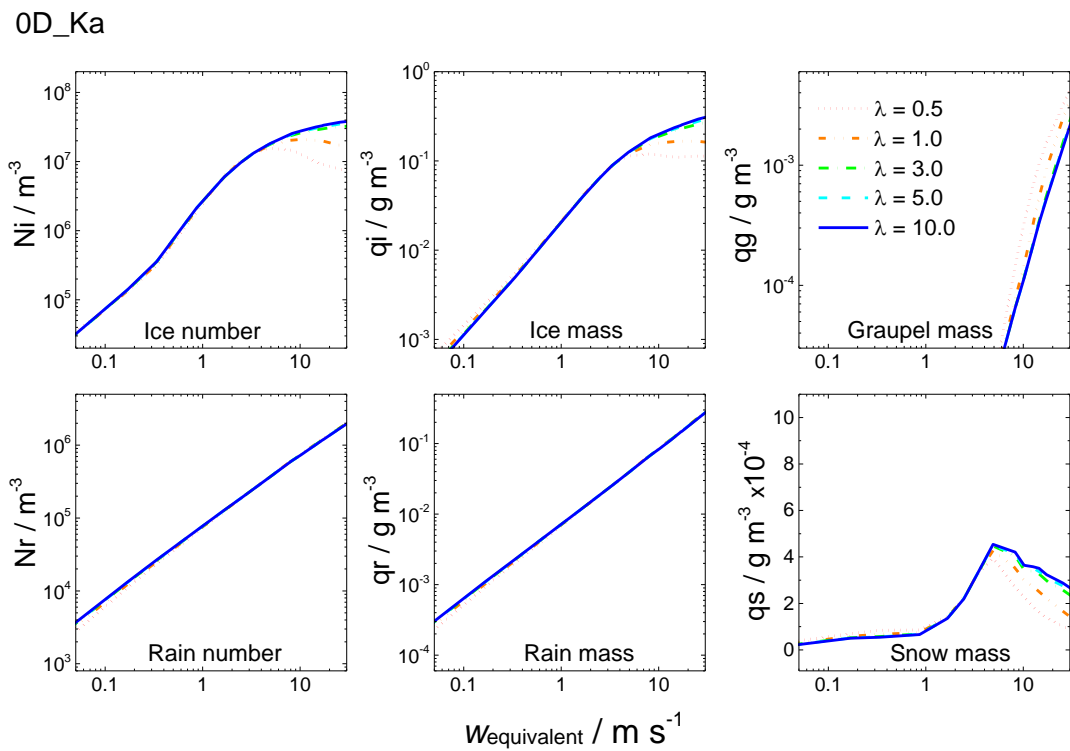


Figure 5.11. Mean number concentrations and mixing ratios for cloud hydrometeor species as a function of $w_{\text{equivalent}}$ and λ as in Figure 5.9 but for simulations using the nucleation rate of the mineral dust kaolinite. Mean values determined between -8 and -38 °C.

It is clear that the variation in immersion freezing rate from λ -dependence has a direct effect on the evolution of cloud ice in these simulations, and that a corresponding effect is also

seen in the other hydrometeor species. Importantly, the cloud lifetime varies considerably with λ at low updraught speeds, and the resulting IWC is also sensitive to λ , especially in clouds with high LWC. Estimates of the mean cloud hydrometeor diameters also show a considerable sensitivity to λ at both extremes of updraught speed. The variation in λ for atmospherically relevant INP species from Chapter 4 was in the range $0.4 \leq \lambda \leq 23$ which shows that the range of values being used here is representative.

5.4 1D Modelling Studies

The results from the previous 0D simulation will be re-examined using a series of 1D simulations with various mixed-phase cases. These simulations are more complex than the idealised simulations in that advection between cells can occur, and the prescribed dynamics vary in height and time.

Following the results from Sect. 5.3 in each set of simulations the λ -dependence will be examined through the variation in mixing ratio, LWC, IWC, and a column mean characteristic hydrometeor diameter. The total column mixing ratio, or mass path (MP), of each will be used as a proxy for mixing ratio. Similarly a liquid water path (LWP) and ice water path (IWP) will be used instead of LWC and IWC. The total cumulative number of liquid hydrometeors frozen via the immersion mode will also be presented as a function of simulation time.

5.4.1 Stratus Cases

5.4.1.1 Mixed1 – SHEBA Profile

The mixed1 case consists of oscillating updraughts and downdraughts, with a linearly increasing magnitude with height. The SHEBA profile is characterised by an inversion at ~500 m.

The results from the simulation are summarised in Figure 5.12 as the mixing ratios of cloud water, cloud ice, and snow. A variation with respect to λ is an indication that the time-dependence has an effect on the cloud's properties. After 30 mins the ice mass path (iMP)

shows large variation between $\lambda = 0.5$ and 5; this persists for a further 30 mins. The sudden decrease in iMP between 30 and 60mins is an artefact due to the 20 minute frequency in maximum updraught. At 6 hrs no ice is present during simulations for $\lambda < 0.5$. Snow follows a similar trend but is present at 6 hrs for all λ due to the combination of continued growth and slow sedimentation rates. Cloud water is not present below $\lambda = 0.5$, whereas above this value cMP increases substantially over the remaining λ values. Due to the low updraught speeds ($w_{\max} \approx 0.3 \text{ m s}^{-1}$) the immersion freezing rate is substantially enhanced at low values of λ . This is shown as an early burst in ice production, followed by a rapid collapse in the cloud water content, hence why $\text{cMP} = 0$ below $\lambda = 0.5$. Above this value immersion freezing does not out-compete the cloud water production and ice is produced throughout the simulation. As λ increases, the ice production rate decreases and the iMP also decreases. For $\lambda \geq 2$ an equilibrium in iMP appears to be reached after 60 mins. These results show that this stratus case is sensitive to λ , and that changes to the immersion mode freezing rate affect the development of other hydrometeor species.

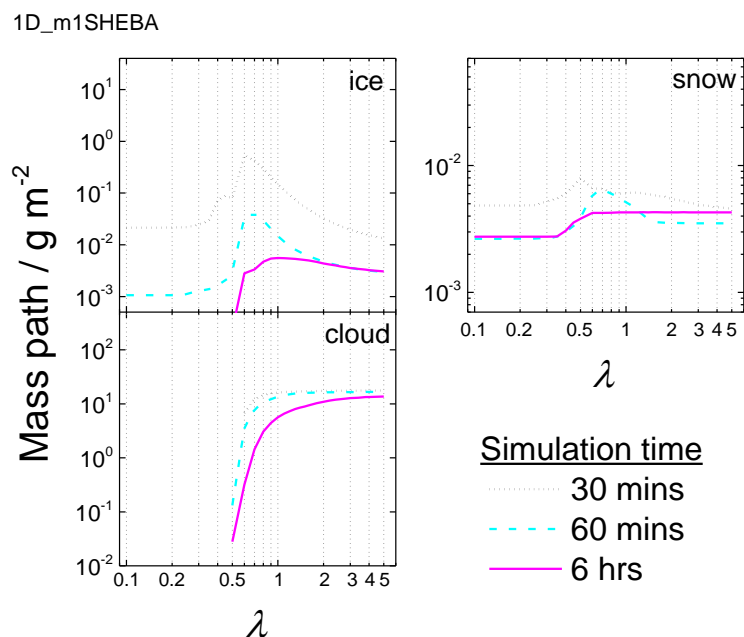


Figure 5.12. 1D_m1SHEBA simulations: Total column mass path of cloud ice, snow, and cloud water as a function of λ determined after 30 mins (dotted line), 60 mins (dashed line), and 6 hrs (solid line).

The sensitivity to λ can also be seen in the IWP and LWP evolution shown in Figure 5.13 for four values of λ . In the $\lambda_{0.5}$ simulation the IWP rapidly reaches a maximum of 4 g m^{-2} due to immersion freezing and then within 40 mins is $\sim 0.1 \text{ g m}^{-2}$. Correspondingly, the

LWP decreases rapidly to 0, showing that the cloud has fully glaciated. As λ increases the IWP maximum decreases, but a mixed-phase state persists for longer periods of time. After 6 hrs in the $\lambda_{1.0}$ simulation the IWP = 0.03 g m⁻² and LWP = 5 g m⁻², and in the $\lambda_{4.0}$ simulation IWP = 0.015 g m⁻² and LWP = 14 g m⁻². This demonstrates a substantial dependence of key cloud radiative properties on the time-dependence of the immersion mode INP species.

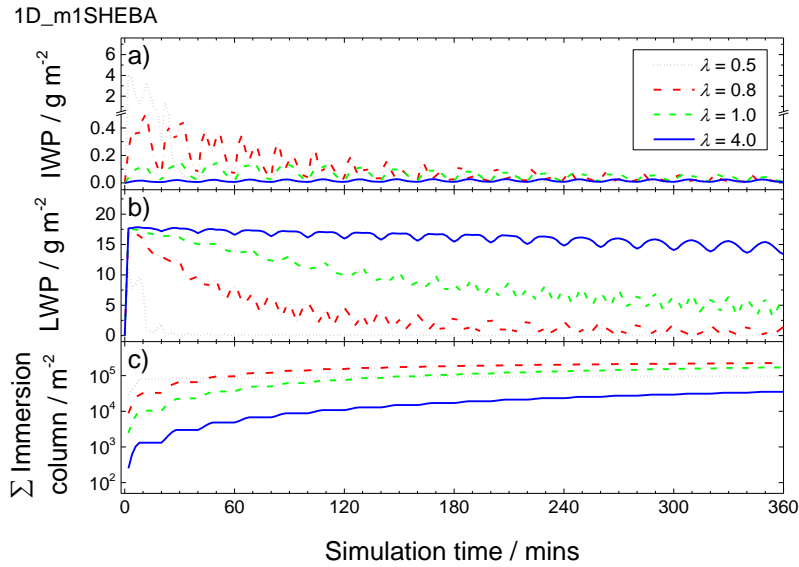


Figure 5.13. 1D_m1SHEBA simulations: evolution of IWP, LWP, and cumulative number of liquid droplets frozen as a function of simulation time for a range of λ .

5.4.1.2 Mixed3 – SHEBA Profile

The mixed3 case is characterised by a low-level oscillating updraught and downdraught with $w_{\max} = 0.17 \text{ m s}^{-1}$, and additionally by a constant prescribed q_v forcing, with which a steady rain-rate is expected. Figure 5.14 shows the λ -dependent total column mass paths of the five hydrometeor species and Figure 5.15 shows the evolution of the IWP and LWP.

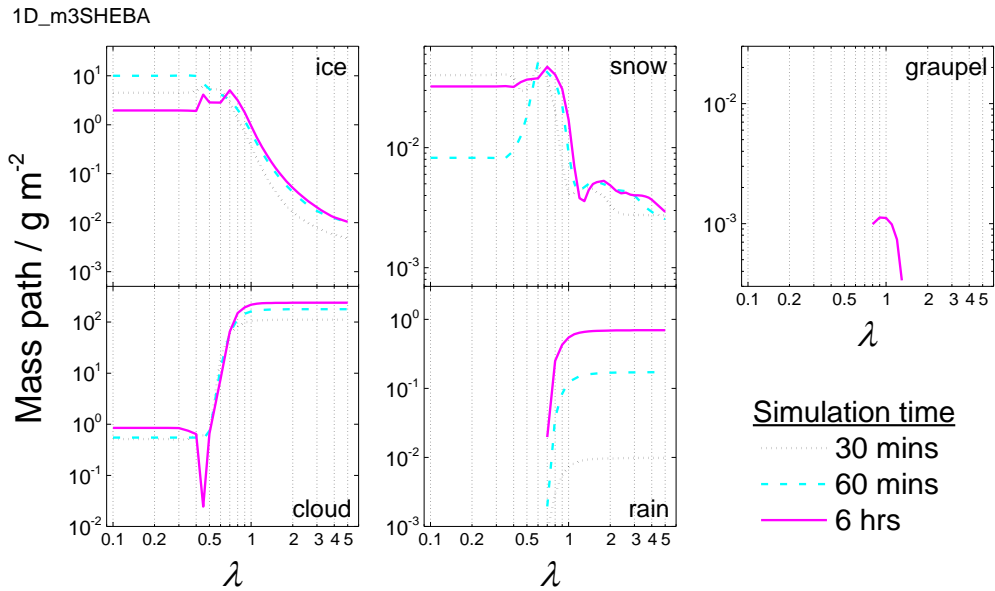


Figure 5.14. Same as Figure 5.12 but for 1D_m3SHEBA simulations.

Similar to the 1D_m1SHEBA simulations, below $\lambda = 0.5$ the production of ice via the immersion mode is enhanced to such a degree that all newly condensed water is immediately frozen. This suppresses droplet growth and as such suppresses the production of rain; this is highlighted in Figure 5.15 by the evolution of the IWP and LWP for $\lambda = 0.5$. Between $\lambda = 0.5$ and 0.7 a transition period is observed where the immersion mode freezing rate starts to decrease and the cMP increases by nearly two orders of magnitude. Above this value of λ rain is present and rapidly increases, whilst the iMP decreases by over two orders of magnitude at $\lambda = 5.0$. A rapid decrease in sMP between $\lambda = 0.7$ and 1 is also observed. Due to the prescribed forcing of q_v in all simulations where $\lambda > 0.7$ a steady mixed-phase state is reached after ~ 2 hrs of simulation; this can be seen in Figure 5.15. The steady-state LWP and IWP are dependent on λ , with an increasing magnitude leading to higher and lower values, respectively. This case demonstrates a distinct change in regime between INP species exhibiting strong (small λ) and weak (large λ) time-dependent behaviour. All hydrometeor species varied by around two orders of magnitude, simply due to the time-dependence of immersion mode freezing.

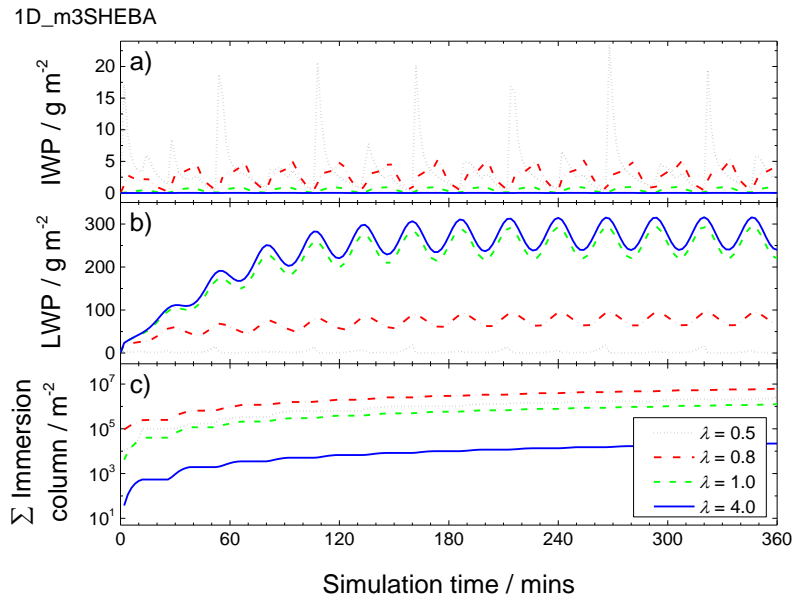


Figure 5.15. Same as Figure 5.13 but for 1D_m3SHEBA simulations.

5.4.1.3 Comparisons to M-PACE Profile

The two cases, mixed1 and mixed3, were additionally run using the M-PACE profile shown in Figure 5.1 in order to expand on the results from the previous mixed-phase stratus cases. The λ -dependent variation of IWP, LWP, D_c , and D_i were determined from the simulations and are presented together with the SHEBA simulations in the following figures.

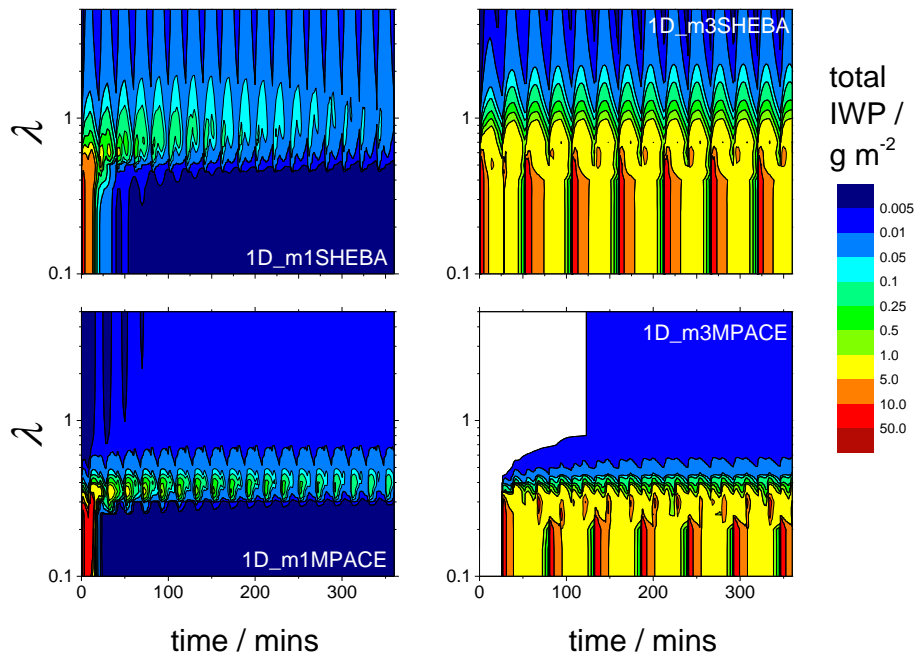


Figure 5.16. Comparison of IWP evolution as a function of λ for the four 1D stratus cases. All plots share the same contour range.

The IWP provides information on how the cloud ice hydrometeors evolve throughout the simulation. The IWP data from the SHEBA simulations are summarised alongside data from the M-PACE simulations in Figure 5.16. In all cases there is considerable λ -dependent variability as well as distinct regime changes dependent on λ . An offset in λ between the M-PACE and SHEBA simulations can be seen, which has an effect on the resulting value of λ at which the regime changes occur. The offset occurs due to the colder SHEBA profile; the nucleation rate exponentially increases with temperature, and therefore any variations due to time-dependence will be similarly enhanced. This behaviour is analogous to using a less efficient nucleation rate as observed in the 0D simulations. This result shows that the effect that time-dependence has on the developing cloud is dependent on temperature as well as the characteristic value of λ . The sensitivity to λ is highlighted by the distinct regime changes.

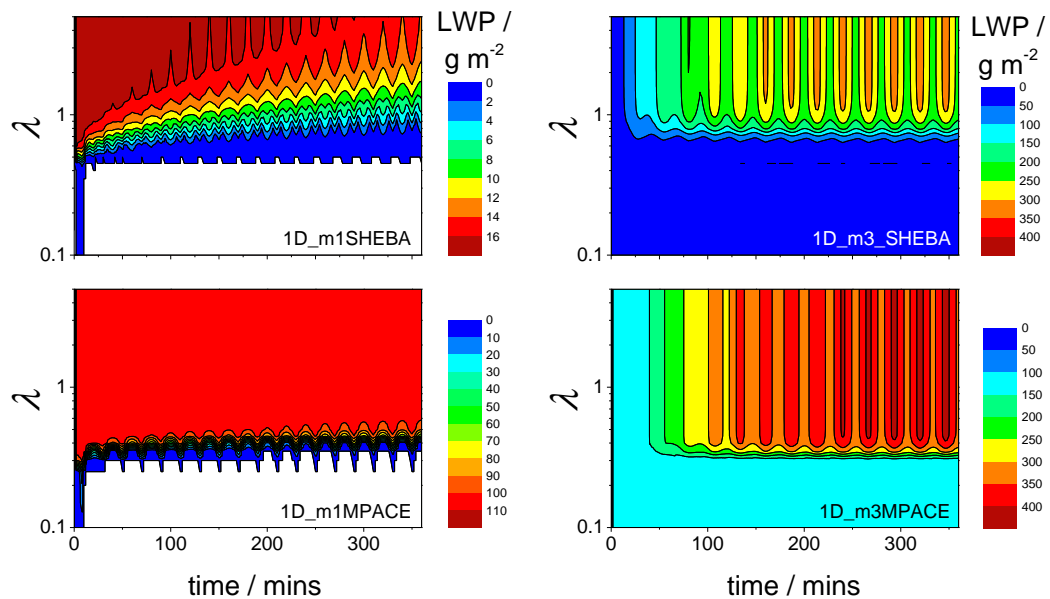


Figure 5.17. Same as Figure 5.16 but for LWP. Contours ranges are unique to each case.

Mixed-phase arctic stratus have been found to persist for long periods (hours to days) of time (Rogers et al., 2001; Uttal et al., 2002; Shupe et al., 2010; Morrison et al., 2012). The evolution of the LWP can be used to understand the impact of immersion mode time-dependence on the persistence of these clouds. Figure 5.17 shows the LWP data. There are distinct differences between the two cases due to the prescribed forcing of q_v in the mixed3 case. Without this forcing the LWP quickly reaches a maximum and then decreases with time. The maximum, and rate of decrease, are both dependent on λ . With the forcing applied

a steady, if not increasing LWP is reached which is independent of λ apart from where rain is suppressed by enhanced freezing rates. Again, similarities between profiles can be seen. The results suggest that nucleation by a strongly time-dependent species ($\lambda < \sim 0.5$) will rapidly deplete all liquid water and glaciate the cloud. However, with weaker time-dependent species ($\lambda > \sim 1$) the cloud may persist for periods of time closer to the observations. de Boer et al. (2009) summarised observations from several campaigns and showed that arctic stratus have LWP values ranging from near zero to $>300 \text{ g m}^{-2}$, with the mean varying between location and season. This makes it difficult to compare the results to observations.

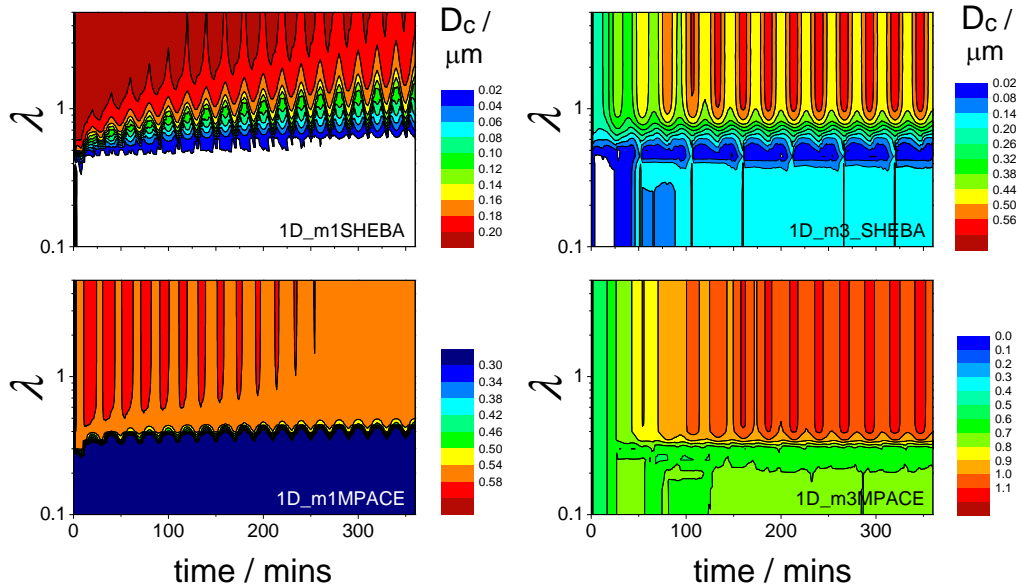


Figure 5.18. Same as Figure 5.16 but for the column mean characteristic diameter of the cloud water droplet distribution. Contour ranges are unique to each case.

Along with IWP and LWP, radiatively important properties of the cloud in each simulation can be inferred from the characteristic diameter of the hydrometeors. The mean cloud droplet characteristic diameter, shown in Figure 5.18, describes a similar λ -dependence as observed with the LWP. Most significantly distinct regimes can be seen, which could result in either a large radiative effect or a negligible radiative impact, i.e., cloud vs no cloud. The D_i values in Figure 5.19 show variability with respect to time as a result of the rapid ice production at cloud tops. Similar to D_c the sensitivity of D_i to λ is primarily made apparent from significant regime changes as a result of rapid glaciation at low λ values. A degree of

λ -dependence can be seen in all cases, but it is the regime changes that appear to dominate the λ -dependence. In combination with the variability in IWP and LWP (Figures 5.16 and 5.17) this could have significant radiative effects that could be explored in future work.

These simulations provide evidence that the evolution of arctic stratus and their resulting properties are sensitive to the characteristic value λ of the INP population. In these simulations the persistent behaviour of the clouds is due to a slow weakly time-dependent (large λ) production of ice; the slow production limits the glaciation of the cloud. However, in these simulations it is assumed that the INP population is dependent on the mass of cloud droplets, and therefore INP depletion does not occur as would be expected in the atmosphere.

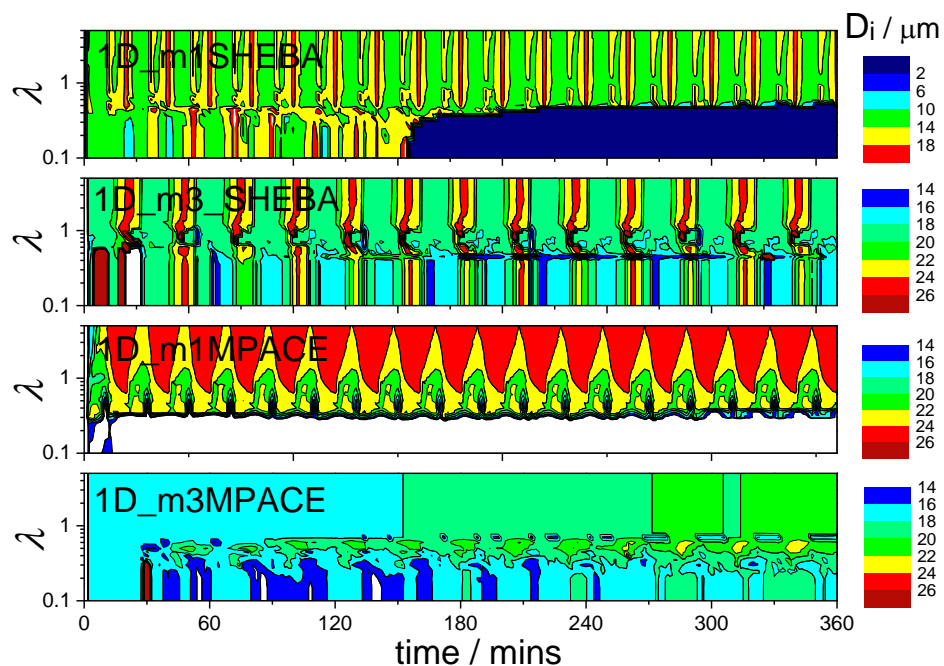


Figure 5.19. Same as Figure 5.16 but for column mean characteristic diameter of the cloud ice size distribution.

5.4.2 Convective Cases

5.4.2.1 Deep1 Convective Case ($w_{\max} = 10 \text{ m s}^{-1}$)

A series of simulations using deep convective cases were performed to test the λ -dependence at higher updraught speeds. The 0D sensitivity studies showed that at high w

the freezing rate was suppressed when λ was small (i.e., strongly time-dependent). Therefore in the deep convective case the hypothesis is that iMP will increase with increasing λ .

The deep1 case is characterised by a constant updraught centred at an altitude of 5 km, which corresponds to a temperature of $\sim 0^\circ\text{C}$ in the prescribed temperature profile. Figure 5.20 shows the mass paths for cloud ice, snow, cloud, and rain as a function of λ . Contrary to the initial hypothesis the iMP decreases with an increasing value of λ . This occurs because the upper-level of the convective cell has a weakening updraught speed and also a colder temperature. Therefore, although $w_{\text{max}} = 10 \text{ m s}^{-1}$, the largest contribution of droplets frozen via the immersion mode occurs at the top of the cell where $w < w_{\text{max}}$. In this case it is clear that there is much less sensitivity to λ than in the stratus cases. In the deep1 case the iMP decreases by a factor of ~ 4 upon a change from $\lambda = 0.1$ to 5, whereas the same change resulted in factor of ~ 100 change in iMP for the stratus cases. A comparable effect is also seen in the other hydrometeor species. This highlights that at higher updraught speeds there is much less sensitivity to time dependence.

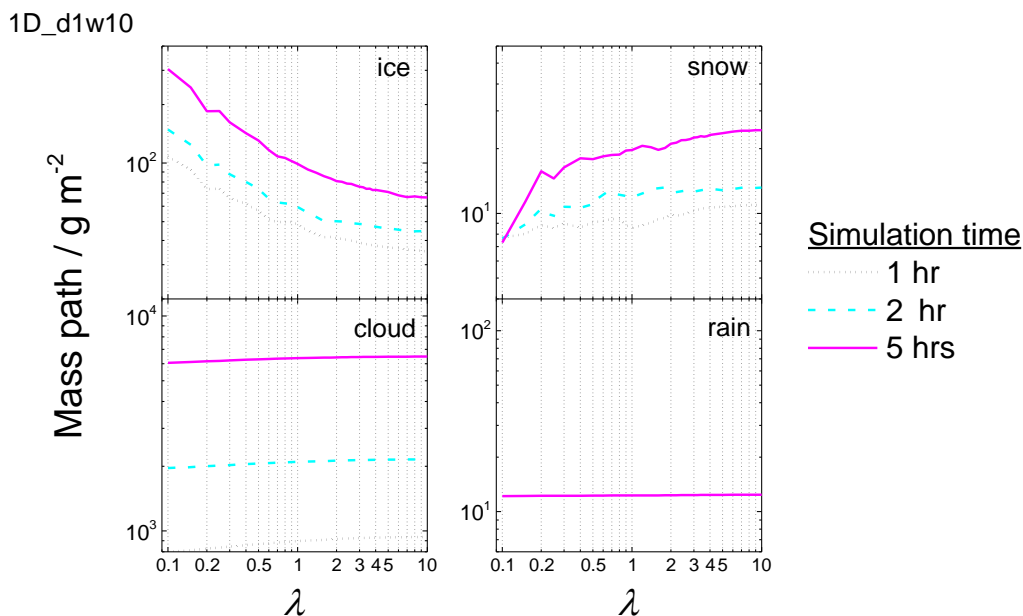


Figure 5.20. 2D_d1w10 simulations: total column mass path of cloud ice, snow, and cloud water as a function of λ determined after 30 mins (dotted line), 60 mins (dashed line), and 6 hrs (solid line).

5.4.2.2 Comparison to Slowly Ascending Clouds ($w_{\max} = 5 \text{ cm s}^{-1}$)

A second set of simulations were performed using the deep1 case where w_{\max} was decreased to 5 cm s^{-1} . This will provide information on how λ -dependence varies with updraught speed and also provides a case of slowly ascending clouds. The simulated mass paths at 5 hrs have been plotted in Figure 5.21 along with those from the $w_{\max} = 10 \text{ m s}^{-1}$ simulations. There is a clear distinction between the two sets of simulations; the weak ascent simulations show substantially more λ -dependence as made apparent by the increased iMP sensitivity. The variability in iMP consequently impacts the cloud water content and both D_c and D_i . A comparison to D_c and D_i in the strong convective simulations shows very little sensitivity to λ . This suggests that as w_{\max} increases the cloud becomes less sensitive to time-dependence in the immersion mode.

To examine this behaviour further, a series of simulations were performed where w_{\max} was systematically increased from 0.04 to 40 m s^{-1} . For each w_{\max} two simulations were performed where a value of $\lambda = 0.5$ and 4 was used. The difference in mass path between the two values of λ at a simulation time of 3 hrs was used to examine the λ -dependent variability at different updraught speeds. Figure 5.22 shows the resulting data for ice, snow, cloud, and D_c . The results show that as w_{\max} increases the difference between each species decreases and converge. As discussed earlier upon further increases in w_{\max} the two simulations would be expected to diverge, reflecting the relative enhancement of immersion freezing in the high λ simulation. These results show that the sensitivity to time-dependence decreases as updraught speed increases, which corresponds to the 0D simulation results.

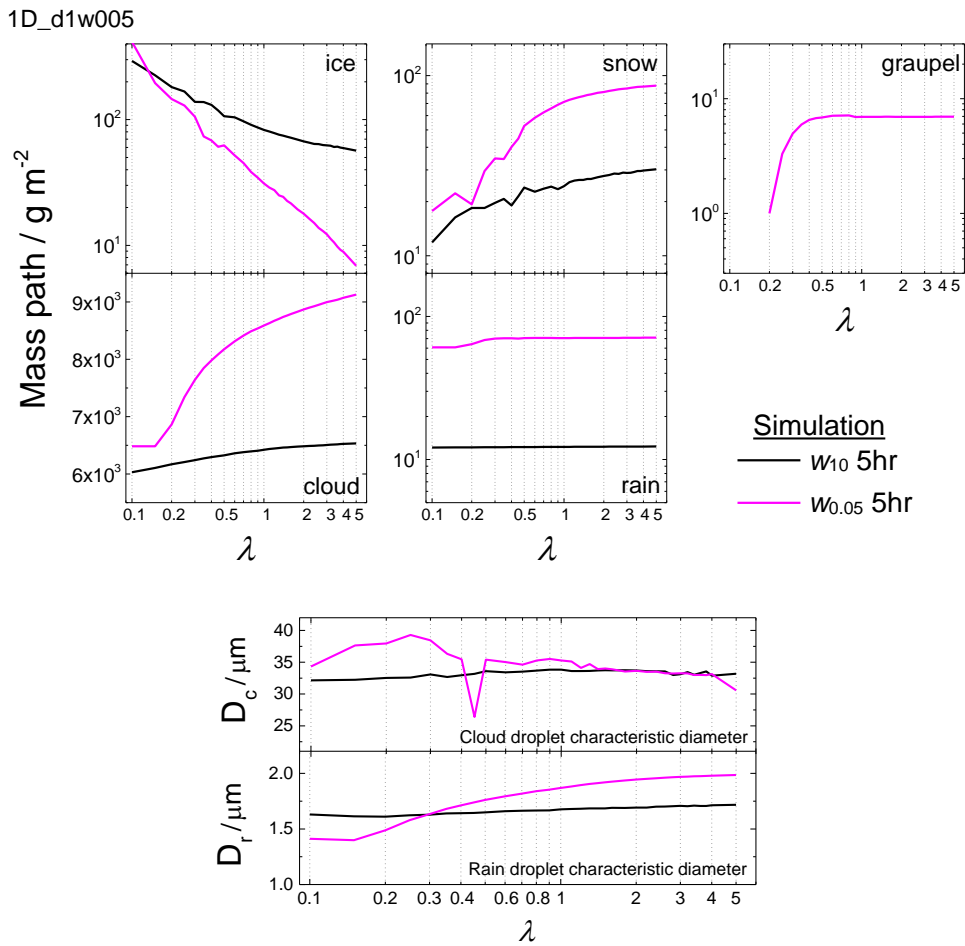


Figure 5.21. Same as Figure 5.20 but showing a comparison between the 1D_d1w10 and 1D_d1w005 simulations. The column mean cloud and rain droplet characteristic diameter is also included.

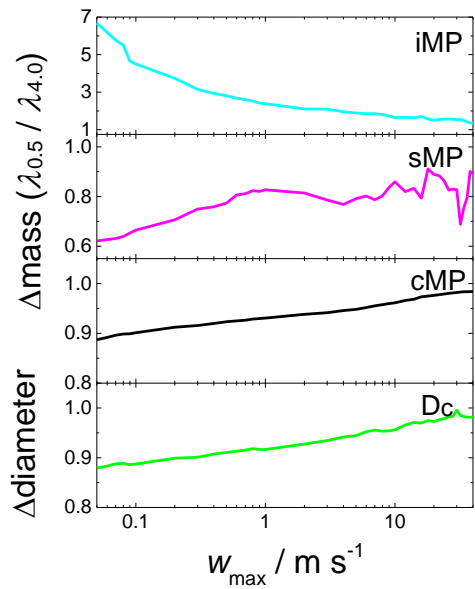


Figure 5.22. The fractional difference of iMP, sMP, cMP, and D_c at 3 hrs between simulations where $\lambda = 0.5$ and $\lambda = 4.0$ as a function of w_{max} using the deep1 case. A tendency towards 1 describes a decreasing sensitivity to λ .

5.4.2.3 Deep2 Case

The deep2 case uses the same prescribed profile of θ_T and q_v as deep1, but dynamics are characterised by a transient deep convective cell with $w_{\max} = 20 \text{ m s}^{-1}$ varying in height and time, as shown in Figure 5.1. There is no q_v forcing in this case.

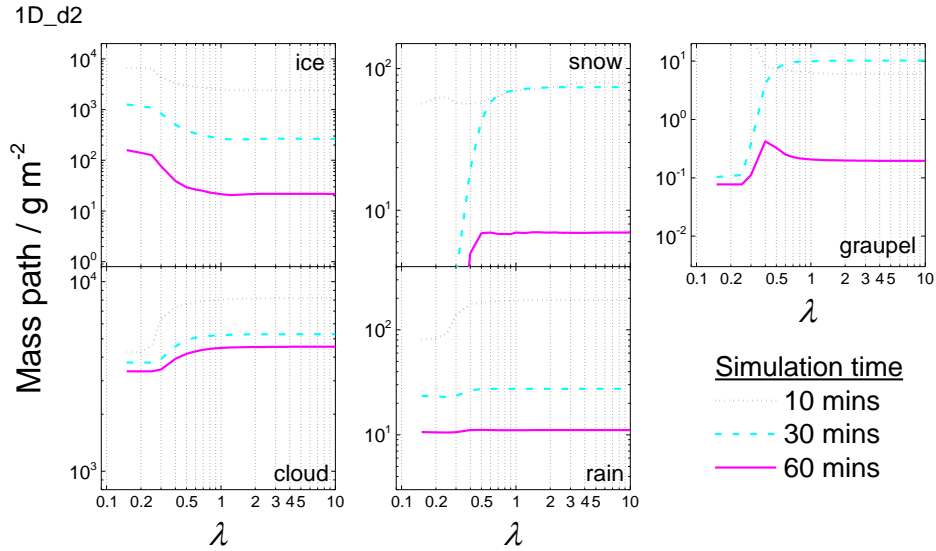


Figure 5.23. 1D_d2 simulations: total column mass path of cloud ice, snow, and cloud water as a function of λ determined after 30 mins (dotted line), 60 mins (dashed line), and 6 hrs (solid line).

The cloud hydrometeor mass paths are shown in Figure 5.23 as a function of λ . In this case there is only time-dependent behaviour observed when $\lambda < \sim 0.5$. Above this the mass path of each species is nearly constant. As with the deep1 case, immersion mode freezing (not shown) predominantly occurs within the upper-levels of the updraught region where $w \approx 10 \text{ m s}^{-1}$ but is also enhanced around the updraught edges (where $w \approx 1 \text{ m s}^{-1}$) when λ is small. This shows that the presence of a strongly time-dependent INP species in a cloud may switch on ice production in regions where weakly time-dependent INP species do not. In these simulations the HM process was not active, but in slightly colder cases secondary ice production mechanisms such as the HM process could be impacted.

The results from the deep1 and deep2 simulations show that at high updraught speeds time-dependence does not play a significant role in the resulting cloud properties unless the INP species is strongly time-dependent. The results also suggest that ice forming in weakly

ascending clouds ($w \approx 5 \text{ cm s}^{-1}$) will have a substantial dependence on λ . This supports the findings from the stratus cases.

5.5 2D Modelling Studies

In these simulations the dynamics and initial values of θ_T and q_v are prescribed on a 2D domain as shown in Figure 5.3. A mixed-phase stratocumulus case and a deep convective case will be used to examine the λ -dependence following the results from the 0D and 1D simulations.

5.5.1 Stratocumulus ISDAC Case

The stratocumulus case is characterised by an updraught and downdraught cell with a linearly decreasing temperature profile. The upper-levels of both cells are saturated with respect to water.

The 1D stratus simulations provided evidence that the development and resulting properties of these clouds are sensitive to the time-dependence of the INP population. These simulations are more complex and will be used to test the results from the 1D cases. A simulation was performed for each prescribed value of λ ($0.1 \geq \lambda \geq 5$). The horizontally averaged mixing ratio profiles of cloud ice and snow for three of the simulations are shown in Figure 5.24. Each colour represents a different simulation and thus λ . Throughout the evolution of the cloud the ice mixing ratio q_i shows a substantial λ -dependence. Above 150 m there is a four order-of-magnitude difference in q_i between $\lambda = 0.2$ and 1.0. Snow also shows a comparable difference at the beginning of the simulation but at the end of the simulation (2 hrs) the difference is ~ 2 orders-of-magnitude. The apparent enhanced evolution of snow, as compared to the $\lambda = 0.2$ simulation, is due to the increased sedimentation rate in the $\lambda = 0.2$ simulation. These differences represent a significant effect on the cloud properties, including precipitation and potential radiative effects.

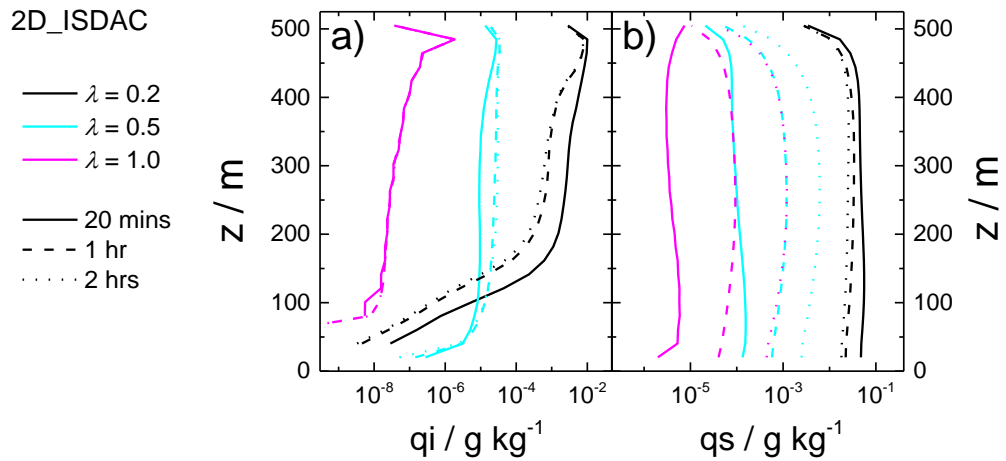


Figure 5.24. Horizontally averaged mixing ratio profiles for cloud ice and snow from the 2D_ISDAC simulations. Solid, dashed, and dotted lines correspond to simulation times of 20, 60, and 120 minutes, respectively. The different colours correspond to different values of λ .

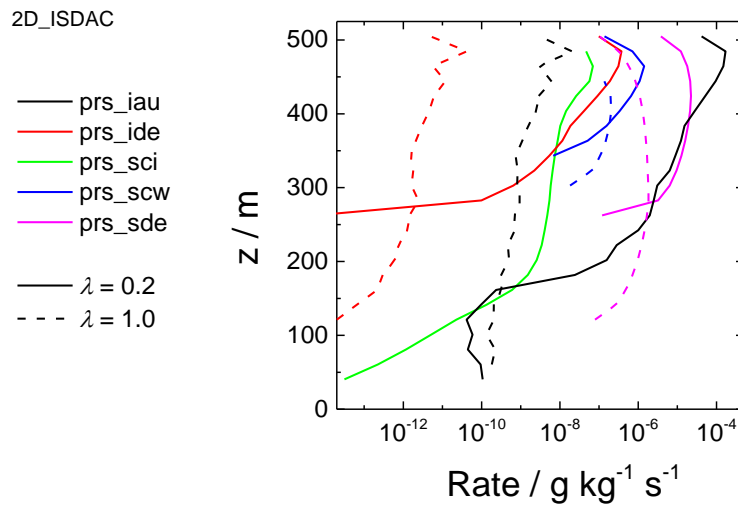


Figure 5.25. Horizontally averaged growth rate profiles for different sources of snow mass from the 2D_ISDAC simulations after 2 hrs. Solid lines correspond to simulations where $\lambda = 0.2$ and dashed lines where $\lambda = 1.0$. Variable descriptions can be found in Table 5.3

From Figure 5.24 it is clear that in these simulations snow constitutes the largest component on the ice water content. To understand how the growth of snow is affected by λ the snow mass growth sources have been plotted in Figure 5.25. The results show that the autoconversion of cloud ice and the depositional growth from the vapour are the largest source terms. Growth by the collection of water droplets is not significant in this simulation. These results show that a direct effect on the cloud ice distribution (through enhanced or suppressed immersion mode freezing) will have an equivalent effect on the snow mass, hence why comparable λ -dependent differences are seen between ice species in Figure 5.24.

This is important as a strong correlation between cloud ice production and total ice water content is evident.

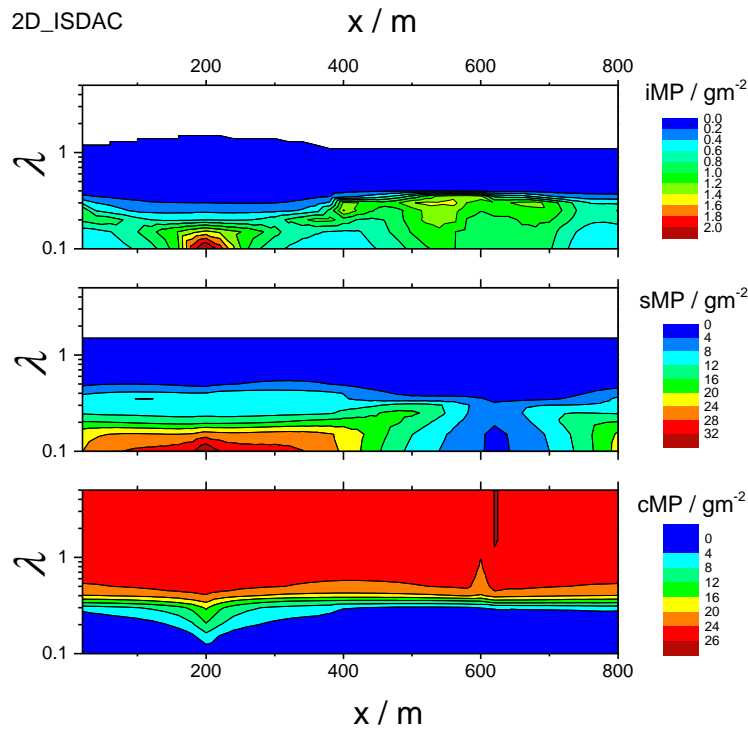


Figure 5.26. Cloud ice, snow, and cloud water mass paths as a function of λ in the 2D_ISDAC simulations.

To understand the sensitivity to λ the mass path of cloud ice, snow, and cloud water after 2 hrs is shown in Figure 5.26 as a function of λ . As also seen in the 1D stratus cases distinct regimes are apparent. Above values of $\lambda \approx 1.5$ the immersion mode freezing rate is suppressed to such a degree that ice production is not initiated and the cloud remains liquid. Below $\lambda \approx 1.5$ there is a strong dependence on λ , especially within the updraught region where an increase in λ from 0.2 to 1 results in over an order of magnitude decrease in iMP and sMP. Similar to the 1D stratus cases, a strong sensitivity to λ is observed in these simulations.

In order to understand how the nucleation rate of the INP population affects the sensitivity to λ the simulations were also performed using the nucleation rate of kaolinite, rather than the default, K-feldspar. The λ -dependent effects on the iMP, sMP, and cMP are shown in Figure 5.27. On comparing to Figure 5.26 it can be seen that the variation from λ is systemically shifted to lower values of λ . This is a result of kaolinite exhibiting a weaker

nucleating efficiency relative to K-feldspar; at a specific temperature the kaolinite simulation will have a relatively lower ice production rate. The apparent ‘offset’ in variation is observed because a decrease in λ counteracts the reduced nucleation rate. A similar response can be expected for changes in the temperature profile. This simulation highlights two points: first, the efficiency of the nucleating species will to a degree impact it’s λ -dependence with more efficient species exhibiting a greater sensitivity to λ ; and secondly, the sensitivity to λ will increase with decreasing temperature.

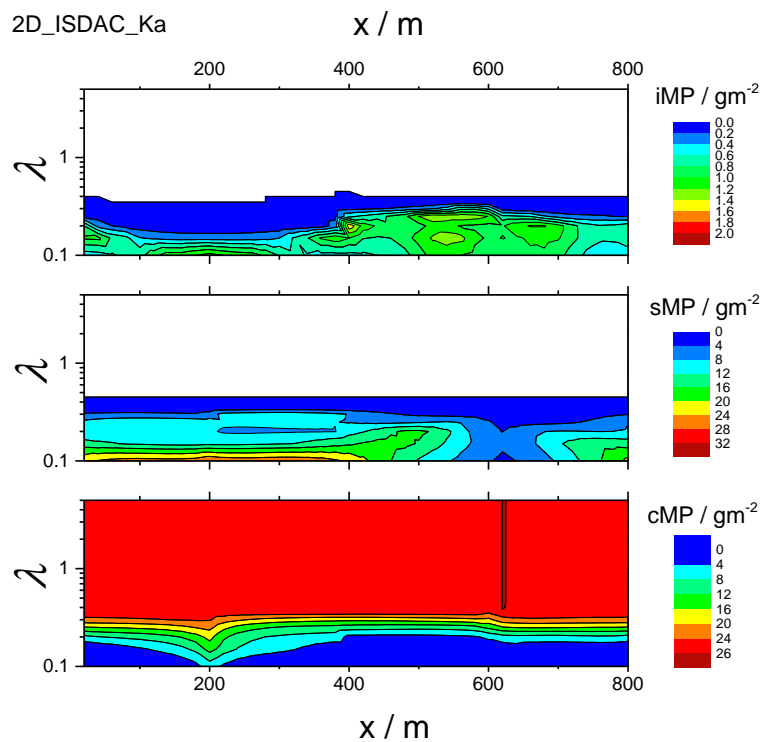


Figure 5.27. Same as Figure 5.26 but for simulations using the nucleation rate of the mineral dust kaolinite.

As with changes to the nucleation rate, a change to the available surface area per droplet will affect the probability of freezing, and therefore enhance the ice production rate. This was examined further by increasing the available surface area per droplet by a factor of 100 in the model. For these simulations the K-feldspar nucleation rate was used. The λ -dependence, shown in Figure 5.30, follows the conclusions of the previous example; the increased surface area has enhanced the ice production rate and as such the mass of the hydrometeor species are now more sensitive to λ . In this simulation the variation has again been offset, but towards high values of λ whereas the kaolinite simulation was towards

lower values of λ . As well as supporting the conclusions from the kaolinite simulation, this additionally shows that the surface area per droplet is an important factor in λ -dependent variation to the cloud properties.

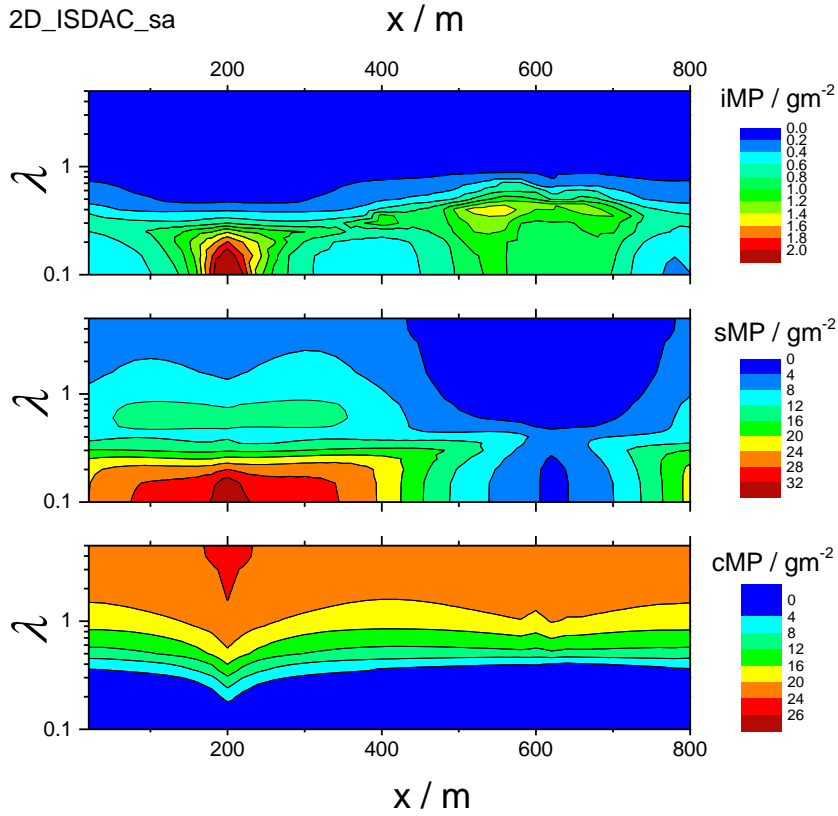


Figure 5.28. Same as Figure 5.26 but for simulations using a surface area per droplet s_{K-fe} of 1×10^{-7} ; a factor of 100 increase from the default.

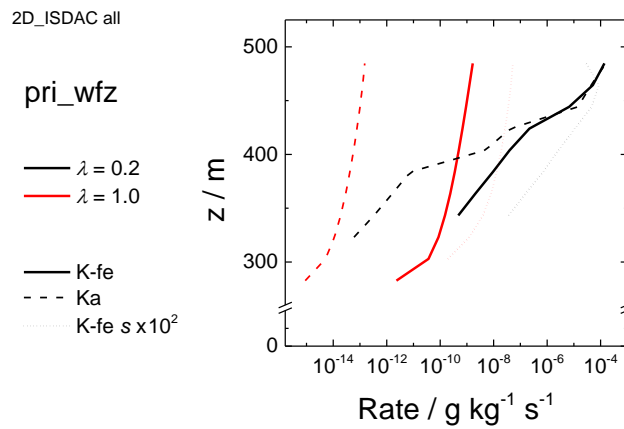


Figure 5.29. Comparison of horizontally averaged immersion mode freezing rate profiles between the three sets of simulations using the 2D_ISDAC case. Black and red lines correspond to $\lambda = 0.2$ and $\lambda = 1.0$, respectively.

The sensitivity to changes in the nucleation rate and s were looked at further to understand how these changes impact the growth and interaction of the hydrometeor species. The effect on immersion mode freezing rates is shown in Figure 5.29. With a value $\lambda = 1.0$ the freezing rate profiles systemically shift, whilst for $\lambda = 0.2$ the lower half of the profile shows the same comparable shift but the upper half does not change considerably. The lack of variation upon a change in s and nucleation rate suggests that the immersion mode freezing rate has already reached a maximum due to the low value of λ . The impact that the variation in s has on the growth of snow is demonstrated in Figure 5.30. The growth rates for $\lambda = 0.2$ show little change, which corresponds to the small change seen in the ice production rates. However, for the simulations where $\lambda = 1$ the increase in s substantially affects the growth rate of snow through all processes. This suggests that the weaker time-dependent INP species are more sensitive to changes in the nucleation rate and surface area than those with a strong time-dependence. However, this sensitivity is difficult to quantify without extensive simulations with different cases.

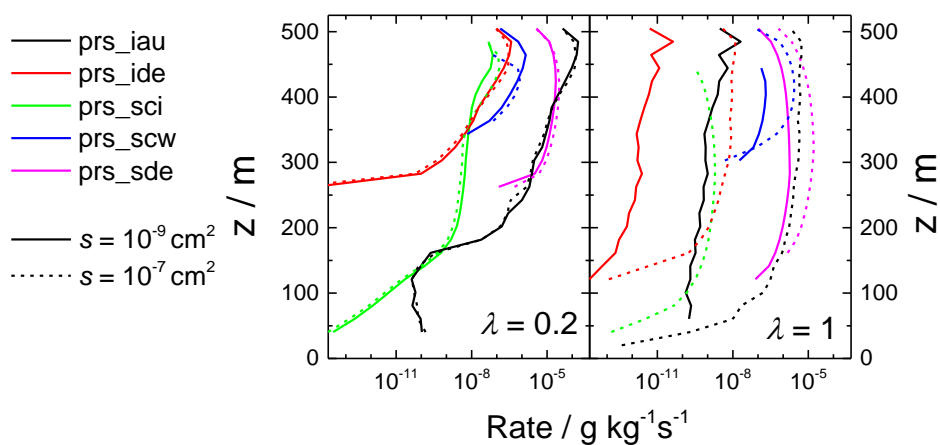


Figure 5.30. A comparison of horizontally averaged growth rate profiles for snow between simulations where the surface area per droplet s was increased by a factor of 100. Data obtained after 2 hrs of simulation. Solid lines correspond to the 2D_ISDAC_Kfe simulation, and dotted lines to the 2D_ISDAC_sa simulation.

These results provide additional evidence that time-dependence plays a substantial role in the resulting cloud properties of mixed-phase stratus clouds where updraught speeds are low, in this case $w_{\max} < 1 \text{ m s}^{-1}$.

5.5.2 Squall Line Case

The final case is of a deep convective cell within a squall line described in Slawinska et al. (2009). The convective region in the prescribed domain consists of a saturated 9 km deep convective cell with $w_{\max} = 10 \text{ m s}^{-1}$ and a freezing level at $\sim 4 \text{ km}$. In these simulations λ was varied between 0.1 and 10. Through prior testing it was found that the simulation reached a steady-state after 6 hrs, and hence 6 hrs was used as the total simulation duration.

In the 0D simulations the sensitivity to λ was apparent at both extremes of w , whereas the 1D deep cases show that as w increased the sensitivity to λ decreased. The difference in the 1D simulations was explained by the domination of ice production in cloud top regions where w was low. In this 2D case freezing is expected to occur in regions other than the cloud top and so provides a more realistic deep convective case. The evolution of the cloud iMP as a function of λ is shown in Figure 5.31. Initially λ -dependence is only seen below $\lambda = 0.5$ but as the simulation progresses a clear dependence is seen at all λ . At the end of the simulation when a steady state has been reached the highest iMP values are found at high values of λ at 40 km, and also at very low values of λ at 50 km. The maximum at high values of λ corresponds to ice production in the core updraught region; as seen in the 0D sensitivity studies at an updraught speed of 10 m s^{-1} the immersion mode ice production rate is suppressed at low values of λ . Hence a higher value of λ leads to an increased ice production rate. Conversely, the maximum at low values of λ corresponds to the saturated, low updraught, region on the edge of the updraught core. The large variation from changes to λ shows that time-dependence has a substantial impact on the primary production of cloud ice in this case.

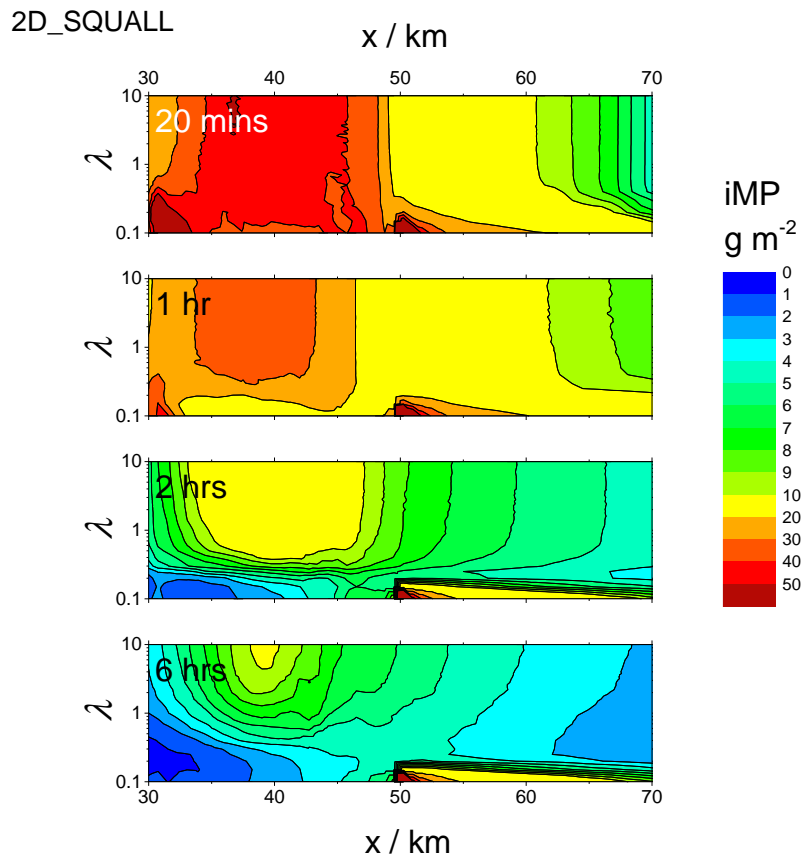


Figure 5.31. Ice mass path as a function of λ throughout the evolution of the cloud. At 6 hrs the simulation has reached a steady-state. Data from 2D_SQUALL simulations.

The sources of cloud ice production and growth are shown in Figure 5.32 for the simulations where $\lambda = 0.5$ and 4.0 . The dominant source of ice is from the immersion mode freezing of water droplets and rain. At the top of the cloud the immersion mode competes with homogeneous freezing of rain and both have similar production rates. In the $\lambda = 4.0$ simulations the production rates show very little change. The differences that are present are due to the regions in which ice is dominantly produced, i.e., ice production in the core updraught is suppressed when λ is low but conversely enhanced in the updraught edges as seen in the 0D simulations. Secondary-ice production through the Hallett-Mossop process is active near the base of the cloud but is independent of λ . The same simulations were performed with deposition mode ice nucleation switched on; the ice production rate through this mode was negligible and played no role the sensitivity to λ . In this case the immersion mode is the dominant source of cloud ice production which is why there is a strong sensitivity to λ in the iMP.

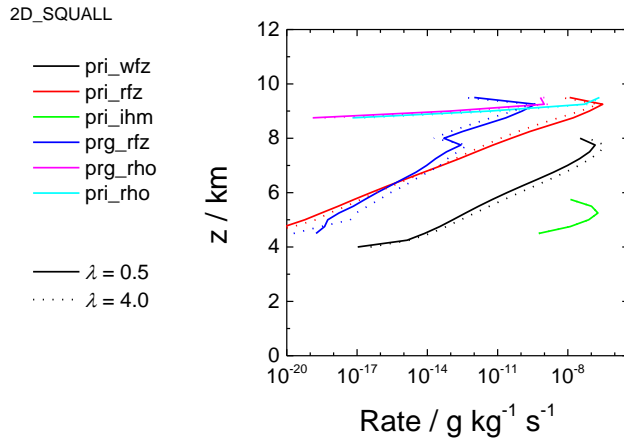


Figure 5.32. Horizontally averaged growth rate profiles for cloud ice mass sources. Solid lines correspond to simulations where $\lambda = 0.5$ and dashed lines where $\lambda = 5.0$. Data from 2D_SQUALL simulations.

In the 2D stratocumulus case the impact on the ice production rate had a direct influence on the production and growth of snow. The λ -dependent sMP from the convective simulations is shown in Figure 5.33. For the first hour a similar variation to the iMP can be seen but as a steady state is reached there is no observable dependence on λ ; this similarity in the first hour occurs due to the high magnitude of iMP and consequential conversion into snow. As the simulation progresses the production rate of ice decreases and therefore has less influence on the growth of snow. This can be inferred from Figure 5.34 where the processes of depositional growth of snow and the collection of water substantially dominate the growth of snow; the processes that involve the presence of cloud ice are roughly two orders-of-magnitude lower. This is an opposite effect to what was seen in the stratocumulus case where ice related processes dominated the growth of sMP.

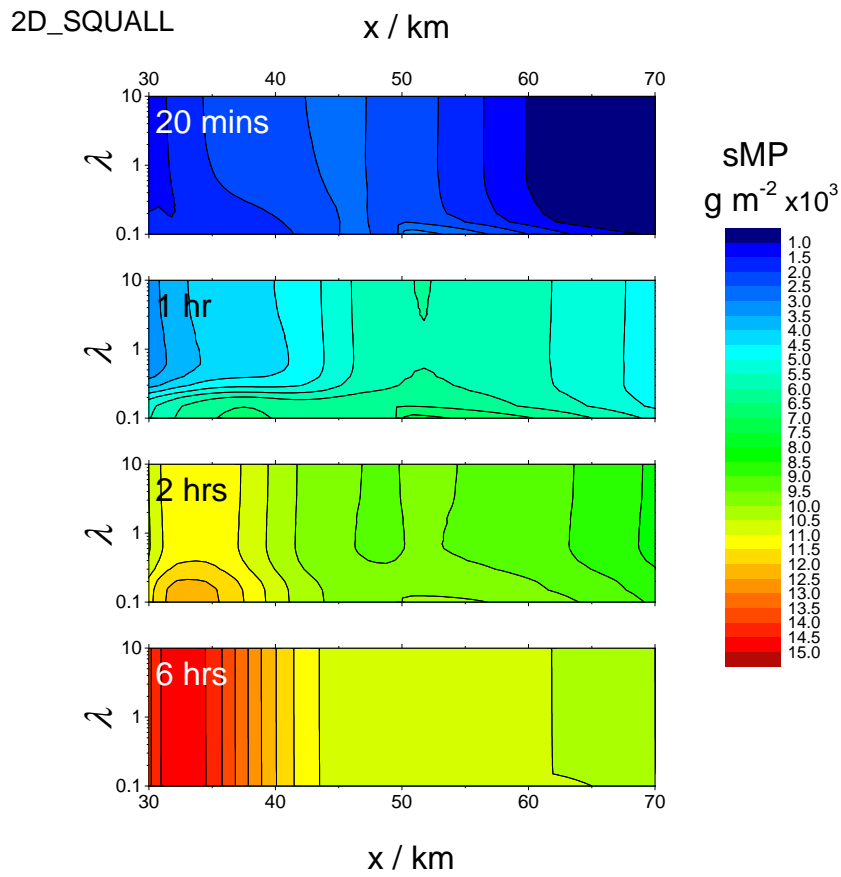


Figure 5.33. . Snow mass path as a function of λ throughout the evolution of the cloud as in Figure 5.31.

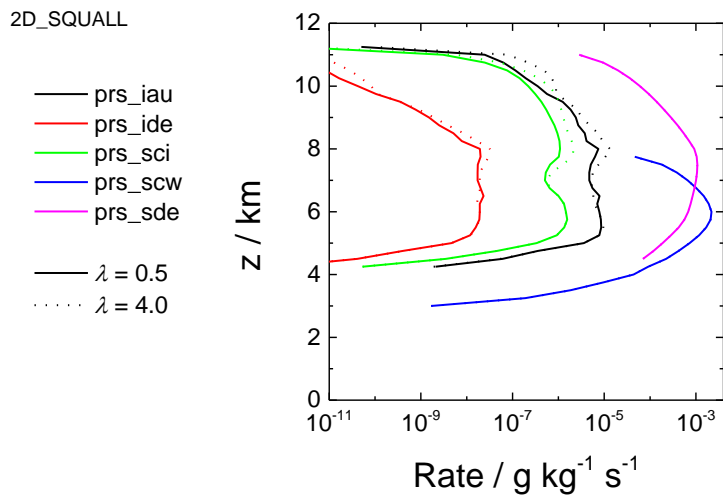


Figure 5.34. Horizontally averaged growth rate profiles for cloud snow mass sources. Solid lines correspond to simulations where $\lambda = 0.5$ and dashed lines where $\lambda = 5.0$. Data from 2D_SQUALL simulations.

2D_SQUALL

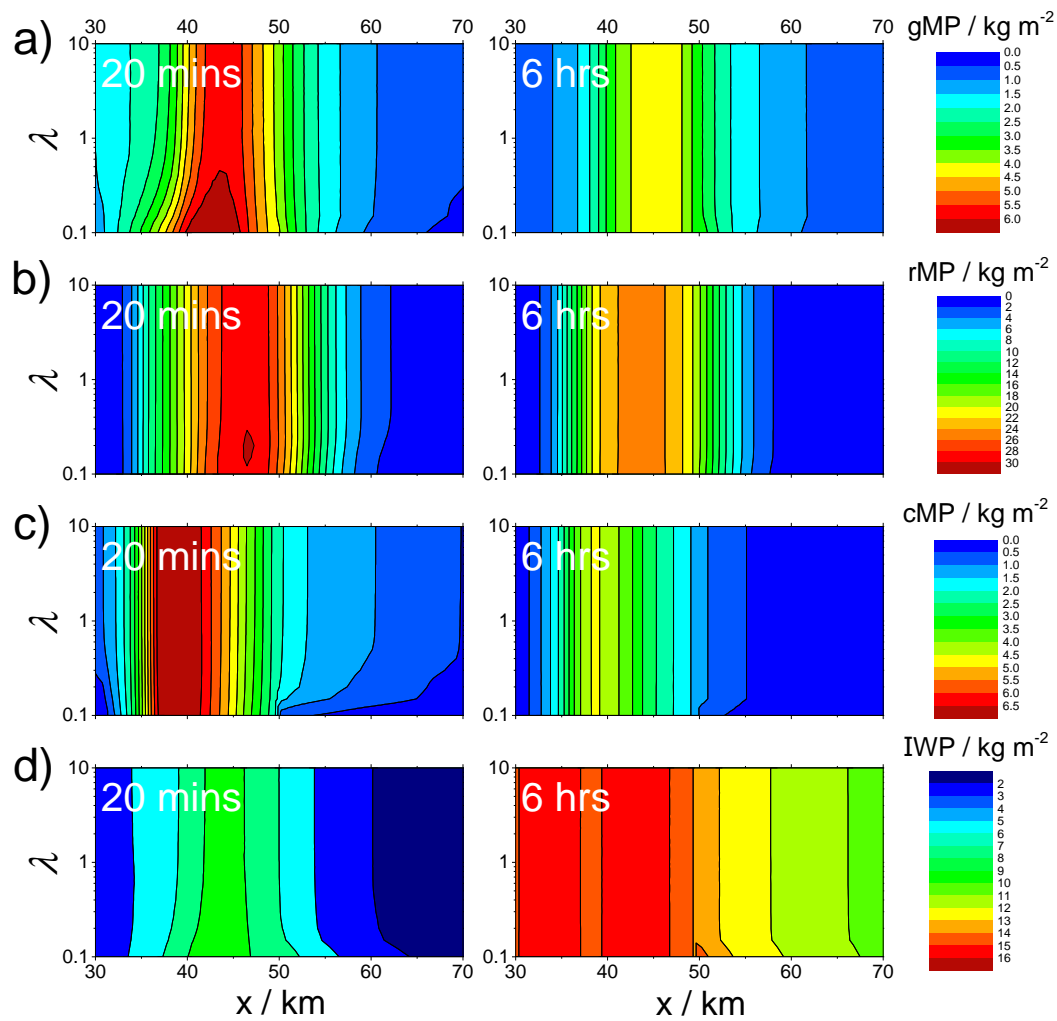


Figure 5.35. Graupel mass path (a), rain mass path (b), cloud water mass path (c), and total ice water path (d) as a function of λ at a simulation time of 20 mins and 6 hrs. Data from 2D_SQUALL simulations.

The sensitivity of the remaining ice and liquid species to λ was also investigated. The graupel, rain, and cloud mass paths along with the ice water path (IWP) are shown in Figure 5.35 at times of 20 mins and 6hrs. Graupel shows a small dependence on λ at the beginning of the simulation but is independent of λ when a steady state is reached. The two liquid species show no dependence throughout the simulation. The total IWC shown in Figure 5.35d is similarly independent of λ which is at odds with the variation seen in the iMP. On inspection of the magnitudes of iMP, sMP, and gMP it is apparent that the IWC is substantially dominated by graupel and snow. The simulations show that time-dependence has a considerable impact on the production of cloud ice for all λ , but the subsequent growth of snow and graupel through interactions with liquid species and water vapour dominates

the IWC. Therefore, in convective cases where the LWC is high time-dependence is not important.

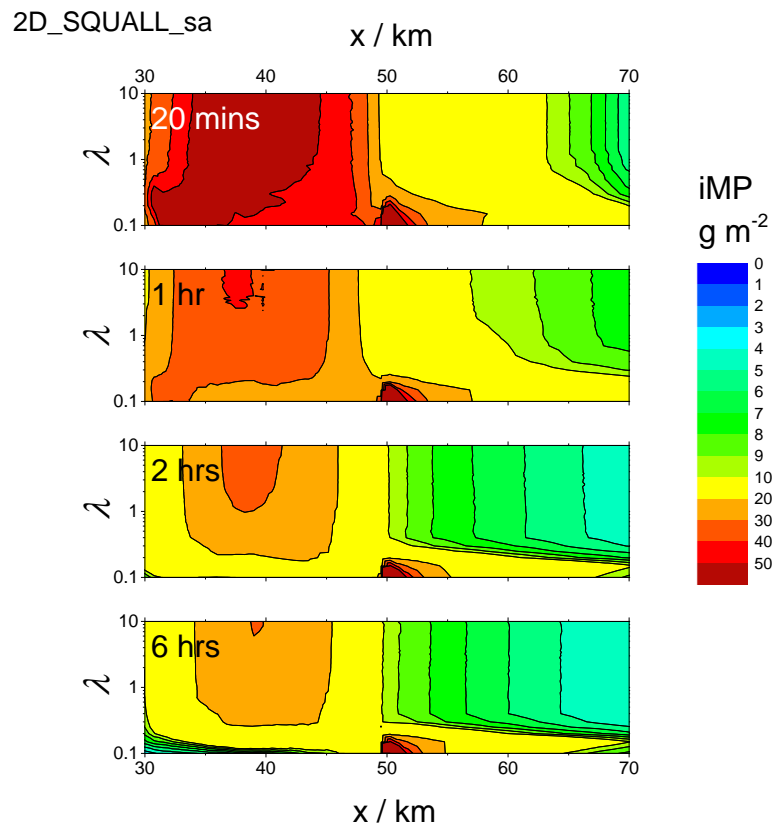


Figure 5.36. Ice mass path as a function of λ throughout the evolution of the cloud for the 2D_SQUALL_sa simulations where s_{K-fe} was increased to $1 \times 10^{-7} \text{ cm}^2$.

In cases where the ice production rate is enhanced further it is possible that the importance of other ice species may be suppressed, and that time-dependence will play a role in the resulting IWC. To test this as in the 2D stratus case the surface area was increased to produce an enhanced ice production rate. The evolution of the iMP in Figure 5.36 shows that the enhanced ice production systematically increases the iMP throughout the simulation. However, on inspection of the corresponding sMP evolution in Figure 5.37 the snow still shows no λ -dependence when a steady state is reached.

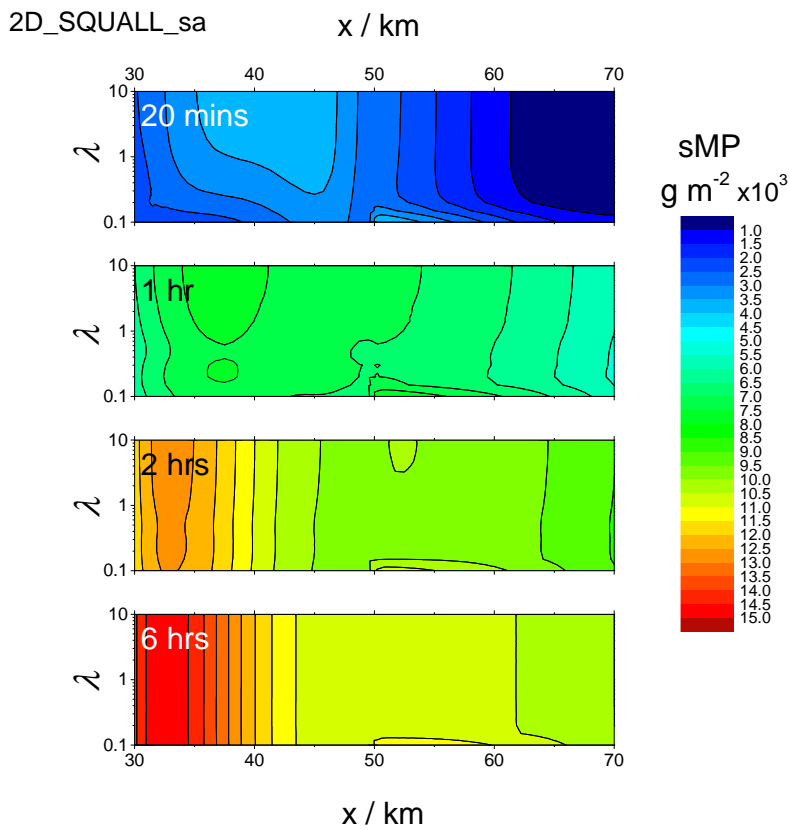


Figure 5.37. Same as Figure 5.36 but for the snow mass path in the 2D_SQUALL_sa simulations.

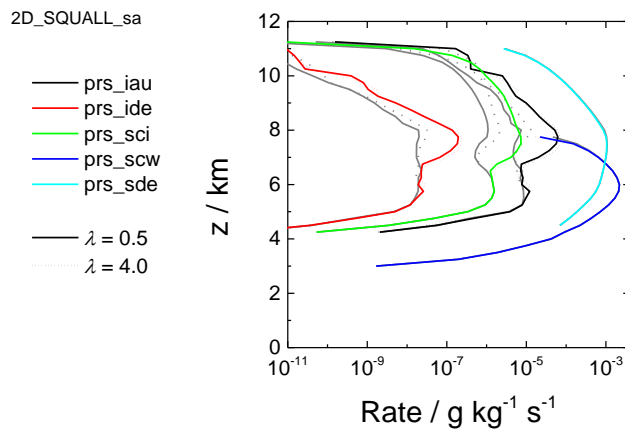


Figure 5.38. Comparing snow mass growth rate profiles from 2D_SQUALL simulations (grey lines) and 2D_SQUALL_sa simulations (coloured lines). Solid lines refer to simulations where $\lambda = 0.5$ and both dashed and dotted lines to simulations where $\lambda = 4.0$.

As observed in Figure 5.33 snow dominated the total IWP in the default simulation, and as seen in Figure 5.34 the growth of snow was dominated by processes that did not depend on

cloud ice. Therefore in order for time-dependent to have an impact on snow the cloud ice interactions must become the dominant growth source of snow. The affect of an increased surface area on snow growth is shown in Figure 5.38 . The enhanced ice production does increase the growth rate of snow via cloud ice processes, but the collection of water and depositional growth from vapour still dominate. However, these latter processes are not affected by the enhanced ice production and suggest that if the surface area was increased further still, or the nucleation rate increased, then the cloud ice would dominate.

5.6 Conclusions

In this chapter the FROST framework was applied to a detailed microphysical model in order to assess, for the first time, the sensitivity of mixed-phase clouds to the time-dependent variability observed in immersion mode freezing experiments.

Results from 0D simulations show that the production of ice via the immersion mode is sensitive to λ at both low and high updraught speeds. This occurs due to the sensitivity of low λ values to the timescale. The λ -dependent variability has a substantial affect on evolution of all other cloud hydrometeors, and also the final state of the cloud. This has implications for radiatively important properties such as liquid and ice water content, hydrometeor sizes, and cloud lifetime.

A series of 1D simulations were performed using arctic stratus cases and a range of convective cases. Clouds with low updraught speeds ($< 1 \text{ m s}^{-1}$) are highly sensitive to the time-dependent properties of the INP population, whereas above $\lambda \approx 4$ time-dependence does not play a significant role. In all arctic stratus cases the lifetime of the mixed-phase state was sensitive to λ ; at low values of λ the substantial ice production rapidly glaciated the clouds, whereas for high vales of λ the slow production rate allowed the cloud to persist for long periods of time. The value of λ at which this regime change occurred varied between cases. A relationship between the variability in immersion mode ice production and other hydrometeor species was observed, as in the 0D simulations.

Finally, a series of 2D simulations were performed using a mixed-phase stratocumulus case and a deep convective case. As in the previous simulations, slow updraught speeds lead to greater λ -dependent variability. In cases such as the stratocumulus where $w_{\max} \leq 1 \text{ m s}^{-1}$, prevalent regions of low updraught speeds lead to an enhanced ice production rate with low values of λ . At very low λ this leads to a rapid glaciation, whereas at high values of λ the cloud persists. In cases with prevalent regions of high updraught speeds, such as the deep convective case where $w \geq 10 \text{ m s}^{-1}$, the ice production rate is also substantially sensitivity to λ . However, in the 2D deep convective simulations the total ice water content was dominated by snow and graupel and therefore the net sensitivity of the cloud to λ was negligible.

Chapter 6: Conclusions, Implications, and Further Work

6.1 Summary of Results

In this thesis the role of time-dependence in immersion mode heterogeneous ice nucleation was investigated. A unique conceptual freezing model was developed and used to understand how time-dependence affects the freezing behaviour in laboratory experiments. Based on the principles of this model a new framework was presented for use in reconciling and reproducing data obtained on different time-scales, and using different experimental techniques. Finally, a new parameterisation was incorporated into a detailed microphysics scheme to assess, for the first time, the sensitivity of mixed-phase clouds to time-dependence in immersion mode ice production.

In *Chapter 2* a Classical Nucleation Theory (CNT) based Multiple-Component Stochastic (MCS) model was used to reproduce K-feldspar and NX-illite droplet freezing data obtained from a range of cooling rates. In both examples the CNT-based MCS model was unable to reproduce the cooling-rate dependence. A series of simulations were used to show that the time-dependence in CNT-based models is primarily a function of temperature, with time-dependent behaviour becoming more apparent with a decreasing temperature.

A new Simplified MCS (Si-MCS) model was developed in order to provide a freezing model that is able to represent the observed variability in time-dependent behaviour. This model allows the temperature dependence (λ) of the nucleation rate coefficient (J_s) to be varied. Data from cooling experiments with K-feldspar were used to determine the time-dependent characteristics of the species, and successfully predict the freezing behaviour of this complex INP species in an isothermal experiment.

A series of simulations were then performed using the Si-MCS model in order to understand the relationship between INP nucleating properties and time-dependent

behaviour in cooling, isothermal, and freeze-thaw experiments. It was found that time-dependent behaviour in all experimental methods is solely dependent on λ . In cooling experiments a change in cooling-rate systematically shifts the cumulative fraction frozen (f) curve by a temperature β which is directly dependent on λ . In isothermal experiments the decay rate of liquid droplets increases with λ , and in freeze-thaw experiments the variability in freezing temperature $\sigma_{T,\text{freeze}}$ also increases with λ . It was additionally found that a freeze-thaw experiment can be simulated using a cooling simulation with a monodisperse population of droplets.

In *Chapter 3* the principles of the Si-MCS were used to derive and develop a novel Framework for Reconciling Observable Stochastic Time-dependence (FROST). The framework uses the relationship between λ and time-dependence to reconcile observational data obtained on different time scales in cooling, isothermal, and freeze-thaw experiments. The FROST framework was then incorporated into a deterministic freezing model to produce a computationally efficient parameterisation for use in cloud modelling studies. The new parameterisation is unique as it is able to accurately represent the variability in both nucleation efficiency and time-dependent behaviour.

The application of the FROST framework was demonstrated in *Chapter 4* using experimental data for K-feldspar, kaolinite (KGa-1b), a kaolinite rich mineral (FLUKA), and a volcanic ash sample from the 2010 Eyjafjallajökull eruption. The determination of characteristic values of λ (which define the time-dependent behaviour) for each INP species shows that the kaolinite and volcanic ash INPs are considerably sensitive to the timescale, whereas the K-feldspar and kaolinite rich mineral were less sensitive. As demonstrated, knowledge of λ can be used with FROST to predict the freezing behaviour of complex INP species in cooling, isothermal and freeze-thaw experiments.

A comprehensive method for determining whether an INP species behaves as a single-component species (constant nucleating efficiency per droplet) or multiple-component species (distinct nucleating efficiency per droplet) species was outlined. Using this method it was found that the kaolinite and volcanic ash samples behave

as single-component species, whilst K-feldspar and the kaolinite rich mineral sample are multiple-component species. This distinction has implications for how f is expected to be affected by changes to the cooling rate or residence time.

FROST was applied to immersion mode freezing data from previous experimental studies and λ values for a wide range of samples were determined. Atmospherically relevant INPs exhibit a wide range in λ ($0.4 \leq \lambda \leq 23$) which corresponds to a wide range in observable time-dependent behaviour ($5.8 \leq \beta \leq 0.1$ for a factor of ten increase in cooling rate). Volcanic ash, and kaolinite (KGa-1b) have the smallest values of λ , whilst Icemax™, Arizona Test Dust (ATD), and K-feldspar consistently have the highest λ values. The majority of the INP species are characterised by $1 \leq \lambda \leq 3$; this range represents a considerable time-dependent variability.

Finally the framework was used to highlight the possible implications for in-situ measurements of INP concentrations using instruments with short residence times. A typical range of $1 \leq \lambda \leq 3$ was used to approximate representative INPs. Assuming the in-situ measurements were obtained using a residence time of 30 s, modelled clouds with low updraught speeds ($w < 1 \text{ m s}^{-1}$) will substantially under-predict the concentration of INPs. For $\lambda = 1$ ($\lambda = 3$) the measured INP concentration only accounts for 15% (50%) of the predicted concentration. The magnitude of the under-prediction will increase with decreasing λ and w . Conversely, modelled clouds where $w > 10 \text{ m s}^{-1}$ will over-predict the INP concentration by between 150% and 500% (for $\lambda = 1$ and $\lambda = 3$ respectively). These results were calculated assuming a single-component system and therefore represent the maximum magnitude; in a multiple-component system the percentage difference would be expected to decrease with increasing nucleating diversity.

In *Chapter 5* the parameterisation from the FROST framework was incorporated into detailed microphysical model. Simulations were then performed in order to determine the sensitivity of mixed-phase clouds to time-dependence in the immersion mode production of ice. Results from idealised 0D simulations show that at extremes of w , ice production is sensitive to λ . Relative to high λ values, low values of λ lead to an enhanced rate of ice

production at low updraught speeds ($w < 1 \text{ m s}^{-1}$) and a suppressed rate at high updraught speeds ($w > 10 \text{ m s}^{-1}$).

Results from 1D and 2D simulations show that the production rate of ice in clouds that exhibit slow updraught speeds ($w < 1 \text{ m s}^{-1}$) such as arctic stratocumulus and mid-latitude stratus, is highly sensitive to the characteristic λ of the INP population. The enhancement, or suppression, of ice production directly affects the development of the cloud and its subsequent bulk properties. This includes radiative properties such as characteristic hydrometeor diameter, liquid and ice water paths, and cloud lifetime. At low values of λ the enhanced ice production results in a rapid glaciation of the cloud, whilst the persistence of the mixed-phase state increases with λ . In deep convective clouds the cloud ice mass is sensitive to λ . However, due to the dominance of other ice hydrometeor species the variability in cloud ice mass has a negligible net impact on the resulting cloud.

6.2 Implications for Experimental Measurements

The results from this thesis highlight the significant role that time-dependence plays in the freezing behaviour of droplets in immersion mode experiments. The implications relate to the accuracy and robustness of the data that is obtained, and to how the data is then used to represent freezing behaviour under conditions outside of those of the experiment.

The relative efficiency of an INP species is typically determined and presented without a consideration for time-dependent effects. Therefore, a nucleation rate function based on this data may be incorrectly describing the nucleating behaviour of the species. For high λ species this may be appropriate but as shown in *Chapter 4* atmospherically relevant INP species exhibit a wide range of characteristic λ values.

An assessment of the relative importance of INP species must take into account the variability in experimental temporal conditions. It is reasonable to suggest that in using a short residence time, or high cooling rate, the relative importance of a species is biased towards those with high values of λ ; the efficiency of low λ species will be increasingly biased towards artificially low values. On application of the FROST framework, data from

cooling and isothermal experiments can be normalised to a standard cooling rate (of 1 °C min^{-1}), which then allows an unbiased comparison of the relative efficiency of different INPs. Additionally, the modelling studies in *Chapter 5* show that the relative importance of an INP species is a function of nucleation efficiency, characteristic λ , and cloud updraught speed. Previously this has been framed simply around the nucleating efficiency and abundance. For example, an abundant but inefficient INP that exhibits a low λ , such as kaolinite ($\lambda = 1.12$), may be more important than the rare but efficient species K-feldspar ($\lambda = 3.4$) in clouds with low updraught speeds.

The modelling studies in *Chapter 5* also show that the correct representation of time-dependence in simulating immersion mode freezing can considerably influence the development of clouds and their resulting bulk properties. The substantial variability observed in some cases demonstrates the need to correctly characterise the time-dependent properties of all atmospherically relevant INPs. The FROST framework provides a simple means for determining this value from experimental data. A second point for consideration is the assumption that all droplets contain a viable INP. The sensitivity studies in *Chapter 5* were performed assuming that every droplet contained a particle with the same nucleating behaviour; atmospheric populations will likely contain a variety of INP species and will likely not be present in every cloud droplet. In the case where a population exhibits diversity in nucleating behaviour (through a range in surface area or species) the more efficient INPs will preferentially freeze first and leave the weaker nucleating droplets. The time-dependent properties of the remaining droplets may then lead to a slow production of ice, and therefore represent a more important subset of INP than the efficient ones. Further work would require the additional use of multiple INP species and a means for prognostically determining the probability that a water droplet or rain droplet will contain a viable INP for immersion mode freezing to occur.

The implications for in-situ INP measurements were demonstrated in *Chapter 4*. The instruments that are currently being used to measure atmospheric INP concentrations do not take time-dependent effects into consideration; this can have a substantial impact on the data that is obtained, and also how it is implemented in models. This supports the

conclusions of Fridlind et al. (2012) and Westbrook and Illingworth (2013) who found that the modelled number of available INPs was insufficient to reproduce their observations of long-lived mixed-phase clouds. Westbrook and Illingworth (2013) proposed that the discrepancy could be as a result of the short timescales used in INP counters. These results support their conclusion. In cases where experimental data may be affected by the temporal conditions, it is possible to normalise the data using the FROST framework. This requires knowledge of λ which can be obtained through either cooling experiments performed at multiple rates, isothermal experiments performed at different temperatures, or a freeze-thaw experiment.

The fundamental process of heterogeneous ice nucleation is still poorly understood. Classical Nucleation Theory (CNT) was shown to be an unrepresentative model for heterogeneous ice nucleation in several cases. This was demonstrated by the failure to reproduce the observed cooling-rate dependence in *Chapter 2* and the failure of CNT to describe the nucleation rate coefficient of kaolinite in *Chapter 4*. Ervens and Feingold (2013) used a CNT-based model in series of simulations and concluded that the timescale played a minor role in immersion mode ice production. Following the results from *Chapter 2* the range of values used in their study corresponds to $\sim 2 \leq \lambda \leq 3$, which when compared to the range of λ for atmospherically relevant INPs presented in *Chapter 4* ($0.6 \leq \lambda \leq \sim 10$) shows that the parameter space that was tested is unrepresentative.

6.3 Implications for Modelling Ice Formation in the Atmosphere

Mixed-phase stratus have been observed to persist for long periods of time (Uttal et al., 2002; Verlinde et al., 2007; de Boer et al., 2009; Shupe et al., 2010) but modelling studies are unable to reproduce this behaviour (Fridlind et al., 2012). Based on observations of long-lived mixed-phase clouds over the UK Westbrook and Illingworth (2013) suggested that this persistence could be described by the slow production of ice through a time-dependent process. The results from *Chapter 5* support this conclusion, and show that the lifetime of the cloud is substantially sensitive to the time-dependent properties of the INP species.

In the simulations performed in *Chapter 5* only a single INP species was considered. In reality the droplet population may be a combination of different INP species and therefore freezing behaviours; Wright et al. (2013) observed that the rainwater samples they collected contained a mixture of dissolved and undissolved aerosol components which could potentially act as multiple constituents. The range in λ shown for the INP species in *Chapter 4* leads to the question of how best to implement time-dependent characteristics for a complex multiple-constituent INP population, where each constituent has a characteristic time-dependence, in a cloud model. The time-dependent behaviour of a population of INPs containing many separate species may be dominated by a single species, and therefore a single value or temperature dependent function of λ . Where distinct species are dominant in different temperature ranges it would be possible to have a temperature dependent function of λ to reflect the relative dominance of each. For multiple-constituent species where no single species is observably dominant, the population of particles/droplets would need to be split into separate populations and treated as an externally mixed population. Whilst many current ice nucleation schemes (Diehl and Wurzler, 2010; Phillips et al., 2008; Barahona, 2012) are capable of describing separate species it may be more realistic to represent a series of dominant components so that the time-dependence and inter-particle variability can be accurately described for a complex, evolving INP population. This may involve an increased computational demand and so the first step in correctly representing time-dependent variability in a cloud model is to determine under which conditions it is an important process to include. To achieve this, the λ characterisation of each component needs to be determined through a series of isothermal, cooling, and freeze-thaw experiments on a representative material. Once λ has been determined for the individual or dominant component of the species then the normalised data can be used with the FROST framework to produce a representative parameterisation.

A second assumption used in *Chapter 5* that should be considered for future work is the assumed availability of INP-containing-droplets. In the simulations it was assumed that each droplet contained a single INP; this is likely an over prediction. Following on from the previous paragraph, the sources and sinks of INP-containing-droplets should primarily be linked to either an aerosol scheme or based on the formation of cloud water droplets.

Secondly, for a multiple-component species or multiple-constituent droplet population the more efficient INPs would be expected to freeze earlier; this would result in a preferential depletion of the more efficient INPs and therefore impact the overall INP distribution. However, a continued entrainment of additional INPs may counteract this behaviour.

6.4 Further Work

The results from this thesis highlight three primary pathways for further work which are all aimed at expanding on current knowledge of heterogeneous ice nucleation. These are summarised below.

6.4.1 Improving Knowledge of Fundamental Heterogeneous Ice Nucleation Mechanisms

The Si-MCS model can be applied to experimental data in order to infer how an INP's physicochemical properties determine its freezing behaviour. This would require a comprehensive experimental dataset where key dependencies are identified, and then systematically varied. In order to limit sporadic events a large number of droplets would ideally be required, along with a system that can be carefully controlled and replicated over many cycles. Microfluidic devices have been previously used in such a manner for homogeneous ice nucleation (Riechers et al., 2013) and other instruments for heterogeneous ice nucleation are in development (Haarig, 2013). These results could be used in conjunction with molecular dynamics simulations to understand the dependencies on a molecular scale. The information from this work could then be used to improve CNT or alternatively, develop a new theoretical framework.

6.4.2 The Continued Characterisation of Atmospherically Relevant INP Species

As demonstrated, the FROST framework provides a comprehensive means for identifying the time-dependent characteristics of INP species, and the Si-MCS provides a means for identifying PDF parameters that describe the inter-particle variability in the ice nucleating efficiency of a species. These may be combined to characterise INP species which would provide a comprehensive dataset of INP properties. As suggested in Sect. 6.3 the use of

representative materials would help constrain the individual behaviour of each component. A comparison between these and complex species could be used to further test the FROST framework and Si-MCS model. The continuation of in-situ measurements, with the added application of FROST, could be used in combination with global modelling studies to develop a representative climatology for use in global cloud modelling studies. As highlighted in Sect. 6.3 it may be appropriate to identify the key INP species in order to reduce complexity.

6.4.3 Improving the Representation of Ice Nucleation in Models

Feedbacks on clouds due to climate change are considered a major uncertainty in climate predictions, with mixed-phase clouds representing a large proportion of this uncertainty (Bony et al., 2006). As shown in this thesis, the representation of time-dependence in the immersion mode can have a substantial impact on the development and properties of the cloud.

Experimental observations should play a more significant role in the development of new heterogeneous ice nucleation parameterisations and schemes; the Bigg immersion mode freezing scheme (Bigg, 1953a) is outdated yet still widely used. This thesis has presented the most comprehensive study into the sensitivity of time-dependent immersion mode freezing behaviour in cloud models; however the representation of this mechanism can be further improved. In order to examine the sensitivity of this, and other freezing modes, the KiD model could be used to understand how other nucleation rate dependencies affect the formation and evolution of mixed-phase clouds. This can be achieved following the progression of results from the further work previously outlined; key dependencies could then be identified and used to produce a new representative ice nucleation scheme. The development of a new INP scheme for use in tracking the sources and sinks of INPs would also improve on the results of this thesis.

References

Ansmann, A., Mattis, I., Müller, D., Wandinger, U., Radlach, M., Althausen, D., and Damoah, R.: Ice formation in Saharan dust over central Europe observed with temperature/humidity/aerosol Raman lidar, *Journal of Geophysical Research: Atmospheres*, 110, D18S12, 10.1029/2004jd005000, 2005.

Ansmann, A., Tesche, M., Seifert, P., Althausen, D., Engelmann, R., Fruntke, J., Wandinger, U., Mattis, I., and Müller, D.: Evolution of the ice phase in tropical altocumulus: SAMUM lidar observations over Cape Verde, *J. Geophys. Res.*, 114, D17208, 10.1029/2008jd011659, 2009.

Atkinson, J. D., Murray, B. J., Woodhouse, M. T., Whale, T. F., Baustian, K. J., Carslaw, K. S., Dobbie, S., O'Sullivan, D., and Malkin, T. L.: The importance of feldspar for ice nucleation by mineral dust in mixed-phase clouds, *Nature*, 498, 355-358, 10.1038/nature12278, 2013.

Barahona, D.: On the ice nucleation spectrum, *Atmos. Chem. Phys.*, 12, 3733-3752, 10.5194/acp-12-3733-2012, 2012.

Berry, E. X., and Reinhardt, R. L.: An Analysis of Cloud Drop Growth by Collection Part II. Single Initial Distributions, *J. Atmos. Sci.*, 31, 1825-1831, 10.1175/1520-0469(1974)031<1825:aaocdg>2.0.co;2, 1974.

Bigg, E. K.: The formation of atmospheric ice crystals by the freezing of droplets, *Q. J. R. Meteorol. Soc.*, 79, 510-519, 10.1002/qj.49707934207, 1953a.

Bigg, E. K.: The Supercooling of Water, *Proceedings of the Physical Society. Section B*, 66, 688, 1953b.

Bodenschatz, E., Malinowski, S. P., Shaw, R. A., and Stratmann, F.: Atmospheric science. Can we understand clouds without turbulence?, *Science*, 327, 970-971, 10.1126/science.1185138, 2010.

Bony, S., Colman, R., Kattsov, V. M., Allan, R. P., Bretherton, C. S., Dufresne, J.-L., Hall, A., Hallegatte, S., Holland, M. M., Ingram, W., Randall, D. A., Soden, B. J., Tselioudis, G., and Webb, M. J.: How Well Do We Understand and Evaluate Climate Change Feedback Processes?, *J. Clim.*, 19, 3445-3482, 10.1175/jcli3819.1, 2006.

Boucher, O., Randall, D., Artaxo, P., Bretherton, C. S., Feingold, G., Forster, P., Kerminen, V. M., Kondo, Y., Liao, H., Lohmann, U., Rasch, P., Satheesh, S. K., Sherwood, S. C., Stevens, B., and Zhang, X. Y.: Clouds and Aerosols. In: *Climate Change 2013: The Physical Science Basis. Contribution of Working Group I to the Fifth Assessment Report of the Intergovernmental Panel on Climate Change*, Cambridge University Press, Cambridge, United Kingdom and New York, NY, USA., 2013.

Broadley, S. L., Murray, B. J., Herbert, R. J., Atkinson, J. D., Dobbie, S., Malkin, T. L., Condliffe, E., and Neve, L.: Immersion mode heterogeneous ice nucleation by an illite rich powder representative of atmospheric mineral dust, *Atmos. Chem. Phys.*, 12, 287-307, 10.5194/acp-12-287-2012, 2012.

Cess, R. D., Potter, G. L., Blanchet, J. P., Boer, G. J., Ghan, S. J., Kiehl, J. T., H, L. E. T., Li, Z. X., Liang, X. Z., Mitchell, J. F., Morcrette, J. J., Randall, D. A., Riches, M. R., Roeckner, E., Schlese, U., Slingo, A., Taylor, K. E., Washington, W. M., Wetherald, R. T., and Yagai, I.: Interpretation of cloud-climate feedback as produced by 14 atmospheric general circulation models, *Science*, 245, 513-516, 10.1126/science.245.4917.513, 1989.

Chen, J. P., Hazra, A., and Levin, Z.: Parameterizing ice nucleation rates using contact angle and activation energy derived from laboratory data, *Atmos. Chem. Phys.*, 8, 7431-7449, 10.5194/acp-8-7431-2008, 2008.

Christner, B. C., Morris, C. E., Foreman, C. M., Cai, R., and Sands, D. C.: Ubiquity of Biological Ice Nucleators in Snowfall, *Science*, 319, 1214, 10.1126/science.1149757, 2008.

Connolly, P. J., Möhler, O., Field, P. R., Saathoff, H., Burgess, R., Choulaton, T., and Gallagher, M.: Studies of heterogeneous freezing by three different desert dust samples, *Atmos. Chem. Phys.*, 9, 2805-2824, 10.5194/acp-9-2805-2009, 2009.

Cooper, W. A.: Ice Initiation in Natural Clouds, *Meteorological Monographs*, 21, 29-32, 10.1175/0065-9401-21.43.29, 1986.

Cox, S. J., Kathmann, S. M., Purton, J. A., Gillan, M. J., and Michaelides, A.: Non-hexagonal ice at hexagonal surfaces: the role of lattice mismatch, *Phys. Chem. Chem. Phys.*, 14, 7944-7949, 10.1039/C2CP23438F, 2012.

Crosier, J., Bower, K. N., Choulaton, T. W., Westbrook, C. D., Connolly, P. J., Cui, Z. Q., Crawford, I. P., Capes, G. L., Coe, H., Dorsey, J. R., Williams, P. I., Illingworth, A. J., Gallagher, M. W., and Blyth, A. M.: Observations of ice multiplication in a weakly convective cell embedded in supercooled mid-level stratus, *Atmos. Chem. Phys.*, 11, 257-273, 10.5194/acp-11-257-2011, 2011.

Cui, Z. Q., Carslaw, K. S., Yin, Y., and Davies, S.: A numerical study of aerosol effects on the dynamics and microphysics of a deep convective cloud in a continental environment, *J Geophys Res-Atmos*, 111, D05201, Artn D05201
Doi 10.1029/2005jd005981, 2006.

Cziczo, D. J., DeMott, P. J., Brock, C., Hudson, P. K., Jesse, B., Kreidenweis, S. M., Prenni, A. J., Schreiner, J., Thomson, D. S., and Murphy, D. M.: A method for single particle mass spectrometry of ice nuclei, *Aerosol Science and Technology*, 37, 460-470, 2003.

de Boer, G., Eloranta, E. W., and Shupe, M. D.: Arctic Mixed-Phase Stratiform Cloud Properties from Multiple Years of Surface-Based Measurements at Two High-Latitude Locations, *J. Atmos. Sci.*, 66, 2874-2887, 10.1175/2009jas3029.1, 2009.

de Boer, G., Morrison, H., Shupe, M. D., and Hildner, R.: Evidence of liquid dependent ice nucleation in high-latitude stratiform clouds from surface remote sensors, *Geophys. Res. Lett.*, 38, L01803, 10.1029/2010gl046016, 2011.

Demott, P. J.: An Exploratory-Study of Ice Nucleation by Soot Aerosols, *J. App. Meteorol.*, 29, 1072-1079, 1990.

DeMott, P. J.: Quantitative descriptions of ice formation mechanisms of silver iodide-type aerosols, *Atmos. Res.*, 38, 63-99, 1995.

DeMott, P. J., Cziczo, D. J., Prenni, A. J., Murphy, D. M., Kreidenweis, S. M., Thomson, D. S., Borys, R., and Rogers, D. C.: Measurements of the concentration and composition of nuclei for cirrus formation, *Proceedings of the National Academy of Sciences of the United States of America*, 100, 14655-14660, 2003a.

DeMott, P. J., Sassen, K., Poellot, M. R., Baumgardner, D., Rogers, D. C., Brooks, S. D., Prenni, A. J., and Kreidenweis, S. M.: African dust aerosols as atmospheric ice nuclei, *Geophys. Res. Lett.*, 30, 1732, 10.1029/2003GL017410, 2003b.

DeMott, P. J., Prenni, A. J., Liu, X., Kreidenweis, S. M., Petters, M. D., Twohy, C. H., Richardson, M. S., Eidhammer, T., and Rogers, D. C.: Predicting global atmospheric ice nuclei distributions and their impacts on climate, *Proceedings of the National Academy of Sciences*, 107, 11217-11222, 10.1073/pnas.0910818107, 2010.

DeMott, P. J., Möhler, O., Stetzer, O., Vali, G., Levin, Z., Petters, M. D., Murakami, M., Leisner, T., Bundke, U., Klein, H., Kanji, Z. A., Cotton, R., Jones, H., Benz, S., Brinkmann, M., Rzesanke, D., Saathoff, H., Nicolet, M., Saito, A., Nillius, B., Bingemer, H., Abbatt, J., Ardon, K., Ganor, E., Georgakopoulos, D. G., and Saunders, C.: Resurgence in Ice Nuclei Measurement Research, *B. Am. Meteorol. Soc.*, 92, 1623-1635, 10.1175/2011bams3119.1, 2011.

Diehl, K., and Wurzler, S.: Heterogeneous Drop Freezing in the Immersion Mode: Model Calculations Considering Soluble and Insoluble Particles in the Drops, *J. Atmos. Sci.*, 61, 2063-2072, doi:10.1175/1520-0469(2004)061<2063:HDFITI>2.0.CO;2, 2004.

Diehl, K., and Wurzler, S.: Air parcel model simulations of a convective cloud: Bacteria acting as immersion ice nuclei, *Atmos. Environ.*, 44, 4622-4628, DOI 10.1016/j.atmosenv.2010.08.003, 2010.

Durant, A. J., and Shaw, R. A.: Evaporation freezing by contact nucleation inside-out, *Geophys. Res. Lett.*, 32, L20814, 10.1029/2005gl024175, 2005.

Eidhammer, T., DeMott, P. J., and Kreidenweis, S. M.: A comparison of heterogeneous ice nucleation parameterizations using a parcel model framework, *J. Geophys. Res.*, 114, D06202, 10.1029/2008jd011095, 2009.

Elbert, W., Taylor, P. E., Andreae, M. O., and Pöschl, U.: Contribution of fungi to primary biogenic aerosols in the atmosphere: wet and dry discharged spores, carbohydrates, and inorganic ions, *Atmos. Chem. Phys.*, 7, 4569-4588, 10.5194/acp-7-4569-2007, 2007.

Ervens, B., and Feingold, G.: On the representation of immersion and condensation freezing in cloud models using different nucleation schemes, *Atmos. Chem. Phys. Discuss.*, 12, 7167-7209, 10.5194/acpd-12-7167-2012, 2012.

Ervens, B., and Feingold, G.: Sensitivities of immersion freezing: Reconciling classical nucleation theory and deterministic expressions, *Geophys. Res. Lett.*, n/a-n/a, 10.1002/grl.50580, 2013.

Field, P. R., Hogan, R. J., Brown, P. R. A., Illingworth, A. J., Choullarton, T. W., and Cotton, R. J.: Parametrization of ice-particle size distributions for mid-latitude stratiform cloud, *Q. J. R. Meteorol. Soc.*, 131, 1997-2017, 10.1256/qj.04.134, 2005.

Field, P. R., Heymsfield, A. J., Shipway, B. J., DeMott, P. J., Pratt, K. A., Rogers, D. C., Stith, J., and Prather, K. A.: Ice in Clouds Experiment–Layer Clouds. Part II: Testing Characteristics of Heterogeneous Ice Formation in Lee Wave Clouds, *J. Atmos. Sci.*, 69, 1066-1079, 10.1175/jas-d-11-026.1, 2012.

Flatau, P. J., Walko, R. L., and Cotton, W. R.: Polynomial Fits to Saturation Vapor Pressure, *J. App. Meteorol.*, 31, 1507-1513, 10.1175/1520-0450(1992)031<1507:pftsvp>2.0.co;2, 1992.

Fletcher, N. H.: *The Physics of Rainclouds*, Science, 3603, Cambridge University Press,= New York, 236 pp., 1962.

Fornea, A. P., Brooks, S. D., Dooley, J. B., and Saha, A.: Heterogeneous freezing of ice on atmospheric aerosols containing ash, soot, and soil, *J Geophys Res-Atmos*, 114, D13201, Artn D13201
Doi 10.1029/2009jd011958, 2009.

Fridlind, A. M., Ackerman, A. S., McFarquhar, G., Zhang, G., Poellot, M. R., DeMott, P. J., Prenni, A. J., and Heymsfield, A. J.: Ice properties of single-layer stratocumulus during the Mixed-Phase Arctic Cloud Experiment: 2. Model results, *J Geophys Res-Atmos*, 112, 2007.

Fridlind, A. M., van Diedenhoven, B., Ackerman, A. S., Avramov, A., Mrowiec, A., Morrison, H., Zuidema, P., and Shupe, M. D.: A FIRE-ACE/SHEBA Case Study of Mixed-Phase Arctic Boundary Layer Clouds: Entrainment Rate Limitations on Rapid Primary Ice Nucleation Processes, *J. Atmos. Sci.*, 69, 365-389, 10.1175/JAS-D-11-052.1, 2012.

Haarig, M.: *Cold-Stage-Experimente zur heterogenen Eisnukleation im Immersionsmodus*, Masters Thesis, Karlsruhe Institute of Technology, 2013.

Hallett, J., and Mossop, S. C.: Production of secondary ice particles during the riming process, *Nature*, 249, 26-28, 1974.

Hobbs, P. V., Bluhm, G. C., and Ohtake, T.: Transport of ice nuclei over the north pacific ocean, *Tellus*, 23, 28-39, 10.1111/j.2153-3490.1971.tb00544.x, 1971.

Hobbs, P. V., and Rangno, A. L.: Ice Particle Concentrations in Clouds, *J. Atmos. Sci.*, 42, 2523-2549, 10.1175/1520-0469(1985)042<2523:IPCIC>2.0.CO;2, 1985.

Hogan, R. J., Behera, M. D., O'Connor, E. J., and Illingworth, A. J.: Estimate of the global distribution of stratiform supercooled liquid water clouds using the LITE lidar, *Geophys. Res. Lett.*, 31, L05106, 10.1029/2003gl018977, 2004.

Hoose, C., and et al.: How important is biological ice nucleation in clouds on a global scale?, *Environ. Res. Lett.*, 5, 024009, 2010.

Hoose, C., and Möhler, O.: Heterogeneous ice nucleation on atmospheric aerosols: a review of results from laboratory experiments, *Atmos. Chem. Phys.*, 12, 9817-9854, 10.5194/acp-12-9817-2012, 2012.

Hoyle, C. R., Pinti, V., Welti, A., Zobrist, B., Marcolli, C., Luo, B., Höskuldsson, Á., Mattsson, H. B., Stetzer, O., Thorsteinsson, T., Larsen, G., and Peter, T.: Ice nucleation properties of

volcanic ash from Eyjafjallajökull, *Atmos. Chem. Phys.*, 11, 9911-9926, 10.5194/acp-11-9911-2011, 2011.

Hu, X. L., and Michaelides, A.: Ice formation on kaolinite: Lattice match or amphotericism?, *Surface Science*, 601, 5378-5381, doi.org/10.1016/j.susc.2007.09.012, 2007.

Hu, Y., Rodier, S., Xu, K.-m., Sun, W., Huang, J., Lin, B., Zhai, P., and Josset, D.: Occurrence, liquid water content, and fraction of supercooled water clouds from combined CALIOP/IIR/MODIS measurements, *Journal of Geophysical Research: Atmospheres*, 115, D00H34, 10.1029/2009JD012384, 2010.

Huang, J., Minnis, P., Chen, B., Huang, Z., Liu, Z., Zhao, Q., Yi, Y., and Ayers, J. K.: Long-range transport and vertical structure of Asian dust from CALIPSO and surface measurements during PACDEX, *J. Geophys. Res.*, 113, D23212, 10.1029/2008jd010620, 2008.

Hudson, P. K., Murphy, D. M., Cziczo, D. J., Thomson, D. S., de Gouw, J. A., Warneke, C., Holloway, J., Jost, J. R., and Hubler, G.: Biomass-burning particle measurements: Characteristic composition and chemical processing, *J Geophys Res-Atmos*, 109, 2004.

Isono, K., Komabayasi, M., and Ono, A.: Volcanoes as a Source of Atmospheric Ice Nuclei, *Nature*, 183, 317-318, Doi 10.1038/183317a0, 1959.

Kanitz, T., Seifert, P., Ansmann, A., Engelmann, R., Althausen, D., Casiccia, C., and Rohwer, E. G.: Contrasting the impact of aerosols at northern and southern midlatitudes on heterogeneous ice formation, *Geophys. Res. Lett.*, 38, L17802, 10.1029/2011gl048532, 2011.

Khvorostyanov, V. I., and Curry, J. A.: The Theory of Ice Nucleation by Heterogeneous Freezing of Deliquescent Mixed CCN. Part I: Critical Radius, Energy, and Nucleation Rate, *J. Atmos. Sci.*, 61, 2676-2691, doi:10.1175/JAS3266.1, 2004.

Klein, H., Nickovic, S., Haunold, W., Bundke, U., Nillius, B., Ebert, M., Weinbruch, S., Schuetz, L., Levin, Z., Barrie, L. A., and Bingemer, H.: Saharan dust and ice nuclei over Central Europe, *Atmos. Chem. Phys.*, 10, 10211-10221, DOI 10.5194/acp-10-10211-2010, 2010.

Knippertz, P., and Todd, M. C.: Mineral dust aerosols over the Sahara: Meteorological controls on emission and transport and implications for modeling, *Rev. Geophys.*, 50, RG1007, 10.1029/2011rg000362, 2012.

Kokhanovsky, A.: Optical properties of terrestrial clouds, *Earth-Sci. Rev.*, 64, 189-241, [http://dx.doi.org/10.1016/S0012-8252\(03\)00042-4](http://dx.doi.org/10.1016/S0012-8252(03)00042-4), 2004.

Koop, T.: Homogeneous ice nucleation in water and aqueous solutions, *Zeitschrift Fur Physikalische Chemie-International Journal of Research in Physical Chemistry & Chemical Physics*, 218, 1231-1258, 2004.

Kumai, M.: Electron-microscope study of snow-crystal nuclei, *Journal of Meteorology*, 8, 151-156, doi:10.1175/1520-0469(1951)008<0151:EMSOSC>2.0.CO;2, 1951.

Kumai, M.: Snow crystals and the identification of the nuclei in the northern Unites States of America, *Journal of Meteorology*, 18, 139-150, doi:10.1175/1520-0469(1961)018<0139:SCATIO>2.0.CO;2, 1961.

Leonard, B. P.: Positivity-preserving numerical schemes for multidimensional advection, National Aeronautics and Space Administration ; National Technical Information Service, distributor, [Washington, DC] : [Springfield, Va., 1993.

Lindow, S. E., Lahue, E., Govindarajan, A. G., Panopoulos, N. J., and Gies, D.: Localization of ice nucleation activity and the iceC gene product in *Pseudomonas syringae* and *Escherichia coli*, *Molecular plant-microbe interactions : MPMI*, 2, 262-272, 1989.

Lüönd, F., Stetzer, O., Welti, A., and Lohmann, U.: Experimental study on the ice nucleation ability of size-selected kaolinite particles in the immersion mode, *J. Geophys. Res.*, 115, D14201, 10.1029/2009jd012959, 2010.

Ma, H. Y., Köhler, M., Li, J. L. F., Farrara, J. D., Mechoso, C. R., Forbes, R. M., and Waliser, D. E.: Evaluation of an ice cloud parameterization based on a dynamical-microphysical lifetime concept using CloudSat observations and the ERA-Interim reanalysis, *Journal of Geophysical Research: Atmospheres*, 117, D05210, 10.1029/2011JD016275, 2012.

Marcocoli, C., Gedamke, S., Peter, T., and Zobrist, B. A.: Efficiency of immersion mode ice nucleation on surrogates of mineral dust, *Atmos. Chem. Phys.*, 7, 5081-5091, 10.5194/acp-7-5081-2007, 2007.

Mason, B.: *The Physics of Clouds*, Clarendon Press, Oxford, UK, 1971.

McFarquhar, G. M., Zhang, G., Poellot, M. R., Kok, G. L., McCoy, R., Tooman, T., Fridlind, A., and Heymsfield, A. J.: Ice properties of single-layer stratocumulus during the Mixed-Phase Arctic Cloud Experiment: 1. Observations, *J Geophys Res-Atmos*, 112, 2007.

Meyers, M. P., Demott, P. J., and Cotton, W. R.: New Primary Ice-Nucleation Parameterizations in an Explicit Cloud Model, *J. App. Meteorol.*, 31, 708-721, 1992.

Möhler, O., Field, P. R., Connolly, P., Benz, S., Saathoff, H., Schnaiter, M., Wagner, R., Cotton, R., Kramer, M., Mangold, A., and Heymsfield, A. J. A.: Efficiency of the deposition mode ice nucleation on mineral dust particles, *Atmos. Chem. Phys.*, 6, 3007-3021, 10.5194/acp-6-3007-2006, 2006.

Morrison, H., and Grabowski, W. W.: Comparison of Bulk and Bin Warm-Rain Microphysics Models Using a Kinematic Framework, *J. Atmos. Sci.*, 64, 2839-2861, doi:10.1175/JAS3980, 2007.

Morrison, H., and Grabowski, W. W.: A Novel Approach for Representing Ice Microphysics in Models: Description and Tests Using a Kinematic Framework, *J. Atmos. Sci.*, 65, 1528-1548, doi:10.1175/2007JAS2491.1, 2008.

Morrison, H., de Boer, G., Feingold, G., Harrington, J., Shupe, M. D., and Sulia, K.: Resilience of persistent Arctic mixed-phase clouds, *Nature Geosci*, 5, 11-17, 2012.

Murray, B. J., Broadley, S. L., Wilson, T. W., Bull, S. J., Wills, R. H., Christenson, H. K., and Murray, E. J.: Kinetics of the homogeneous freezing of water, *Phys. Chem. Chem. Phys.*, 12, 10380-10387, 10.1039/c003297b, 2010.

Murray, B. J., Broadley, S. L., Wilson, T. W., Atkinson, J. D., and Wills, R. H.: Heterogeneous freezing of water droplets containing kaolinite particles, *Atmos. Chem. Phys.*, 11, 4191-4207, 10.5194/acp-11-4191-2011, 2011.

Murray, B. J., O'Sullivan, D., Atkinson, J. D., and Webb, M. E.: Ice nucleation by particles immersed in supercooled cloud droplets, *Chem Soc Rev*, 41, 6519-6554, 10.1039/c2cs35200a, 2012.

Myhre, G., Shindell, D. T., Breon, F. M., Collins, W., Fuglestevidt, J., Huang, J., Koch, D., Lamarque, J.-F., Lee, D., Mendoza, B., Nakajima, T., Robock, A., Stephens, G., Takemura, T., and Zhang, H.: The Physical Science Basis. Contribution of Working Group I to the Fifth Assessment Report of the Intergovernmental Panel on Climate Change, Cambridge University Press, Cambridge, United Kingdom and New York, NY, USA., 2013.

Nasiri, S. L., and Kahn, B. H.: Limitations of Bispectral Infrared Cloud Phase Determination and Potential for Improvement, *Journal of Applied Meteorology and Climatology*, 47, 2895-2910, 10.1175/2008JAMC1879.1, 2008.

Niedermeier, D., Hartmann, S., Clauss, T., Wex, H., Kiselev, A., Sullivan, R. C., DeMott, P. J., Petters, M. D., Reitz, P., Schneider, J., Mikhailov, E., Sierau, B., Stetzer, O., Reimann, B., Bundke, U., Shaw, R. A., Buchholz, A., Mentel, T. F., and Stratmann, F.: Experimental study of the role of physicochemical surface processing on the IN ability of mineral dust particles, *Atmos. Chem. Phys.*, 11, 11131-11144, 10.5194/acp-11-11131-2011, 2011.

Phillips, V. T. J., Choullarton, T. W., Illingworth, A. J., Hogan, R. J., and Field, P. R.: Simulations of the glaciation of a frontal mixed-phase cloud with the Explicit Microphysics Model, *Q. J. R. Meteorol. Soc.*, 129, 1351-1371, 2003.

Phillips, V. T. J., Donner, L. J., and Garner, S. T.: Nucleation Processes in Deep Convection Simulated by a Cloud-System-Resolving Model with Double-Moment Bulk Microphysics, *J. Atmos. Sci.*, 64, 738-761, 10.1175/JAS3869.1, 2007.

Phillips, V. T. J., DeMott, P. J., and Andronache, C.: An Empirical Parameterization of Heterogeneous Ice Nucleation for Multiple Chemical Species of Aerosol, *J. Atmos. Sci.*, 65, 2757-2783, doi:10.1175/2007JAS2546.1, 2008.

Popovicheva, O., Kireeva, E., Persiantseva, N., Khokhlova, T., Shonija, N., Tishkova, V., and Demirdjian, B.: Effect of soot on immersion freezing of water and possible atmospheric implications, *Atmos. Res.*, 90, 326-337, doi.org/10.1016/j.atmosres.2008.08.004, 2008.

Pratt, K. A., DeMott, P. J., French, J. R., Wang, Z., Westphal, D. L., Heymsfield, A. J., Twohy, C. H., Prenni, A. J., and Prather, K. A.: In situ detection of biological particles in cloud ice-crystals, *Nature Geosci*, 2, 398-401, 10.1038/ngeo521, 2009.

Prenni, A. J., Demott, P. J., Rogers, D. C., Kreidenweis, S. M., McFarquhar, G. M., Zhang, G., and Poellot, M. R.: Ice nuclei characteristics from M-PACE and their relation to ice formation in clouds, *Tellus B*, 61, 436-448, 10.1111/j.1600-0889.2009.00415.x, 2009a.

Prenni, A. J., Petters, M. D., Kreidenweis, S. M., Heald, C. L., Martin, S. T., Artaxo, P., Garland, R. M., Wollny, A. G., and Poschl, U.: Relative roles of biogenic emissions and Saharan dust as ice nuclei in the Amazon basin, *Nature Geosci*, 2, 402-405, 2009b.

- Prospero, J. M., Bullard, J. E., and Hodgkins, R.: High-Latitude Dust Over the North Atlantic: Inputs from Icelandic Proglacial Dust Storms, *Science*, 335, 1078-1082, 2012.
- Pruppacher, H. R., and Klett, J. D.: *Microphysics of Clouds and Precipitation*, 2 ed., Kulwer Academic Publishers, Dordrecht, 1997.
- Pummer, B. G., Bauer, H., Bernardi, J., Bleicher, S., and Grothe, H.: Suspensible macromolecules are responsible for ice nucleation activity of birch and conifer pollen, *Atmos. Chem. Phys.*, 12, 2541-2550, 10.5194/acp-12-2541-2012, 2012.
- Randall, D., Khairoutdinov, M., Arakawa, A., and Grabowski, W.: Breaking the Cloud Parameterization Deadlock, *B. Am. Meteorol. Soc.*, 84, 1547-1564, 10.1175/BAMS-84-11-1547, 2003.
- Reisin, T., Levin, Z., and Tzivion, S.: Rain Production in Convective Clouds As Simulated in an Axisymmetric Model with Detailed Microphysics. Part I: Description of the Model, *J. Atmos. Sci.*, 53, 497-519, doi:10.1175/1520-0469(1996)053<0497:RPICCA>2.0.CO;2, 1996.
- Richardson, M. S., DeMott, P. J., Kreidenweis, S. M., Cziczo, D. J., Dunlea, E. J., Jimenez, J. L., Thomson, D. S., Ashbaugh, L. L., Borys, R. D., Westphal, D. L., Casuccio, G. S., and Lersch, T. L.: Measurements of heterogeneous ice nuclei in the western United States in springtime and their relation to aerosol characteristics, *J Geophys Res-Atmos*, 112, 2007.
- Riechers, B., Wittbracht, F., Hutten, A., and Koop, T.: The homogeneous ice nucleation rate of water droplets produced in a microfluidic device and the role of temperature uncertainty, *Phys. Chem. Chem. Phys.*, 10.1039/C3CP42437E, 2013.
- Riihimaki, L. D., and McFarlane, S. A.: Frequency and morphology of tropical tropopause layer cirrus from CALIPSO observations: Are isolated cirrus different from those connected to deep convection?, *Journal of Geophysical Research: Atmospheres*, 115, D18201, 10.1029/2009JD013133, 2010.
- Rogers, D. C., DeMott, P. J., Kreidenweis, S. M., and Chen, Y. L.: Measurements of ice nucleating aerosols during SUCCESS, *Geophys. Res. Lett.*, 25, 1383-1386, 1998.
- Rogers, D. C., DeMott, P. J., and Kreidenweis, S. M.: Airborne measurements of tropospheric ice-nucleating aerosol particles in the Arctic spring, *J Geophys Res-Atmos*, 106, 15053-15063, 2001.
- Sassen, K.: Indirect climate forcing over the western US from Asian dust storms, *Geophys. Res. Lett.*, 29, 2002.
- Sear, R. P.: Generalisation of Levine's prediction for the distribution of freezing temperatures of droplets: a general singular model for ice nucleation, *Atmos. Chem. Phys.*, 13, 7215-7223, 10.5194/acp-13-7215-2013, 2013.
- Shipway, B. J., and Hill, A. A.: *The Kinematic Driver model (KiD)*, Met Office, 2011.
- Shipway, B. J., and Hill, A. A.: Diagnosis of systematic differences between multiple parametrizations of warm rain microphysics using a kinematic framework, *Q. J. R. Meteorol. Soc.*, n/a-n/a, 10.1002/qj.1913, 2012.

Shupe, M. D., Walden, V. P., Eloranta, E., Uttal, T., Campbell, J. R., Starkweather, S. M., and Shiobara, M.: Clouds at Arctic Atmospheric Observatories. Part I: Occurrence and Macrophysical Properties, *Journal of Applied Meteorology and Climatology*, 50, 626-644, 10.1175/2010JAMC2467.1, 2010.

Slawinska, J., Grabowski, W. W., and Morrison, H.: The impact of atmospheric aerosols on precipitation from deep organized convection: A prescribed-flow model study using double-moment bulk microphysics, *Q. J. R. Meteorol. Soc.*, 135, 1906-1913, 10.1002/qj.450, 2009.

Steinke, I., Möhler, O., Kiselev, A., Niemand, M., Saathoff, H., Schnaiter, M., Skrotzki, J., Hoose, C., and Leisner, T.: Ice nucleation properties of fine ash particles from the Eyjafjallajökull eruption in April 2010, *Atmos. Chem. Phys.*, 11, 12945-12958, 10.5194/acp-11-12945-2011, 2011.

Straka, J. M.: Cloud and Precipitation Microphysics, *Boundary-Layer Meteorol.*, 135, 177-178, 10.1007/s10546-009-9454-7, 2010.

Sun, J., and Ariya, P. A.: Atmospheric organic and bio-aerosols as cloud condensation nuclei (CCN): A review, *Atmos. Environ.*, 40, 795-820, doi.org/10.1016/j.atmosenv.2005.05.052, 2006.

Thompson, G., Field, P. R., Rasmussen, R. M., and Hall, W. D.: Explicit Forecasts of Winter Precipitation Using an Improved Bulk Microphysics Scheme. Part II: Implementation of a New Snow Parameterization, *Monthly Weather Review*, 136, 5095-5115, 10.1175/2008mwr2387.1, 2008.

Tompkins, A. M.: Organization of Tropical Convection in Low Vertical Wind Shears: The Role of Water Vapor, *J. Atmos. Sci.*, 58, 529-545, 10.1175/1520-0469(2001)058<0529:OOTCIL>2.0.CO;2, 2001.

Uttal, T., Curry, J. A., McPhee, M. G., Perovich, D. K., Moritz, R. E., Maslanik, J. A., Guest, P. S., Stern, H. L., Moore, J. A., Turenne, R., Heiberg, A., Serreze, M. C., Wylie, D. P., Persson, O. G., Paulson, C. A., Halle, C., Morison, J. H., Wheeler, P. A., Makshtas, A., Welch, H., Shupe, M. D., Intrieri, J. M., Stamnes, K., Lindsey, R. W., Pinkel, R., Pegau, W. S., Stanton, T. P., and Grenfeld, T. C.: Surface Heat Budget of the Arctic Ocean, *B. Am. Meteorol. Soc.*, 83, 255-275, doi:10.1175/1520-0477(2002)083<0255:SHBOTA>2.3.CO;2, 2002.

Vali, G., and Stansbury, E. J.: Time-Dependent characteristics of the heterogeneous nucleation of ice, *Canadian Journal of Physics*, 44, 477 - 502, 10.1139/p66-044, 1966.

Vali, G.: Nucleation terminology, *J. Aerosol Sci.*, 16, 575-576, doi.org/10.1016/0021-8502(85)90009-6, 1985.

Vali, G.: Freezing Rate Due to Heterogeneous Nucleation, *J. Atmos. Sci.*, 51, 1843-1856, doi:10.1175/1520-0469(1994)051<1843:FRDTHN>2.0.CO;2, 1994.

Vali, G.: Repeatability and randomness in heterogeneous freezing nucleation, *Atmos. Chem. Phys.*, 8, 5017-5031, 10.5194/acp-8-5017-2008, 2008.

Vardiman, L.: The Generation of Secondary Ice Particles in Clouds by Crystal-Crystal Collision, *J. Atmos. Sci.*, 35, 2168-2180, 10.1175/1520-0469(1978)035<2168:TGOSIP>2.0.CO;2, 1978.

Verlinde, J., Flatau, P. J., and Cotton, W. R.: Analytical Solutions to the Collection Growth Equation: Comparison with Approximate Methods and Application to Cloud Microphysics Parameterization Schemes, *J. Atmos. Sci.*, 47, 2871-2880, 10.1175/1520-0469(1990)047<2871:asttcg>2.0.co;2, 1990.

Verlinde, J., Harrington, J. Y., McFarquhar, G. M., Yannuzzi, V. T., Avramov, A., Greenberg, S., Johnson, N., Zhang, G., Poellot, M. R., Mather, J. H., Turner, D. D., Eloranta, E. W., Zak, B. D., Prenni, A. J., Daniel, J. S., Kok, G. L., Tobin, D. C., Holz, R., Sassen, K., Spangenberg, D., Minnis, P., Tooman, T. P., Ivey, M. D., Richardson, S. J., Bahrmann, C. P., Shupe, M., DeMott, P. J., Heymsfield, A. J., and Schofield, R.: The mixed-phase Arctic cloud experiment, *B. Am. Meteorol. Soc.*, 88, 205-+, 2007.

Welti, A., Lüönd, F., Kanji, Z. A., Stetzer, O., and Lohmann, U.: Time dependence of immersion freezing, *Atmos. Chem. Phys. Discuss.*, 12, 12623-12662, 10.5194/acpd-12-12623-2012, 2012.

Westbrook, C. D., and Illingworth, A. J.: Evidence that ice forms primarily in supercooled liquid clouds at temperatures $> -27\text{C}$, *Geophys. Res. Lett.*, 38, 10.1029/2011gl048021, 2011.

Westbrook, C. D., and Illingworth, A. J.: The formation of ice in a long-lived supercooled layer cloud, *Q. J. R. Meteorol. Soc.*, 139, 2209-2221, 10.1002/qj.2096, 2013.

Whale, T. F., Murray, B. J., O'Sullivan, D., Umo, N. S., Baustian, K. J., Atkinson, J. D., and Morris, G. J.: A technique for quantifying rare ice nucleation events, *In prep.*, 2014.

Winiwarter, W., Bauer, H., Caseiro, A., and Puxbaum, H.: Quantifying emissions of primary biological aerosol particle mass in Europe, *Atmos. Environ.*, 43, 1403-1409, doi.org/10.1016/j.atmosenv.2008.01.037, 2009.

Wright, T. P., and Petters, M. D.: The role of time in heterogeneous freezing nucleation, *Journal of Geophysical Research: Atmospheres*, 118, 3731-3743, 10.1002/jgrd.50365, 2013.

Wright, T. P., Petters, M. D., Hader, J. D., Morton, T., and Holder, A. L.: Minimal cooling rate dependence of ice nuclei activity in the immersion mode, *Journal of Geophysical Research: Atmospheres*, 118, 50535-510,543, 10.1002/jgrd.50810, 2013.

Zobrist, B., Koop, T., Luo, B. P., Marcolli, C., and Peter, T.: Heterogeneous Ice Nucleation Rate Coefficient of Water Droplets Coated by a Nonadecanol Monolayer, *The Journal of Physical Chemistry C*, 111, 2149-2155, 10.1021/jp066080w, 2007.

The end.